TITLE PAGE

UNIVERSITI TEKNOLOGI PETRONAS

Markov-Gibbs Random Field Approach for Modeling of Skin Surface Textures

By

Nazr e Batool

A THESIS

SUBMITTED TO THE POSTGRADUATE STUDIES PROGRAMME AS A

REQUIREMENT FOR THE

DEGREE OF MASTER OF SCIENCE

ELECTRICAL AND ELECTRONICS ENGINEERING

BANDAR SERI ISKANDAR,

PERAK

2008

STATUS OF THESIS

Title of thesis | **Markov-Gibbs Random Field Approach for Modeling of Skin Surface Textures**

I, NAZR E BATOOL ,

hereby allow my thesis to be placed at the Information Resource Center (IRC) of Universiti Teknologi PETRONAS (UTP) with the following conditions:

1. The thesis becomes the properties of UTP.
2. The IRC of UTP may make copies of the thesis for academic purposes only.
3. This thesis is classified as

☐ Confidential

☑ Non-confidential

If this thesis is confidential, please state the reason:

\-

The contents of the thesis will remain confidential for - years.

Remarks on disclosure:

\-

Endorsed by

Signature of Author

H. 392, St. 167,
G 11/1, Islamabad,
Pakistan.

Date : 3/3/08

Signature of Supervisor

Prof. Dr. Ahmad Fadzil M. Hani

Universiti Teknologi
PETRONAS

Date : 3.7.2008

UNIVERSITI TEKNOLOGI PETRONAS

Approval by Supervisor (s)

The undersigned certify that they have read, and recommend to The Postgraduate Studies Programme for acceptance, a thesis entitled "Markov-Gibbs Random Field Approach for Modeling of Skin Surface Textures" submitted by (Nazr e Batool) for the fulfillment of requirements for the degree of Master of Science in Electrical and Electronics Engineering.

Date 3/3/08

Signature :

Main supervisor : Prof. Dr. Ahmad Fadzil M. Hani

Date : 3-3-2008

Signature :

Co-Supervisor : Dr. Vooi Voon Yap

Date : 3/3/2008

TITLE PAGE

UNIVERSITI TEKNOLOGI PETRONAS

Markov-Gibbs Random Field Approach for Modeling of Skin Surface Textures

By

Nazr e Batool

A THESIS

SUBMITTED TO THE POSTGRADUATE STUDIES PROGRAMME AS A

REQUIREMENT FOR THE

DEGREE OF MASTER OF SCIENCE

ELECTRICAL AND ELECTRONICS ENGINEERING

BANDAR SERI ISKANDAR,

PERAK

2008

DECLARATION

I hereby declare that the thesis is based on my original work except for quotations and citations which have been duly acknowledged. I also declare that it has not been previously or concurrently submitted for any other degree at UTP or other institutions.

Signature : 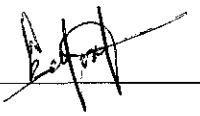

Name : NAZR E BATOOL

Date : 3/3/08

This thesis is dedicated to my parents.

To my mother ... my strength

To my father ... my guidance

ACKNOWLEDGEMENT

I am sincerely thankful to my advisors Prof. Ahmad Fadzil M. Hani and Dr. Vooi Voon Yap. This thesis would not have been possible without their guidance and support. Prof. Fadzil's desire to introduce computer-based tactile inspection for dermatology was a major inspiration for this work. Under their supervision, it was possible to accomplish this thesis by merging technologies of Stochastic Image Processing, 3D Computer Graphics and Haptic Technology for Skin Imaging.

I greatly appreciate the help of Puan Sri Dr. Suriya H. Hussein and Dr. Azura Affandi, Dermatology Department, Hospital Kuala Lumpur, for their effort in helping and providing me with all the data that was necessary to conduct this research.

I would also like to acknowledge Prof. Georgy Gimel'farb (Department of Computer Science, University of Auckland, New Zealand), Prof. Maria Petrou and Dr. Daniel Heesch (Department of Electrical and Electronics Engineering, Imperial College, London, UK). Their suggestions helped me in developing MATLAB code for texture analysis and synthesis for this work.

Special thanks also to my postgraduate research fellows Dani Ihtatho, Hermawan Nugroho and Maryam Mahsal Khan. They helped me and encouraged me in my tough times during this research work.

Last but not the least, I would express my gratitude to my friend Ms. Illani Nawi (Lecturer, Electrical and Electronics Engineering Department, UTP) who was always there to help me out on countless occasions.

ABSTRACT

Medical imaging has been contributing to dermatology by providing computer-based assistance by 2D digital imaging of skin and processing of images. Skin imaging can be more effective by inclusion of 3D skin features. Furthermore, clinical examination of skin consists of both visual and tactile inspection. The tactile sensation is related to 3D surface profiles and mechanical parameters. The 3D imaging of skin can also be integrated with haptic technology for computer-based tactile inspection. The research objective of this work is to model 3D surface textures of skin. A 3D image acquisition set up capturing skin surface textures at high resolution (~0.1 mm) has been used. An algorithm to extract 2D grayscale texture (height map) from 3D texture has been presented. The extracted 2D textures are then modeled using Markov-Gibbs random field (MGRF) modeling technique. The modeling results for MGRF model depend on input texture characteristics. The homogeneous, spatially invariant texture patterns are modeled successfully. From the observation of skin samples, we classify three key features of 3D skin profiles i.e. curvature of underlying limb, wrinkles/line like features and fine textures. The skin samples are distributed in three input sets to see the MGRF model's response to each of these 3D features. First set consists of all three features. Second set is obtained after elimination of curvature and contains both wrinkle/line like features and fine textures. Third set is also obtained after elimination of curvature but consists of fine textures only.

MGRF modeling for set 1 did not result in any visual similarity. Hence the curvature of underlying limbs cannot be modeled successfully and makes an inhomogeneous feature. For set 2 the wrinkle/line like features can be modeled with low/medium visual similarity depending on the spatial invariance. The results for set 3 show that fine textures of skin are almost always modeled successfully with medium/high visual similarity and make a homogeneous feature. We conclude that the MGRF model is able to model fine textures of skin successfully which are on scale of ~ 0.1 mm. The surface profiles on this resolution can provide haptic sensation of roughness and friction. Therefore fine textures can be an important clue to different skin conditions perceived through tactile inspection via a haptic device.

ABSTRAK

Imej medik memainkan peranan penting di dalam bidang perubatan dermatologi dengan menyediakan bantuan berasaskan komputer yang melibatkan imej dijital 2 dimensi dan pemprosesan imej. Sistem berasas imej untuk dermatologi didapati akan lebih efektif apabila karakteristik 3 dimensi daripada kulit turut disertakan di dalam analisis. Pemeriksaan klinikal terhadap kulit terdiri kepada pengamatan secara visual and sentuhan. Sensasi sentuhan terhadap kulit berhubung kait dengan parameter permukaan 3 dimensi dan parameter mekanikal. Imej 3 dimensi daripada kulit juga dapat digabungkan dengan teknologi 'haptic' untuk pemeriksaan secara sentuhan berasaskan komputer. Objektif penelitian ini adalah untuk menghasilkan model 3 dimensi tekstur permukaan kulit. Proses pengambilan imej 3 dimensi dilakukan pada ketelitian yang tinggi (~0.1 mm). Sebuah algoritma digunakan untuk mendapatkan informasi grayscale 2 dimensi (informasi ketinggian permukaan) daripada data 3 dimensi. Tekstur yang diekstrak kemudiannya dimodelkan menggunakan teknik 'Markov-Gibbs random field modeling'. Hasil pemodelan menggunakan MGRF bergantung kepada karakteristik tekstur masukan. Pola yang seragam telah berjaya dimodelkan. Dari pengamatan terhadap contoh kulit sihat dan luka yang didapatkan dari pesakit, kami telah mengklasifikasikan 3 parameter utama kulit kepada lekukan, kerutan, dan tekstur mulus kulit. Contoh kulit dikelompokkan kepada tiga kelompok untuk mendapatkan gambaran akan tindakbalas MGRF model terhadap setiap parameter tersebut. Kelompok pertama terdiri kepada tiga parameter. Kelompok kedua didapatkan setelah menghilangkan informasi lekukan dan hanya menyisakan informasi kerutan dan tekstur mulus kulit. Kelompok ketiga juga didapatkan setelah menghilangkan informasi lekukan, namun hanya menyisakan informasi tekstur mulus kulit.

Model MGRF untuk kelompok pertama tidak menghasilkan kesamaan secara visual. Lekukan tidak dapat dimodelkan dengan baik dan selalu menghasilkan tekstur yang tidak seragam. Pada kelompok kedua, kedutan dapat dimodelkan dengan menggunakan persamaan 'low/medium visual' bergantung kepada perbezaan 'weak/moderate spatial' karakteristik ini. Hasil dari pemodelan kelompok ketiga menunjukkan bahwa tekstur kulit yang mulus sentiasa dapat dimodelkan dengan baik menggunakan persamaan 'medium/high visual' dan dapat

disimpulkan sebagai karakteristik yang seragam. Kami menyimpulkan bahawa pemodelan tekstur mulus kulit dalam skala ~0.1 mm dapat digunakan pada algoritma pembentukan tekstur untuk aplikasi 'haptic'. Karakteristik permukaan pada tingkat ketelitian ini menyediakan sensasi 'haptic' atas tingkat kekasaran dan geselan. Oleh itu tekstur merupakan informasi penting bagi kondisi kulit yang berbeza yang dirasakan melalui sentuhan menggunakan alat 'haptic'.

TABLE OF CONTENTS

LIST OF FIGURES

LIST OF ABBREVIATIONS

2D	Two dimensional
3D	Three dimensional
CAD	Computer-Aided Design
CCD	Charge-coupled Device
CRI	Colour Rendering Index
DOF	Degree of Freedom
GLCH	Gray Level Co-occurrence Histogram
GPD	Gibbs Probability Distribution
GRF	Gibbs Random Field
HIS	Hue, Intensity, Saturation
IRF	Independent Random Field
MCMC	Markov Chain Monte Carlo
MGRF	Markov-Gibbs Random Field
ML	Maximum Likelihood
MLE	Maximum Likelihood Estimation
MRF	Markov Random Field
MRI	Medical Resonance Imaging
PASI	Psoriasis Area and Severity Index
RGB	Red Green Blue
SA	Simulated Annealing

Chapter 1

Introduction

1.1 Background

Medical imaging has been contributing to dermatology by providing computer-based assistance in detection, classification and monitoring of skin diseases. It generally involves digital imaging of skin lesions (diseased skin) and their processing. The major topic of the research in this context has been the early detection of skin cancer and its classification from other similar looking diseases as skin cancer poses life threats in its later stages. Several techniques have been developed over the period of last fifteen years for the 2D images obtained in infra-red and monochromatic light in addition to normal RGB images. This prior research concentrates on analyzing the color content of 2D images for extraction of color, texture and edge/border features to draw conclusions about skin condition. For example, Figure 1-1 shows two examples where 2D images have been analyzed based on color and texture characteristics to segment diseased and healthy skin. However, the skin color is not the only feature changed by the presence of a disease. Several other features e.g. skin surface texture, roughness/softness, hardness/smoothness are also effected. For example, the skin is inflamed in diseases liker allergies, eczema, psoriasis. It is damaged or removed in skin burns, wounds and ulcers. The overall skin texture is changed due to ageing, sunlight exposure or usage of cosmetics. In addition skin can also get hard or soft in several skin conditions. Although these features of skin surface and hardness are important clues to the precise condition of skin, the conventional 2D imaging of skin is not able to capture them.

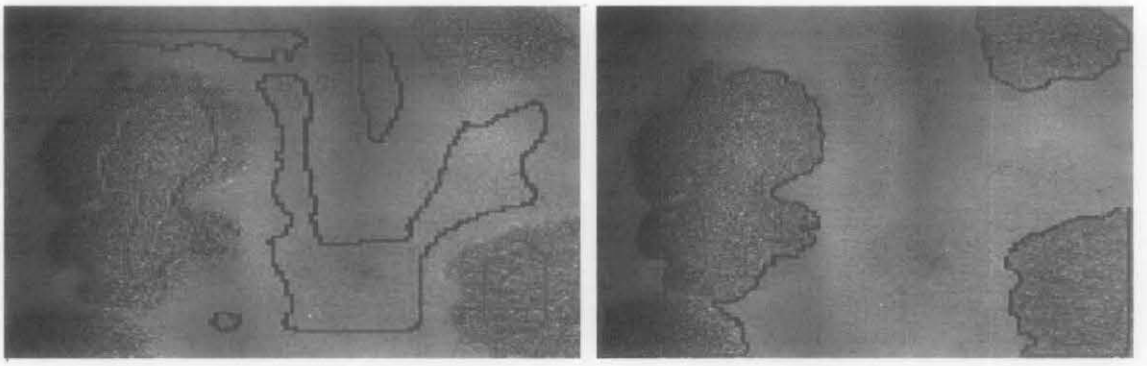

Figure 1-1: Results for region detection and segmentation of psoriasis lesions from 2D images [Taur 2002, Taur 2003]

An important advancement in skin imaging is the 3D imaging techniques. Skin features like surface textures and roughness are related to surface height profiles[1] which can be obtained by 3D imaging and incorporated in analysis to make precise conclusions about skin conditions. Several attempts have been made towards 3D image analysis for dermatology e.g. monitoring the severity of skin diseases like ulcers and psoriasis which alter the normal skin surface. Figure 1-2 shows an example of 3D skin images acquired with laser scanning. However, these systems are less in number to those based on 2D imaging and mostly depend on extraction of 3D features indirectly, e.g. stereo imaging and image sequences taken from different illumination angles, which may result in less precision. It is generally understood that the image based systems for dermatology can be more effective if 3D features of skin, captured with high precision, are included in the analysis for skin condition.

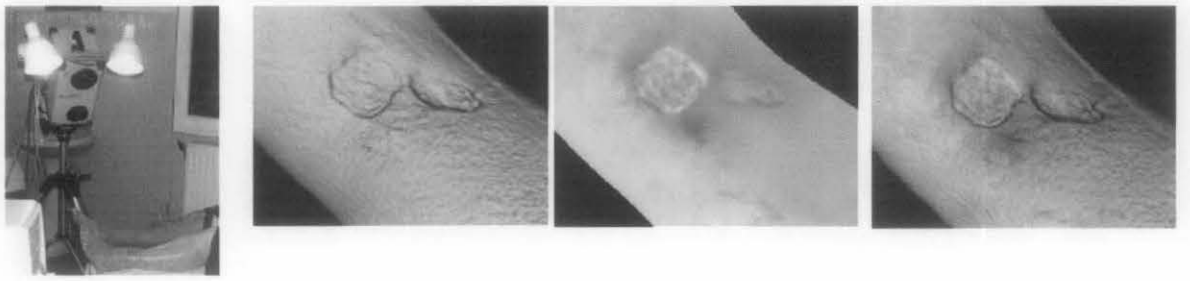

Figure 1-2: (a) Laser scanner (b) surface geometry of skin lesion (c) 2D image (d) combined surface geometry & 2D image (reproduced from [Callieri 2003])

[1] In this thesis, the terms 'surface texture' and 'surface profile' are used interchangeably where both terms denote the surface heights of an object (skin, in this case) in 3D.

Where most of the current computer-based expert systems for dermatology are based on visual data, the visual examination of skin is not the only mode of clinical inspection of skin diseases. In many cases the tactile inspection i.e. touching the skin is helpful in assessing the overall condition of disease. The analysis of skin images for extraction of parameters related to tactile inspection still remains unaddressed. It is readily understood that the touch of skin is related to its 3D surface profile and other mechanical parameters where color information plays no role. The skin surface, its elasticity, stiffness and moisture give the overall sense of touch to the examiner. Hence, it can be deduced that the accurate capturing and processing of 3D surface profiles of skin can not only improve the current image-based systems but also provide necessary data for tactile inspection. This data would be critical in any computer-based application targeting the assistance in tactile inspection of skin condition.

This thesis proposes the computer-based tactile inspection of skin suggesting the integration of haptic technology from virtual environments with 3D imaging of skin to serve the purpose. Haptic technology is applied along with virtual environment where it allows interaction with virtual objects through devices called haptic devices/interfaces (See Figure 1-3 below for examples).

Figure 1-3 Examples of virtual environments and user interactions via haptic devices

In a haptic virtual environment the user can touch/deform the surface/shape of the virtual object as well as move and collide with it to feel the feedback force. The haptic technology has been used in medical applications for surgical simulations and long-distance surgery. This thesis suggests that the virtual skin can be reconstructed in a virtual environment using the 3D surface profiles and mechanical parameters. Thus an expert would be able to touch and sense the virtual skin through haptic device. This will make the computer-based tactile

inspection possible in situations where the skin cannot be touched directly. In addition, the skin features of 3D surface profiles and mechanical parameters can also be an input to analysis for non haptic applications to examine the skin condition. Several future haptic applications in dermatology can be envisaged based on this computer-based tactile inspection of virtual skin. For example, the tele-dermatology can be more comprehensive with inclusion of haptic applications where the dermatologists would be able to touch patient's diseased skin even though the patient is absent or at distance (See Figure 1-4). It can allow the computer assisted training where the tactile inspection of case studies of skin diseases would be possible. Similarly it can provide with the tactile inspection of infected or injured skin where the direct contact with effected skin for inspection is not possible. Moreover it can also enhance the realism of virtual environments containing human objects. For example, in a recent piece of work synthetic artificial skin was constructed with tactile characteristics similar to real skin to be used with haptic evaluation systems and robots [Shirado 2006]. Figure 1-5 shows the envisaged applications of haptic technology for dermatology in future.

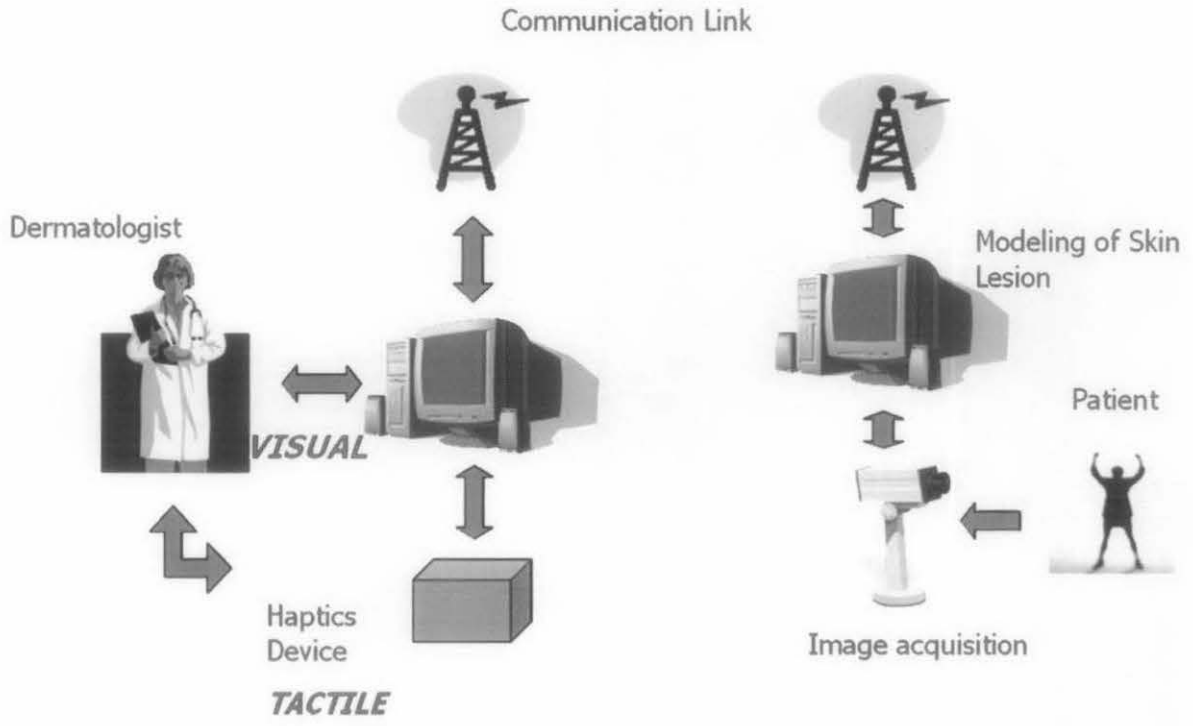

Figure 1-4: Tele-dermatology with inclusion of Haptic technology

Haptic applications consist of three major sections, a haptic device, virtual environment where the virtual objects are presentwith appropriate haptic display properties (e.g. shape,

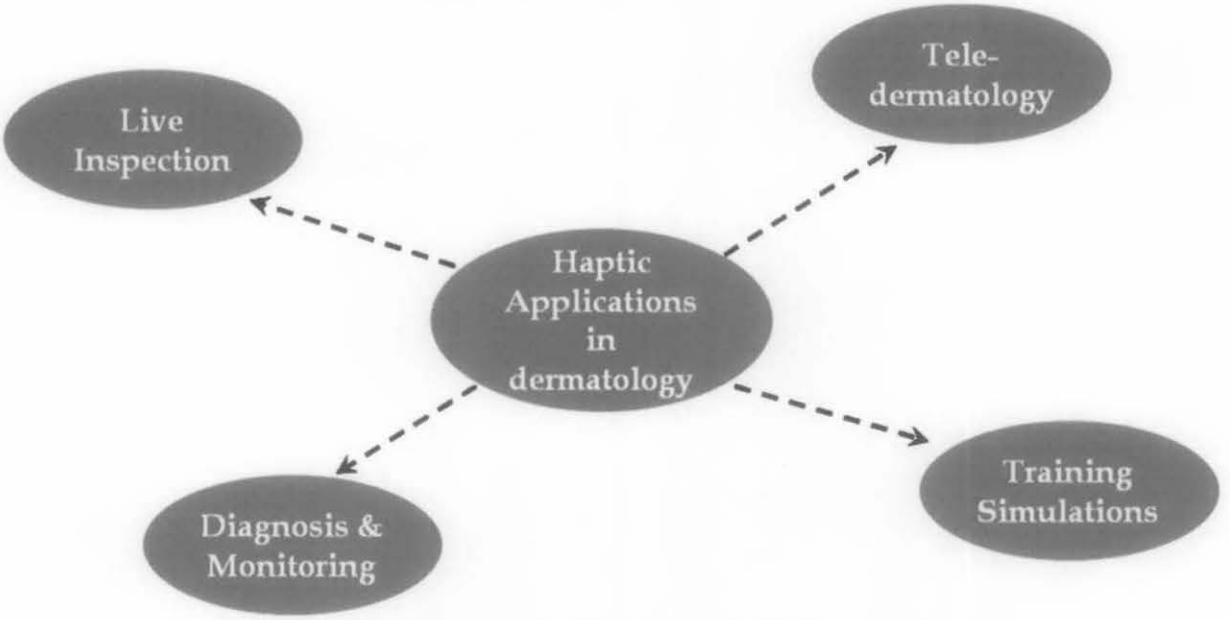

Figure 1-5: Envisaged Applications of Haptic technology in dermatology

surface, friction) and an interaction paradigm to calculate and apply the interaction forces between the both. Thus several virtual environments can be created for the same haptic device and interaction paradigm. Where many research efforts are targeting the improvement in the designs of haptic devices and performance of haptic interaction algorithms (or haptic rendering algorithms), the haptic display of real objects with varying shapes and materials in a virtual environment with high interaction quality (realism in this case) demands extensive research. For example, the haptic displays of organic tissues and fabric like materials have been reported [Govindaraj 2003, Acosta 2001]. Similarly, the *virtual representation* of skin with haptic display properties is essential for any haptic application incorporating skin. It requires the 3D shape and surface profiles of skin as well as the mechanical parameters of surface friction and stiffness to completely define the skin material. Evidently, these properties are to be captured from real human skin and displayed accurately for realistic virtual representation. The parameters of friction and stiffness for skin can be obtained through mechanical experimentation. However, the capturing of 3D shape and surface profiles of skin with high accuracy and their representation for haptic display are challenging and has been the main topic of this work. Once gathered from real human skin accurately and

processed, this 3D data can be used for virtual skin representation and rendered with haptic device.

1.2 Problem Statement

As discussed above, haptic rendering of skin is a vast, relatively new field with research potential in many dimensions where the focus of this work is the 3D geometry of skin. It is observed that the overall, large-scale shape feature in 3D for skin is due to the underlying limb and is not altered by skin diseases or other factors e.g. ageing, sun exposure, etc. Also, the sensation of touch is due to local surface of skin and not the shape of limb. For this reason, the shape of limb in skin geometries is ignored and the local 3D skin surface profiles (or skin surface textures) which are altered by skin conditions have been considered. However, skin surface textures are viable to change at very small scale in addition to large scale, easily perceived wrinkles, wounds, lesions, etc. This will require high-tech 3D image acquisition set up able to capture skin surface texture details on this much small scale, at resolution as high as ~0.1 mm.

Another aspect of the problem is the representation of skin surface textures in virtual environments to be integrated with haptic device. The 3D data are to be processed in a way to be integrated with haptic applications. An overview of current haptic technology (Chapter 3) tells us that out of key haptic display properties of virtual objects (shape, surface textures, friction and stiffness) surface textures are the most difficult to render but most critical for realistic perception of touch. This is due to the requirement of force updates at very high rates for real time haptic rendering. The surface textures require enormous number of calculations with their small scale geometry details and pose a problem in high rate force updating. Until now, the popular haptic texture rendering algorithms, ensuring fast force calculations, have been similar to bump mapping in computer graphics for texture rendering. These algorithms are called 'force mapping'. Hence, any skin surface texture representation should also be compatible to these fast rendering algorithms.

Third and most important aspect of the problem is that how accurately the real surface textures of skin, captured by 3D image acquisition set up, can be represented virtually for

haptic rendering i.e. to bridge the 3D skin texture acquisition and force mapping algorithms with as much accuracy as possible. A similar problem of modeling 3D skin textures can be found in computer graphics and animations where skin textures are considered for realistic skin rendering or for cosmetic industry to assess the effectiveness of cosmetics. However, such applications consider the approximations of real skin textures only which are then modeled on animated objects for real-time rendering. For this work, the approximations will not suffice as dermatology applications will require detection of minute skin surface changes. Therefore this work not only concentrates on 3D image capturing of skin surface textures and their modeling for fast haptic rendering algorithms but also on as much accuracy as possible.

1.3 Research Objectives and Scope of Work

The objective of this work is to model real 3D skin surface textures which can be used for future haptic applications in dermatology. As discussed in last section, the acquisition of surface textures should fulfill the requirement of high resolution 3D surface details keeping in view the dermatological applications. And the modeling should maintain the accuracy of surface details while being compatible to fast haptic texture rendering algorithms.

First of all, the acquired, high-resolution surface textures are in 3D whereas fast haptic texture rendering algorithms (force mapping algorithms) require texture inputs in the form of 2D grayscale textures called as 'height maps'. In a height map the gray level in 2D corresponds to the height in 3D. Therefore, a processing algorithm is presented which extracts 2D grayscale textures from acquired 3D images of skin while filtering unnecessary geometry details. The 2D grayscale textures extracted from 3D surface textures through this algorithm present high visual similarity to real skin. For example, in Figure 1-6 the high visual resemblance of extracted 3D surface texture to the original skin can be observed.

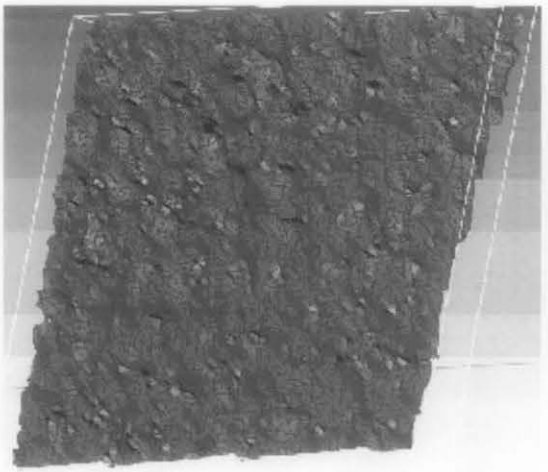

(a) 3D surface texture without skin color

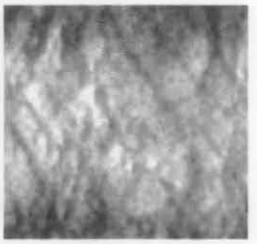

(b) 2D grayscale texture (height map) without skin color

Figure 1-6: 2D grayscale textures extracted from 3D skin texture

The next step is to model the 2D grayscale skin textures using a technique which preserves the accuracy of details. The integration of model with haptic applications leaves us with two approaches for handling the 2D grayscale textures i.e. deterministic or stochastic. The input to haptic rendering algorithms can be both deterministic and stochastic. However, the stochastic approach has been basis for fast haptic texture rendering algorithms. The stochastic approach involves the drawing of similar texture samples from a given stochastic process. It has been proposed that the device need not follow the surface texture exactly (as in deterministic approach) for the reason that on such a small scale a user is not able to determine exact details of surface textures but only perceives overall roughness and surface irregularities. Thus, only an accurate haptic perception to the user is sufficient. A given grayscale surface texture can be modeled as stochastic process and rendering any sample of the corresponding process will give the similar haptic perception [Fritz 1996, Sirra 1996].

In this work, skin textures are modeled using Markov-Gibbs random field (MGRF) modeling technique. As it has been discussed before, accurate representation of textures is necessary and the modeling should be able to reproduce texture samples with high visual similarity. Skin textures pose a type of natural textures and Markov-Gibbs random field modeling has been shown to model natural textures successfully [Gimel 1999]. This thesis will present the modeling results of skin texture using MGRF model developed by Gimel *et al* [Gimel 1999].

For stochastic modeling, a skin texture is treated as a unique stochastic process with corresponding probability distribution. Modeling involves analysis of given texture sample to estimate parameters of probability distribution. The model parameters can be stored or transmitted to synthesize similar texture samples.

In this thesis, key features of 3D skin surface textures, namely curvature, wrinkles/lines and fine textures, observed from wide variety of skin textures obtained from patients have been enlisted as well as results of MGRF modeling for skin textures have been presented. The characteristics of these 3D features when appearing in 2D grayscale textures and the accuracy with which these skin features are modeled using the Markov-Gibbs random field modeling technique have also been discussed.

According to the above outlined research objectives, the scope of work for this thesis includes the following:

1. Acquisition of 3D surface profiles of skin at high resolution with high accuracy (This involves set up for laser scanning and selection of real case studies in collaboration with dermatologists)

2. Extraction of 3D skin surface textures by processing raw 3D data obtained from laser scanner and its conversion to 2D textures

3. Assessing the modeling of 2D textures using the technique of Markov-Gibbs Random Field Modeling

4. Developing the programming routines for extraction of skin surface textures and MGRF modeling in MATLAB^{TM}

1.4 Thesis Organization

This thesis consists of six chapters. The literature survey is presented in chapters 2 and 3. This work is an effort to integrate the existing technologies of Skin Imaging, 3D Computer Graphics and Haptic Technology. Hence the literature survey reviews the aspects of these areas relevant to this research work. In Chapter 2, 3D imaging and modeling techniques for skin have been reviewed. A brief introduction on psoriatic and healthy skin is also included. Chapter 3 is devoted to an overview of haptic technology in general and looking into details of haptic rendering of surface textures. In Chapter 4, the mathematical background of the proposed stochastic modeling technique for this work, Markov-Gibbs random field modeling, has been reviewed. Chapter 5 concentrates on the work done for modeling of 3D skin surface textures. It also presents the overall framework of modeling, data acquisition and preprocessing. The results of modeling the 3D skin textures and their analysis are covered in Chapter 5. Finally, Chapter 6 concludes the thesis, presents the contribution of this work and discusses possible avenues for further research work.

Chapter 2

Skin Imaging and Modeling

This chapter gives an overview of skin imaging and modeling techniques. Skin imaging and modeling analyze color and surface characteristics of skin and has applications in dermatology, computer graphics and cosmetic industry. The literature review shows that 3D image analysis of skin is not as much developed as 2D imaging and that the modeling of skin for computer animation is based on approximations of skin textures only.

The first section of chapter describes the structure of healthy and, under scope of this work, psoriatic skin. The structure and physiology of healthy and psoriatic skin are covered in sections 2.1 and 2.2. Section 2.3 overviews imaging techniques of skin, both 2D and 3D, and their applications in both dermatology and cosmetic industry. Several important image acquisition problems for 2D are also discussed which can be avoided by applying advanced 3D imaging. Apart from capturing of skin imaging, modeling and re-construction of skin features are also important for computer animation. Modeling of 3D features of skin on animated characters provides with more realistic rendering and has been addressed extensively in recent years. Section 2.4 discusses some of the work done in 3D modeling of skin features for computer graphics.

2.1 Healthy Skin

Human skin is the largest organ of human body. It makes around 10% of body mass and regulates the inflow and outflow of different materials from body e.g. heat and water. It also protects body from harmful chemicals and microorganisms by blocking them. The structure and function of human skin are categorized into four main layers (Figure 2.1).

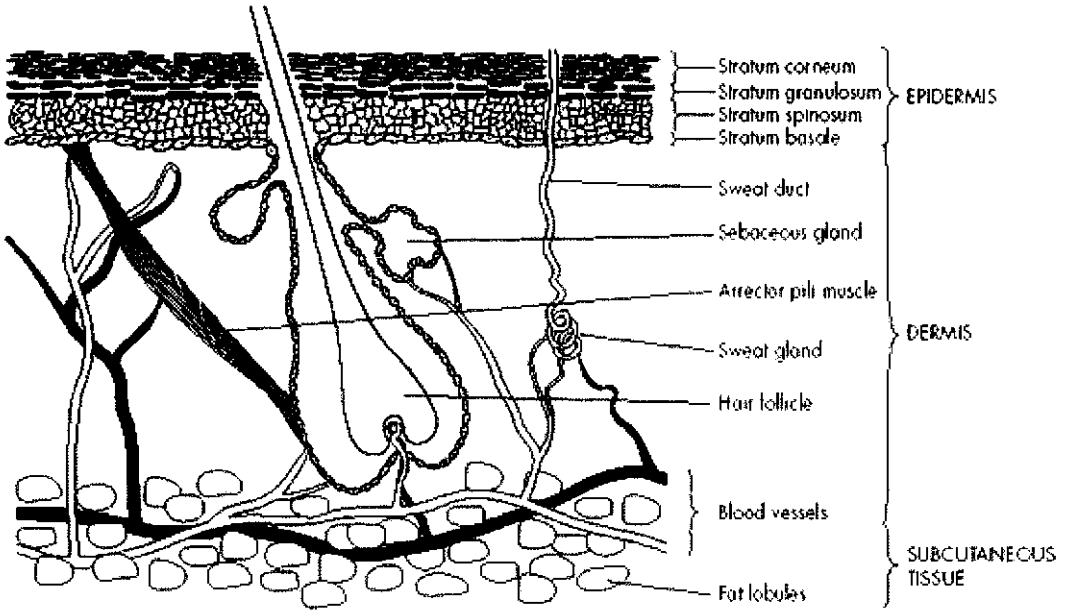

Figure 2-1: Structure of healthy skin

1) The Subcutaneous Fat Layer/ Hypodermis

The subcutaneous fat layer, or hypodermis, bridges between the overlying dermis and the underlying body constituents. This layer principally serves to insulate body and to provide mechanical protection against physical shock. It also carries the principal blood vessels and nerves to the skin.

2) The Dermis/ Corium

The dermis (or corium) is typically 3 to 5 millimeter thick and is the major component of human skin. It is composed of a network of connective tissue, predominantly collagen fibrils

providing support and elastic tissue providing flexibility. The dermis has numerous structures embedded within it; blood and lymphatic vessels, nerve endings, hair follicles, sebaceous glands, and sweat glands.

3) The Epidermis

The epidermis is a complex multi-layered membrane. It contains four histologically distinct layers (Figure 2-1). The stratum corneum, comprising dead cells, provides the main barrier and hence is often treated as a separate layer.

The cells of stratum basale or basal layer are similar to those of other tissues within body and are metabolically active. This layer thus contains the only cells (keratinocytes) within epidermis that undergo cell division. On average, dividing basal cells replicate once every 200 to 400 h. In addition to the keratinocytes, the stratum basale contains Melanocytes which synthesize the pigment *melanin*. One other specialised cell type is found within the basale layer, the Merkel cell. These cells are found in greatest numbers around the touch sensitive sites of the body, such as the lips and fingertips and are associated with nerve endings and cutaneous sensation. . As they pass from the stratum basale to the stratum granulosum (or granular layer), the keratinocytes continue to differentiate, synthesize keratin and start to flatten. This granular layer is only one to three cell layers thick. The stratum lucidum is the layer in which the cell nucleus disintegrates and there is an increase in keratinisation of the cells with further morphological changes such as cell flattening.

4) The Stratum Corneum/ Horny Layer

The stratum corneum (or horny layer) is the final product of epidermal cell differentiation, and though it is an epidermal layer, it is often viewed as separate. The stratum corneum serves to regulate water loss from body whilst preventing the entry of harmful materials, including microorganisms. Typically, it takes 14 days for a daughter cell from the stratum basale to differentiate into a stratum corneum cell, and the stratum corneum cells are typically retained for a further 14 days prior to shedding, thus making a 24-28 days cycle of a normal skin cell division.

2.2 Psoriasis

Psoriasis [pronounced sore-EYE-ah-sis] is a common skin disease worldwide. It appears on skin as raised, red patches or lesions covered with silvery white buildup of dead skin cells, called 'scales' (Figure 2-2). The disease does not pose fatal threats like skin cancer but it results in disfiguring lesions on skin and the quality of social life of patients is deteriorated badly.

Psoriasis can be well-defined as a 'non contagious, chronic, lifelong, immune-mediated, genetic' disease. Non contagious means that the disease is not spread by physical contact with patients. Chronic means continual; symptoms may go away, but the underlying disease remains and the symptoms may return. And since the disease remains it is lifelong, patients, once diagnosed, have to be monitored for the symptoms for the rest of their lives. Chronic also means incurable, as the disease and its causes are not cured. Therefore, in successful treatments of psoriasis, symptoms are controlled to create an effective cure, even if not a permanent one. Immune-mediated means that the disease works through the immune system. It is not a disease of immune system, such as HIV, in which immune system is affected or destroyed. Instead, the disease is working *through* immune system. A particular part of the immune system is triggered into improper activity by the disease. This improper activity causes skin cells to grow much faster than normal (3-7 days from new cell to flaking off rather than the normal 28-30 days), at about the rate the body normally uses to heal a skin wound. The result is a build up of skin cells that also are not properly developed, leading to flakiness, the redness of inflammation, and all the other symptoms of psoriasis. Genetic means the disease is rooted in the genes. Patients get the disease only through inheritance or environmental factors causing the right mutation in genes for psoriasis [Psoriasis Treatments 2006].

Statistics

Psoriasis is a common, life altering disease worldwide, affecting all ethnic groups. However, severity of symptoms of disease varies among regional environmental conditions and skin properties of different ethnic groups. Psoriasis affects an estimated 2-3 percent of the world's

population making 125 million patients. Referring to the genetic origin of disease, if one parent has psoriasis, a child has about a 10 percent chance of having psoriasis. If both parents have psoriasis, a child has approximately 50 percent chance of developing the disease [Bowcock 2004]. About 10 percent to 30 percent of people with psoriasis also develop psoriatic arthritis, a disease of joints. There are five types of psoriasis namely Plaque, Guttate, Erythrodermic, Inverse and Pustular psoriasis which appear on skin in the form of skin lesions. Plaque psoriasis is the most prevalent form of the disease making about 80 percent. For this reason, major portion of research work in psoriasis concentrates on plaque psoriasis. It is characterized by raised, inflamed, red lesions covered by a silvery white scale. Figure 2-2 below shows an example of inflamed plaque psoriasis lesions with silvery patches.

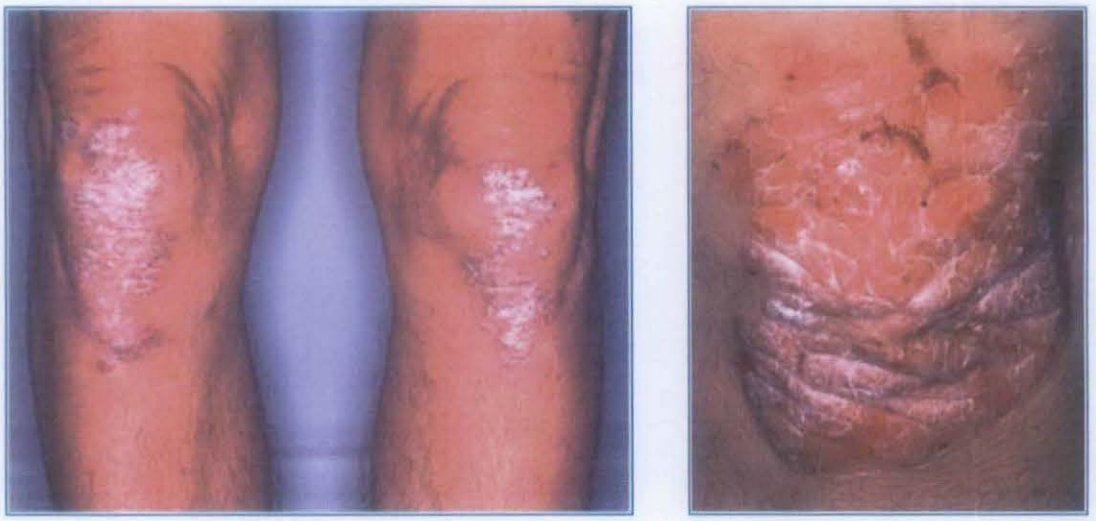

Figure 2-2: Examples of plaque psoriasis lesions on knees

In addition to threats of possible disabling posed by psoriatic arthritis it affects quality of social life of patients badly. Most of the patient reported their disease to be a large problem in their everyday life whereas patients with psoriasis covering more of their body (more extensive skin disease) experience a greater negative impact on their quality of life. The impacts on quality of life in women and younger patients are even worse [NPF 2006].

Psoriatic Skin

The physiology of psoriatic skin involves malfunctioning of immune system. A normal immune system protects body against invaders by destroying bacteria, viruses and other foreign proteins. In patients having specific genetic pattern responsible for psoriasis, immune system is triggered by some external factors into this malfunctioning. The immune system gets over-active, sends false signals to skin cells, similar to skin healing from a wound or reacting to a stimulus such as infection accelerating growth of skin. Cells are created and pushed to the surface in as little as 2 to 4 days, and the skin cannot shed the cells fast enough. The excessive skin cells build up and form elevated, scaly lesions. The white scale (called as 'plaque') that usually covers the lesion is composed of dead skin cells. The redness of the lesion is caused by increased blood supply to the area of rapidly dividing skin cells, blood vessels expand and multiply, and blood flow to the skin increases ending in redness. Figure 2-3 below shows cross-section of structures of both healthy and psoriatic skin [Psoriasis Treatments 2006].

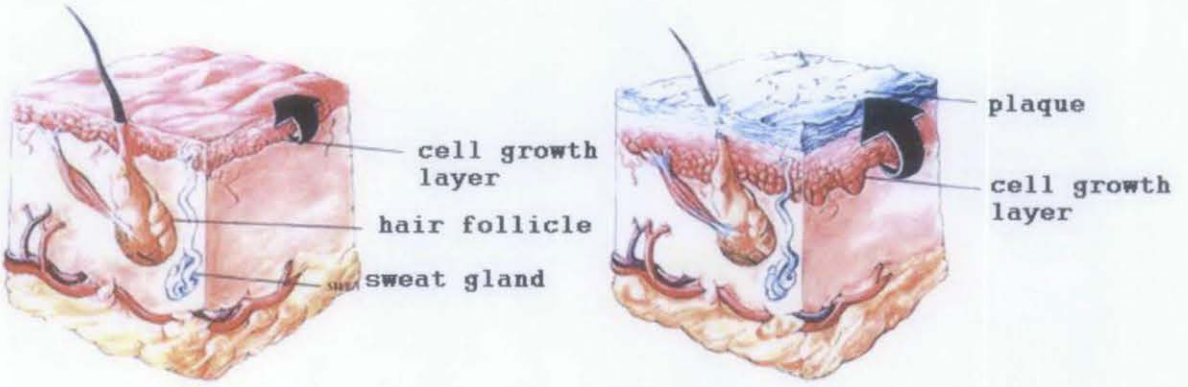

Figure 2-3: Comparison of structure of healthy skin (left) and psoriatic skin (right)

Psoriasis is incurable with genetic origin and several treatments are there only to cure the symptoms i.e. skin lesions and arthritis. Clinical treatment of psoriasis involves experimentation with available treatments to find the best one for every patient. For this reason monitoring plays an important role in determining the best treatment for a specific patient [Psoriasis Treatments 2006]. Monitoring, for lesions of any skin disease, is defined as 'keeping temporal, objective and quantitative records for the severity of disease'. For scoring and monitoring of psoriasis, Psoriasis Area and Severity Index (PASI) has been the leading [Louden 2004]. When using PASI, psoriatic lesions are graded based on area and severity.

Severity of disease includes further three criteria: redness (R), thickness (T), and scaliness (S). PASI has been the most widely used standard to assess the severity of disease in clinical trials and research. However, in every day visits, it comes up with some complexities mainly due to its being cumbersome in calculations. The situation becomes even worse when subjectivity is introduced in PASI scores owing to the traditional ways of scoring i.e. visual inspection, taking notes/images/drawings for recording. These non-objective methods often cannot serve monitoring purposes enough to find the best treatment. The result is variations of scores from examiner to examiner, unfit for record-keeping purposes for a patient.

Realizing this limitation of PASI in every day use, researchers have tried to automate PASI scoring, mainly for the purposes of objectivity and speed, to make monitoring in daily trials more fruitful for a patient. Several studies have targeted the different aspects of monitoring of psoriasis and PASI [Delgado 2003, Delgado 2004, Juha 1999]. These studies propose some sort of automated computer-based system, analyzing images of disease lesions and calculating some features objectively e.g. area, PASI scores for area, scaliness, and thickness. A detailed overview of these is following in section 2.3. It should be mentioned that these systems cover different aspects of monitoring of psoriasis. So far none has been developed that is a combination of all these aspects of psoriasis i.e. capturing the area, scaliness, thickness, redness of disease and their scoring, in one integrated comprehensive system. Such system should also keep temporal and objective records of PASI scores for a patient to monitor the progress of disease for a treatment as has been done for monitoring of skin ulcers [Callieri 2003].

2.3 Medical Imaging in Dermatology

Medical imaging is the process by which physicians evaluate an area of the subject's body that is not externally visible. Medical imaging may be clinically motivated, seeking to diagnose and examine disease or, alternatively, it may be used by researchers in order to understand processes in living organisms. Medical imaging often involves the solution of mathematical inverse problems. This means that cause (the properties of living tissue) is

inferred from effect (the observed signal). It includes several techniques to have images of a subject's body e.g. Radiography (X-Rays), Fluoroscopy, Tomography, Ultrasound, Magnetic Resonance Imaging (MRI) and Electron Microscopy. In dermatology, medical imaging mostly consists of digital imaging of the diseased surface, or the immediate underlying layers, with visible, infra-red or monochromatic light. These images are later used for computer-based image processing for different applications or just for record keeping. The applications mainly include diagnosis, monitoring and scoring the severity of skin diseases. Imaging of lesions with infra-red light has been used for early diagnosis of Malignant Melanoma [Cotton 2002]. Monochromatic light of different wavelengths has also been used for the same purpose [Patwardhan 2005]. Recently, with the development in 3D imaging techniques, 3D imaging of skin has been applied for dermatology. 3D imaging is more promising than conventional 2D imaging to give information about skin features. Section 2.3.1 below presents an overview of popular image acquisition techniques for skin.

2.3.1 Image Acquisition

The human skin tends to change slowly and gradually because of its inherent physiological function of cell regeneration. It responds in the same manner to any of the treatments applied for different purposes e.g. healing of skin lesions and improvement in overall skin texture for cosmetic purposes. For this reason, dermatologists and other skin researchers have to keep track of the very slow responses of skin. Sometimes, very small and minute differences in skin conditions are an indication of the positive response of skin to the applied therapy. Imaging systems in dermatology, assisting the experts, are required to be sensitive to these minute details of variation in skin to draw conclusions for diagnosis, monitoring, etc. Most of the current computer-based image analysis systems for dermatology are based on 2D images. The 2D image acquisition of skin apparently seems straightforward. However, the image acquisition setups, often, are not able to capture small variations because of skin's drastically changing appearance with changing illuminating environment factors. This results in overshadowing of actual, minute changes in skin conditions by those due to improper imaging. The restriction to 2D skin features only worsens the situation when 3D surface geometries, important for evaluating skin textures, are not considered. This situation leads to

inaccurate input images, depicting actual state of the skin poorly, and erroneous results by image processing systems. Therefore, it is indispensable for an image processing system to have reliable input images for making precise and accurate decisions and to incorporate 3D skin features in as much detail as possible.

Illumination of skin for image acquisition: Image acquisition has been a significant problem in digital imaging of skin because of the typical illumination problems posed by the unique texture and optical properties of human skin. The main reasons of inaccurate acquisition are reflectivity of skin and limitations of illuminating/capturing equipment. The typical reflectivity of skin is because of its surface texture and optical characteristics. Human skin exhibits very specific response to the illumination and imaging because of its reflectivity. There is a great variation in color and texture of skin when illuminated and viewed from different angles of light as shown in Figure 2-4.

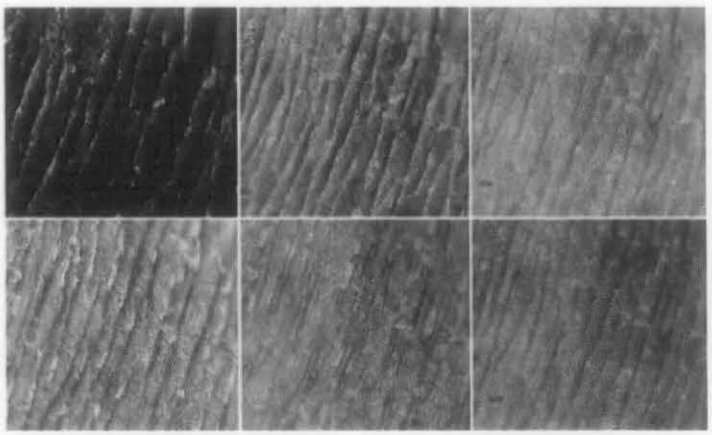

Figure 2-4: Variation in texture and color of skin with different light directions (reproduced from [Cula 2004])

Specular and diffused reflections, and shadows are typical with skin which create this variation. Specular reflections are caused by smoothness of skin whereas the diffused reflections by its roughness. Whenever the light rays, in parallel, are incident on an oily skin, it will produce the bright spots (specular reflections) in the captured image. Skin presents diffused reflections and shadows from within the furrows and wrinkles of the specific texture of skin on very small scale. Shadows are also present owing to the structure of skin on large scale e.g. at curvatures of limbs and on junctions of fingers, visible bones on specific portions of human body. Figure 2-5 shows the specular and diffused reflections from skin.

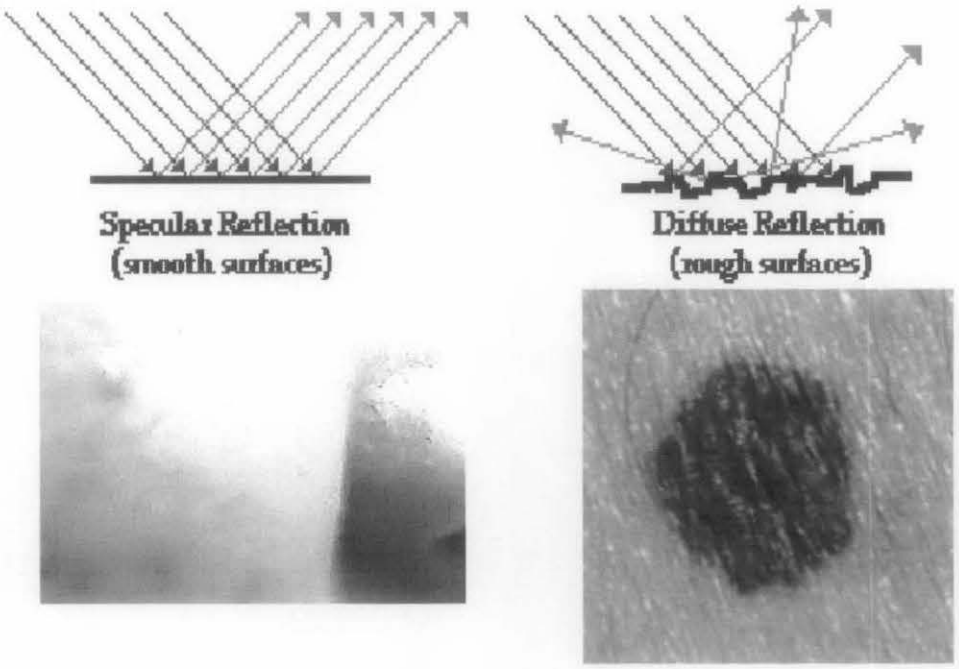

Figure 2-5: Specular and Diffused Reflections on Skin (reproduced from [Illias 2005])

The limitations of illuminating and capturing equipment add to the problems posed by the reflectivity of skin. The source of light should be of high luminous flux (See Appendix A) to illuminate the scene with enough brightness. The orientation of light source in the scene is important as it determines the angle of incidence of light rays over the skin. Uniform illumination of skin is required to eliminate shading i.e. variation of brightness across the field of view. It is achieved when illuminance (See Appendix A) is equal all over the imaged area. The angle of incidence of rays may also enhance the distortion posed by reflectivity of skin. As mentioned in previous section, it can give rise to specular and diffused reflections, and shadows of skin in captured images, leading to variation of color and textures of skin. Then light source should be able to capture the 'true color' i.e. the color seen in the natural day light and captured same in the same conditions. CRI (Color Rendering Index) and Color temperature are used to define the color rendering quality of light source in capturing true colors. (See Appendix A)

Figure 2-6: Same Object captured from two light sources of different CRI and Color Temperature

To render true colors, light sources of high color temperature and high CRI are preferred with wavelengths of emitted light in full visible spectrum. Low color temperature or CRI will result in imprecise skin colors and textures. The typical problems with camera are the resolution, color calibration and noise [Illias 2005]. The textures of healthy and diseased skin are on the scale as small as 0.1 mm requiring high resolution camera. The color calibration of camera allows the capturing of same color irrespective of the illumination condition. Noise can be both due to limitations of camera hardware and unwanted skin elements e.g. hair, scars, moles.

A proper imaging system targets to capture reliable images by eliminating both reflectivity problems and limitations of equipment and requires proper engineering of scene. Delgado *et. al.* [Delgado 2003] used the integrating sphere illuminating the target area of skin with diffused light as shown in Figure 2-7. Light rays from three halogen light sources placed in equilateral triangle positions are reflected internally within the sphere, forming homogeneous, diffused illumination i.e. light coming from all angles and not from a certain angle. This eliminates the problems of specular reflections and shadows. However, the sphere assumes the captured object to be planar and cylindrical portions of body pose the non-uniform illumination errors which are corrected mathematically in an illumination correction scheme [Maletti 2003]. The CCD camera is used for capturing images after color calibration of the camera has been done using calibration sheets.

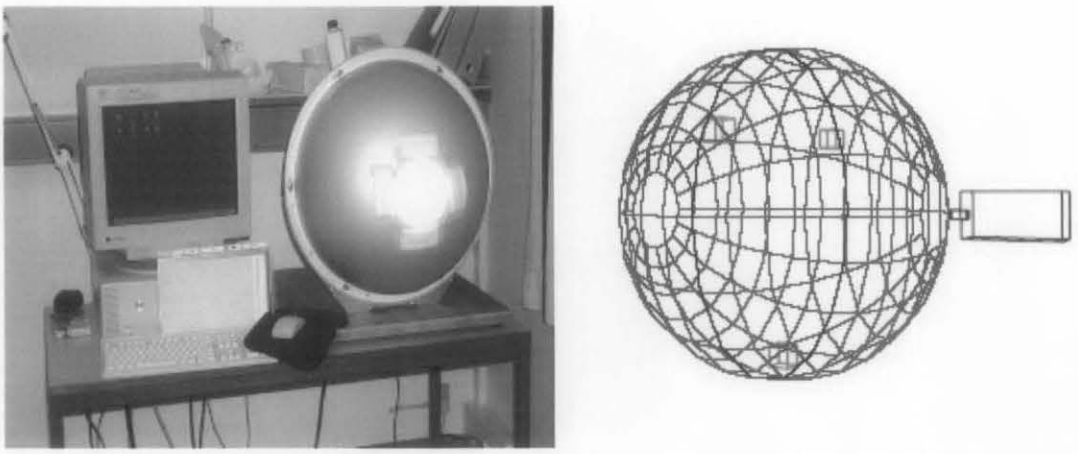

Figure 2-7: Integrating sphere and illumination geometry for image acquisition in [Delgado 2003]

In the image acquisition system proposed by Illias, the internationally established illumination and capturing geometry for color measurements is utilized [Illias 2005]. A light source with high color temperature and relatively smooth color spectrum is used. The light rays are incident on skin at an angle of 45° and collected at 0° to eliminate most of the specular reflections and shadows on small scale. Figure 2-8 shows the geometry for acquisition used in their system. The remaining reflections are eliminated using polarizers on camera and light source. The high resolution CCD camera is used for capturing images. The color calibration, shading corrections and noise removal are achieved by software corrections.

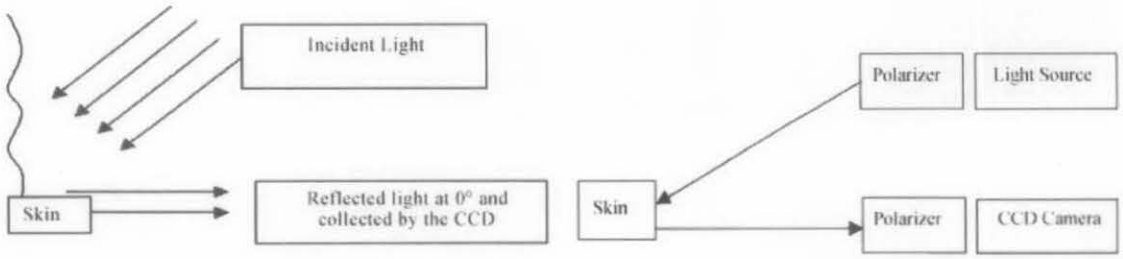

Figure 2-8: Illumination geometry used for image acquisition system in [Illias 2005]

Patwardhan *et al* [Patwardhan 2005] presents an imaging system called 'Nevoscope' for early diagnosis of skin cancer which is based on transilluminace rather than normal RGB acquisition. Figure 2-9 shows the basic schematic of a Nevoscope apparatus. The

surrounding skin of lesion is illuminated by visible light at an angle. The light penetrates through skin to reach the underlying layers of skin lesion and its unabsorbed portion contributes to diffused reflectance after scattering. The diffused light is captured from above and provides information from underlying skin layers which are affected by skin cancer in initial stages. An extension of suggests that, in addition to correct detection, the depth of skin cancer lesions can also be obtained from trans-illuminated images if the monochromatic light is used instead of visible light [Patwardhan 2005]. Based on the optical properties of skin, monochromatic light has variable penetration depth based on its wavelength. For this reason, it can be used through nevoscopy to gather information from underlying skin layers at different depths. Several wavelengths of monochromatic light, more sensitive to underlying skin structure caused by skin cancer, have been sought out through Monte Carlo simulation of light interaction with skin. The voxel-based model of skin lesions is constructed where every voxel has different light interaction properties based on the optical properties of skin layer it represents. The lesions are constructed from voxels in cylindrical shape with different sizes. From Monte Carlo simulation of incident light of various wavelengths interacting with voxel-based skin lesions and correlation analysis of reflectance of voxel based skin layers, the representative wavelengths are selected and used for further analysis. The reflectance of skin is observed at the selected wavelengths as a function of lesion depth. It is shown that at certain wavelengths, around 495 mm and above 600 mm, the absorption is low and light can penetrate the depth of skin lesions. Thus the monochromatic light at this wavelength can be used in Nevoscope in real cases to gather the depth information of lesions. The combined surface information from visible light illumination and depth information from monochromatic illumination increases the effectiveness of Nevoscope based diagnosis of skin cancer lesions.

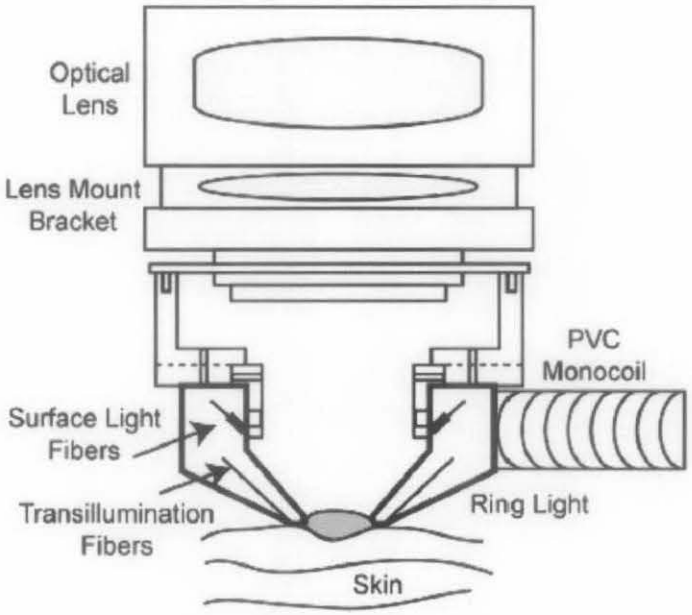

Figure 2-9: Nevoscope schematic – Transilluminating light incident at an angle and captured from above [Patwardhan 2005]

Cula *et. al.* [Cula 2004] presents the 'bidirectional imaging' in which both illumination and capturing angles are parameterized to take images of skin textures from different angles. Multiple images of same skin texture, taken from different angles of light and camera, present skin more clearly. The apparatus includes a light source and camera planted on an arc and tripod which are able to give different azimuthal and polar angles of a hemisphere for both camera and light as shown in Figure 2-10 The apparatus does not target to eliminate the skin reflections and non-uniform skin color/texture appearance. However, a series of images of same skin area, with different angles of illumination and capturing provides a better picture of actual skin appearance.

Figure 2-10: The light source and camera planted on arc and tripod moving in a hemisphere (reproduced from [Cula 2004])

The 2D imaging does not capture 3D surface textures (height profiles) of skin, instead, these features cause varying color and texture appearance under illumination conditions. As discussed above, some acquisition systems target to eliminate these variations. However, 3D skin features provide critical detailed information about skin condition and for this reason the work by Cula *et. al.* [Cula 2004] above incorporates them by bidirectional imaging. The straightforward way to capture skin surface profiles is 3D imaging techniques which can be classified mainly in two categories 1) there are methods which construct the 3D skin height profiles by processing a set of 2D images e.g. stereo imaging 2) the information of height profile is directly captured by the capturing equipment and no processing of 2D images is required e.g. laser scanning. A review of some of 3D capturing techniques used for skin imaging follows.

Stereo imaging (Stereoscopy), based on binocular human vision, is a popular technique to extract 3D information from 2D images [Moon 2002]. The human vision system views the same object with small difference in viewing angles of two eyes. The small differences in two images of two eyes arising from different viewing angles are called 'disparity'. The human brain produces depth information of the scene by processing this disparity map. Similarly, in stereo imaging, the object is imaged with two cameras which are placed at small distance from each other. Figure 2-11 shows the typical set up to capture a pair of such images. The disparity in two images is then analyzed to give the depth/height information of the object.

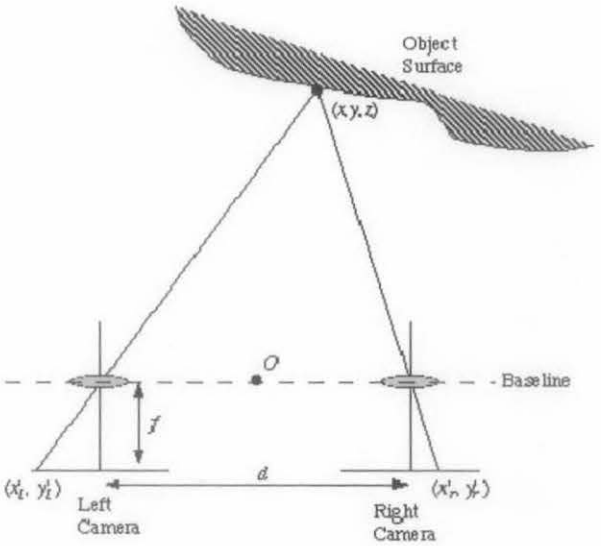

Figure 2-11: A typical set up for acquisition of stereo images. Two cameras placed at small distance to view the object surface with small difference in viewing angles.

Stereoscopy has been used for acquisition of 3D features of skin [Park 2004, Moon 2002]. A combination of stereo microscope and two CCD cameras is used to take stereo images of small scale features of skin. A disparity map is obtained by stereo matching of two images. A height map of skin called topograph, constructed from the disparity map, gives the skin structure in 3D (Figure 2-12). The topograph is analyzed to evaluate features for cosmetic and dermatology applications.

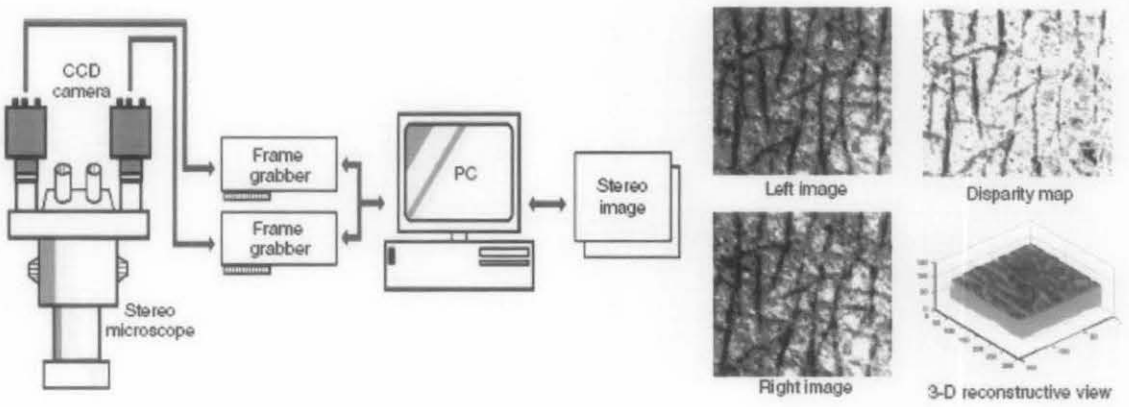

Figure 2-12: (Left) The organization of SOT (Right) Two stereo images, disparity map and 3D height view (Reproduced from [Moon 2002])

In the work by Yamada, 3D skin features are extracted from 2D images [Yamada 1998]. In this case the 2D images for input are taken from three light sources placed at angle

differences of 120° which are then moved to get an image sequence. These resulting images have multiple shading patterns arising from height fluctuations, specular reflections and inter reflections. The shading patterns contain sufficient information to extract 3D skin surface features. The intensity data from three images of three light sources taken at one point can give 3D information. However, it becomes impossible due to the noise added from skin shading and reflections. The images in sequence solve this problem by providing sufficient data to get the intensity value at every surface point. Figure 2-13 shows the arrangement for acquisition of image sequences and an example of 3D reconstruction of surface profiles.

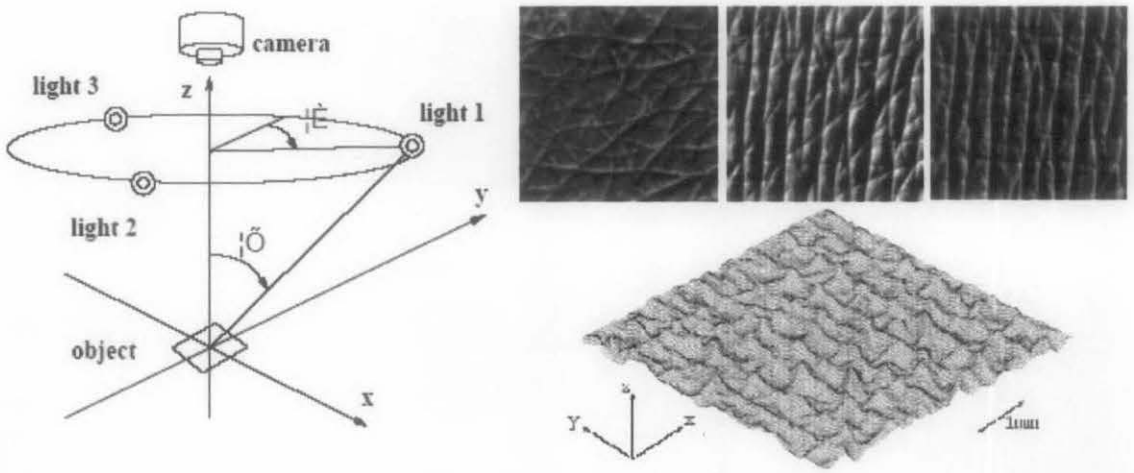

Figure 2-13: 3D reconstruction of skin surface from image sequence [Yamada 1998] (Left) arrangement to capture images from different angles (Right) captured images and reconstructed 3D surface profile

Apart from 2D images, 3D volumetric images have also been used to extract skin surface profiles [Wang 2003]. The volumetric images are obtained using confocal microscope which obtains slices of skin at different depths. The slices are combined together to give the volumetric image of skin (Figure 2-14). The volumetric data is made up of voxels where each voxel presents the intensity value in confocal microscope, representing external and internal layers of skin. This work mainly targets to extract the boundary layer between internal skin layers dermis and epidermis. The active contour model based on energy minimization for edge detection is extended in 3D to extract the open surface corresponding to this boundary between two layers. The same approach is used to extract the skin surface (upper epidermal surface) which gives the skin contour in 3D.

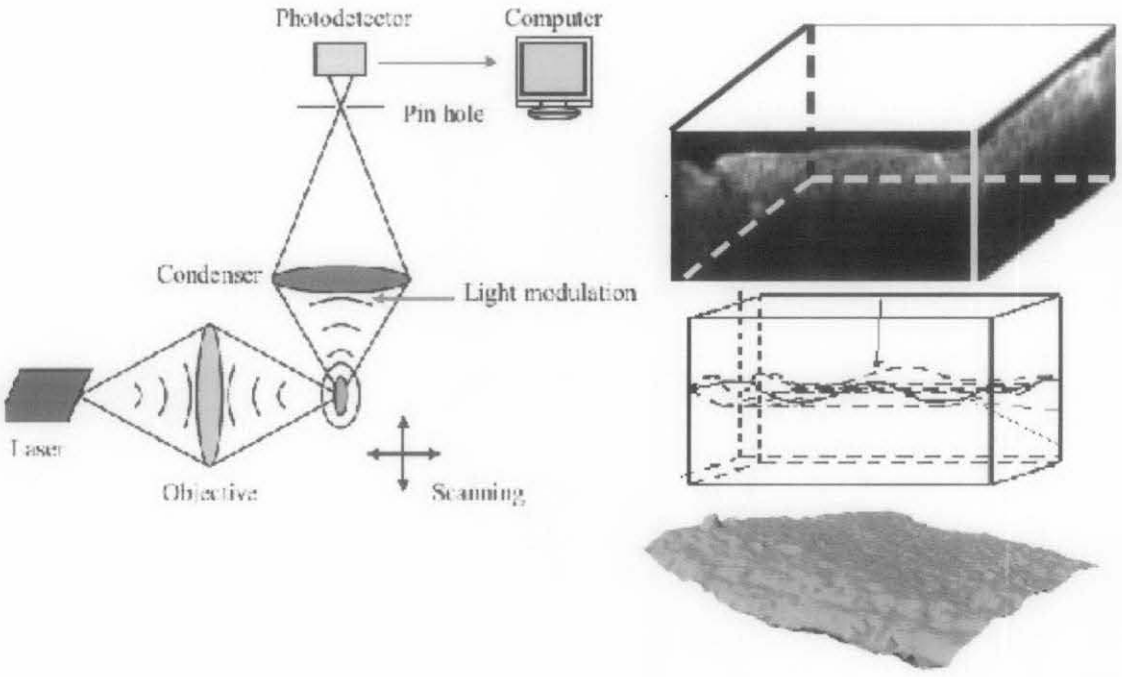

Figure 2-14: (Left) organization of a confocal microscope (Right) volumetric skin image and extraction of upper epidermal skin surface (reproduced from [Wang 2003])

Laser scanning is an advanced and widely used technology to capture depth information and provide 3D surface profiles of objects. The laser particles are reflected back from the surface of object and thus provide depth measurements. Instead of processing 2D/volumetric data, laser scanning provides the surface information directly with high resolution and accuracy. The application of laser scanning for skin has been reported by Calleiri *et al* [Callieri 2003] to build an integrated system for monitoring of skin lesions. The depth information and 2D images of skin are captured simultaneously by laser scanner. The captured surface geometry is in the form of mesh model which is combined with 2D image to give the overall model of skin. The system has been used successfully to monitor the healing of skin ulcers. Laser scanning is an advanced 3D imaging technique with high resolution and accuracy and has been used for our work.

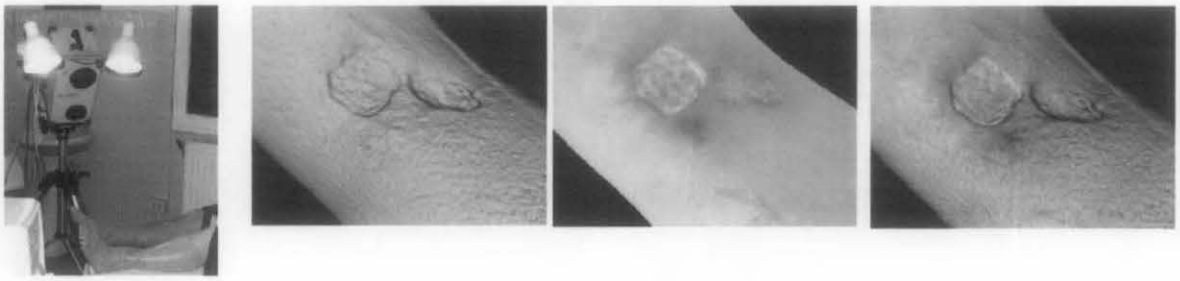

(a) (b) (c) (d)

Figure 2-15: (a) Laser scanner (b) surface geometry of skin lesion (c) 2D image (d) combined surface geometry & 2D image (reproduced from [Callieri 2003])

2.3.2 Segmentation

After image acquisition the next step, for most of applications, is to separate the diseased skin portions (lesions) from healthy skin. The process is called 'segmentation'. The segmented skin lesions are then analyzed to draw conclusions about skin condition depending on the type of application. Several segmentation schemes have been proposed which take into account the color/texture characteristics of the diseased vs. healthy skin.

One of the segmentation schemes for skin lesions of psoriasis is based on bi-modality of color features of 2D images and consists of several processing steps [Savolainen 1997, Juha 1999]. The main segmentation is done by variable thresholding of color features in sub-images. The variable thresholding overcomes the illumination variations on different portions of skin. The variable thresholding of sub images, based on the statistics of Gaussian distributions of grayscale levels, is completed in several passes which eventually label pixels with more than two strict labels of diseased and healthy skin. The labels demonstrate the confidence with which the pixels can be assigned to two different classes of diseased and healthy skin. The labeled image is then classified into healthy and diseased skin by thresholding the labels. Some post processing steps improve the classification and result in segmented lesions. The image of psoriasis lesions and results of this segmentation scheme are shown in Figure 2-16.

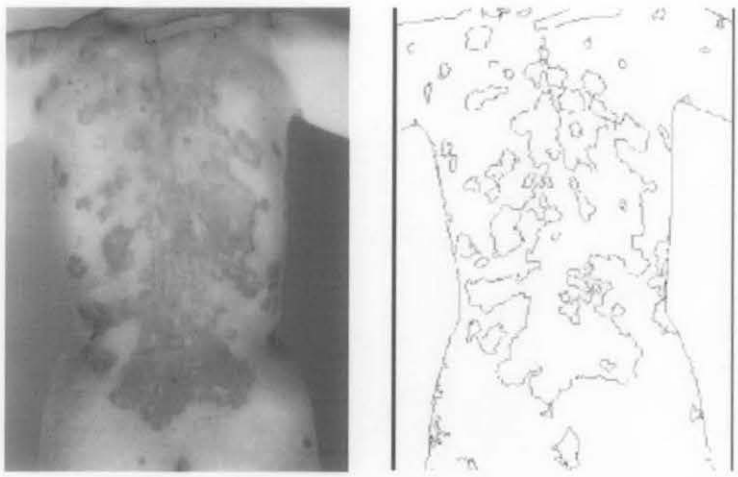

Figure 2-16: 2D image of psoriasis lesions and segmentation results for scheme used in [Savolainen 1997, Juha 1999]

A more advanced segmentation scheme is proposed by Taur *et al* [Taur 2002, Taur 2003] involving color as well as texture characteristics of psoriasis lesions. The color characteristics consist of two-dimensional Hue-Saturation space which is derived from three-dimensional RGB color space. Texture is analyzed by fuzzy texture spectrum which describes the inter-pixel gray level relationship. The homogeneous regions based on these color/texture features are detected from training image by comparing feature vectors in small windows. The smaller distance than a threshold among the feature vectors in the selected small window implies the homogeneous region in that window. This results in several homogeneous regions which are then combined to result in overall two regions corresponding to healthy and diseased skin. Figure 2-17 shows the detected homogeneous regions and their combined region for a psoriasis lesion. These two regions are then used to train the Neuro-fuzzy classifier using clustering scheme which segments any given image in two classes of healthy and diseased skin.

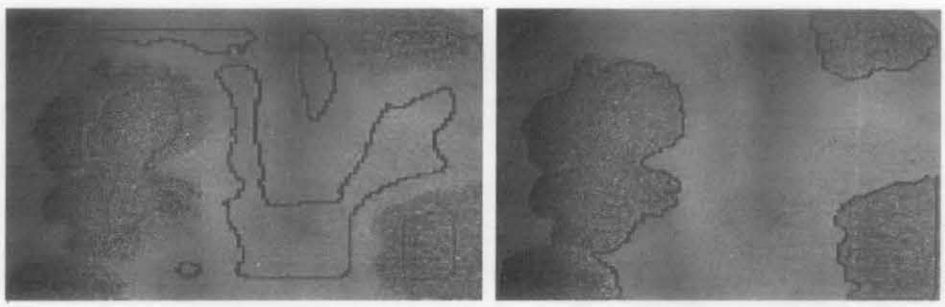

Figure 2-17: Results for homogeneous region detection and segmentation of psoriasis lesions for Neuro-Fuzzy scheme in [Taur 2002, Taur 2003]

The segmentation scheme described by Maletti *et al* [Maletti 2005] also considers the color characteristics only. In the first step the green background is separated from skin by thresholding in red band. In second step, psoriasis skin lesions are separated from healthy skin. After applying the linear discriminant analysis for finding the discriminating feature in RGB space, the value of Green-Blue band is used to separate the skin lesions. In both steps the discriminating features for background, healthy skin and skin lesions are assumed to be Gaussian distributions of different parameters which are estimated with an expectation maximization algorithm. The diseased skin is then segmented by discriminant analysis based on the estimated parameters. Figure 2-18 shows segmentation results for nine psoriasis images.

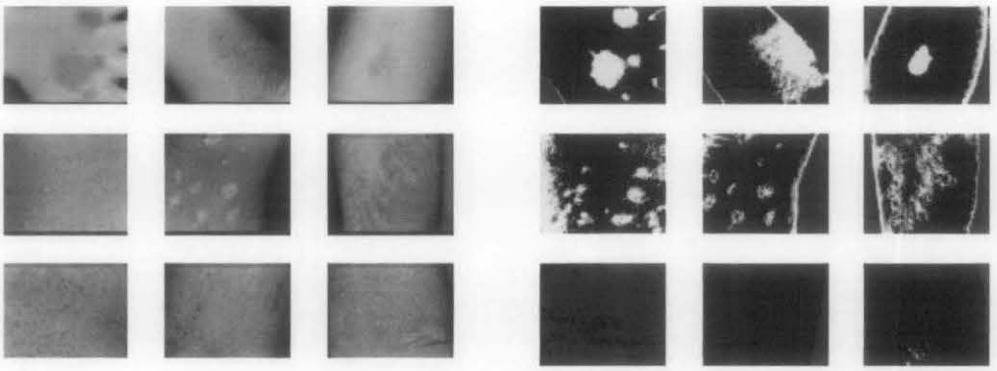

Figure 2-18: Segmentation results for psoriasis images for system in [Maletti 2005]

A comparison of several segmentations schemes for skin lesions of malignant melanoma and dysplastic nevus has been reported in the work by Illias *et al* [Illias, Kosmopoulos 2003, Illias 2003, Illias, Pavlopoulos 2005]. Again, the segmentation techniques are based on RGB color characteristics of healthy and diseased skin. These include thresholding, usage of weighted functions, region growing, Principal Component Transform, CIELab color transform and spherical coordinates transform. The segmentation results for different techniques are compared with the manually segmented lesions by physicians and found to be acceptable (Figure 2-19).

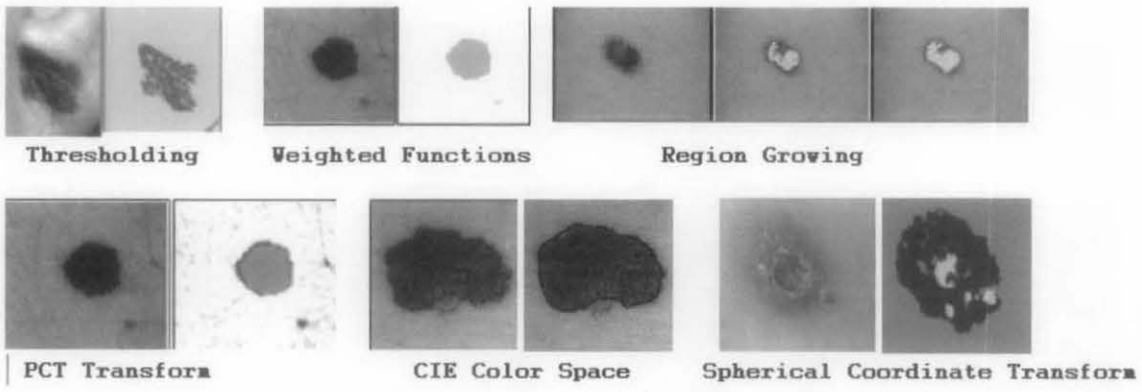

Figure 2-19: Segmentation results for different schemes proposed in [Illias 2005]

After segmentation, skin lesions are processed by analyzing different features depending on the application. The applications of images processing for skin can mainly be categorized as diagnosis, classification, monitoring and scoring of severity. However, for different diseases different problems need to be addressed. For example, early detection of skin cancer and its classification from other diseases is important. For skin diseases like psoriasis, vitiligo and ulcers, monitoring of healing to evaluate the treatment's efficacy is the main issue. In next sections some of applications for dermatology are reviewed. It is worth being noted that some of the techniques do not require segmentation of skin lesions and diseased area can be separated and analyzed as a single step e.g. in optical modeling of skin for detection of skin cancer [Cotton 2002, Patwardhan 2005].

2.3.3 Diagnosis

As discussed above, early diagnosis of skin lesions is the main concern of some diseases; the most important of which has been skin cancer. The early diagnosis of skin cancer is crucial for patient's life and classification of pigmented skin lesions of cancer from other diseases in early stages has been main topic of research for last decade. Any computer-based diagnosis system is based on some of critical features of skin lesions. And diseases are classified by discriminating the values of these features. In this section some of the systems for detecting skin cancer as an example of diagnosis applications in dermatology have been discussed.

The system by Illias *et al* [Illias, Kosmopoulos 2003, Illias 2003, Illias, Pavlopoulos 2005] classifies the skin lesions in two groups of malignant melanoma and dysplastic nevi. The classification is based on features derived from border-shape and color descriptors. The border-shape descriptors are based on the area and perimeter of skin lesions. The color descriptors are based on RGB, HIS and color variegation measurements of the skin lesions. After segmentation, the values of above descriptors are measured from pixels of known skin lesions to get the typical values of features corresponding to the two classes. Two different methods, discriminant analysis from statistical modeling and neural networks from artificial intelligence, are then used for classification based on typical values. It was shown that the lesions of skin cancers can be classified successfully from other diseases.

Another example of diagnosis system for skin cancer based on optical properties of skin layers is presented by Cotton *et al* [Cotton 2002]. The system interprets the color images of skin lesion in terms of histological parameters namely melanin, hemoglobin and thickness of papillary dermis. Once interpreted, the abnormalities in these parameters give clue to the presence of skin cancer. For the interpretation in between RGB color and skin parameters, a model of tissue coloration based on the optical properties of skin tissues is first constructed once. Kubelka-Munk theory of light interaction with matter is applied for this purpose. The skin is assumed to be structured in layer, each layer having its own reflectance and absorption properties. By providing the optical properties of layered skin and spectral composition of incident light, the spectral composition of reflected light from skin, as a function of wavelength, is computed from Kubelka-Munk theory. This spectral response is then convolved with suitable spectral response functions to get the RGB value of skin color. The model gives one-to-one mapping between RGB values of skin image and histological parameters which is used later to interpret the skin color in images to derive parameter values. Figure 2-20 shows the one-to-one mapping between RGB values and histological parameters.

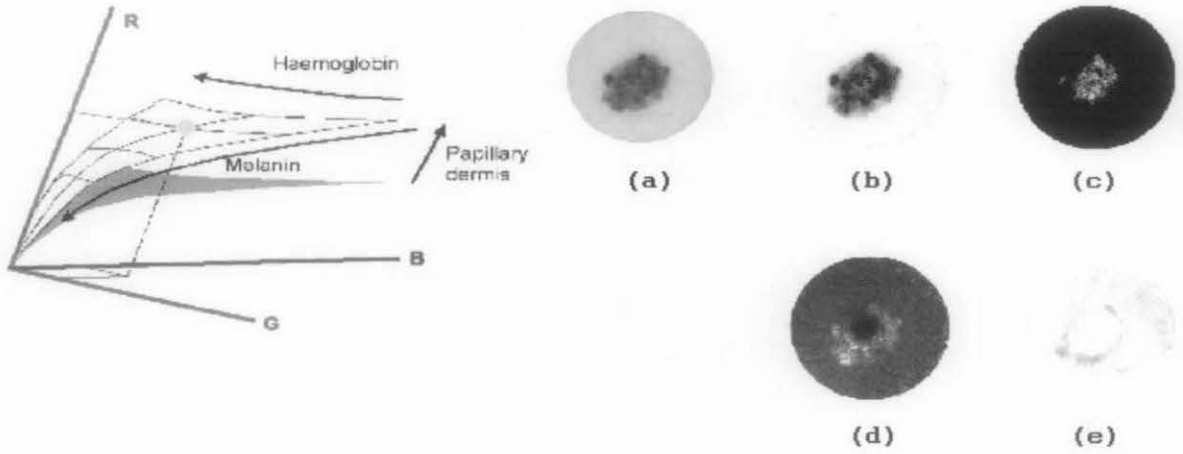

Figure 2-20: (Left) Tissue coloration model – RGB values to histological parameters (Right) A color image of skin lesion (a) and its parametric maps showing total melanin (b) dermal melanin (c) thickness of papillary dermis (d) and blood (e) (Reproduced from [Cotton 2002,])

The tissue coloration model is used to detect the melanin deposits in skin lesions. The deviation of parameter values from those of normal skin indicates the presence of skin cancer. An extension of this work [Preece 2004] improves the parametric mapping by replacing typical RGB spectral response filters by optimal spectral filters and has been shown to reduce error in recovered histological parameters.

2.3.4 Monitoring

For some skin diseases e.g. psoriasis, skin ulcers and vitiligo, the monitoring of skin lesions is more important than detection. The skin lesions for these diseases can be detected easily but keeping track of slow evolution of lesions with time is challenging. Several treatments are available for these diseases and accurate monitoring of lesions plays a critical role in selection of the best treatment for a patient. For this reason, computer-based systems regarding these diseases mostly target monitoring of lesions with time. Following is an overview of some of monitoring and scoring systems for psoriasis.

As mentioned in section 2.2, the severity of psoriasis is graded by giving PASI scores for involved area, redness, scaliness and thickness. The record of PASI scores with time gives clue to evolution of skin lesions. Deladgo *et al.* [Delgado 2003] proposes a general imaging system to capture and analyze images of psoriasis lesions for scoring the severity and a

further piece of work scores the scaliness of psoriasis lesions specifically [Delgado 2004]. Scales appear as white flaky patches on psoriasis lesions and can be analyzed by color properties. Lesions are segmented from healthy skin and analyzed to detect the scales within. A technique based on watersheds and clustering is applied to segment the scaly area. The automated scoring is based on area of scales incorporating decision trees and is mostly in agreement with the physician's scoring (Figure 2-21).

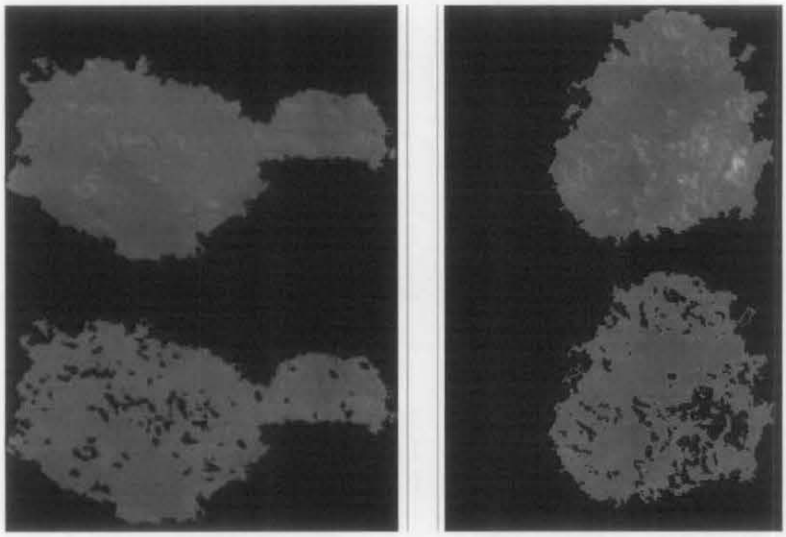

Figure 2-21: Psoriasis Lesions with white scales (Top) Lesions with segmented scales (Bottom) using the technique in [Delgado 2004]

The general pattern of time evolution of psoriasis lesions has also been sought out in addition to scoring for severity [Maletti 2004, Gomez 2004]. The images of same psoriasis lesions are captured on the duration of four weeks. The lesions in images are segmented and aligned for comparison. A statistical technique Multi-variate Detection (MAD) Transform, which is invariant to both linear and affine scaling, is used for temporal analysis [Maletti 2004] to detect the changes within lesions. The absolute value of first MAD component shows magnitude of the overall change between images whereas a correlation analysis between image color bands and MAD components shows the contribution of each color band to the overall change. The results for few cases show the pattern of time evolution of psoriasis lesions i.e. at initial stages the changes occur mostly in the center which are gradually shifted towards border and that the blue and green bands contribute more to the temporal changes. The work by Gomez *et al* [Gomez 2004] analyzes similar images a different statistical

technique Mulit-set Canonical Correlation Technique (MCCA) to track changes within lesions with treatment.

In contrast with all above 2D imaging based systems an interesting integrated system called 'derma' is based on 3D imaging and also targeted for monitoring [Callieri 2003]. It is an integrated tool to monitor evolution of several types of skin lesions. The system consists of laser scanning for 3D image acquisition and a database to monitor the progress of skin diseases by managing the corresponding data of patients. The data of patients recorded in timely manner aids dermatologists for in best effective treatment of disease.

2.3.5 Cosmetic Industry

The 3D images of healthy skin provide more comprehensive information about skin features e.g. wrinkles, fine lines, smoothness. The analysis of these features has significance in both cosmetic industry and computer graphics in addition to dermatology. The changes in skin features indicate the effectiveness of topical agents in cosmetic industry. For computer graphics, these skin features when modeled on skin of animated objects, constitute more realistic animation. Section 2.4 will review the modeling of 3D skin features for computer graphics.

The skin contours with ageing have been analyzed to quantify the ageing process [Uchida 1996]. An apparatus based on laser scanning is used to capture the surface profile of skin. At high resolution the patterns on skin appear to consist of longitudinal, transverse and oblique ridges. The Fourier analysis quantifies these patterns as spatial frequency characteristics and gives clue to the changes in skin with ageing process. It is concluded that the dominant spatial pattern on skin changes from high frequency ridges to low frequency ridges with increasing age. The work by Moonalso targets to quantify the ageing contours of skin captured through stereo imaging (Section 2.3.1) [Moon 2002]. Five new parameters namely mean surface roughness, mean depth of roughness, three-dimensional length, three-dimensional area and three-dimensional volume, are defined on three coordinates to quantify the surface features of skin. It was observed that some of parameters increase with ageing

indicating the increasing roughness of skin. It was also proposed that the 3D acquisition system and the set of defined parameters can be used to evaluate the skin response to topical agents and cosmetics as well as to monitor the skin diseases like psoriasis, ulcers and ichthyosis. Accordingly, a further piece of work uses this system to evaluate the severity of psoriasis quantitatively [Park 2004].

2.4 3D Modeling of Skin

The 3D structure of skin surface has been studied for computer graphics more than for cosmetics/dermatology, however, with a different perspective in this case. The healthy skin surface features are analyzed to be modeled on human characters in computer animations for a more realistic look. The goal is not only the accurate capturing of patterns from skin surface and their synthesis but also the fast rendering of these patterns. The complexity of surface detail increases largely and fast rendering becomes difficult. The modeling of 3D skin features and its fast rendering has been an active area of research in computer graphics. In this section, it is discussed to review the modeling of 3D surface features of healthy skin.

The 3D structure of skin can be categorized in two types, wrinkles and fine lines/fine texture. The wrinkles can be localized on body portions (e.g. on fingers, elbows) or expressive (e.g. facial wrinkles on forehead, cheeks) or due to ageing process present on most of the body. Fine texture of skin is present on the whole body with patterns varying locally. The modeling techniques for rendering attempt to synthesize these skin structures on animated object as well as reproduce their dynamics with body movements.

In the work by Wu *et al* [Wu 1996], both wrinkles and fine textures on human skin and their dynamics are modeled. The fine lines pattern, based on observation of microscopic photographs of skin is modeled as triangular mesh with several layers. Delaunay triangulation is used to create the layered triangular pattern. A hierarchical triangulation with different levels of triangulations creates the pattern similar to fine lines on human skin. The edges of triangles are then raised/lowered to create bulges. The resulting height field is used for bump mapping on human skin in animation. The pattern of triangulation and height can

be changed for different portions of body by changing input parameters. Figure 2-22 shows the microscopic pattern found on human skin, hierarchical triangular mesh with bulges and bump mapping of this mesh on skin.

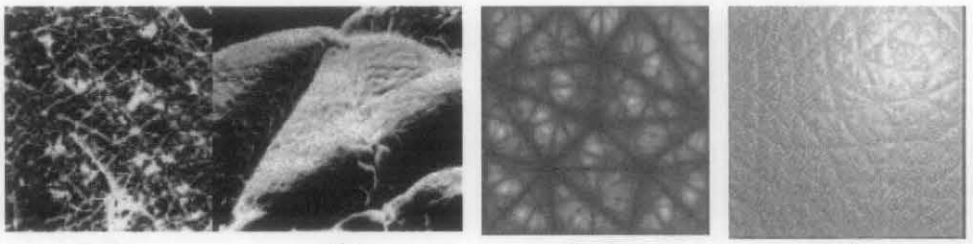

Figure 2-22: Modeling of fine texture of skin [Wu 1996] - (a, b) microscopic triangular patterns on skin (c) hierarchical triangular mesh (d) bump mapping on skin

For modeling of wrinkles, the 'constrained' Delaunay triangulation is applied which maintains the location of large scale wrinkles determined interactively while triangulating fine scale texture (Figure 2-23). For the bulges of skin in between wrinkles several shape functions are applied. The combination of pattern and bulges of both wrinkles and fine line texture gives more realistic skin model of human skin appearance for rendering. This work does not follow the actual patterns of skin completely. However, the simplification by assuming the overall triangular pattern of skin structure results in fast rendering.

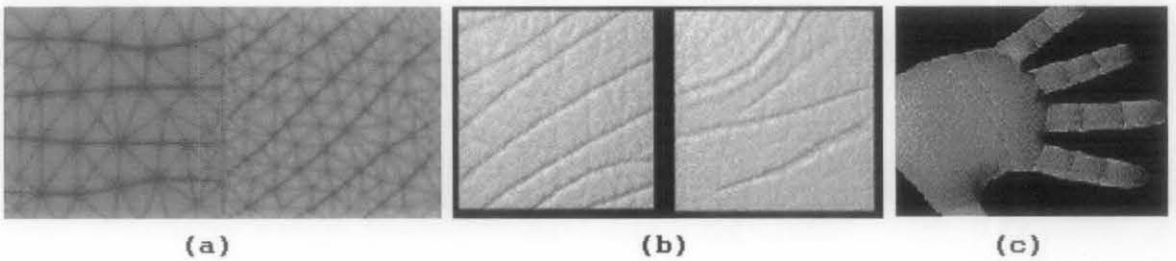

Figure 2-23: Modeling of wrinkles of skin [Wu 1996] - (a) constrained triangulation for wrinkles (b) bump mapping on skin (c) rendering of hand skin with fine lines and wrinkles

The work by Boissieux addresses large scale wrinkles where effects of aging are also incorporated [Boissieux 2000]. Two approaches, namely image-based and model-based, have been proposed that depend on both visual and biomechanical properties of skin. The image-based method is simple, incorporating no biomechanical properties, and producing wrinkles

due to aging only. A 2D texture image of a subject's face is transformed to incorporate the aging effects by darkening effect. From pre-computed masks of aged faces (2-24), the wrinkles are darkened in the texture images which are then used for bump mapping the 3D meshes for rendering. During rendering the wrinkle depth is increased with age..

Figure 2-24: Typical ageing masks used for darkening subject's faces for ageing effects [Boissieux 2000]

The model based method is complex, considering physical biomechanical properties of skin, and models formation of wrinkles due to mechanical deformation of skin layers. In this method the 3D mesh of skin is deformed directly instead of bump mapping. Skin is considered to be composed of two layers with different thickness and mechanical properties. Temporary wrinkles are produced by deforming the two layers according to their mechanical properties. The permanent wrinkles (due to aging) are produced by introducing the 'shape memory' as the rest shape. The rest shape is changed gradually with each deformation. This slow adaptation depicts skin history as permanent wrinkles and also guides the pattern of further wrinkles.

Bando *et al* [Bando 2002] addresses the modeling of both large scale wrinkles and small scale fine lines. The model of small scale fine lines is based on observation of photographs of real skin like the work by Wu *et al* [Wu 1996] to provide more user control over patterns of skin structure. However, in this case the fine lines are assumed to be more complex than the simple triangular mesh i.e. the fine lines run parallel locally in two directions and end at their intersection point. The pattern created according to these observations achieves more visual similarity but requires user interaction. A user will define local directions of fine lines at selected points of object which are interpolated to produce complete direction field. An algorithm based on this height field creates the pattern of furrows in 2D texture image which is then used as height field for bump mapping (Figure 2-25).

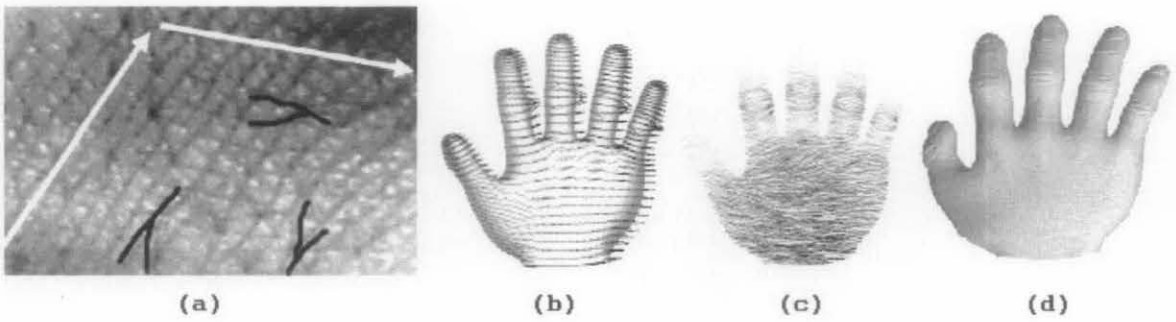

Figure 2-25: Modeling of fine lines of skin in [Bando 2002] – (a) pattern of fine lines on skin (b) direction fields on hand specified by user interaction (c) interpolated height fields (d) the hand after bump mapping

In this work the large scale wrinkles are also modeled and validated by comparison with the actual wrinkles on skin. A user identifies the location and shape of the wrinkle in 2D texture space by drawing a cubic Bezier curve. An exponential shape function gives the bulges and depressions due to large scale wrinkles on skin by deforming the 3D mesh. Figure 2-26 shows the wrinkles drawn on 3D mesh and the corresponding real wrinkles captured by a digital camera. The deformation in wrinkles and fine lines produced by shrinkage of skin due to movements of the object is also rendered. This is achieved by modulating their amplitudes by calculating the shrinkage of skin on vertices of mesh.

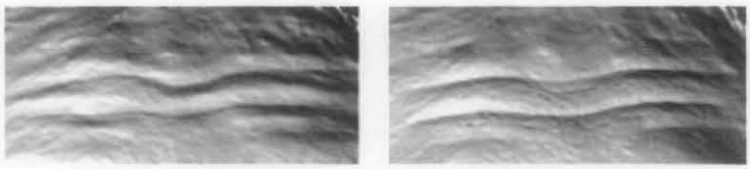

Figure 2-26: (Left) wrinkles captured by digital camera (Right) wrinkles rendered by modeling scheme in [Bando 2002]

The capturing, modeling and rendering of skin structures discussed above do not follow the actual patterns on skin *exactly* and in every case some simplification is applied for fast rendering. Haro *et al.* [Haro 2001] addresses this problem by capturing patterns from skin samples directly. Their attempt is to model fine textures by following real physical patterns and to render them efficiently. The first step is to obtain skin patterns. Silicone molds of skin record fine details of skin. A set of images is taken from the mold with different light source positions. The 'shape from shad*ing*' algorithm gives surface normal at every pixel of image

by solving simultaneous linear equations in light vectors and intensity. Several normal maps are captured for a face. However, these samples are quite small in size. The stochastic modeling (by Markov random field) of fine scale textures yields synthesis of larger samples which are joined together by applying multi-resolution splines on random curves. The resulting multi-texture model for face gives the normal map used for more realistic skin rendering (Figure 2-27).

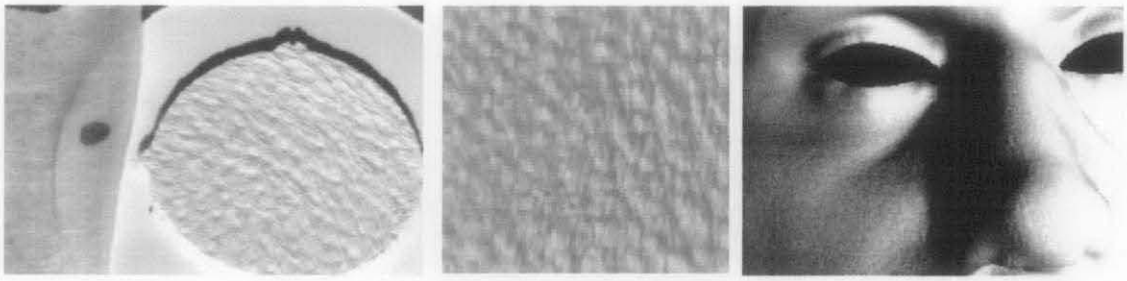

Figure 2-27: (Left) silicone mold with skin pattern on it (Middle) Normal map captured from images of silicone mold (Right) bump mapping of mesh model (reproduced from [Haro 2001])

2.5 Summary

For dermatology, the 3D images provide information about diseased skin whose surface features deviate from healthy skin. Many diseases cause inflammation of skin e.g. psoriasis, eczema while skin ulcers, wounds, burns can result in removal of upper layers of skin. In this chapter, within scope of this work, an overview of healthy and psoriatic skin was given. The structure of healthy skin was described and then how the psoriasis can alter this healthy structure to create psoriatic lesions. It is seen from different types of psoriasis that all of them result in some sort of inflamed, scaly, red and thick skin lesions. It was mentioned that psoriasis is a worldwide prevalent disease which cannot be cured because of its genetic origin. The only way to treat it is to get rid of the symptoms, skin lesions in this case. Experimentation is done with treatments while monitoring the evolution of skin lesions to find the best one. For monitoring purposes, it was mentioned that several characteristics of the lesions (e.g. redness, thickness, roughness, scaliness) are important which also involve the 3D features of skin lesions such as thickness and scaliness. The dermatologists examine these 3D characteristics visually and sometimes by tactile (touch) inspection also to perceive

the roughness and hardness of the skin lesions. Therefore, any computer-based system targeting to aid dermatologist in inspection/monitoring of the diseases must not overlook these 3D features of skin lesions. But what can be found from this literature review of skin imaging is that the majority of computer based systems for dermatology are based on 2D images. The 3D imaging techniques for skin are mostly indirect i.e. the 3D skin surface profiles are extracted from some sort of processing of 2D images. Laser scanning is the only imaging tool capturing skin geometries directly and with high precision. It can also be observed that, in case of modeling of 3D skin features, the research efforts mostly target computer animation for more realistic look. For this reason, 'approximations' of wrinkles and fine textures of healthy skin are modeled and rendered only. The capturing and modeling of actual skin features faithfully has not been the main concern in these attempts. Only the work in by Haro *et al* [Haro 2001] follows real skin textures and that also through an indirect technique of recording it through a synthetic mould and then processing 2D images of the mould. This research work follows a similar approach i.e. modeling of skin based on real textures of skin but incorporates more advanced 3D imaging techniques for high precision and including both healthy and diseased skin textures. The 3D imaging system will be described in Chapter 5 which involves laser scanning [http://www.konicaminolta-3d.com] for capturing purposes.

Chapter 3

Haptic Technology

The word 'haptic' means pertaining to the sense of touch. The sense of touch, *haptics*, provides a unique bidirectional communication among all five human senses. The human-computer interaction has been limited to visual and auditory display of information. Haptic technology takes this interaction one step further by allowing the haptic manipulation of virtual objects in computer by user. At present, the technology is incorporated in applications like medical/surgical simulations/training, tele-surgery, digital sculpting, painting and CAD, scientific visualization, assistance for the visually impaired, museum displays, tele-robotics, neurological rehabilitation and military [Taylor 2005, McLaughlin 2001]. Haptic technology aims to provide virtual environments allowing user interaction with virtual objects or data in computer through haptic devices. A virtual environment has three key components namely the haptic (and sometimes graphic) display of virtual objects, haptic display interface/haptic device and rendering algorithms for haptic display properties of objects which connect the first two. The user interaction can be of several types. A user can merely feel the shape/surface/volume properties of virtual objects or, as advanced interactions, can move/deform the virtual objects. All these interactions are mainly based on 'force feedback' through haptic devices which provide user with accurate forces for the haptic feelings of shape, surface roughness, deformation, movements and even the strong forces of collisions. Calculation of these forces based on user movements on haptic device and transmission of updated forces to haptic device as a response is called 'haptic rendering'. Haptic rendering has been a main area of research in last decade. The main problem is the provision of *realistic* haptic perception. Humans are expert at haptics and any abnormal interaction with haptic device gives unrealistic haptic perception. For this reason, forces have to be calculated and updated at as high rate as 1 kHz and that also following the user

interaction accurately to give the stable perception. The research has been focusing on force calculation algorithms which are fast and efficient in calculating stable and realistic force feedback. Section 3.2 will review some of the haptic rendering techniques for realistic, fast rendering.

Haptic Display Properties: The virtual objects can have several haptic display properties e.g. 3D shape, stiffness, friction, surface texture and volumetric properties. The detail of haptic properties depends on the requirement of application. For some applications e.g. visualization for the blind, only the shape would suffice whereas for others e.g. surgical simulations, shape as well as surface details are required. However, the rendering algorithms have to be altered to reflect every haptic display property in force feedback and therefore detailed object properties are difficult to render. Specially, the display of surface textures poses a significant problem, the reason being the high frequency details present on the surfaces. For example, a small virtual cube can be presented by only six faces in a mesh but the same cube with textures surface having small variations in surface heights may required hundreds even thousands of faces. The calculation of user interaction with so many components (faces) in the virtual object will be computationally too expensive to be updated at high rates. On the other hand, textures are crucial for realistic display of virtual objects. That is why, rendering of surface textures make an active area of research as well and many algorithms are being proposed and improved. Section 3.3 concentrates on reviewing the rendering techniques for surface textures. Currently most of the haptic devices are probe based having pen-like user tools. The perception of roughness arising from exploration of surface textures via these tools becomes an addressable topic. Section 3.4 discusses some work done in this area. Finally, as examples of applications of haptic textures, section 3.5 discusses the scientific visualization through haptic textures and the haptic display properties of materials like skin and cloth.

3.1 Haptic Display Interfaces

Haptic display interfaces or haptic devices provide the bidirectional communication in between user and computer. The user exerts force on haptic device and feels the response

force according to the virtual object's properties. On the other side, the computer application monitors the movement of user and provides the response forces through device. Thus the major task of device is to sense user movements and to exert response forces at high rates.

Tactile and Kinesthetic: Haptics mainly deals with two types of touch perception namely tactile and kinesthetic. Tactile is related with the skin stimuli. A user perceives the spatial distribution of forces through skin stimuli when he touches some surface with the finger tip. This distribution results in perception of roughness and other surface details. Kinesthetic, however, is related with the net force on a muscle. This gives the perception of one's own position. Interaction with objects like moving and colliding are result of kinesthetic [Salisbury 1997]. Several haptic devices have been developed by research laboratories, many of which have been commercialized as well. These devices vary in their design and performance. Most of them are targeted for kinesthetic and very few provide the tactile perception. Currently no device is available commercially dealing with tactile perception.

Degrees of Freedom DOF: Another important property of haptic devices is 'Degrees of Freedom' or DOF. Degrees of freedom for an object describe the set of independent displacements the object can move. For example, an object in 3 dimensions has 6 DOF including three translations in three dimensions and three axes of rotations. The DOF of a haptic device determines the user movements on device based on its design. For some devices, which are combination of more than one moving part, the combined DOF is the sum of individual DOF of all moving parts.

Sensable Technologies [Sensable Tech.], FCS Robotics [FCS robotics], Force Dimension Technologies [FD Tech.], Quanser Incorporation [Quanser Inc.], Immersion Corporation [Immersion Corp.], Virtual Technologies [Virtual Tech.] and Cybernet Systems Corporation [Cybernet Corp.] are some of the commercial manufactures of haptic devices. The haptic devices mostly differ in designs and specifications. Users can work through pen/stylus-like probes (e.g. PHANToM devices [Sensable Tech.]) in applications like virtual painting, surgical simulations, data visualization, where the probe may replace the real tool or is used to explore the surface features. Some devices allow plate/ball/thimble like exploration tools

(e.g. Pantograph Quanser Inc.], DELTA [FD Tech]). Users can also work through gloves/grasps (CyberGrasp/CyberForce/CyberGlove) [Immersion Corp.] which allow force feedback through several degrees of freedom through fingers. Figure 3-1 shows some of commercially available haptic devices. Some larger haptic devices are in progress to provide force feedback at arms and shoulders. The user working area is determined by DOF. The haptic devices range from 2 DOF to 6 DOF for single portion device and more than that for multiple joint devices. Lower DOF usually allows movements in coordinates but higher DOF allows the rotations as well. An appropriate device is selected according to the application's requirements which determine the shape of the exploration tool and degrees of freedom.

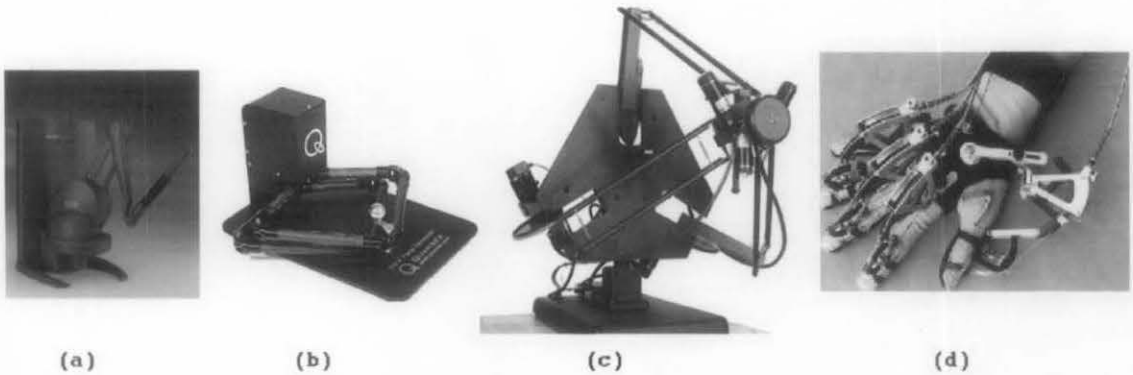

Figure 3-1: Haptic Devices with different designs and working area (a) Phantom (b) Pantograph (c) DELTA (d) CyberGrasp

The performances of different haptic devices are probable to vary for the same application and their comparison becomes addressable before selecting a specific device for the application. For this reason, research studies target to compare them in different aspects as well. For example, Yu *et al* [Yu 2002] compared two haptic display interfaces, SensAble PHANToM [Sensable Tech.] and Logitech WingMan force feedback mouse [http://www.logitech.com/], in presenting graphical data to the visually impaired in a *multimodal* condition. The WingMan mouse is much cheaper device than PHANToM. Their application presents data as bar graph in both haptic and audio modes to the blind participants. The participants can touch bars through the devices. The results of experiments show that the participants' perception of data, in multimodal condition, is almost the same for both WingMan and PHANToM. Therefore, in a combined haptic and audio feedback application, the inexpensive WingMan can replace PHANToM.

Penn *et al* [Penn 2001] investigated the perception of roughness from 'virtual textures' using two haptic devices, IE3000 [Immersion Corp.] and PHANToM, and compared them with the prior work about perception of roughness from 'real textures'. In the experiments, both sighted and blind participants rated the roughness of several virtual textures using stylus and thimble endpoints. It was shown that both devices gave similar results in perception of roughness as function of groove width i.e. perceived roughness decreases with groove width. This result was in contrast with earlier experiments with real textures for which the perceived roughness increased with groove width. The authors conclude this as a result of differences in exploration endpoints i.e. thimble/stylus (in virtual textures) vs. finger point (in real textures). The similar results for two devices strengthen authors' guidelines for future applications based on virtual textures. A similar work investigated the perceived size and angularity of virtual objects though a similar procedure involving blind and sighted participants [Penn 2000]. Again, the results did not show significant differences in perception through two haptic devices.

Salisbury *et al* [Salisbury 1997] discusses the PHANToM haptic interface in detail and presents the results of haptic rendering of several virtual objects through different rendering algorithms. The performances of potential field rendering for small spheres and thin composite objects, constraint-based and ray-based rendering for polyhedral solid objects of many shapes, and implicit-based rendering of shapes have been analyzed. Based on the device characteristics, several haptic and multimodal (including haptic, auditory and visual channels) applications e.g. medical training, educations, entertainment, have also been proposed.

Tactile Haptic Devices: Although tactile devices have not been commercialized yet, their development and rendering capabilities are in progress. Tactile is a vital portion of human haptics sensing small surface details of objects and hence, their incorporation in current haptic technology is inevitable in future. Several tactile display interfaces are being developed and investigated in research laboratories worldwide. For example the **STReSS Tactile Display** (McGill University) provides the stretch stimuli to fingertip skin by sending

strain signals through an array of miniature actuators. The **MORPHEOTRON Haptic Interface** (McGill University) is another device. Its first version has been used to study the tactile cues by implying a finger pad. The studies will serve as basis for developing a state-of-the-art tactile device. A haptic device consisting of both force feedback and tactile display **PhilaU Haptic Device** has been developed at Philadelphia University. It makes use of an array of pins and has been used to simulate fabric textures. A similar device was also developed at university of Kalsruhe. Figure 3-2 shows several tactile haptic displays which resemble each other through a working pad for finger-tip and an array of actuators. A survey of tactile interface design techniques has been presented by Khoudja *et al* [Khoudja 2004].

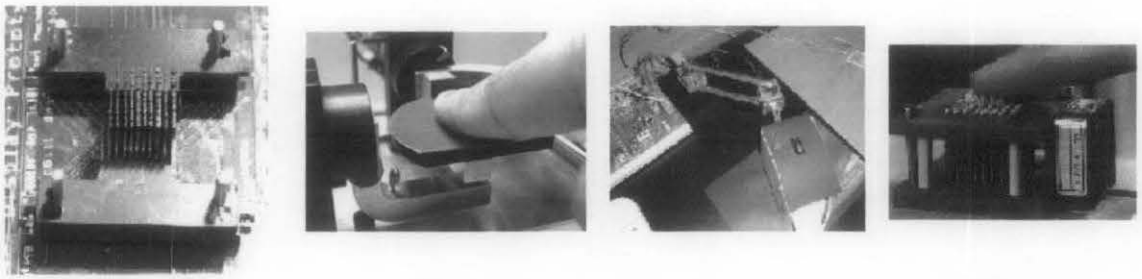

Figure 3-2: Tactile Haptic Displays (a) STReSS (b) MORPHEOTRON (c) PhilU Tactile device (d) Tactile Device Kalsruhe

3.2 Haptic Rendering Techniques

Haptic rendering means to display haptic properties of virtual objects in real time via haptic device. The haptic properties are displayed by computing the feedback forces based on object properties and user movements on haptic device. As discussed earlier, haptic feedback forces are to be calculated and updated at as high rates as ~1 kHz for realistic haptic interaction. For this reason haptic rendering algorithms targeting less computational time have been proposed in most of the haptic related research studies. Generally, any haptic rendering algorithm has two portions to be addressed a) how the object properties are displayed b) the type of virtual haptic cursor (exploring virtual object) and how the forces are calculated based on this haptic cursor and object properties. The algorithm keeps track of haptic cursor movement which is moved by user movements on haptic device. Once a collision between haptic cursor and

virtual object is detected, the resulting force and torque is calculated by some force model and applied on user hand via the device. Figure 3-3 below shows a schematic of overall haptic interaction schematic. The rendering algorithm includes collision detection, and fast updates of collision response forces depending on object properties and user movement.

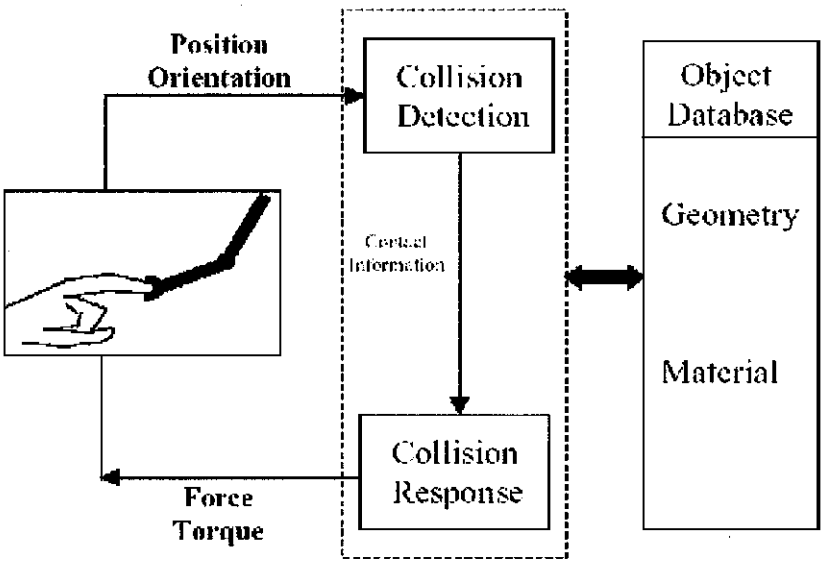

Figure 3-3: A schematic of haptic interaction paradigm

The initial haptic rendering algorithms were simple and interacted with simple shapes. For example, in a point-based penalty method [Ho 1999], the end-point of probe is considered as a virtual point which can penetrate the virtual object whereas actual probe cannot penetrate the real object. The response force is calculated from the penetration depth of the virtual point. The model works well with simple objects but has limitations for complex interactions and objects. Figure 3-4 illustrates the calculation of response forces based on penetration depth. Small darker sphere shows the user movement in virtual environment which can penetrate the virtual sphere. Response force is dependent on its penetration depth $(R-r)$.

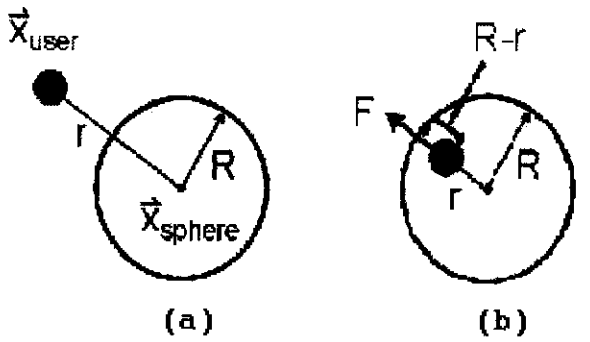

Figure 3-4: Point-based penalty method for haptic rendering

After the simple point-based methods, more sophisticated constraint-based methods have been developed which allow the rendering of more complex generic polygon meshes. In constrained-based methods, the haptic cursors are accompanied by some 'proxy/god' cursors. After a collision with the virtual object, the haptic cursor can penetrate but the proxy cursors are *constrained* to remain on the surface just like the real probes. The algorithm then tries to calculate the force by minimizing the distance between haptic cursor and its proxy cursor in some efficient way depending on the polygonal display of virtual object. Figure 3-5 shows a general schematic of constrained based haptic rendering. While the haptic cursor (blue sphere) can penetrate the object's surface, proxy/god objects are constrained to the surface. Both are tied with each other virtually and the response force depends the separation distance. Several improved versions of this general algorithm have been proposed over time. For example, Ho *et al* [Ho 1999] presents a more sophisticated form by introducing neighborhood-watch. The polygonal data of virtual object primitives (polygon, vertex, edge) is stored in a database along with its neighbor primitives. The database based on neighboring data results in a reduced search space. For every force computation, the algorithm looks for neighboring primitives only instead of every polygon of the object. This way force computations are no longer dependent on polygon count of virtual objects and result in more computational efficiency.

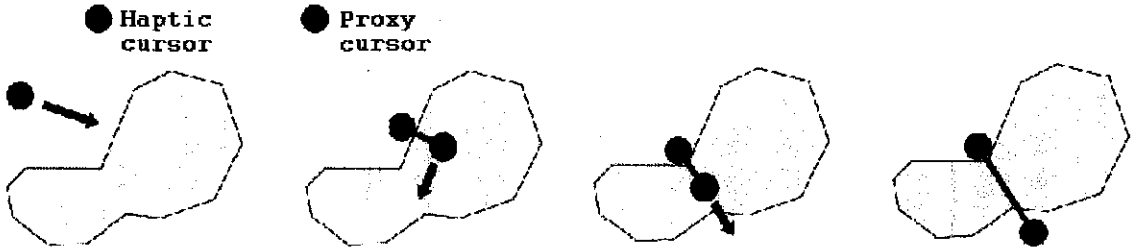

Figure 3-5: Constraint-based method for haptic rendering incorporating haptic and proxy cursors

The above algorithms have 3D objects presented as geometrical polygon data. Kim *et al* [Kim 2002] uses a different Implicit-based surface representation for 3D objects. The geometrical, polygon-based surface of object is changed to an implicit surface. The implicit surface is in the form of implicit equation and gives location of co-ordinate points (inside, outside or on the 3D object) as the sign and value of potential function. This representation reduces the complexity of collision detection problem, which traditionally tried to search the whole polygon space, by changing it to a simple inside/outside property. After fast collision detection, the force is calculated following the constrained-based approach. An extension of this work combines the geometric and implicit surface representations as 'Hybrid surfaces' and presents haptic editing algorithms for haptic decoration of objects, editing of material properties locally and engraving/embossing of objects [Kim 2004].

3.3 Haptic Display of Surface Textures

The haptic display of virtual objects is getting more complex and realistic by inclusion of more haptic properties than polygonal or implicit shape representation. Friction, stiffness and surface textures are the other detailed haptic display properties critical to the realistic feeling of touch.

Friction: The haptic property of friction allows user to distinguish between slippery and resistive surfaces e.g. ice, glass, wood. A popular way of modeling friction is to use lateral forces in addition to normal constraint forces on probe [Ho 1999, Kim 2002, Kim 2004]. Static and dynamic friction coefficients in lateral force calculations can be changed to present

different frictional surfaces. The simulation of stick-slip phenomenon to model static and dynamic friction respectively adds more realism to haptic interaction [Ho 1999].

Stiffness: Stiffness of virtual objects is needed in applications which allow the deformation of virtual objects by user interaction e.g. sculpting. The stiffness distinguishes the rigid bodies like metals and woods from easily deformable bodies like skin, fabric and clay. Stiffness is modeled as elasticity of the object surface and the spring-based mechanical model provides the appropriate force feed-back to give the feeling of surface deformation and stiffness. Different stiff and elastic surfaces can be modeled by changing the values of spring constants [Kim 2004].

Surface Texture: The textures of surfaces add high resolution detail to the surface of a virtual object. Surface textures result in haptic feelings of bumpy surfaces and roughness of the virtual object. As mentioned earlier, surface texture is the most challenging haptic display property due to its computational cost and high update rate requirements of haptic application. If the texture is added by changing the geometry of object explicitly i.e. changing the polygon mesh, the resulting mesh will result in enormous number of polygons and the real-time rendering will be impossible (Figure 3-6). Instead, alternative techniques are used to incorporate textures in feed-back forces. Most of these techniques are similar to those for texture rendering in computer graphics e.g. bump mapping. Following is a review of some of popular texture rendering techniques.

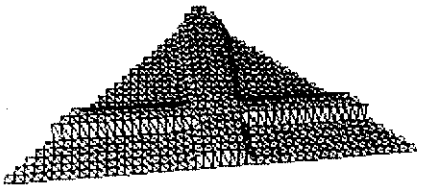

Figure 3-6: A simple texture results in enormous number of polygons

3.3.1 Haptic Rendering of Surface Textures

The most popular way of haptic texturing is 'force mapping' inspired by bump mapping for texture rendering in computer graphics. In force mapping, based on height fields (grayscale images), the magnitude and direction of calculated normal forces are modulated some appropriate way by height field values. For example, the position of proxy cursor is changed by adding height, thus changing the penetration depth and modulating the magnitudes of normal forces [Ho 1999]. Figure 3-7 illustrates force mapping. Small sphere shows the position of penetrated haptic cursor. The height from texture **H** is added to the penetration depth **d**. The direction of forces is also changed by the bump mapping algorithm. The algorithm perturbs the surface normals of the normal forces according to the height fields and thus produces the feelings of bumps in an otherwise smooth surface. The height fields for textures are either obtained from 2D image data or from synthesized textures generated from mathematical functions (procedural approach).

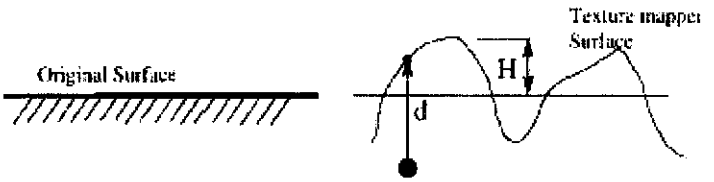

Figure 3-7: Force mapping – original surface vs. textured surface [Ho 1999]

Theoktisto proposes a new algorithm 'height field rendering' and compares it with the force mapping technique mentioned above. The algorithm allows triangles in mesh models to have different textures. Forces are calculated the same way as in penalty-based method but the collision detection is different. The collision detection includes surface textures based on height fields by building virtual triangles over mesh triangles according to the height field values (Figure 3-8). Collision of probe with these virtual triangles triggers the force feedback [Theoktisto 2005].

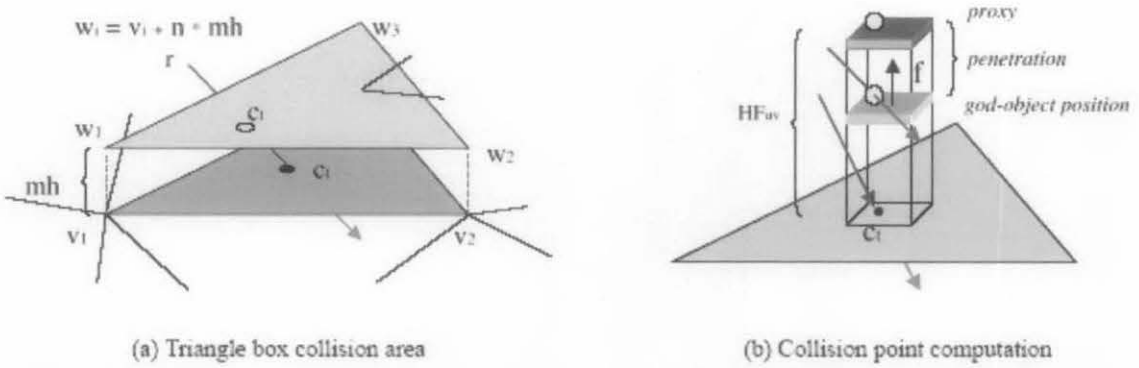

(a) Triangle box collision area (b) Collision point computation

Figure 3-8: Height-field collision mapping using virtual triangles (shown in pink) [Theoktisto 2005]

The experiments show that the proposed technique is better in perception of shape like textures but for high resolution textures, giving the feeling of roughness, it does not outperform force mapping. Figure 3-9 shows examples of shape like textures in one polygon and high resolution textures.

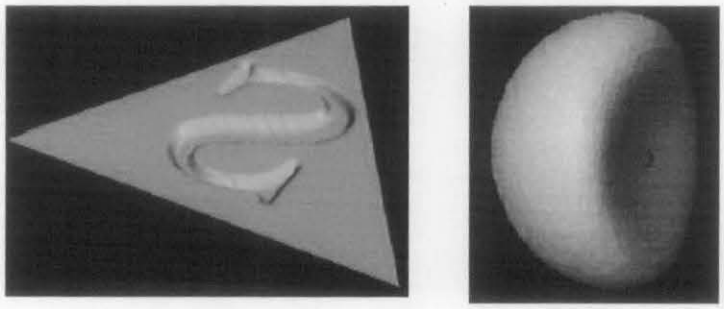

Figure 3-9: (Left) shape like texture in one polygon (Right) high resolution texture

Mercier *et al* [Mercier 2005] also uses the 2D texture images for haptic texture rendering. However, the texture images are not used simply to perturb the forces as is done in bump mapping. The algorithm computes the height/elevation map from luminance/brightness values at every pixel of texture image and raises the asperities on virtual object's surface in actual polygon mesh accordingly (Figure 3-10). The magnitude and direction of forces are then calculated by taking into account these small asperities due to texture.

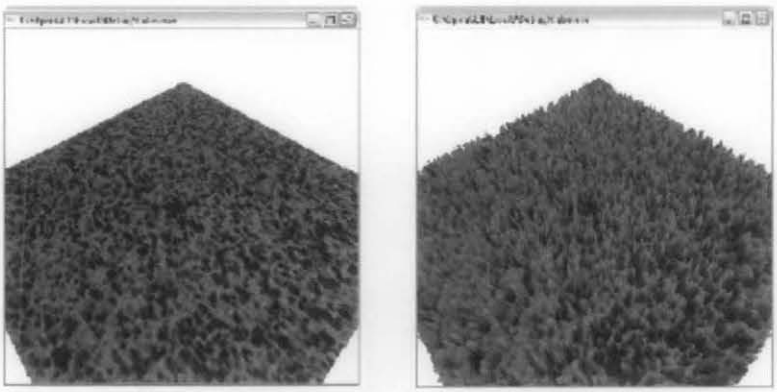

Figure 3-10: Surface rising from texture images in [Mercier 2005] – (a) 2D texture image (c) heightened surface

Aside from image based textures and the corresponding height fields, synthetic textures can be generated from mathematical models as well in procedural haptic texturing and are mainly used in data visualization applications. Sirra presented the idea of stochastic modeling of surface textures for less computational cost and real-time haptic rendering [Sirra 1996]. It was proposed that the device need not follow the texture exactly and only an accurate haptic illusion to the user is required. Thus a texture can be modeled as stochastic process and rendering any sample of the corresponding probability distribution will give the similar haptic perception. By using the statistics of a random texture field, the heights and forces can directly be generated on the object space and the computations of conversions from texture space to object space can be saved which increases the overall efficiency of algorithm. The method was shown to produce realistic and real-time haptic textures. Fritz *et al* [Fritz 1996] also discusses several stochastic models (Figure 3-11) to generate perceivable synthetic haptic textures whose parameters can be tuned by data values. Several sampling techniques in 2D and 3D are presented to convert the desired stochastic textures from texture space to object space for rendering. Aysal *et al* [Aysal 2006] uses several stochastic and harmonic models to create pseudo haptic textures for data visualization.

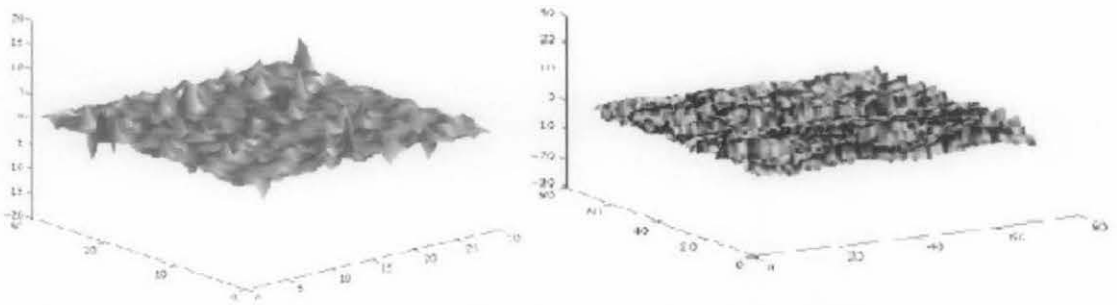

Figure 3-11: Stochastic textures used in [Fritz 1996] – (Left) mixture of Gaussian distributions (Right) sinusoids with noise

Apart from defining appropriate models for haptic textures and techniques to integrate them in haptic rendering, a recent work presents developed user-programmable modules to integrate procedural textures with current haptic applications [Shopf 2006]. The modules consist of texture programming procedures with several input parameters like stiffness, damping, and friction. These modules are executed after every collision detection event to output the resulting forces based on surface texture properties. The application provider can shade every object in virtual environments by changing input parameters to these texture shading procedures.

3.3.2 Performance Issues in Rendering

The surface textures play very important role in giving users the realistic haptic experience of virtual objects. In addition to the computational costs required at this high resolution of details, the *realism* provided by surface textures becomes an addressable issue. For this reason, along with the work found on efficient rendering of surface textures, attempts have also been made to validate the realism of haptic experiences of surface textures from different aspects. Since almost all of the commercial haptic devices available today are point based devices, the perception of surface textures and resulting roughness through single point based probes poses a fundamental question. Lederman and Klatzky conducted extensive research on roughness perception of 'real' surface textures (made of metal plates) through probes [Lederman 1999, Klatzky 2003]. Their experiments are based on real texture stimuli, metal plates with equally spaced grooves cut or etched lengthways into them. The user can explore these textures through a pen-like probe (Figure 3-12). The experiments study the

effect of several factors e.g. exploration speed, mode of touch, probe shape and surface geometries on the perceived roughness. These experiments provide guidelines for roughness perception through probes which can be considered in virtual environments where exploration of virtual textures is done through pen-line probes. In contrast with these experiments with real textures and probe, work is also done in roughness perception of virtual textures via probe-based haptic devices to study the effects of different factors on roughness perception [McGee 2001, Penn 2001].

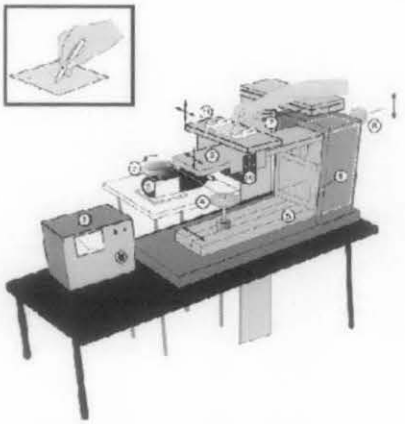

Figure 3-12: The apparatus used by Lederman to study perception of real textures with probe-like exploration tools [Lederman 1999]

Choi *et al* [Choi 2003, 2004] presents extensive research work to determine instabilities in perception of haptic textures through point based devices. Several types of instabilities arising from haptic rendering of simple textures have been identified by their experiments and corresponding causes are investigated. The work reports three major types of instabilities namely buzzing, aliveness and ridge instability. These instabilities are caused by instable control of haptic devices and inaccurate modeling of virtual environment dynamics. The underlying reasons have been studied point out the discrepancies in current rendering algorithms.

A further piece of work investigates the limits a haptic device will pose on rendering of textures due to its inherent mechanical properties e.g. device resolution and structural dynamics [Campion 2005]. Instead of discrepancies in psychological perception of textures, the work concentrates on limitations in texture rendering due to mechanics of devices.

Certain limitations have been identified on the design of gratings in a texture beyond which the textures cannot be rendered accurately. These limitations are shown to arise from characteristics of device, noise injected due to sampling and constraints imposed by feedback dynamics loop.

3.3.3 Applications

The addition of surface textures greatly increases the realism of user interaction with a haptic device e.g. adding textures to wood, fabric like surfaces. However there are applications where haptic textures are used stand-alone. The most popular of these are scientific visualization for blind users. In any visualization application, the haptic texture is generated using some mathematical model with input parameters. The input parameters are turned by data values to modulate the textures. The visually impaired user can perceive the data by feeling the haptic textures.

Data Visualization: Wall and Brewster *et al* [Wall 2003] presents the idea of data visualization via scaling of haptic display properties rather than visualizing through haptic display of traditional visual counterpart like bar charts, graphs, etc. It is argued that the traditional visualization methods require blind users to keep track of 'temporally' varying clues e.g. how high the bar was, placing short-term memory demands. For this reason the shape and size of charts, graphs cannot be perceived as good via haptic device as can be done visually. Therefore, scaling other richer haptic properties like stiffness and textures would be more effective alternative. Their experiments include the user perception of haptic properties of friction, stiffness and spatially periodic texture. The results show that users are well able to discriminate among different levels of haptic properties and their magnitudes. However, the friction was concluded to be the better perceived property. The work provides basis for future work in data visualization through tuning of haptic properties of textures.

Accordingly, the work by Asysal concentrates on synthesizing pseudo textures for data visualization [Aysal 2006]. The textures are similar to the procedural approach where a texture is derived from some mathematical model. In this work several stochastic, harmonic

and half-toning models are presented which can be tuned to the input data values to generate the scaled haptic textures. The changes in input parameters required to produce perceivable texture changes are determined through psychophysical experiments. It is shown that the stochastic and harmonic models make good choice for data discrimination as well as to present boundary/edge based data to the blind users. Figure 3-13 shows synthesized textures from different models used for data visualization.

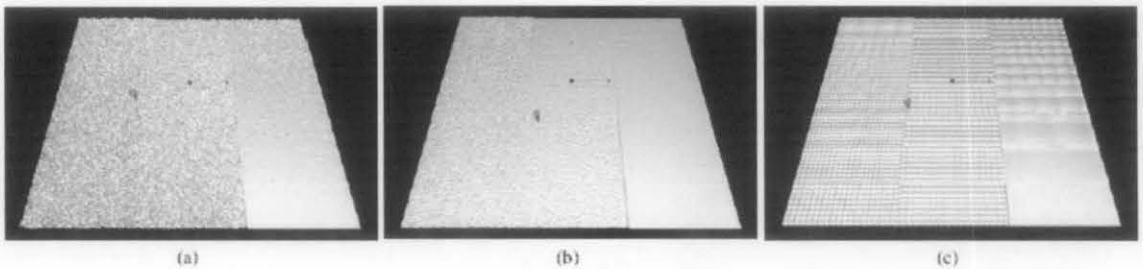

Figure 3-13: Different models used for pseudo-texture synthesis – (a) stochastic (b) correlated (harmonic) [Aysal 2006]

Apart from using textures for data visualization, systems have also been developed which exploit other display properties of haptic environment to train the visually impaired. For example, Tzovaras presents a prototype system for the training of blind people which mostly concentrates on complete 3D object manipulation rather than concentrating on one haptic property only [Tzovaras 2004]. Several applications can be built to train users for different purposes. The system composes of a software consisting of interactive application (interacting with haptics device) and 3D modeling application to create the 3D virtual environments. CyberGrasp [immersion] is used as haptic interface to allow users more degrees of freedom by using all fingers of hands. The system allows many types of applications and has been tested for object recognition/manipulation and cane simulation to train users with virtual cane.

Materials: Although rendering of haptic textures, different models for pseudo haptic textures and their applications have been studied, not much work is done to incorporate the materials found in real world completely to the haptic environment. Any such attempt would require the scanning of surface texture profiles of real objects, capturing of their mechanical properties i.e. stiffness and friction and their integration in virtual environment. This will not

only allow a user to feel a textured surface but also to differentiate between materials like cloth, wool, skin, wood, glass, clay, etc. A significant attempt to scan the physical interaction of real objects, recording their response and its modeling in virtual environment has been presented by Pai *et al* [Pai 2001]. A highly robotic measurement facility has been used to record several aspects of physical interaction. The features of an object modeled are geometrical shape, stiffness, surface textures and contact sounds. The models of measured features can be incorporated in virtual environments for more realistic interactions. Figure 3-14 illustrates apparatus and scanning of the objects.

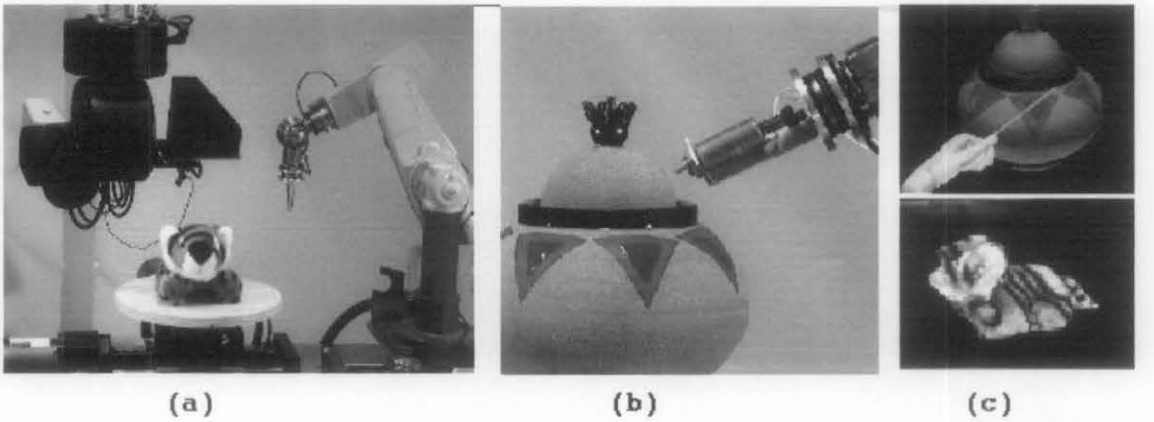

Figure 3-14: The physical interaction scanning setup – (a) shape/texture and stiffness measurement (b) sound measurement (b) scanned and modeled objects in virtual environment [Pai 2001]

A different type of work attempts to develop a *virtual handling* experience of fabric [Govindaraj 2003]. Surface profiles (textures) and friction are two properties incorporated to give tactile feedback of fabric to user. A system of highly sensitive touch response transducers captures the surface profile and friction of the fabric. A new tactile device, PhilU (Figure 3-2), instead of traditional point-based haptic devices, is developed for thorough touching experience of fabrics.

Finally, the human soft tissues have also been considered to be incorporated in haptic applications. However, they pose a significant challenge for the reason that their elasticity and surface properties vary greatly. The presentation of surface properties of soft tissues is believed to improve the current experience of users in medical haptic applications to great

extent. For this reason, the measurement of in vivo tissue properties, their mathematical modeling and simulation for virtual environments has become a major research topic in recent years. However, it will take time to reach a perfect representation of human tissues in virtual environments. Acosta *et al* [Acosta 2001] presents an alternative approach to incorporate haptic properties of soft tissues in virtual environments. Instead of following the typical modeling of physical parameters of human tissues, they use a heuristic approach in which the user can define and store the haptic properties of different portions of human body heuristically. The users should be experts from anatomy and surgery who are well familiar with the haptic sensation of different tissues in the human body. The Virtual Body Structures (VBS) system allows to select any of the human body portions from database of human body and to view it in 3D. The user can then tweak the haptic parameters of selected portion of body while sensing the resulting change with haptic device. This feedback eventually results in proper tuning of biomechanical properties of tissue to give the haptic sensation suited best to user's knowledge of real tissues. Initially the system tunes the parameters of stiffness, damping and friction.

Shirado *et al* [Shirado 2006] also presents an indirect approach to consider skin for haptic applications. They have developed the artificial synthetic skin structure (Figure 3-15) which possesses human skin like surface textures and elastic properties and can be used for haptic evaluation systems or to produce robot skin. The structure consists of multi layers of rubber sheet having different elasticity and hexagonal surface patterns. A cognitive model of skin based on different physical parameters is also built to correlate the tactile perception of real skin with the parameters involved in synthetic skin. However, the integration of real skin, with all the haptic properties of surface textures and elasticity, in virtual environments still remains unaddressed.

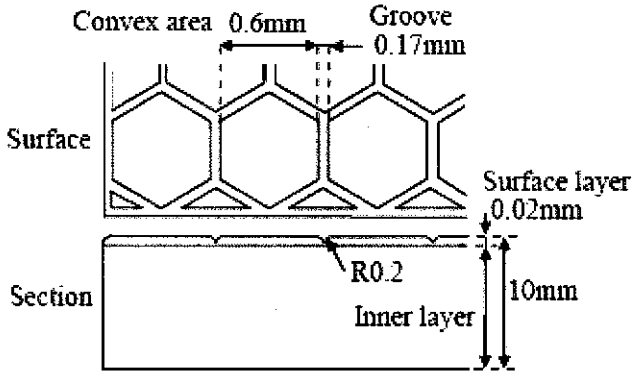

Figure 3-15: Structure of synthetic human-like skin proposed in [Shirado 2006]

3.4 Summary

In this chapter an overview of haptics technology including haptic devices and rendering has been presented while focusing on haptic rendering of textures. From recent rendering techniques of surface textures, it can observed that most of rendering algorithms require 3D surface texture information to be presented as 2D grayscale images. These images are used for perturbing the haptic forces the same way as is done for bump mapping in computer graphics.

In regard with complete virtual representation of soft tissues found in body, the research work is only in its initial stages. For this reason a heuristic approach was proposed by Acosta *et al* [Acosta 2001] for haptic representation. Similarly virtual presentation of human skin in a haptic environment is challenging requiring several physical characteristics to be modeled including surface features, stiffness and friction for a realistic touch experience. As was mentioned section 2.5, 3D surface features play an important role in determining the condition of skin. This work concentrates on the modeling and representation of 3D textures of skin. In Chapter 5, the 3D features of skin will be detailed which are modeled as 2D texture images and can be used as bump maps for haptic texture rendering techniques. In Chapter 4 the theoretical background of modeling techniques used for this purpose will be detailed.

Chapter 4

Image Textures and Markov-Gibbs Random Field Modeling

This chapter reviews the theoretical background of the modeling technique used in this work for grayscale textures obtained representing 3D skin textures. Any probabilistic image modeling targets the generation/simulation of random samples having visual resemblance to the training image. For this purpose, a suitable probabilistic model is selected and its parameters are estimated from the given training image to identify the model completely. The random samples of this identified model correspond to the synthesized images with visual similarity. Several sampling algorithms are available for synthesizing images from the identified model. Therefore, parameter estimation and image synthesis are the integral parts of probabilistic image modeling techniques.

For this work, Markov random field modeling is applied as a probabilistic modeling technique. Chapter 5 will describe in detail the modeling scenario in context with this work whereas this chapter presents detailed description of the modeling technique.

4.1 Markov Random Fields

Markov random field (MRF) is a popular probabilistic modeling technique. It is a non-causal extension of Markov chain (see Appendix B) in a two dimensional lattice. Every site of the lattice is associated with an event and random variable (see Appendix B). As with Markov chain, these sites in 2D lattice are dependent on their neighbouring sites only. Markov

random field modeling deals with the probabilities associated with these random variables. The same probability distribution function, also called image model, is associated with all sites and random variables in the image lattice. Modeling involves complete identification of this distribution function for the given image and producing similar images from the identified function.

4.1.1 Image Probabilities

A random field is a set of random variables defined on a two dimensional lattice. Consider a lattice of MxN dimensions $\mathbf{R} = \{i = (x, y) : 0 \le x < M, 0 \le y < N\}$ where every site (or a pixel for a digital image) i is associated with a random variable s_i. The result is a family of 2D random variables called random field denoted by $\mathbf{S} = \{s_i, i \in \mathbf{R}\}$. The random variable at every site takes the signal value from signal space $\mathbf{Q}$. A digital image $\mathbf{G} = \{g_i, i \in \mathbf{R}\}$ can be considered as a realization (sample) of the random field $\mathbf{S}$. For example, Figure 4-1 shows 2D lattice and associated random field with a realization sample. A set of all possible realizations of the random field $\mathbf{S}$ for lattice $\mathbf{R}$ is denoted by $\mathbf{U}$.

The probability of the random variable s_i at site i having signal value g_i is denoted as $P(s_i = g_i)$. The random variables in the random field are considered statistically dependent and their joint probability distribution is given as $P(\mathbf{S} = \mathbf{G})$ representing the probability of observing the digital image $\mathbf{G}$ out of realization space $\mathbf{U}$ for the random field $\mathbf{S}$. The conditional probability of observing signal value $q \in \mathbf{Q}$ at site i given signal value $q' \in \mathbf{Q}$ at site i' is denoted by $P(s_i = q \mid s_{i'} = q')$ or shortly as $P(q \mid q')$.

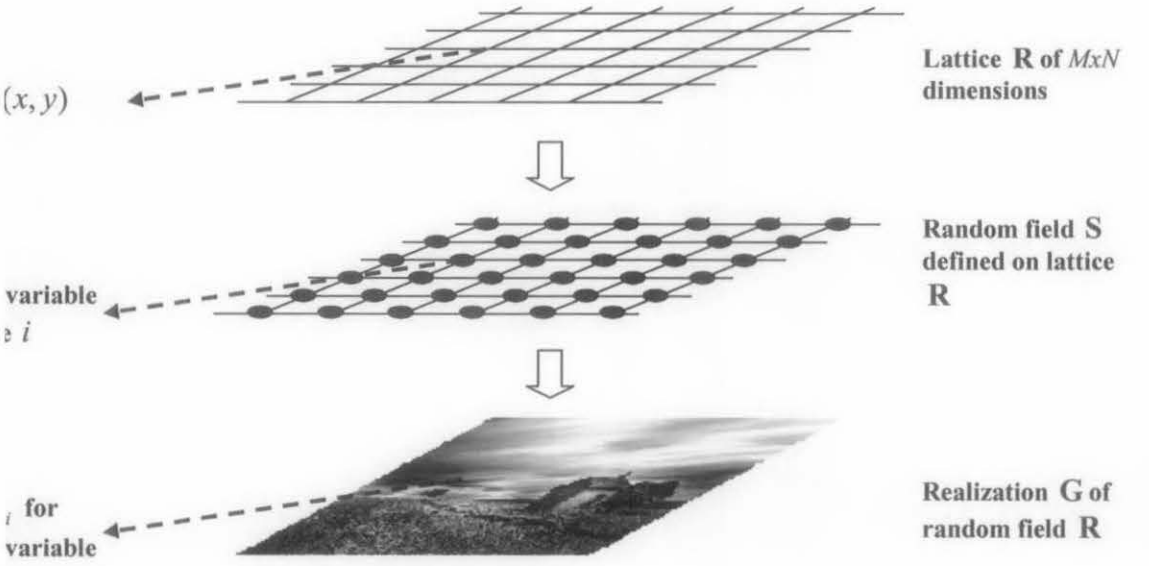

Figure 4-1: A random field defined for a digital image

4.1.2 Neighbourhood system and cliques

Consider the random field $\mathbf{S}$ associated with lattice $\mathbf{R}$ and a given realization $\mathbf{G}$ of it. Let $\mathbf{S}^i$ denote the random field *excluding* the random variable s_i at site i and $\mathbf{G}^i$ as the signal values in the realization *excluding* the signal value g_i at site i. A pixel $i' \in \mathbf{R}$ is called the neighbour of a pixel $i \in \mathbf{R}$ if the conditional probability $P(s_i \mid \mathbf{S}^i)$ of signal value s_i depends on the signal value $s_{i'}$. A collection of all the neighbours of the site i in the lattice $\mathbf{R}$ forms the 'neighborhood' of the pixel i denoted by $\mathbf{N}_i$. A set of all the neighbourhoods in the lattice $\mathbf{N}_S = \{\mathbf{N}_i : i \in \mathbf{R}\}$ is called the neighbourhood system for random field $\mathbf{S}$ [Gimel 1999]. For a neighbourhood system the following properties hold.

1) A site is not neighbouring to itself $i \notin \mathbf{N}_i$

2) The neighbouring relationship should be mutual, $i \in \mathbf{N}_{i'} \Leftrightarrow i' \in \mathbf{N}_i$, i.e. if site i' is present in neighbourhood of site i then site i must be present in neighbourhood of site i'

Given a neighbourhood system $\mathbf{N}_S$ a *clique* $\mathbf{c} \subset \mathbf{R}$ is a single site or a subset of sites in which every pair of distinct sites is the neighbour of each other under the neighbourhood system. The number of sites in a clique defines the order of neighbourhood system and the statistical dependence between neighbours of a clique is called the 'pixel interaction'. Figure 4-2 shows two examples of simple 2nd order pair-site neighbourhood systems and their cliques.

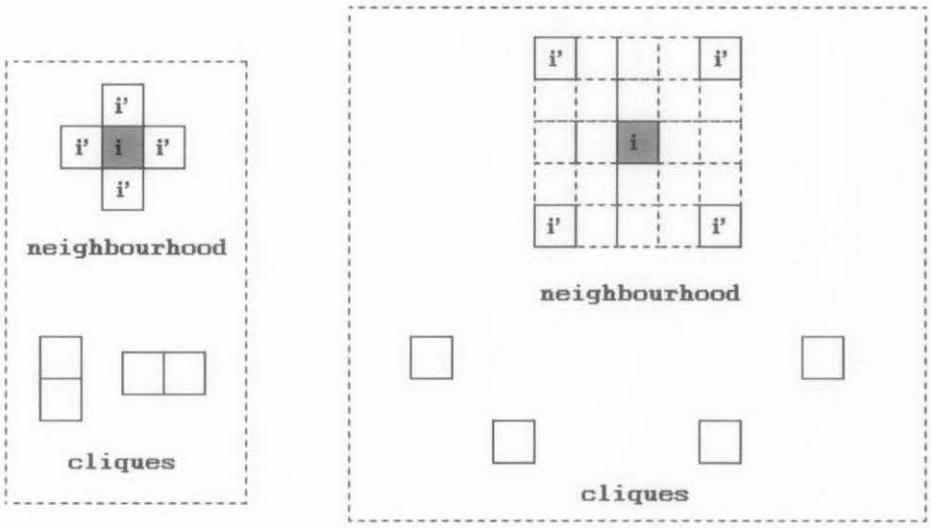

Figure 4-2: Two examples of 2nd order neighbourhood systems and their cliques, sites i and i' are neighbours of each other under given system

4.1.3 Markov Random Fields

The random field $\mathbf{S}$ is a Markov random field under the neighbourhood system $\mathbf{N}_S$ if and only if the following two conditions are satisfied.

1) For every sample $\mathbf{G}$ in the image configuration space $\mathbf{U}$, the joint probability is strictly positive i.e. $P(\mathbf{S} = \mathbf{G}) > 0$.

2) For every site in the image lattice, $P(s_i \mid \mathbf{S}^i) = P(s_i \mid s_{i'} : i' \in \mathbf{N}_i)$.

The first property is called *positivity* and is trivial for the probability distributions. The second property is called *markovianity*. It describes the local characteristics of random fields and suggests that the signal value at a site is dependent on the signal values in its neighbourhood only, that is, pixel interactions are present among neighbouring sites only.

Let the cardinality (number of elements in a set) of the neighbourhood of a site i be denoted by $|\mathbf{N}_i|$. Then the order of MRF is given by maximum cardinality present in the neighbourhood system i.e. $\max_{i \in \mathbf{R}} |\mathbf{N}_i|$. Markovianity also means that each component of a MRF is independent of some other components. Therefore, the cardinalities of neighbourhoods in $\mathbf{N}_S$ should be less than that of the lattice given by $|\mathbf{R}|$. Thus the order of MRF can be in between 1 and $|\mathbf{R}|-2$ including both values. The field of maximum order $|\mathbf{R}|-1$ will be considered as the *non-Markov* random field. Since the computational complexity of random field image modeling depends on the cardinalities of the neighbourhood system, the MRFs of small order are more popular as image models.

4.1.4 Gibbs Random Fields

A random field $\mathbf{S}$ is a Gibbs random field (GRF) on lattice $\mathbf{R}$ under neighbourhood system $\mathbf{N}_S$ if and only if its probability distribution obeys the Gibbs Probability Distribution (GPD) as follows

$$P(\mathbf{S}=\mathbf{G}) = \frac{1}{Z}\exp\{\frac{-U(\mathbf{G})}{T}\} \tag{4.1}$$

where Z is a normalizing constant called partition function and is given by

$$Z = \sum_{\mathbf{G}\in\mathbf{U}} \exp\{\frac{-U(\mathbf{G})}{T}\} \tag{4.2}$$

T is a constant called temperature and is assumed to be 1 unless stated otherwise. $U(\mathbf{G})$ is an energy function defined in terms of cliques. The partition function sums over the energy

functions for all possible realizations in the set $\mathbf{U}$. As discussed above, the sites in cliques are statistically dependent. Their pixel interaction is given as a function called clique potential denoted by $V_{\mathbf{c}}(g_i : i \in \mathbf{c})$ and depend on the signal values of sites in the clique. The energy function in Gibbs distribution is a sum of clique potentials over all the possible cliques in GRF and is given by

$$U(\mathbf{G}) = -\sum_{\mathbf{c}\in\mathbf{C}} V_{\mathbf{c}}(g_i : i \in \mathbf{c}) \tag{4.3}$$

where $\mathbf{C}$ is the set of all cliques in GRF. The clique potentials are also called Gibbs potentials. A GRF is homogeneous if clique potentials are independent of relative positions of cliques in lattice.

Gibbs probability distribution was first introduced in statistical physics to describe the equilibrium states of a large statistical system of interacting particles like atoms, molecules, etc at an overall system temperature. For image modeling, an analogy is established between the interacting particles of the physical system and the pixels of an image. The famous Hammersley-Clifford theorem proves the equivalence of Markov and Gibbs random fields [Li 1995].

4.1.5 Markov-Gibbs Equivalence

The Markov random field is defined on a lattice $\mathbf{R}$ and is characterized by its 'local' property describing the neighbourhood interactions (Markovianity) whereas Gibbs random field is characterized by its 'global' property describing the probability distribution of equilibrium states of a system of particles (Gibbs Probability Distribution - GPD). Hammersley-Clifford theorem establishes equivalence of the two systems. It states that *a random field* $\mathbf{S}$ *is a MRF on lattice* $\mathbf{R}$ *with respect to neighbourhood system* $\mathbf{N}_{\mathbf{S}}$ *if and only if* $\mathbf{S}$ *is a GRF on lattice* $\mathbf{R}$ *with respect to neighbourhood system* $\mathbf{N}_{\mathbf{S}}$ (See [Li 1995] for proof). The theorem implies that, under the positivity condition, the joint probability

distribution $P(\mathbf{S})$ of a MRF over the parent population can be represented as the GPD in equation (4.1) where the potential functions of random variables are supported by cliques in neighbourhood system of MRF describing the pixel interactions.

The theorem has the practical value that it provides a simple way of specifying the joint probability function for a MRF through Gibbs probability distribution function. Thus, the local interaction function in MRF (the conditional probability $P(s_i = q \mid s_i' = q')$) can be specified in terms of global function, the joint probability function and clique potentials in GPD in equation (4.1). In this case, the conditional probability of a site in MRF $P(g_i \mid \mathbf{N}_i)$ can be written in the form of GPD where the conditional probability depends on the cliques containing the site itself only (denoted by $\mathbf{c}_i$) and rest of the cliques have no effect [Li 1995]. For a simple model, cliques having only two sites i, i' are considered.

$$P(g_i \mid \mathbf{N}_i) = \frac{1}{Z_i} \exp\{\sum_{\mathbf{c}_i \in \mathbf{C}} V_{\mathbf{c}}(g_i, g_{i'} : i, i' \in \mathbf{c}_i, i \neq i')\} \tag{4.4}$$

$$Z_i = \sum_{g_i \in Q} \exp\{\sum_{\mathbf{c}_i \in \mathbf{C}} V_{\mathbf{c}}(g_i, g_{i'} : i, i' \in \mathbf{c}_i, i \neq i')\} \tag{4.5}$$

4.2 Texture Modeling

As mentioned previously, the goal of a probabilistic image (texture) modeling is to generate/simulate random samples (images) from a given joint probability distribution $P(\mathbf{S})$. The joint probability distribution $P(\mathbf{S})$ is called the 'image model' which determines how likely a texture image can occur. By modeling we mean to select the joint probability distribution such that it tends to favor the desired class of textures. For MRF, the modeling process addresses the problem of selecting the neighbourhood system and corresponding conditional probabilities for the lattice. Under Markov-Gibbs equivalence this process means to select the forms and parameters (clique potentials) of the joint probability distribution

GPD for desired system behavior. The resultant GPD is then called the image model. Defining the functional forms of clique potentials and estimating its parameters to completely define GPD is what is done under MRF modeling [Gimel 1999, Li 1995].

The Markov random field modeling has been used for texture synthesis [Chee and Derin 1988, Derin and Elliot 1987], classification and segmentation [Lakshman 1989, Chee and Derin 1987]. For texture synthesis applications, the parameters of MRF are estimated from training texture sample and similar samples are generated by sampling the corresponding GPD. For texture classification and segmentation applications, the MRF parameters correspond to the texture features. Based on MRF parameters estimated from image (texture features), textures are classified by some decision rule/classifier or segmented by performing labeling. Several MRF models have been used for the above applications, the most popular being auto-models with lowest order constraints on two sites neighbourhood. They are simple and have computationally less cost.

4.2.1 MRF Models

The auto-models are the simplest MRF models where only two sites are considered in a neighbourhood. The corresponding GPD contains pair-site clique potentials and the energy function takes the following general form [Li 1995]

$$U(\mathbf{G}) = \sum_{i \in \mathbf{R}} g_i . fn_i(g_i) + \sum_{(i,i') \in \mathbf{C}} g_i g_{i'} . \beta_{i,i'} \tag{4.6}$$

The first term contains the arbitrary function depending on signal value g_i at site i and second term reflects the pair-site interactions between site and its neighbours i, i' through constants $\beta_{i,i'}$ depending on signal values at the neighbouring sites. $\mathbf{C}$ is the set of all pair-site cliques in lattice $\mathbf{R}$. Equation (4.6) is a general expression for auto-models. These models are further classified depending on the form the function $fn_i(g_i)$ takes and the values of constants $\beta_{i,i'}$.

An auto-model is reduced to auto-logistic/Ising model when the signal values take the discrete values from the set $g = \{0,1\}$ and the function $fn_i(g_i)$ takes the form of the constant α_i . For Ising model the neighbourhood system contains only nearest pair-site neighbours (4 nearest neighbours on a 2D lattice). The energy function for an Ising model is given by

$$U(\mathbf{G}) = \sum_{i \in \mathbf{R}} g_i . \alpha_i + \sum_{(i,i') \in \mathbf{C}} g_i g_{i'} . \beta_{i,i'}$$

whereas the conditional probability takes the following form

$$P(g_i \mid \mathbf{N}_i) = \frac{1}{Z_i} \exp\{\sum_{\mathbf{c}_i \in \mathbf{C}} V_{\mathbf{c}}(g_i, g_{i'} : i, i' \in \mathbf{c}_i, i \neq i')\}$$

$$= \frac{\exp\{g_i . \alpha_i + \sum_{(i,i') \in \mathbf{C}} g_i g_{i'} . \beta_{i,i'}\}}{\sum_{g_i \in \{0,1\}} \exp\{g_i . \alpha_i + \sum_{(i,i') \in \mathbf{C}} g_i g_{i'} . \beta_{i,i'}\}}$$

$$= \frac{\exp\{g_i . \alpha_i + \sum_{(i,i') \in \mathbf{C}} g_i g_{i'} . \beta_{i,i'}\}}{1 + \exp\{\alpha_i + \sum_{(i,i') \in \mathbf{C}} g_{i'} . \beta_{i,i'}\}} \tag{4.7}$$

Another popular auto-model is auto-binomial model. For auto-binomial model the conditional probability distribution takes the form of binomial distribution. The signal value g_i at lattice sites can take values from the discrete set of signal values $\mathbf{Q} = \{0,1,2,...,Q-1\}$. The probability of taking value has the conditional probability of Q trials having probability of success q . The conditional probability is given as

$$P(g_i \mid \mathbf{N}_i) = \binom{Q-1}{g_i} q^{g_i} (1-q)^{Q-1-g_i} \tag{4.8}$$

In this case the signal values at neighbouring sites play their role in determining the probability of success q which is given by

$$q = \frac{\exp\{g_i.\alpha_i + \sum_{(i,i')\in C} g_i g_{i'}.\beta_{i,i'}\}}{1+\exp\{\alpha_i + \sum_{(i,i')\in C} g_{i'}.\beta_{i,i'}\}} \tag{4.9}$$

For this model the parameters to be determined are the sets $\{\alpha_i\}$, $\{\beta_{i,i'}\}$.

The most popular auto-modal until now has been the auto-normal or Gaussian model based on two-site neighbourhood only. For auto-normal model the conditional probability distribution takes the form of normal or Gaussian distribution instead of binomial disbtribution. The signal value g_i at lattice sites can take values from the discrete set of signal values $\mathbf{Q} = \{0,1,2,...,Q-1\}$. The conditional probability of signal value has the Gaussian distribution whose form depends on the signal values at neighbouring sites. The conditional probability is given as

$$P(g_i \mid \mathbf{N}_i) = \frac{1}{\sqrt{2\pi\sigma^2}} \exp(-\frac{1}{2\sigma^2}(g_i - \mu_i - \sum_{i'\in \mathbf{N}_i} \beta_{i,i'}(g_{i'} - \mu_{i'}))^2) \tag{4.10}$$

The conditional mean for this Gaussian distribution is given as $\mu(g_i \mid \mathbf{N}_i) = \mu_i - \sum_{i'\in \mathbf{N}_i} \beta_{i,i'}(g_{i'} - \mu_{i'})$ and the conditional variance as σ. Here the set $\{\beta_{i,i'}\}$ makes the model parameters for a specific class of textures.

4.2.2 Model Identification

As discussed earlier, modeling incorporates selection of a suitable underlying mathematical model as well as finding its parameters. In section 4.2.1 we reviewed some of popular MRF models for different image texture applications. Once a suitable MRF model has been selected including its Gibbs distribution and neighbourhood system, the next step is to find its parameters. A model is completely identified only when its form is selected and all of its parameters have been estimated.

4.2.2.1 Bayes Estimation

MRF modeling is characterized as optimization problem like other problems in computer vision. The reason is the non existence of exact or perfect solutions [Li 1995]. For example, in texture segmentation, it would be impossible to find the perfect segmented image of the two texture regions and only the closest solutions can be targeted. Similarly in texture modeling, only an approximated version of the texture in the actual image can be synthesized. Therefore, the search for optimal solutions through some optimization algorithm becomes the natural choice in these situations. In texture modeling scenario, the search for the parameters of the selected probability distribution (model GPD) which can represent the training image is posed as an optimization problem. The set of parameters maximizing the model GPD $P(\mathbf{S})$, or in other words, minimizing the corresponding energy $U(\mathbf{S})$ for the given image is considered to be the optimal solution and is estimated.

Let θ denote the set of model parameters to be identified and $\mathbf{s}$ be the given image. Let θ^* denote the optimal estimate of parameter set. As mentioned above, the optimization will yield a solution *closest* to the unique exact solution. Bayesian estimation from statistical theory provides the basis of many optimization algorithms in computer vision to find the optimal estimates. In Bayesian estimation a risk function 'Bayesian risk' is assigned to the estimated quantity and is defined as

$$R(\theta^*) = \int C(\theta^*, \theta) P(\theta \mid \mathbf{s}) d\theta \tag{4.11}$$

where $C(\theta^*, \theta)$ is the cost function and determines the cost of estimate θ when the truth is θ^*. Thus the risk function $R(\theta^*)$ in equation (4.11) determines the overall cost associated with optimal solution θ^* when the posterior distribution (See Appendix B) of parameters is given as $P(\theta \mid \mathbf{s})$. In Bayesian estimation, the optimal solution is reached by minimizing the risk. In other words, that value of θ^* is considered to be the optimal solution which minimizes the risk $R(\theta^*)$ given the cost function and posterior probability of parameter set

θ. The solution of equation (4.11) (Refer to [Li 1995] for detailed derivation) for different cost functions results as

$$R(\theta^*) = 1 - \nu P(\theta \mid \mathbf{s}) \tag{4.12}$$

where ν is a constant. From above equation it is evident that minimizing the risk function in Bayesian estimation results in maximizing the posterior probability. Hence, the optimal estimate of parameters can be found as

$$\theta^* = \arg\max_{\theta} P(\theta \mid \mathbf{s}) \tag{4.13}$$

According to Bayes rule (See Appendix B), the posterior distribution can be computed by following

$$P(\theta \mid \mathbf{s}) = \frac{P(\mathbf{s} \mid \theta)P(\theta)}{P(\mathbf{s})} \tag{4.14}$$

where $P(\theta)$ is the prior probability of parameters, $P(\mathbf{s} \mid \theta)$ is the conditional probability of observing data (signal values) given the parameters set, also called 'likelihood function' (see Appendix B) of θ for $\mathbf{s}$ fixed, and $P(\mathbf{s})$ is the probability function for observing data. Considering that $P(\mathbf{s})$ is constant when $\mathbf{s}$ is given as training image, the equation (4.14) reduces to

$$P(\theta \mid \mathbf{s}) \propto P(\mathbf{s} \mid \theta)P(\theta) = P(\mathbf{s}, \theta) \tag{4.15}$$

$$\theta^* = \arg\max_{\theta} \{P(\mathbf{s} \mid \theta)P(\theta)\} \tag{4.16}$$

Equation (4.15) and (4.16) imply that the optimal solution for the parameter set can be obtained by maximizing the joint probability $P(\mathbf{s}, \theta)$. Bayes estimation of the optimal

olution leads to the 'maximum likelihood estimation' which has been a popular optimization echnique for parameter estimation in MRF modeling.

.2.2.2 Maximum Likelihood Estimation (MLE)

he goal of parameter estimation is to find the values of underlying model parameters given training image. It was discussed in last section that according to Bayesian estimation, those arameter values are optimal solution which maximize the joint robability $P(\mathbf{s},\theta) = P(\mathbf{s} \mid \theta)P(\theta)$. However, in most cases the distribution of parameter set $P(\theta)$ is considered to be flat. Hence, the probability $P(\theta)$ can be ignored and Bayes stimation reduces to what is called maximum likelihood estimation.

$$\theta^* = \arg\max_{\theta} P(\mathbf{s} \mid \theta) \tag{4.17}$$

The ML (Maximum Likelihood) estimate θ^* maximizes the likelihood of θ i.e. it searches or those values of parameter set θ which maximize the GPD $P(\mathbf{S})$ for the given image **s**.

The concept of maximum likelihood can be understood by following example. Figure 4-3 shows the probability distribution of data with values of two parameters fixed. Figure 4-4 shows the likelihood of one parameter w with the observed data and the other parameter fixed. The graph shows the value of parameter w which would maximize the probability of observing data y=7 with parameter value n=10 fixed.

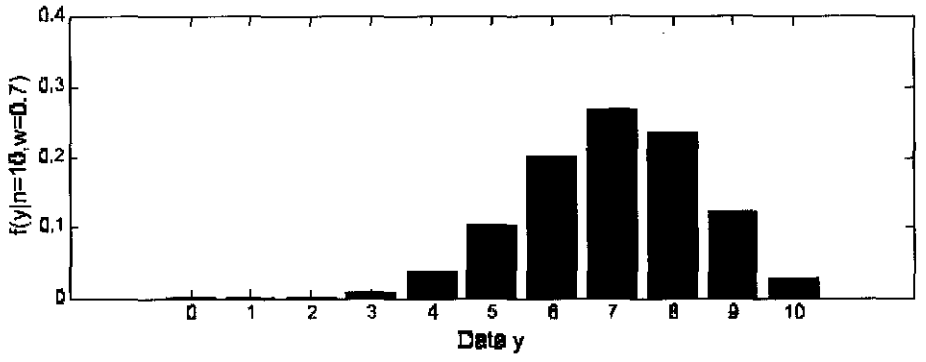

Figure 4-3: The probability distribution of data y with two model parameters n,w given

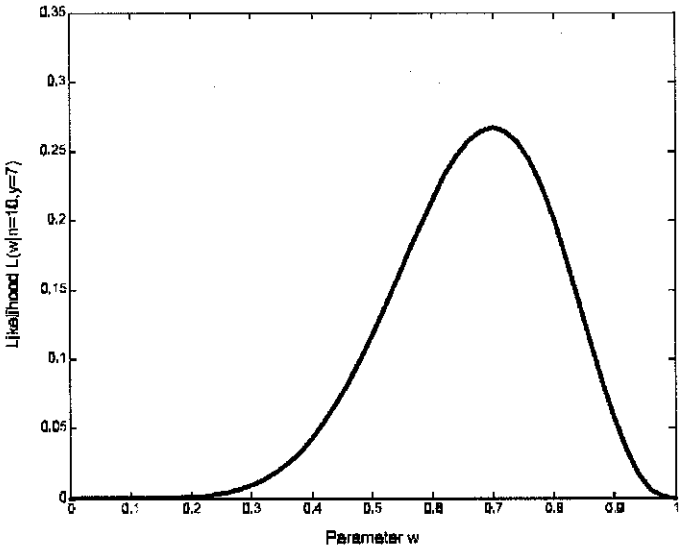

Figure 4-4: The likelihood function of parameter w for observed data y=7 and parameter value n=10

If the function $P(\mathbf{s} \mid \theta)$ is differentiable the search for ML estimate θ^* reduces to solving the following equation

$$\frac{\partial P(\mathbf{s} \mid \theta)}{\partial \theta} = 0 \tag{4.18}$$

Several approximation techniques e.g. Pseudo-likelihood, Coding method, Mean field approximations (See Li [1995]) and MCMC algorithms (Section 4.3.3.1) have been utilized to solve the above for finding ML estimates.

4.2.3 Texture Synthesis

Once the Markov/Gibbs model of a training image has been identified i.e. its form and parameters completely estimated from the training image, the texture images similar to the training one can be synthesized (simulated) from the identified model. The process of synthesizing images from an identified model is called *sampling*. In other words, the synthesized images correspond to the samples of underlying GPD $P(\mathbf{S})$. Sampling of GPD can be understood best on the basis of its two major components a) Markov Chain Monte

Carlo (MCMC) algorithms for sampling probability distributions and b) Simulated Annealing algorithm for global optimization. The process of sampling with optimization through simulated annealing is called stochastic relaxation which is defined as *a process of generating Markov chain of samples that has the given distribution* $P(\mathbf{S})$ *in the equilibrium state..*

4.2.3.1 Markov Chain Monte Carlo (MCMC) algorithms

These algorithms start with a random image and generate a sequence of samples which form a Markov chain. As the definition of Markov chain implies, every sample g^t in the sequence depends only on the previous sample g^{t-1}. A Monte Carlo procedure randomly selects the next sample in the sequence from sample space $\mathbf{U}$ with the conditional probability that depends only on the current sample indicating the Markov property of the chain which is given mathematically as

$$P(g^t \mid g^x \text{ where } x \neq t) = P(g^t \mid g^{t-1}) \tag{4.19}$$

The conditional probability $P(g^t \mid g^{t-1})$ defines the transition probability of the Markov chain. The MCMC algorithm updates the Markov chain based on this transition probability until, after sufficient iterations, the chain reaches the equilibrium state when the joint probability distribution of the sample $P(g^t)$ approaches the stationary desired model GPD $P(\mathbf{S})$. In other words, the MCMC algorithms generate a sequence of random images whose joint probability distribution approaches the given GPD gradually until, in equilibrium state, the generated image has high visual resemblance to the training image. Two sampling algorithms Metropolis Sampler and Gibbs Sampler are well-known MCMC algorithms to generate a sequence of images.

METROPOLIS SAMPLING ALGORITHM: -

(1) initialize g to a random image

(2) repeat
(3) for all $i \in \mathbf{R}$ do
(4) choose g_i at random from $\mathbf{Q}$ to generate g'
(5) let $p = \min(1, P(g')/P(g))$
(6) where P is the given Gibbs distribution
(7) replace g by g' with probability p
(8) until equilibrium is attained

Figure 4-5: Metropolis algorithm for sampling probability distribution P(g)

GIBBS SAMPLING ALGORITHM: -

(1) initialize g to a random image

(2) repeat
(3) for all $i \in \mathbf{R}$ do
(4) calculate $p_q = P(g_i = q \mid \mathbf{N}_i)$ for all $q \in \mathbf{Q}$
(5) where P is the given Gibbs distribution
(7) replace g_i by the signal value q with probability p_q
(8) until equilibrium is attained

Figure 4-6: Gibbs algorithm for sampling probability distribution P(g)

In both algorithms, every iteration consists of visiting all sites in the lattice and updating their values. After sufficient number of iterations, the sequence of images converges to the equilibrium with visual similarity to training texture. However, the samplers differ in updating scheme of the individual site values. The Metropolis algorithm follows a *random walk,* in which the next state is selected randomly whereas in Gibbs sampler the next state is selected after calculating the local conditional probability p_q for every signal value q. Gibbs sampler computes $|\mathbf{Q}|$ exponentials at each step and is computationally costly in comparison with Metropolis sampler which calculates one exponential only but Gibbs sampler converges to equilibrium faster in less number of iterations.

4.2.3.2 Simulated Annealing

Simulated annealing is a simulated version of physical annealing process in which substances are melted and slowly cooled down to reach the lowest energy state. Similarly, it is used in optimization problems to reach the lowest energy state or optimal solutions. In case of texture synthesis via MCMC algorithms, the goal is to reach the equilibrium state with maximized probability (GPD) $P(\mathbf{S})$ which minimizes the energy $U(\mathbf{S})$. Figure 4-7 shows the Metropolis algorithm including simulated annealing.

METROPOLIS SAMPLING ALGORITHM WITH SIMULATED ANNEALING: -

(1) initialize g to a random image and initialize T

(2) repeat
(3) for all $i \in \mathbf{R}$ do
choose g_i at random from $\mathbf{Q}$ to generate g'
(4) $\Delta E \leftarrow E(g') - E(g)$
(5) let $p = \min(1, \exp(-\Delta E / T))$
(6) replace g by g' with probability p
(7) reduce T
(8) until $T \rightarrow 0$

Figure 4-7: Metropolis algorithm for sampling probability distribution P(g) with simulated annealing

Simulated annealing algorithm makes sure that the MCMC sampling algorithm does not get stuck in local minima and reaches the global minimum. The samplers in Figure 4-6 and 4-7 try to reach the equilibrium by random search of the sample space for GPD $P(\mathbf{S})$. Simulated annealing controls this search with a temperature parameter T. The step (5) in algorithm demonstrates that at higher temperatures, large increase in system energy may be accepted whereas, with the gradual decrease of T, small increases are accepted only, until near freezing T, no increase in energy are accepted at all. The procedure is similar to the physical cooling process. Therefore, in initial iterations, the sampler does not get stuck in local minima following the greedy approach. The accepting of large increases in energy allows the

sampler to deviate from greedy approach and searching the whole sample space which enables it to reach the global minimum.

The decreasing scheme for temperate named as cooling schedule is important in determining the convergence of sampling algorithm towards global minimum. Slow cooling schedules ensure the global minimum but are practically too slow to be of use. For this reason heuristic faster cooling schedules are applied for annealing. For example, following are two cooling schedules for temperature T at iteration t.

$$T(t) = \frac{c}{\ln(1+t)} \tag{4.20}$$

$$T(t) = \kappa T(t-1) \tag{4.21}$$

where c is set around 3 or 4 and typical values for κ are around 0.8, 0.99.

Figure 4-8 and 4-9 below show examples of texture synthesis via Metropolis algorithms using cooling schedule in equation (4.21). The different textures are synthesized using different values of parameters for the 2nd order and 3rd order neighbourhoods shown. For textures in Figure 4-8 multi-level logistic model is used whereas the textures in figure 4-9 are generated using auto-normal model.

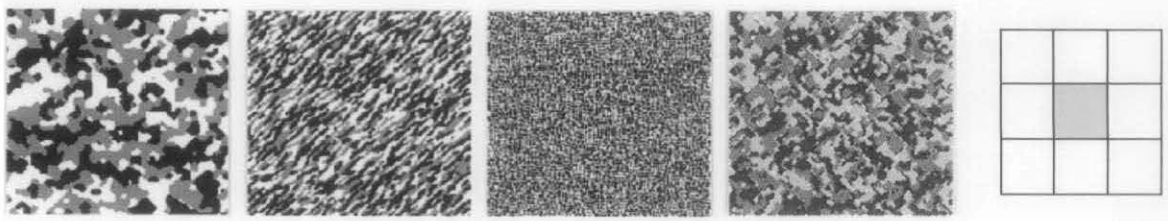

Figure 4-8: Texture samples synthesized using 2nd order neighbourhood and multilevel logistic model

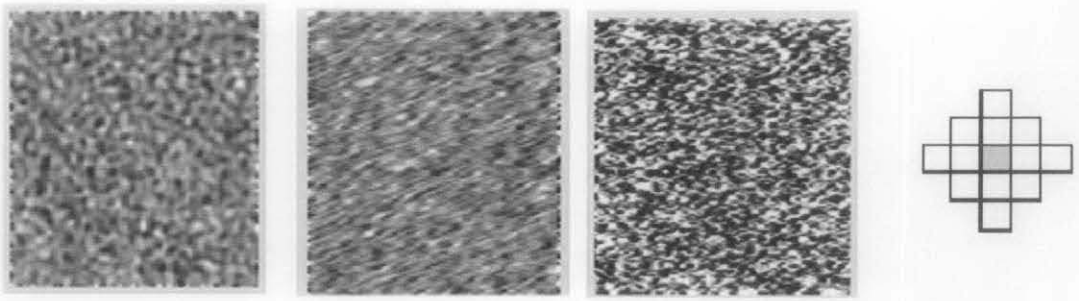

Figure 4-9: Texture samples synthesized using 3rd order neighbourhood and auto-normal model

4.3 Markov-Gibbs Random Field (MGRF) Modeling

For this work the *general* Markov-Gibbs random field (MGRF) model with 'pairwise pixel interactions' has been used to model skin surface textures [Gimel 1999, 2005]. This section details the steps involved in MGRF modeling. The mathematical description of model structure, based on pairwise pixel interactions and its parameters, identification of significant pixel interactions from training image, estimation of parameters through MLE and then image synthesis through MCMC algorithm are the main steps in modeling and have been covered.

The generic MGRF model is dependent on pairwise pixel interactions present in the texture image. As discussed in section 4.1.3 Markov models depend on pixel interaction among neighbourhood pixels in a training image under a given neighbourhood system. For this reason the usual practice for different models of MRF is to assume a neighbourhood system of a specific order (as shown in Figures 4-8 and 4-9) beforehand and to estimate the model parameters from training image accordingly. Gimel *et al* [Gimel 1999] argues that in general the auto-models of MRF, borrowed from physical systems, may not describe the pixel interactions in a texture image adequately. The assumed pixel interactions in pre-defined neighbourhood system do not necessarily represent the actual pixel interactions in a training image. Furthermore, as has been discussed for auto-binomial and auto-normal models of MRF, the estimation of model parameters pose computational difficulties for the reason that estimation techniques have been developed for image modeling specifically and are not adopted from physics like the MRF models. This results in MRF models and parameter estimation techniques which may not be flexible enough to adapt to wide range of training texture images.

On the other hand, the general Markov-Gibbs random field model generalizes Gibbs distribution rather than using pre-defined binomial or normal distributions. An arbitrary structure of pixel interactions is estimated from training image allowing more flexible 2^{nd} order neighbourhood systems. The estimated pairwise interactions are represented as cliques

n corresponding Gibbs distribution. The values of clique potentials are also estimated from he training image. This model offers simplification and generalization over image textures.

4.3.1 Pairwise Pixel Interactions

The general MRGF is based on an arbitrary 'interaction structure' (or neighbourhood system) which incorporates important pixel interactions in the training image. Pixel interaction means he probabilistic dependence of signal value at a pixel on another pixel in the neighbourhood system. For the simple 2nd order system, these interactions are limited to pairs of pixels only. In contrast with traditional MRF models, the pixel interactions need not to be short-range only in MGRF model. Figure 4-10 below shows an example of pairwise pixel interactions of different ranges.

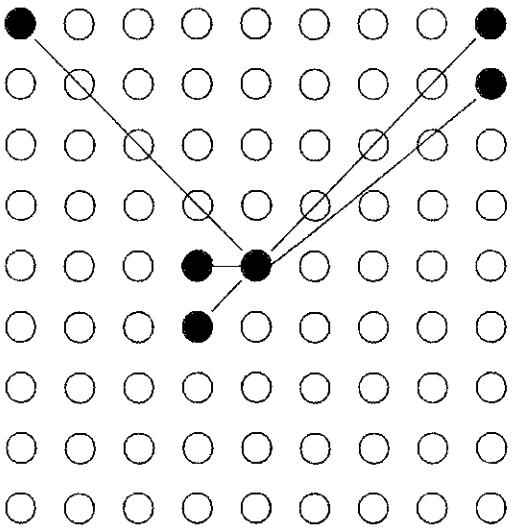

Figure 4-10: Multiple pair wise pixel interactions, short-range and long-range

An interaction structure represents all significant long range and short range interactions in a training image. The general MGRF model is defined only for strictly homogeneous or piecewise homogeneous texture image. This category of images ensures the translation invariance of pairwise pixel interactions i.e. the same pixel interactions are observed throughout the image lattice. The MGRF model determines the characteristic neighbourhood (interaction structure) for a given image as well as the strength of pixel interactions (as Gibbs potential functions) to recover the texture image precisely.

A pairwise pixel interaction is given as a clique $\mathbf{c}_{\mu,\nu} = \{(i,i') : i,i' \in \mathbf{R}\}$ where (μ,ν) denotes the spatial offsets between pixels of the pair. As implied by the translation invariance quality of the homogeneous texture, all cliques present in image under the same offset possess more or less the same combination of signal values. The group of all cliques present in lattice is represented by the clique family $\mathbf{C}_{\mu,\nu} = \{(i,i') \mid i,i' \in \mathbf{R}, i'-i = (\mu,\nu)\}$ for the offset (μ,ν). The characteristic interaction system for the image consists of significant clique families of image denoted by $\mathbf{C}_{\mathbf{N}} = \{\mathbf{C}_{\mu,\nu} : (\mu,\nu) \in \mathbf{N}\}$, where $\mathbf{N} = \{\mu_n, \nu_n : n = 0,1,2,.....,N\}$ denotes the pairwise offsets of the neighbourhood system.

The interaction strength of the members of a clique family is represented by clique potential $V_{\mu,\nu}(g_i, g_{i'} : (i,i') \in \mathbf{C}_{\mu,\nu})$ corresponding to Gibbs potential in GPD in equation (4.1) where $(g_i, g_{i'})$ are signal values at the two sites in a clique. A sum of all clique potentials for a clique family is denoted by partial interaction energy for that family given as $E_{\mu,\nu}(\mathbf{G} \mid V_{\mu,\nu})$. A sum of partial interaction energies for all clique families results in total interaction energy $E(\mathbf{G})$.

$$E_{\mu,\nu}(\mathbf{G} \mid V_{\mu,\nu}) = \sum_{\mathbf{c} \in \mathbf{C}_{\mu,\nu}} V_{\mu,\nu}(g_i, g_{i'} : (i,i') = \mathbf{c}) \tag{4.22}$$

$$E(\mathbf{G}) = \sum_{\mu,\nu \in \mathbf{N}} E_{\mu,\nu}(\mathbf{G} \mid V_{\mu,\nu}) \tag{4.23}$$

The general MGRF model takes into account the interaction structure $\mathbf{N}$, its clique families $\mathbf{C}_{\mathbf{N}}$, their clique potentials $V_{\mu,\nu}(g_i, g_{i'})$, and partial interaction energies $E_{\mu,\nu}(\mathbf{G} \mid V_{\mu,\nu})$. Overall, the GPD for MGRF model can be written as following

$$\begin{aligned} P(\mathbf{G}) &= \frac{1}{\mathbf{Z}} \exp(E(\mathbf{G})) \\ &= \frac{1}{\mathbf{Z}} \exp\Big(\sum_{\mu,\nu \in \mathbf{N}} E_{\mu,\nu}(\mathbf{G} \mid V_{\mu,\nu})\Big) \\ &= \frac{1}{\mathbf{Z}} \exp\Big(\sum_{\mu,\nu \in \mathbf{N}} \sum_{\mathbf{c} \in \mathbf{C}_{\mu,\nu}} V_{\mu,\nu}(g_i, g_{i'} : (i,i') = \mathbf{c})\Big) \end{aligned} \tag{4.24}$$

The value of clique potential shows the significance of clique families. The higher potential value for a family represents high interaction energy and thus influences more on texture patterns. However, the interaction structure $\mathbf{N}$ consists of significant clique families only.

4.3.2 Model Parameters

For a given training image, the signal co-occurrences of pairs are gathered for different clique families and given in the form of Grey Level Co-occurrence Histograms (GLCH). Let $\mathbf{H}_{\mu,\nu}(\mathbf{G}) = \{H_{\mu,\nu}(q,q'|\mathbf{G}) : (q,q') \in \mathbf{Q}^2\}$ denote the vector of grey level co-occurrence histograms gathered for the clique family $\mathbf{C}_{\mu,\nu}$. The histograms are then normalized to get grey level co-occurrence probabilities' for that specific clique family.

$$\mathbf{F}_{\mu,\nu}(\mathbf{G}) = \frac{\mathbf{H}_{\mu,\nu}(\mathbf{G})}{|\mathbf{C}_{\mu,\nu}|} \tag{4.25}$$

$$\sum_{(q,q')\in Q^2} (F_{\mu,\nu}(q,q'|\mathbf{G}) = 1 \tag{4.26}$$

As discussed in last section, the clique potentials $V_{\mu,\nu}(g_i, g_{i'})$ depend upon signal values (q,q') at the two sites in cliques determining how probable the signal values are to appear in that specific type of cliques throughout the image. This allows the partial interaction energies of clique families to be written in terms of GLCHs.

$$\begin{aligned} E_{\mu,\nu}(\mathbf{G}\,|\,V_{\mu,\nu}) &= \sum_{\mathbf{c}\in\mathbf{C}_{\mu,\nu}} V_{\mu,\nu}(g_i, g_{i'} : (i,i') = \mathbf{c}) \\ &= \sum_{(\mathbf{q},\mathbf{q}')\in|\mathbf{Q}|^2} V_{\mu,\nu}(q,q'|\mathbf{G}) H_{\mu,\nu}(q,q'|\mathbf{G}) \\ &= |\mathbf{C}_{\mu,\nu}| \sum_{(\mathbf{q},\mathbf{q}')\in|\mathbf{Q}|^2} V_{\mu,\nu}(q,q'|\mathbf{G}) F_{\mu,\nu}(q,q'|\mathbf{G}) \\ &= |\mathbf{R}|\,\rho_{\mu,\nu} \sum_{(\mathbf{q},\mathbf{q}')\in|\mathbf{Q}|^2} V_{\mu,\nu}(q,q'|\mathbf{G}) F_{\mu,\nu}(q,q'|\mathbf{G}) \end{aligned} \tag{4.27}$$

where the constant $\rho_{\mu,\nu} = \frac{|\mathbf{C}_{\mu,\nu}|}{|\mathbf{R}|}$ denotes the relative cardinality of every clique family. Thus the GPD for general MGRF in equation can be written in the form of GLCHs.

$$P(\mathbf{G}) = \frac{1}{\mathbf{Z}} \exp\Big(\sum_{\mu,\nu \in \mathbf{N}} |\mathbf{C}_{\mu,\nu}| \sum_{c \in \mathbf{C}_{\mu,\nu}} V_{\mu,\nu}(q,q'|\mathbf{G}) F_{\mu,\nu}(q,q'|\mathbf{G}) \Big) \tag{4.28}$$

The above expression has two important constituents for Gibbs energy. Gray level co-occurrence histograms are gathered from the training image and form the sufficient statistics for the model (see Appendix B). The potential vector $\mathbf{V} = (V_{\mu,\nu} \mid (\mu,\nu) \in \mathbf{N})$ forms the model parameters and is to be estimated from the training image. The next step in modeling is to estimate the model parameters through MLE.

4.3.3 MLE Parameter Estimation

Let $L(\mathbf{V}|\mathbf{G})$ denote the logarithm of the likelihood function for the MGRF model called log-likelihood function given as

$$L(\mathbf{V}|\mathbf{G}) = \ln(P(\mathbf{G}|\mathbf{V})) \tag{4.29}$$

It has been shown that the log-likelihood function for GPD meets the requirements for strict log-concavity or unimodality [Gimel 1999]. Unimodality implies a unique finite maximum $\mathbf{V}^*$ where the gradient of log-likelihood is equal to zero. The desired MLE for parameters of log-likelihood $\mathbf{V}^*$ is achieved in two steps. The first step involves analytic approximation of parameters by analyzing log-likelihood function. In second step, a stochastic relaxation algorithm refines analytic approximation of potentials as well as synthesizes the texture [Gimel 1999].

The analytic approximation involves expansion of log-likelihood into truncated Taylor series (See Appendix B) around the zero point $\mathbf{V} = \mathbf{0}$. The point corresponds to the Gibbs

listribution, Independent Random Field (IRF), where all signal values are equiprobable and site signals are independent. The truncated Taylor Series expansion of log-likelihood function around point is obtained as follows.

$$L(\mathbf{V}\,|\,\mathbf{G}) \approx L(\mathbf{0}\,|\,\mathbf{G}) + \mathbf{V}.\frac{\partial L(\mathbf{V}\,|\,\mathbf{G})}{\partial \mathbf{V}}\Big|_{\mathbf{V}=0} + \frac{\mathbf{1}}{\mathbf{2}}.\mathbf{V}^{\mathrm{T}}\,\frac{\partial^2 L(\mathbf{V}\,|\,\mathbf{G})}{\partial^2 \mathbf{V}}\Big|_{\mathbf{V}=0}\,\mathbf{V} \tag{4.30}$$

The marginal probabilities (See Appendix B) of signal co-occurrences for cliques in IRF are $F_{irf}(q,q') = \dfrac{1}{|\mathbf{Q}|^2}$. Let $Var_{irf} = F_{irf}(1 - F_{irf})$ be the variance of signal co-occurrences for IRF. It can be shown from quadratic approximation of above truncated series that the first analytic approximations of clique potentials are given by

$$V_{\mu,\nu}(q,q'|\,\mathbf{G}) = \lambda_0 (F_{\mu,\nu}(q,q'|\,\mathbf{G}) - F_{irf}(q,q')) \tag{4.31}$$

which leads to the following expression for interaction energy of each clique family in equation (4.27) [Gimel 1999].

$$E_{\mu,\nu}(\mathbf{G}\,|\,V_{\mu,\nu}) = |\,\mathbf{R}\,|\,\lambda_0 \rho_{\mu,\nu} \sum_{(q,q')\in|\mathbf{Q}|^2} (F_{\mu,\nu}(q,q'|\,\mathbf{G}) - F_{irf}) F_{\mu,\nu}(q,q'|\,\mathbf{G}) \tag{4.32}$$

The scaling factor λ_0 is same for all clique families and can be derived from the statistics of Independent Random Field (IRF) as follows

$$\lambda_0 = \frac{\sum_{\mu,\nu\in\mathbf{N}} \rho_{\mu,\nu}{}^2 \sum_{q,q'\in|\mathbf{Q}|^2} \Delta_{\mu,\nu}{}^2(q,q')}{\sum_{\mu,\nu\in\mathbf{N}} \rho_{\mu,\nu}{}^3 \sum_{q,q'\in|\mathbf{Q}|^2} Var_{irf} \Delta_{\mu,\nu}{}^2(q,q')} \tag{4.33}$$

where $\Delta_{\mu,\nu}(q,q') = F_{\mu,\nu}(q,q') - F_{irf}$. The equation (4.31) shows that pairwise pixel interactions for every clique family, given by Gibbs potentials, depend mainly on signal co-occurrences in training image and that how far these deviate from those of the IRF.

4.3.4 Most Characteristic Interaction Structure

An interaction structure or characteristic neighbourhood for MGRF contains significant clique families only which implies that in most cases a small proportion of clique families would be making major contribution to the texture pattern. Thus, the reduced number of clique families reduces the computational complexity of model while still preserving the underlying texture pattern of the training image. The clique families are filtered based on their interaction energies. The clique families with weak interaction energies are excluded by setting their Gibbs potentials to zero. The procedure for finding the most characteristic interaction structure is outlined by Gimel *et al* [Gimel 1999]. A search window is selected covering a large range of possible pairwise pixel interactions. The relative partial interaction energies of each clique family in search window are calculated and compared. A 2D relative partial energy function graph 'interaction map' presents visually the clique families in search window and their relative energy contribution. Figure 4-11 below shows an example interaction maps with 40x40 window width where darker clique families show higher interaction strength.

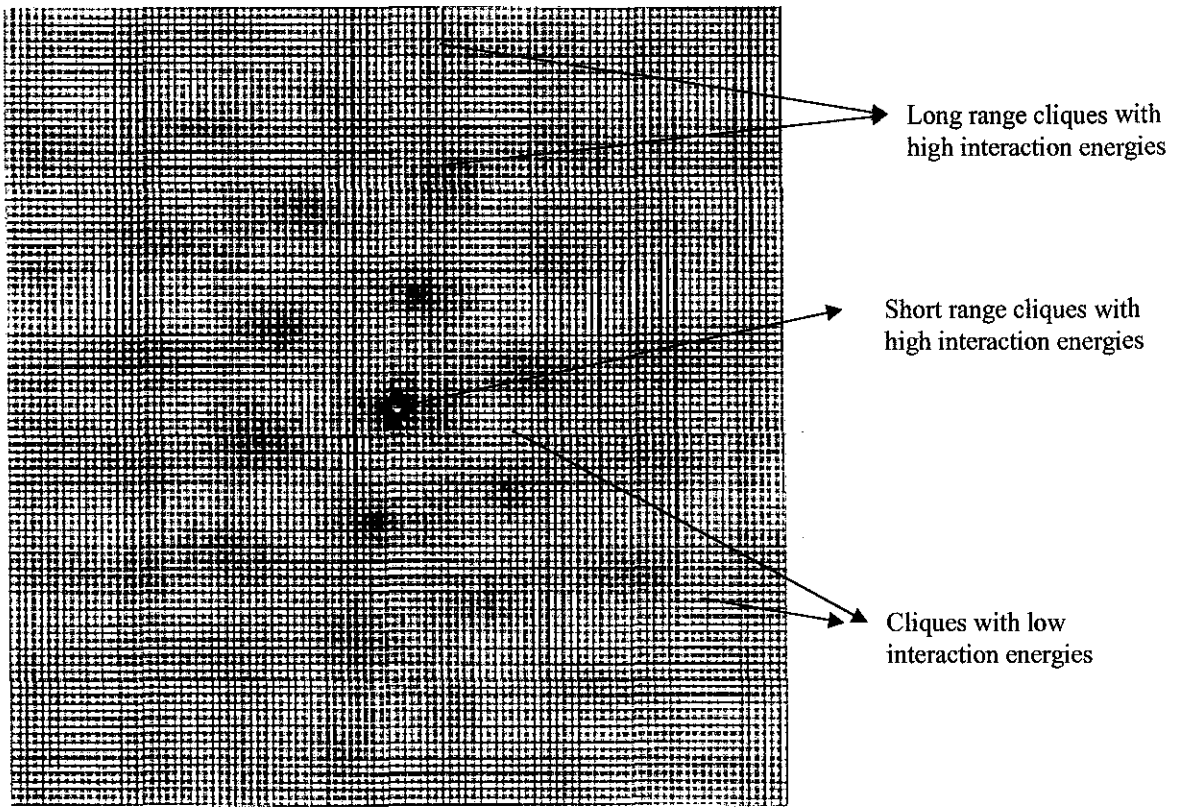

Figure 4-11: Interaction Map on large scale (reproduced from [Gimel 1999])

The characteristic neighbourhood is found by proper thresholding of interaction map. The hreshold is chosen as a function of mean interaction energy $\bar{\varepsilon}$ and standard deviation ϕ_E of nteraction energy in interaction map as follows

$$\theta = \bar{\varepsilon} + c\phi_E \tag{4.34}$$

The constant c is selected heuristically and typically holds a value in between 3 and 4

4.3.5 Synthesis via Simulated Annealing

The stochastic relaxation algorithm Simulated Annealing (SA) is used for texture synthesis as well as refinement of approximates of Gibbs potentials. The characteristic interaction structure and first analytic approximations of Gibbs potentials are used by SA to synthesize

ıe sample images. The algorithm generates a Markov chain of synthesized texture images ′ith gradually changing potential estimates which are refined to desired MLE estimates nally. At each iteration t of SA, the texture image g^t is synthesized from the previous nage in Markov chain g^{t-1} using current GPD $P(g \mid \mathbf{V}^{t-1})$ using Metropolis or Gibbs ampling algorithm. The GLCHs are gathered from current image and Gibbs potentials are efined by changing current potential approximates *in line with* the difference between ;LCHs of current texture image and the training image g^0 [Gimel 1999].

$$V_{\mu,\nu}{}^{t}(q,q') = V_{\mu,\nu}{}^{t-1}(q,q') + \lambda^t \rho_{\mu,\nu}(F_{\mu,\nu}(q,q'|(g^{t-1}) - F_{\mu,\nu}(q,q'|(g^0)) \tag{4.35}$$

'he scaling factor λ^t for each iteration determines a step along the current approximation of ıe gradient for Gibbs potentials. The scaling factor is reduced gradually along the efinement of Gibbs potentials as follows where c_0, c_1, c_2 are the parameters used ıeuristically.

$$\lambda^t = \lambda^0 \frac{c_0 + 1}{c_1 + c_2 t} \tag{4.36}$$

The algorithm achieves visual similarity by reducing differences between GLCHs of ynthesized texture and training texture by refining potential estimates and changing GPD ;radually [Gimel 1999].

ł.4 Summary

n this chapter, the main concepts of Markov random field modeling and the pairwise pixel nodel (MGRF) are discussed in detail. Model identification, parameter estimation and exture synthesis for MGRF have also been covered. These are the main modeling steps for MGRF modeling for any 2D textures and, accordingly, modeling of skin textures also 'ollows these steps. However, 3D skin textures have to be converted to 2D grayscale textures 'or modeling. Chapter 5 will detail the acquisition and pre-processing steps for 3D skin extures. We will also see that how MGRF is applied to skin textures in context of this work.

Chapter 5

Modeling of 3D Surface Textures of Skin

This chapter discusses the acquisition of 3D skin textures and their modeling for this work. An overall frame work of the system is described in section 5.1. A detailed description of acquisition set up for 3D skin data from patients using laser scanner is described in section 5.2. The data requires some pre-processing to be input as 2D texture images to modeling. Section 5.3 details these pre-processing steps. The general types of 3D skin features found in both healthy and diseased, observed from the acquired data, are discussed under section 5.4. Finally the modeling of skin textures is given in section 5.5 followed by analysis of results and discussion.

5.1 Overall framework for Modeling

The goal of this research work is modeling of 3D surface textures of skin. In Chapter 2, it was showed from image acquisition techniques that the 3D acquisition is mostly based on processing of 2D images and may not be very accurate. It was also observed that 3D modeling of skin is mostly focused on computer animation applications. For this reason skin textures are considered for healthy skin only and that some approximation of textures is assumed. The framework of modeling for this work includes accurate 3D image acquisition based on laser scanning which has been the most advanced 3D capturing technique until now. The modeling is based on real texture samples which are gathered from case studies (patients).

As discussed earlier, the complete haptic realization of a material object, skin in this case, requires several display properties. This work covers the 3D surface textures of skin which play a vital role in differentiating skin conditions. Then for fast texture rendering through haptic devices, 3D textures are handled as height maps (2D grayscale textures). Section 3.3.1 detailed many fast 'force-mapping' haptic texturing techniques based on height maps. Since haptic rendering involves the surface variations only, in this work 2D color textures of skin are not considered. The framework for this modeling consists of following important stages.

Stage 1: 3D image acquisition of skin through laser scanning

Stage 2: Pre-processing of 3D data to get 2D grayscale surface textures

Stage 3: Modeling of 2D textures with MGRF technique

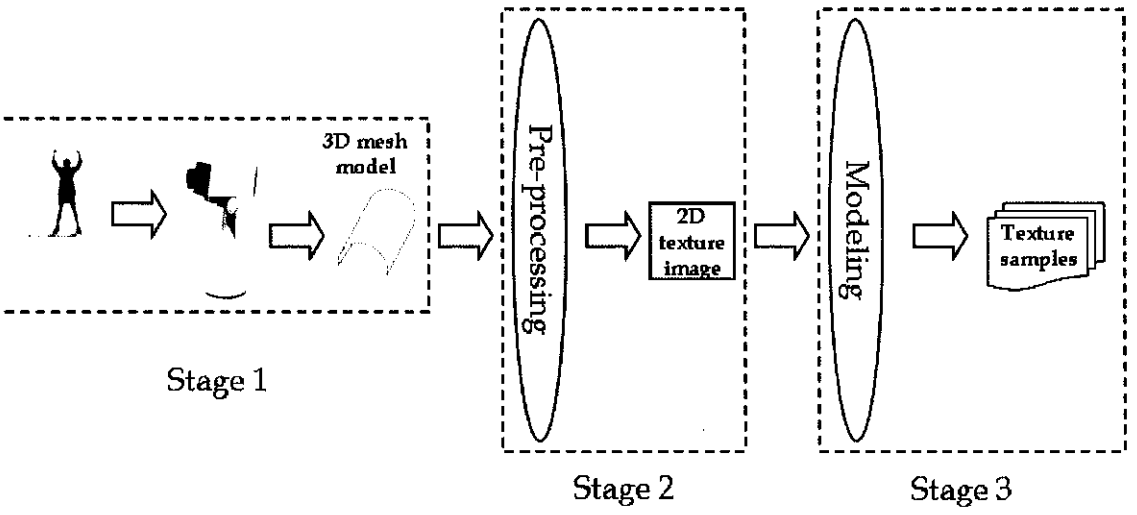

5.2 3D Data Acquisition

This work requires an accurate 3D acquisition system and variety of skin samples to look into real textures found on human skin. The acquisition involves laser scanner capturing 3D surface information at high resolution of ~0.1 mm. The set up consists of laser scanner Konica Minolta VIVID 910 [VIVID 910]. The equipment's working principle is based on 'laser triangulation' and provides non-contact measurement of depth. Figure 5-1 shows the laser scanner with laser beam source and CCD capturing camera.

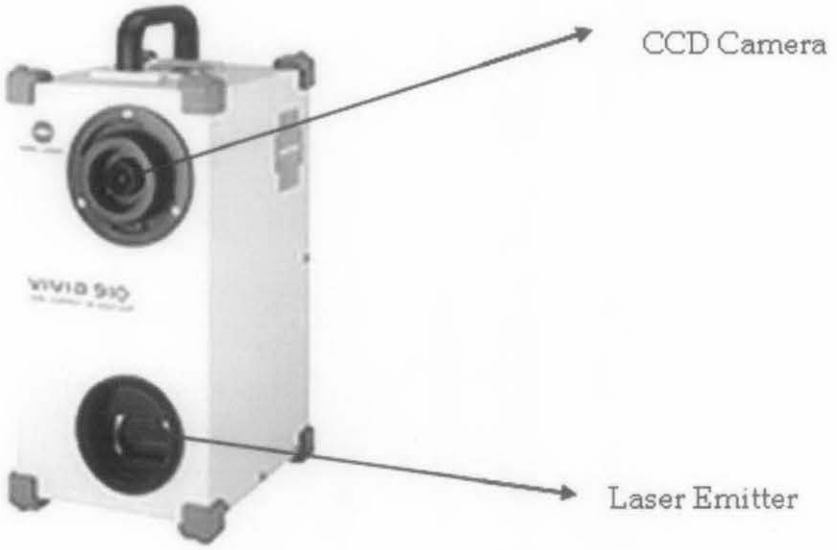

Figure 5-1: The laser scanner used for 3D data acquisition [VIVID 910]

The object, the laser source and CCD camera makes a triangle. Figure 5-2 shows the working principle of the laser scanner. The object is exposed to a laser beam. The camera looks for the laser beam dot on the surface of the object and measures the angle CCD camera makes between laser dot on object and laser emitter. From this angle and other known parameters of this triangle i.e. distance and angle between laser emitter and CCD camera, the distance between scanner and object is calculated accurately. A laser stripe rather than only one laser point allows fast scanning.

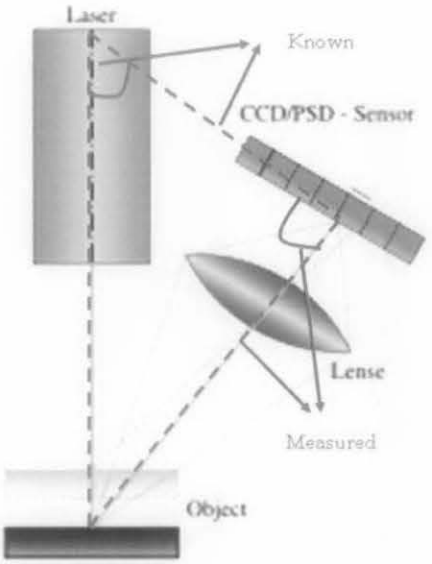

Figure 5-2: Working principle of laser scanner 'laser triangulation'

The depth information of object surface is collected in the form of 'point cloud' which represents the distance calculated at every laser point seen by CCD camera. The data in the form of point clouds is further processed by a reconstruction algorithm. The algorithm transforms points in 3D to a triangular mesh called as 'mesh model'. Figure 5-3 shows examples of point clouds and mesh models of three skin samples taken from trunk, leg and arm respectively.

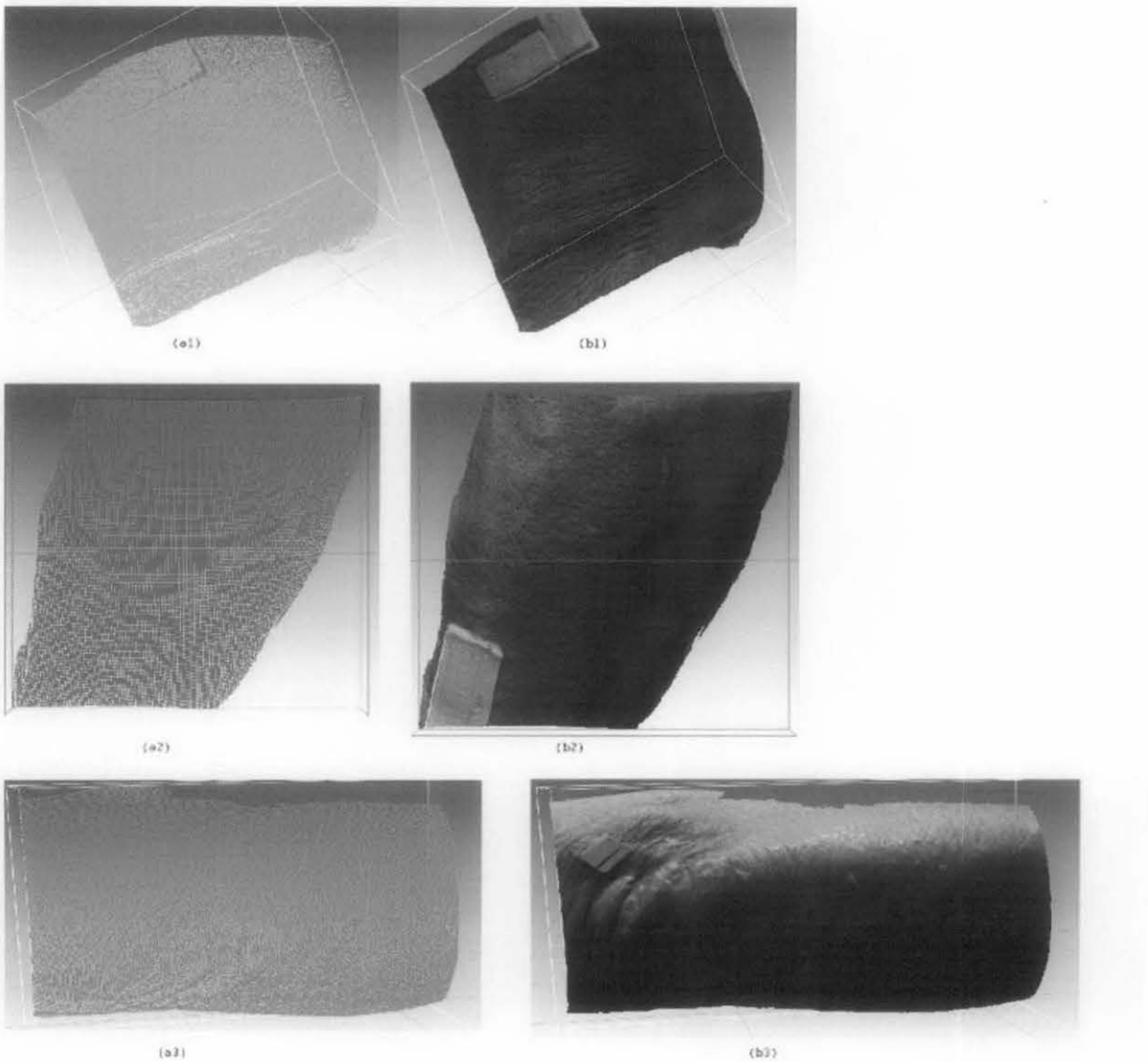

Figure 5-3: 3D data for skin acquired from laser scanner – (a) point clouds (b) mesh models with color texture wrapped

The reconstruction or triangulation process connects the neighbouring points in point cloud to construct triangular mesh by some fast algorithm. The laser scanner is operated via 3D scanning software, rapidform2006 [Rapidform]. The triangulation and some of the pre-processing of 3D data is done via this software (Section 5.3). Figures 5-4 and 5-5 show some screen shots from the software showing point clouds and triangulated mesh model.

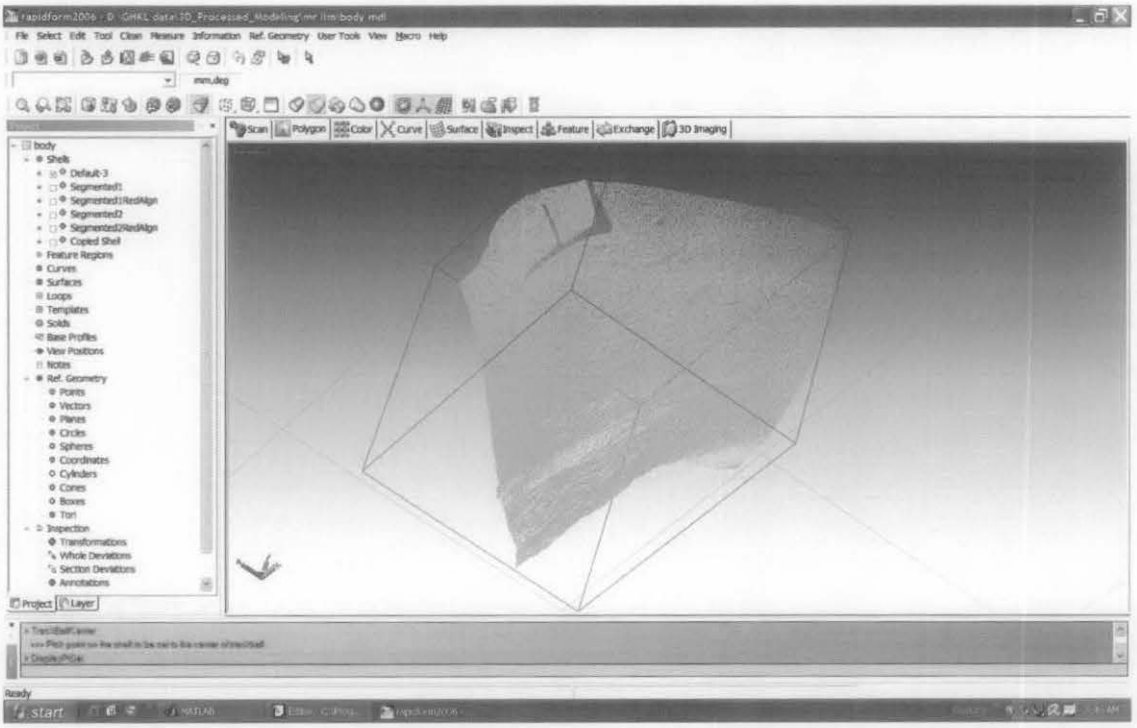

Figure 5-4: Screenshot from rapidform2006 showing point clouds for a skin sample

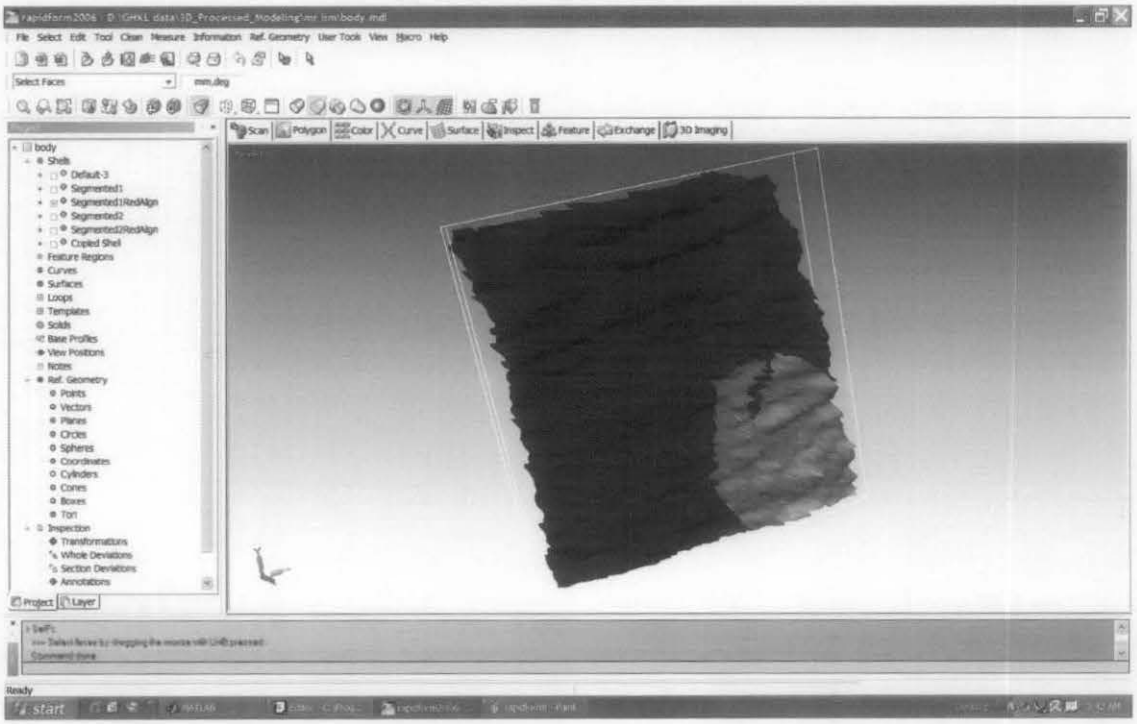

Figure 5-5: Screenshot from rapidform2006 showing segmentation of a skin sample manually

Skin textures of both healthy and diseased skin are considered in this work and for diseased skin conditions psoriasis lesions are selected. Psoriasis makes an active area of research in

skin imaging because of its ubiquity, impact on patient's life and incurability. The most common type of psoriasis namely 'plaque psoriasis' appears in the form of inflamed, scaly patches on the surface of skin. The typical surface textures of psoriatic lesions are important for clinical inspection of disease. These skin textures resulting from inflammation of skin provide insight of types of textures which may be present on skin. The case studies for this work include 9 male patients of psoriasis with age range 18-45. The severity of disease varies among case studies with different level of thickness, scaliness and overall pattern of lesions. In addition, overall skin condition due to ageing also results in diversity of textures in both healthy and diseased skin. Following the PASI standard (Section 2.2), skin samples were captured for psoriatic lesions from areas of the arms, legs and trunks of patients. The set up for capturing 3D images is shown in Figure 5-6 below. The 3D scanner captures the surface profiles of patient's skin while the body limb is held straight facing to the scanner.

Figure 5-6: Set-up for capturing 3D images from patients

5.3 Data Pre-processing for Texture Extraction

The next step after acquisition of data, which is in the form of 3D mesh models after triangulation, is to extract 3D surface textures from mesh models and convert them to 2D grayscale textures. In this pre-processing of data for texture extraction, color information of skin is discarded, and only 3D surface profile (height) is considered. The technique is similar to 'height maps' in computer graphics where gray level represents the height in third dimension. The pre-processing steps are depicted in Figure 5-7 followed by explanation.

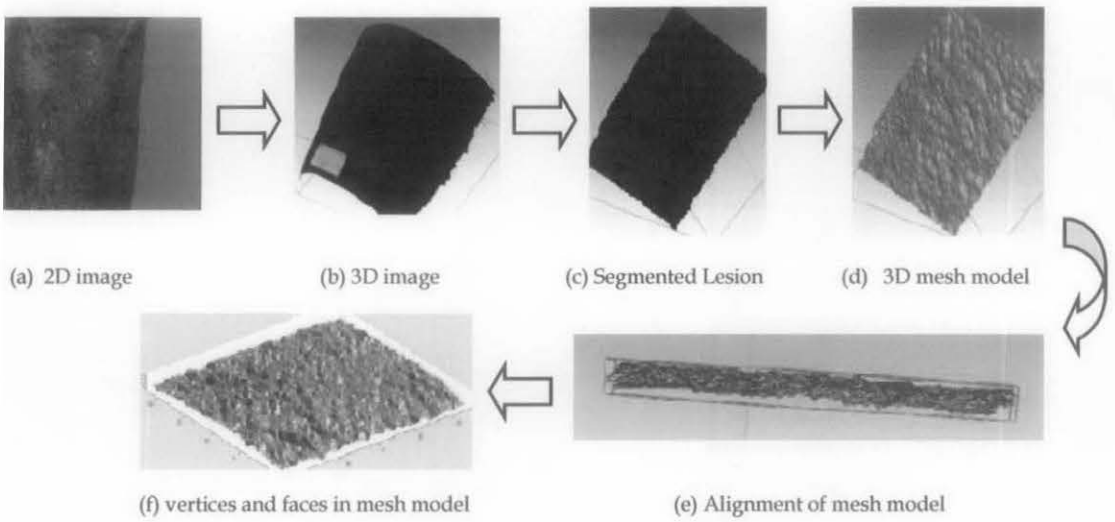

Figure 5-7: Pre-processing steps to extract 2D grayscale texture from 3D mesh model

1) The mesh model (Figure 5-7b) is segmented manually to extract the representative portions of healthy skin and lesions (Figure 5-7 c and Figure 5-7d).

2) The segmented portion is aligned with x-y plane so that height is along z-axis (Figure 5-7e).

3) The mesh models are in the form of vertices and faces which are projected on regular lattice for conversion to 2D grayscale textures. The projection is achieved by conversion of vertices and faces (Figure 5-7f) to 3D parametric surfaces using cubic interpolation (Figure 5-8a).

4) After interpolation, data is defined as points in three dimensional space on regular x-y grid where z presents the height values. The heights on regular grid are scaled to grayscale which can be viewed as a grayscale texture (Figure 5-8d).

5) In certain investigations, the curvature of body is eliminated to extract fine textures on skin. The algorithm for elimination of underlying body curvature is simple (See Appendix C for MATLAB code). It is achieved by fitting a 2D surface among the data points of interpolated surface after step 3 above. The difference between the

fitted surface, representing curvature of body, and interpolated parametric surface, representing actual skin surface profile, gives the fine textures of skin. These steps are shown in Figure 5-8. The fitted surface to the vertices in interpolated parametric surface is shown in Figure 5.8b. Figure 5-8c shows the difference between actual parametric surface (Figure 5-8a) and fitted surface 5-8b which represents find texture on skin. This texture image is scaled to obtain a gray scale image as shown in Figure 5-8d.

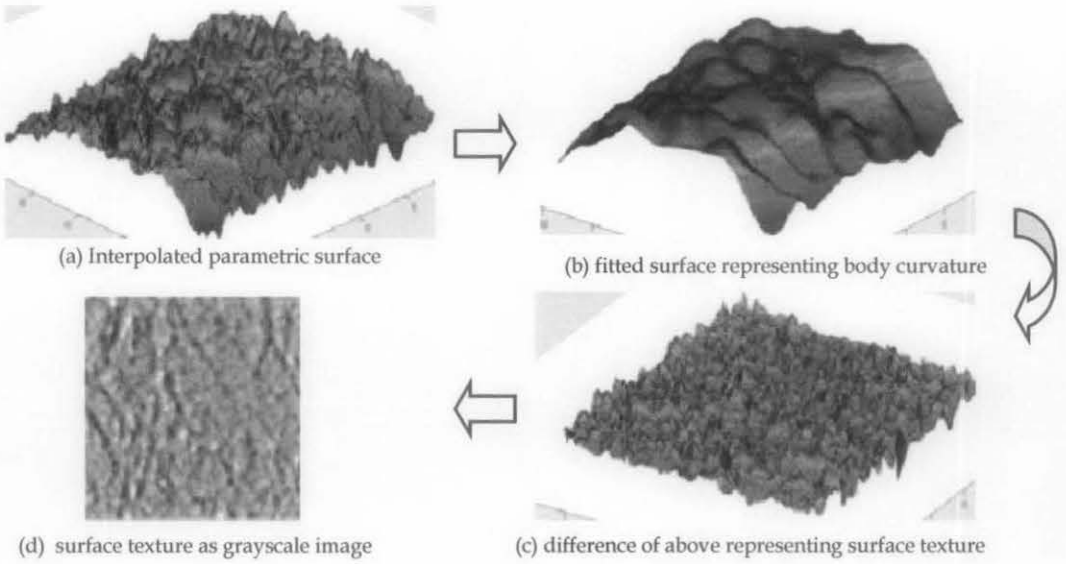

Figure 5-8: Elimination of body curvature to extract surface texture

Figure 5-9 shows some examples of skin textures where the curvature has been eliminated using the surface fitting.

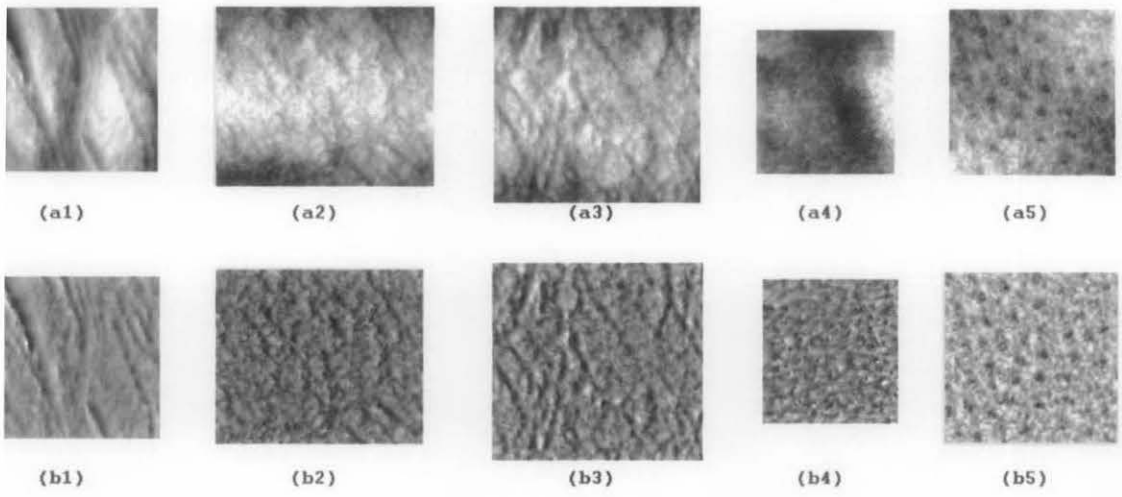

Figure 5-9: Examples of surface textures for curvature elimination using surface fitting – (a) Original skin textures with curvature (b) Skin textures after elimination of curvature

5.4 3D Skin Surface Features

As discussed in Chapter 2 (Section 2.4) the skin surface profiles are mainly caused by large scale and small scale wrinkles. The wrinkles on large scale are due to ageing and body location (e.g. elbows, forehead, and fingers). The small scale fine lines or fine texture remains same locally but varies from location to location on body. For example, the fine textures found on hands are very different from those found on upper arms. When diseased skin (psoriatic skin for this study) is considered, the inflammation of skin resulting in thickness and scaliness of skin lesions also adds to diversity of these textures. The patterns of lesions also change with the location on body. For this reason, it is important to observe the diversity of grayscale textures produced by skin surface profiles, both healthy and diseased. As seen from Chapter 2, not much work has been done to observe this variety of real textures of skin. The research work done in skin animation for computer graphics includes approximation to real textures only and does not take into account this much diversity of textures.

For this work, the samples of skin have been taken from real case studies (9 patients), and include diversity of skin textures from healthy and diseased skin and from various ages and locations of body. These samples give interesting clues about the appearance of skin features, wrinkles, etc. mentioned above, when observed in 3D height profiles. From the observations

)f large number of extracted grayscale texture samples, the 3D skin features are mainly :ategorized in three types, irrespective of the skin condition (healthy or psoriatic).

a) body curvature – large scale non-repetitive feature, appearing as gradual grayscale change similar to illumination variation, due to the curvature of underlying limb
b) wrinkles/lines – large scale feature, repetitive but mostly without any pattern, can be caused by both wrinkles/lines on skin and inflammation on diseased skin
c) fine lines/texture – small scale feature, repetitive and mostly with pattern, due to fine scale locally varying texture of skin both on healthy and diseased skin

'igure 5-10 shows the three features on a texture of skin lesion.

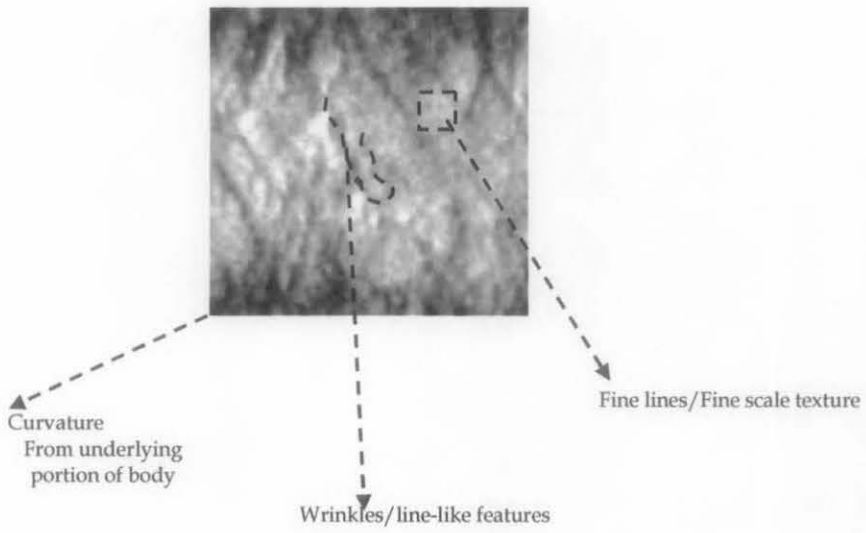

Figure 5-10: General 3D features found on skin and observed from extracted 2D grayscale texture

'or this work, all skin features are given as input to the modeling. However, to observe the esponse of model to the features individually, the input textures are categorized as three sets.

- Set 1: Textures consisting of all three features of curvature, wrinkles/lines and fine texture

- Set 2: Textures consisting of wrinkle/lines and fine texture. The curvature is eliminated by surface fitting and differencing procedure outlined in section 5.3.

- Set 3: Textures consisting of fine textures only. These textures are taken from the body portions where wrinkles/lines are not present on skin. Again, the curvature is eliminated by surface fitting and differencing method as for above set.

The texture images consisting of curvature or wrinkles only are not considered for modeling because of the fact that such skin profiles do not exist in reality. The wrinkles are always found with fine textures whereas the curvature of body is also found with wrinkles and/or fine textures. However, fine textures are found without any wrinkles on most of the body. Figure 5-11 explains the distribution of 3D surface features of skin into three sets of input textures.

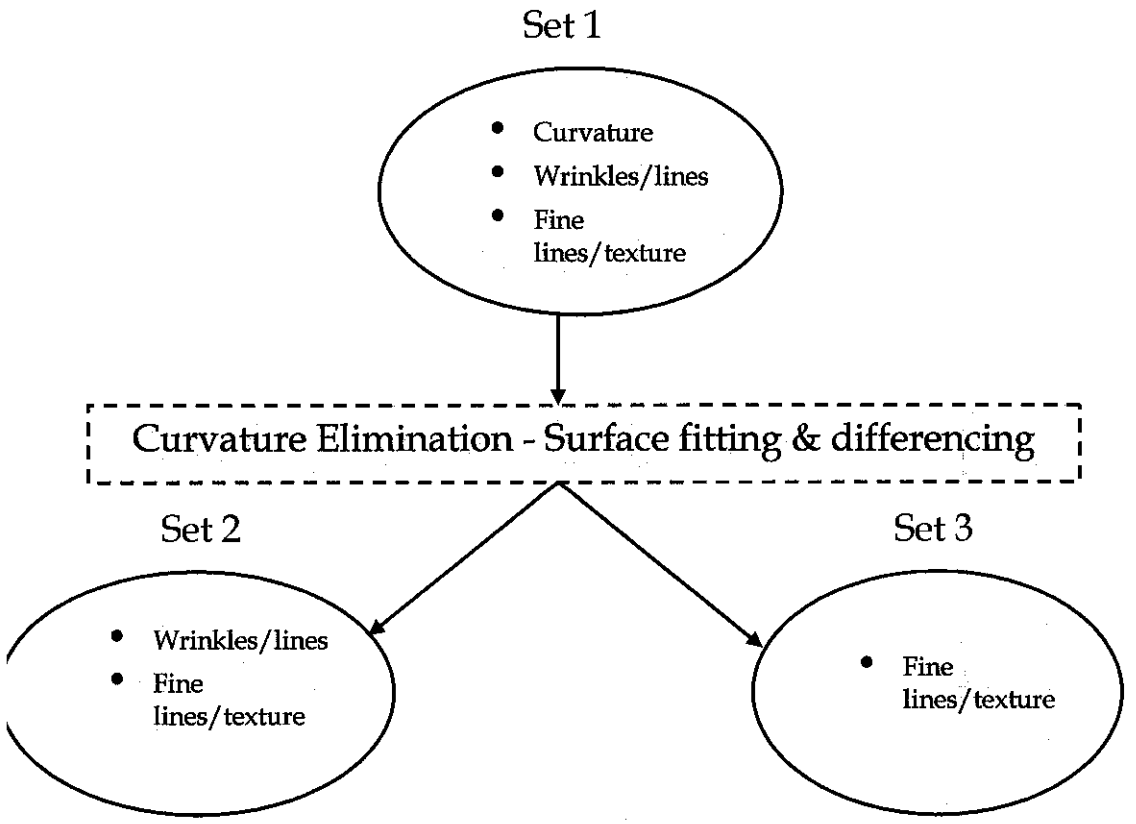

Figure 5-11: Distribution of 3D skin features into three sets for input to modeling

'he healthy and diseased skin samples in three sets are obtained from nine patients. The skin extures include 10 samples for set 1, 15 samples for set 2 and 13 samples for set 3. The nodeling results are presented in Section 5.6 including 5 samples of set 1, 8 samples of set 2 nd 5 samples of set 3 for analysis and discussion. The rest of the samples pose similar esults and have been presented in Appendix F, Appendix G and Appendix H respectively for nree sets.

5.5 MGRF Modeling Algorithms

n Chapter 4, Markov random field modeling in general and pairwise pixel interaction model the MGRF model) were reviewed. This section details the MGRF modeling for skin extures. The input to the modeling should be in the form of 2D grayscale textures. In Section .3, the pre-processing steps which convert the 3D surface textures to 2D grayscale textures vere discussed. In Section 5.4 the important observations regarding the 3D skin surface eatures found on skin were presented. It was also mentioned how the skin textures are ategorized in three input sets to observe the model response to these textures. The next step s to input these texture sets to the model and see how successfully the MGRF model can nalyze and reproduce the visual skin textures. An overview of different steps of MGRF nodeling is shown in Figure 5-12.

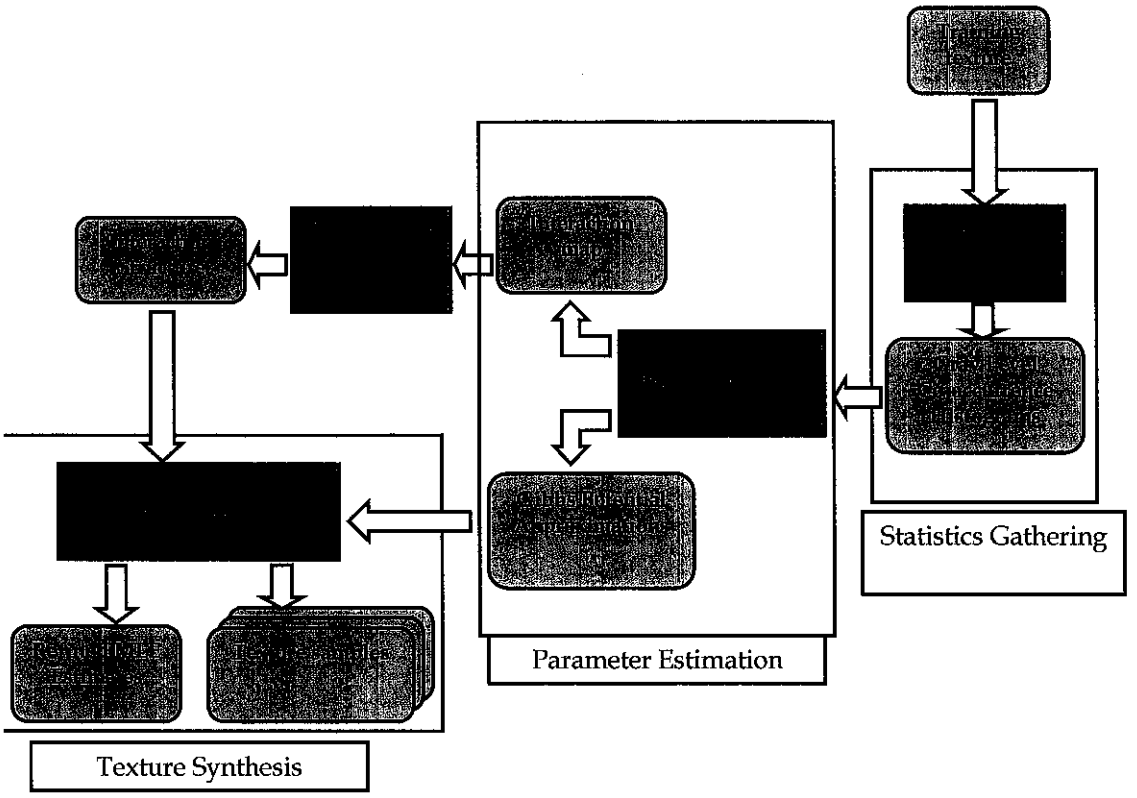

Figure 5-12: Overview of MGRF modeling for skin textures

Modeling of textures is completed in two main steps, analysis and synthesis. The analysis of nput textures is to identify the underlying model parameters and, for MGRF, consists of tatistics gathering, parameter estimation and interaction structure thresholding steps in bove diagram. Once the model has been identified completely in analysis steps, the ynthesis then reproduces the output texture samples incorporating the identified model. The gray-level co-occurrence histograms form the sufficient statistics for the model and their gathering is the fundamental step in analysis. From GLCH, the gray level co-occurrence robabilities (equation 4.25), Gibbs potentials (equation 4.31) and interaction energies equation 4.27) for clique families are derived. Following is the pseudo-code for the analysis f textures under MGRF modeling. The detailed MATLAB code can be found in Appendix).

.NALYSIS ALGORITHM FOR MGRF MODELING: -

nput:
) a gray-level image g=(g[i,j]: i = 1,...,M; j =1,...,N])
) Q=15 or 31 for 16 or 32 gray levels
) search window dimensions [Di, Dj]
) value of 'sigma' in range 3,...,4 for thresholding interaction map

)utput:
) a set of K most characteristic Gibbs potentials represented each by a 2D table
k = (Vk[q,s]: q=0,...,Q-1;s=0,...,Q-1]); k=1,...,K
) and their corresponding gathered co-occurrence probabilities from input image
'eq_image_k[q,s] : q=0,...,Q-1;s=0,...,Q-1]); k=1,...,K
) Calculated value of 'lambda_0'

;ray level co-occurrence histograms (GLCH) gathering:

.. Quantize given image into Q gray levels if it has higher signal resolution

!.. Collect co-occurrence histograms

COOC(di,dj) = (COOC(di,dj)[q,s]: q=0,...,Q; s=0,...,Q) for all inter-pixel shifts (di,dj) in search
/indow
each pair ((i,j),(i+di,j+dj)) is a clique of the clique family with this shift)
W=((di,dj): if dj=0 di=1,...,Di; else di = -Di,...,0,...,Di; dj=1,...,Dj):

2a) Initialise each COOC: for all di,dj,q,s: COOC(di,dj)[q,s]=1

2b) Collect histograms:

```
for j=1 step 1 until N
  for i=1 step 1 until M
      q = g[i,j];
       for dj = 0 step 1 until Dj
        for di = ( if dj is equal to 0 then 1 else -Di ) step 1 until Di
              if  (  i + di is in the range [1,M] AND j+dj is in the range [1,N]  ) then
                    s = g[i+di, j+dj]
                  increment COOC(di,dj)[q,s] by 1
        end for dj
       end for dj
   end for i
end for j
```

;ray level co-occurrence probabilities calculation:

). Normalise histograms to get relative frequencies:

```
for each (di,dj) in W:
  freq(di,dj)[q,s] = COOC(di,dj)[q,s]/sum_(q'=0,...,Q-1,s'=0,...,Q-1)COOC(di,dj)[q',s']
```

nteraction energies calculation:

l. Find relative energies for all clique families: RelEne(di,dj) = variance(freq(di,dj)):
variance(freq(di,dj) = sum_(q=0,...,Q-1;s=0,...,Q-1){freq(di,dj)[q,s]-mean_freq(di,dj)}^2
where mean_freq(di,dj) = sum_(q=0,...,Q-1;s=0,...,Q-1){freq(di,dj)[q,s]}/(Q^2)

'hresholding and Interaction Structure Extraction:

i. Select K top-energy clique families by thresholding the energy distribution
(all cliques with energies RelEne(di,dj) above mean_energy + (sigma)*standard_deviation

iibbs Potentials Learning:

i. Collect the gray-level histogram GLH for g, normalise it similarly to COOCs and
:ompute the scaling factor 'lambda_0'

'. Compute potentials for the selected K clique families:
'OT(di,dj)[q,s] = lambda_0 * (freq(di,dj)[q,s] - mean_freq(di,dj))

i. Output potentials and co-occurrence probabilities for selected clique families where Vk[q,s] =
'OT(di,dj)[q,s] and freq_image_k[q,s] = freq(di,dj)[q,s] for the selected familiy

---

The input image is scaled down in range 0-Q provided by input parameter Q. For this work 16 gray levels or Q=15 has been used. Although 16 gray levels pose much faster modeling, the quality of texture images is not compromised and skin features can still be perceived clearly. For example Figure 5-13 below shows the same skin texture scaled down to different gray levels.

Figure 5-13: Skin texture scaled down to different number of gray levels

.nother important thing is the dimensions of search window [Di, Dj]. The interaction map and ɔnsequently clique families are symmetric around center, as can be observed from Figure 4-0. The reason for this is the gray level co-occurrences which are gathered from texture nage. Hence, for computational efficiency, only half of search window is scanned in step 2 /here the dimensions [di, dj] are determining the actual search window. For example, when ıput dimensions [Di, Dj] are 80x80 pixels, the actual dimensions for search window [di, dj] /ould be [81, 40]. The half window dimensions also enable the algorithm for GLCH athering to consider gray level co-occurrence only once during 'raster scanning' of image. 'he resulting half of interaction map and clique families can be mirrored around centre to get ıe complete interaction map. As an example Figure 5-14 and 5-15 show the half of the 7x7 nd 9x9 pixels wide search windows respectively considered during analysis.

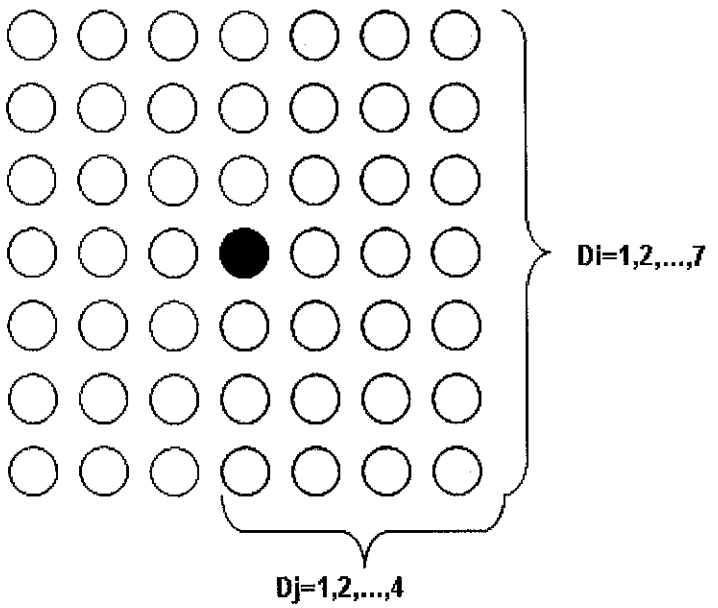

Figure 5-14: Only half of the 7x7 search window will be considered during analysis resulting in 24 clique families

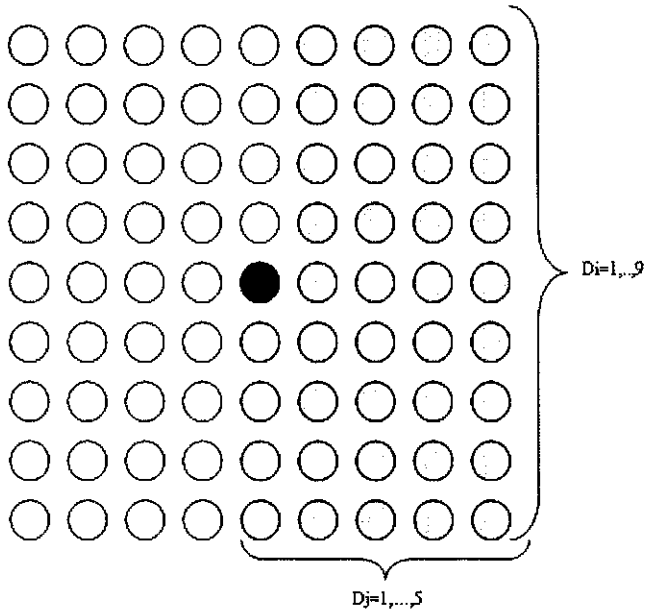

Figure 5-15: Only half of the 9x9 search window will be considered during analysis resulting in 40 clique families

The dimensions of search window are set around 40x40 to 50x50 depending on sample image size to gather most of the pixel interactions. In this case, the texture images are extracted from segmented portions of 3D mesh models and their pixel dimensions depend on the vertices present in the segmented mesh models. Hence image size varies from image to image and window dimensions are adjusted accordingly. The input parameter 'sigma' stands for constant c in equation 4.34 and has been set to 3.5 heuristically for thresholding.

The algorithm outputs the estimated Gibbs potentials for selected clique families in [Di, Dj] search window. Non-significant families are filtered by setting their Gibbs potentials to zero. For every clique family, Gibbs potentials are in the form of QxQ tables, giving co-occurrences of Q gray levels in that clique family. Figure 5-16 shows a sample texture image along with its interaction map and thresholded cliques. Table 5-1 and 5-2 show the gathered GLCHs and estimated Gibbs potentials for the clique family with offset (0,2) for the texture image shown in Figure 5-16(a) respectively. It can be noticed that both GLCHs and Gibbs potentials form the 16x16 matrices which correspond to the 16 gray levels selected for grayscale 2D textures.

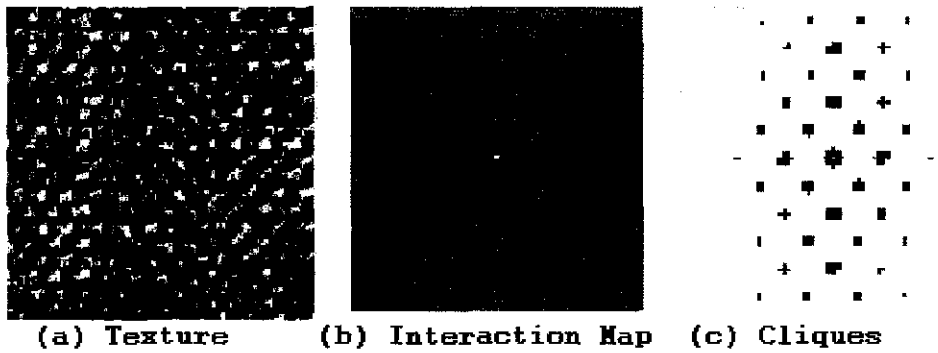

Figure 5-16: (a) Texture sample (b) Interaction Map (c) Thresholded clique families

	1	2	3	4	5	6	7	8	9	10	11	12	13	14	15	16
	10	62	57	13	15	9	4	1	1	3	1	0	1	1	0	0
	72	504	405	176	127	77	32	25	21	7	8	3	10	4	2	0
	54	461	519	294	249	163	77	31	23	38	8	10	16	7	2	1
	27	212	333	307	299	208	90	62	42	43	23	29	15	11	3	1
	8	116	257	304	347	298	181	105	81	65	35	46	50	29	8	3
	12	66	152	195	299	273	176	143	132	80	64	65	49	26	15	4
	3	40	89	123	160	186	130	83	102	79	37	53	51	35	18	0
	3	13	49	65	105	105	101	62	66	45	30	45	51	29	9	8
	3	18	43	52	103	120	94	75	81	50	36	52	59	28	22	4
0	2	11	28	52	78	77	63	46	61	45	30	55	47	33	11	5
1	1	5	9	30	29	47	52	28	37	38	21	35	29	21	6	2
2	0	9	13	36	61	62	73	56	50	37	20	51	45	41	16	3
3	0	6	12	33	51	66	61	41	61	39	36	49	55	41	17	7
4	0	3	13	13	28	42	47	24	43	27	23	32	33	35	14	5
5	0	0	1	12	7	18	17	10	14	19	8	18	20	12	8	4
6	0	1	2	1	3	7	3	7	4	4	0	8	3	3	3	3

Table 5-1: GLCH for for the clique family with offset (0,2) for the texture given in Figure 5-16(a)

	1	2	3	4	5	6	7	8	9	10	11	12	13	14	15	16
1	-1.0571	0.3245	0.1989	-0.8234	-1.0571	-1.1618	-1.3292	-1.3883	-1.3083	-1.3292	-1.3292	-1.3292	-1.3292	-1.3292	-1.3292	-1.3292
2	0.471	11.5652	10.7907	2.313	1.2246	0.1151	-0.8896	-1.1618	-1.1618	-1.2873	-1.2455	-1.3292	-1.3083	-1.3292	-1.3292	-1.3292
3	0.1361	10.0371	11.6071	7.4415	4.3644	1.9781	1.8618	-0.3035	-0.3245	-0.8268	-1.1408	-1.1408	-1.3292	-1.2246	-1.2455	-1.3292
4	-0.9734	3.1294	6.3949	7.1485	70438	3.7574	1.1618	-0.3035	-0.3245	-0.8268	-1.1408	-1.1408	-1.2246	-1.2455	-1.3292	-1.3292
5	-1.0571	1.2455	4.2847	6.5414	8.3207	6.7089	3.6109	0.9943	0.3454	-0.1361	-0.9524	-0.785	-1.078	-1.1837	-1.3083	-1.3292
6	-1.2246	0.0733	1.9572	3.255	6.0809	6.353	4.1551	2.2502	1.4339	0.6803	-0.4291	-0.2198	-0.7222	-1.0571	-1.2873	-1.3292
7	-1.2036	-0.764	0.0942	1.5176	2.8364	3.1609	2.5852	1.3711	1.2036	0.2617	-0.3245	-0.0942	-0.5756	-0.9734	-1.2664	-1.3292
8	-1.3083	-1.099	-0.7431	-0.0533	0.9524	1.1618	1.1827	0.6384	0.9315	0.2826	-0.3873	-0.3035	-0.3873	-1.0152	-1.2455	-1.3292
9	-1.3292	-1.1827	-0.8896	-0.4999	0.2826	1.2664	0.8687	0.7645	1.0362	0.8059	-0.0115	-0.0523	0.0105	-0.6594	-1.1827	-1.3292
10	-1.3292	-1.1827	-1.099	-0.8888	-0.157	0.45	0.1361	0.0523	0.5547	0.1151	-0.3873	0.0733	0.1361	-0.6175	-1.2036	-1.3292
11	-1.3292	-1.287	-2.2455	-1.078	-0.4082	-0.5338	-0.471	-0.5756	-0.5966	-0.0305	-0.7222	-0.3454	-0.3245	-0.764	-1.078	-1.3083
12	-1.3292	-1.3292	-1.2246	-1.0123	-0.6384	-0.3245	-0.1899	-0.5966	0.157	-0.1361	-0.2617	0.0345	0.5128	-0.2617	-0.8268	-1.2873
13	-1.3083	-1.2873	-1.618	-1.0343	-0.8098	-0.3454	-0.45	-0.5338	-0.1989	-0.4919	-0.6803	0.6803	0.3665	0.1779	-0.4919	-1.099
14	-1.3292	-1.3083	-1.2873	-1.223	-1.099	-0.8687	-0.9106	-1.078	-0.8686	-0.764	-0.8059	-0.3873	0.0733	0.3035	-0.471	-1.0152
15	-1.3292	-1.3292	-1.2873	-1.3090	-1.2455	-1.1408	-1.1827	-1.2644	-1.1827	-1.1827	-1.1618	0.9943	-0.5128	-0.6384	-0.9524	-1.0362
16	-1.3292	-1.3292	-1.3292	-1.367	-1.3292	-1.2664	-1.3292	-1.2873	-1.3292	-1.3292	-1.3083	-1.2664	-1.0571	-1.1618	-1.078	-1.1618

Table 5-2: Gibbs potentials for the clique family with offset (0,2) for the texture given in Figure 5-16(a)

he GLCH's for clique families in search window are gathered in step 2. The gray level co-ccurrence probabilities are calculated in step 3 (equation 4.25). The interaction energy for very clique family is calculated from the co-occurrence probabilities in step 4 (equation .32). Thresholding of interaction energies to find the significant clique families is done in :ep 5 (equation 4.34). Step 6 calculates the value of lambda_0 (equation 4.33). And finally rst analytic approximations of Gibbs potentials are calculated in step 7 (equation 4.31) hich are output in step 8.

he analytic approximations of Gibbs potentials and selected clique families are input to the ynthesis algorithm along with the value of lambda_0 which synthesizes the texture samples. he pseudo code for synthesis algorithm is as follows (See Appendix E for detailed IATLAB code).

YNTHESIS ALGORITHM FOR MGRF MODELING: -

nput:
) K most characteristic Gibbs potentials Vk gathered from analysis algorithm
) lambda_0
) Gray level co-occurrence probabilities for selected K families of sample image freq_image_k

)utput: synthesized gray-level image g=(g[i,j]: i = 1,...,M; j =1,...,N]) with Q

itochastic Relaxation:

. Initialize output image with equa-probable gray level values

```
or j=1 step 1 until N
        for i=1 step 1 until M
            g[i,j] = random_number (Q);
```

```
nitialize lambda_t = lambda_0;
```

imulated Annealing:

2. Initialize temperature T

3. repeat for sufficient number of macro steps t

3a. select a random trace over the image lattice

```
b.  for each selected random point [i,j] in random trace
        let g' = random_number(Q)
        calculate  delta_E = e(g' | POT(di,dj)) – e(g[i,j] | POT(di,dj))

        if (delta_E >= 0)
            g[i,j] = g';
        else
            accept g' with probability exp(delta_E * T)
    end for
```

pdate Gibbs Potentials for selected K clique families:

```
. Collect Gray level co-occurrence histograms COOC(di,dj) from current sample g[i,j]
    (step 2b of analysis algorithm for selected K clique families only)

. Calculate Gray level co-occurrence probabilities freq(di,dj) from COOC(di,dj) above
    (step 3 of analysis algorithm for selected K clique families only)

. reduce lambda_t

. update Gibbs Potentials
     POT(di,dj)[q,s] = POT(di,dj)[q,s] +lambda_t * (freq(di,dj)[q,s] – freq_image(di,dj)[q,s])

. Reduce temperature T

ntil T approaches zero

. Output g[i,j]

/ where the function random_number(x) in step 1 and 3b generates random number in range [0,x)
/ and the energy function e(g' | POT(di,dj)) in step 3b calculates the interaction energy of a
/ pixel according to the given Gibbs potentials
/ e(g' | POT(di,dj)) =  POT(di,dj) [g', g[i+di, j+dj]] + POT(di,dj) [g[i+di, j+dj], g']
```

---

he algorithm is similar to simulated annealing with Metropolis sampler in Figure 4-5 with a light change in calculation for energy function. In this case the energy is calculated under MGRF model in step 3b. Energy function e(g' | POT(di,dj)) calculates the energy based on given interaction structure and Gibbs potentials. The energy at a given pixel is considered elative to all cliques in the interaction structure and compared with the old energy. The gray evel with higher energy is selected. The temperature T gives the simulated annealing and is educed with every iteration using the schedule given in equation 4.21 for cooling.

he additional step here in this synthesis algorithm is the refining of Gibbs potentials from ıeir initial analytic approximations (equation 4.35). Step 4 and 5 calculate the GLCH and :ay level co-occurrence probabilities from current image respectively. The potentials are ıanged in line with the difference between GLCHs of sample texture and current texture in ep 7. The value of lambda_0 is reduced in step 6. The updated Gibbs potentials are then sed for next iteration. Gradually the potentials are refined to MLE estimates after sufficient umber of iterations and synthesized image is given as output.

.6 Results of Modeling

his section presents modeling results for three sets of input textures. The textures are given s input to the analysis algorithm outlined in section 5.5 above. The algorithm analyzes input :xtures and calculates analytic first approximations of Gibbs potentials which are then input) synthesis algorithm. The synthesized output textures are then rated for high or low visual imilarity with the input textures. Following are figures for modeling results of skin texture amples taken from case studies including both healthy and diseased skin. The results include) the actual 3D mesh model with color texture wrapped for better visualization b) the 3D ıesh model with color information eliminated c) the 2D grayscale texture obtained after pre-rocessing used as input d) the interaction maps gathered during analysis e) the selected lique families after thresholding f) the synthesized textures. The results also include the real imensions of skin sample in millimeters, dimensions of interaction map and the location on atient's body where the samples have been taken from.

.6.1 Skin Textures – Set 1

he input skin textures in set 1 contain all three features of skin. However, it is observed rom these samples that the curvature of underlying body appears as gradual, non-repetitive ;ray level change and overshadows most of the fine scale details. The reason for this is the ıhysical dimensions of body curvature versus those of finer details. The body curvature for he segmented samples tends to be on scale of 1 mm whereas the fine details are on scale of

0.1 mm. Therefore, when scaled down to 16 levels of grayscale, the curvature mostly dominates other features. It can also be seen that interaction maps show patterns which can be related to the curvature patterns in input texture samples and that the synthesized textures do not show visual similarity. These results will be analysed in detail in section 5.7. Figures 5-18 to 5-22 show modeling results for 3 healthy and 2 diseased skin samples for set 1 (See Appendix F for more results of set 1).

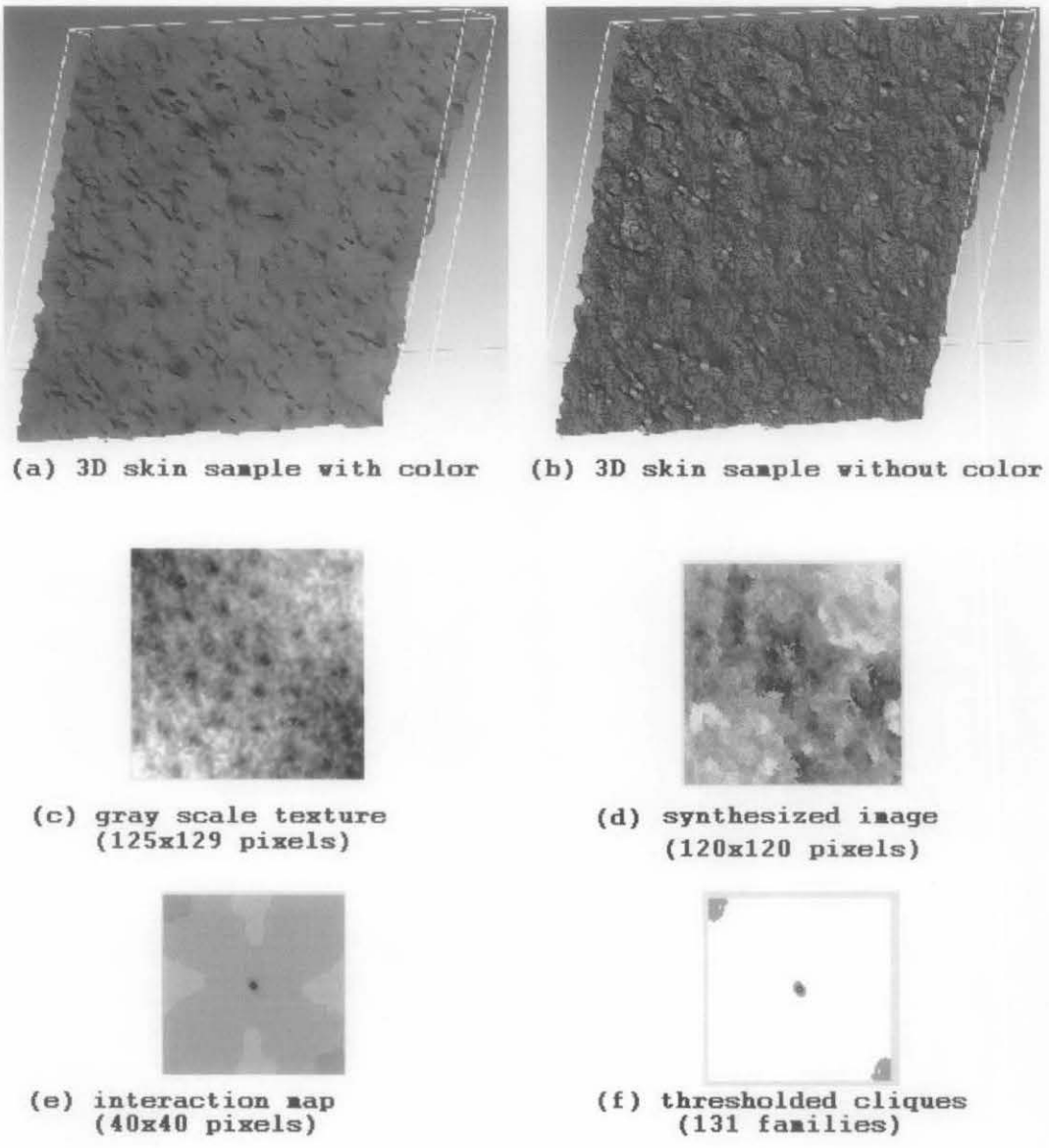

Figure 5-17: Set 1 - Patient 1 – Trunk healthy sample # 1 (24.61mm x 22.56mm x 1.76 mm)

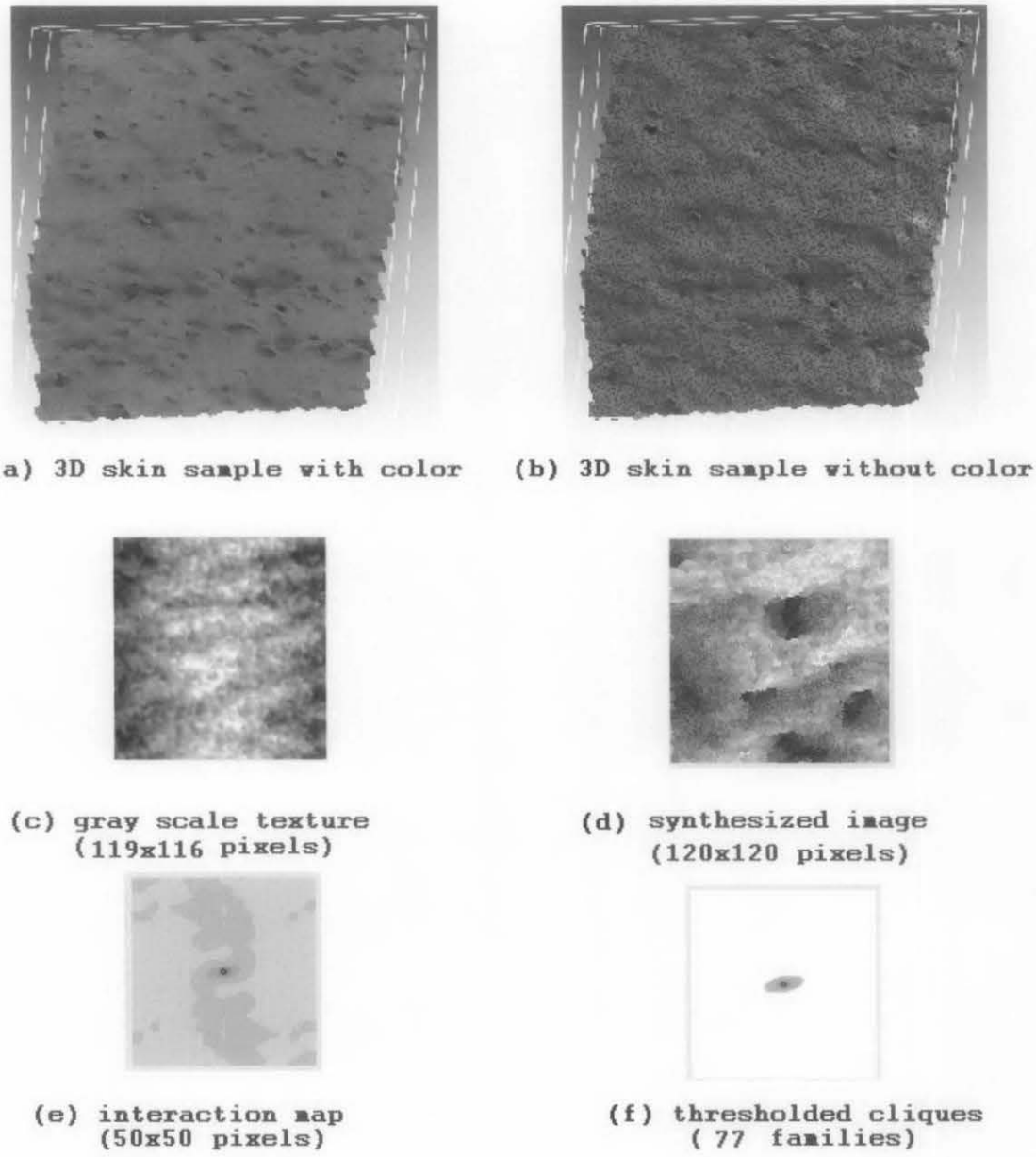

Figure 5-18: Set 1 - Patient 1 – Arm healthy sample # 1 (20.72mm x 20.6mm x 1.26 mm)

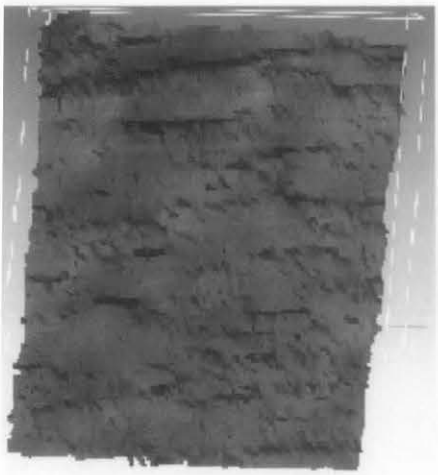

(a) 3D skin sample with color

(b) 3D skin sample without color

(c) gray scale texture
(107x120 pixels)

(d) synthesized image
(120x120 pixels)

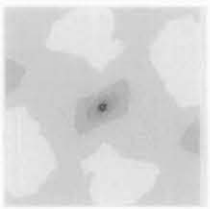

(e) interaction map
(50x50 pixels)

(f) thresholded cliques
(77 families)

Figure 5-19: Set 1 - Patient 1 – Arm diseased sample # 2 (22.01mm x 16.86mm x 2.11mm)

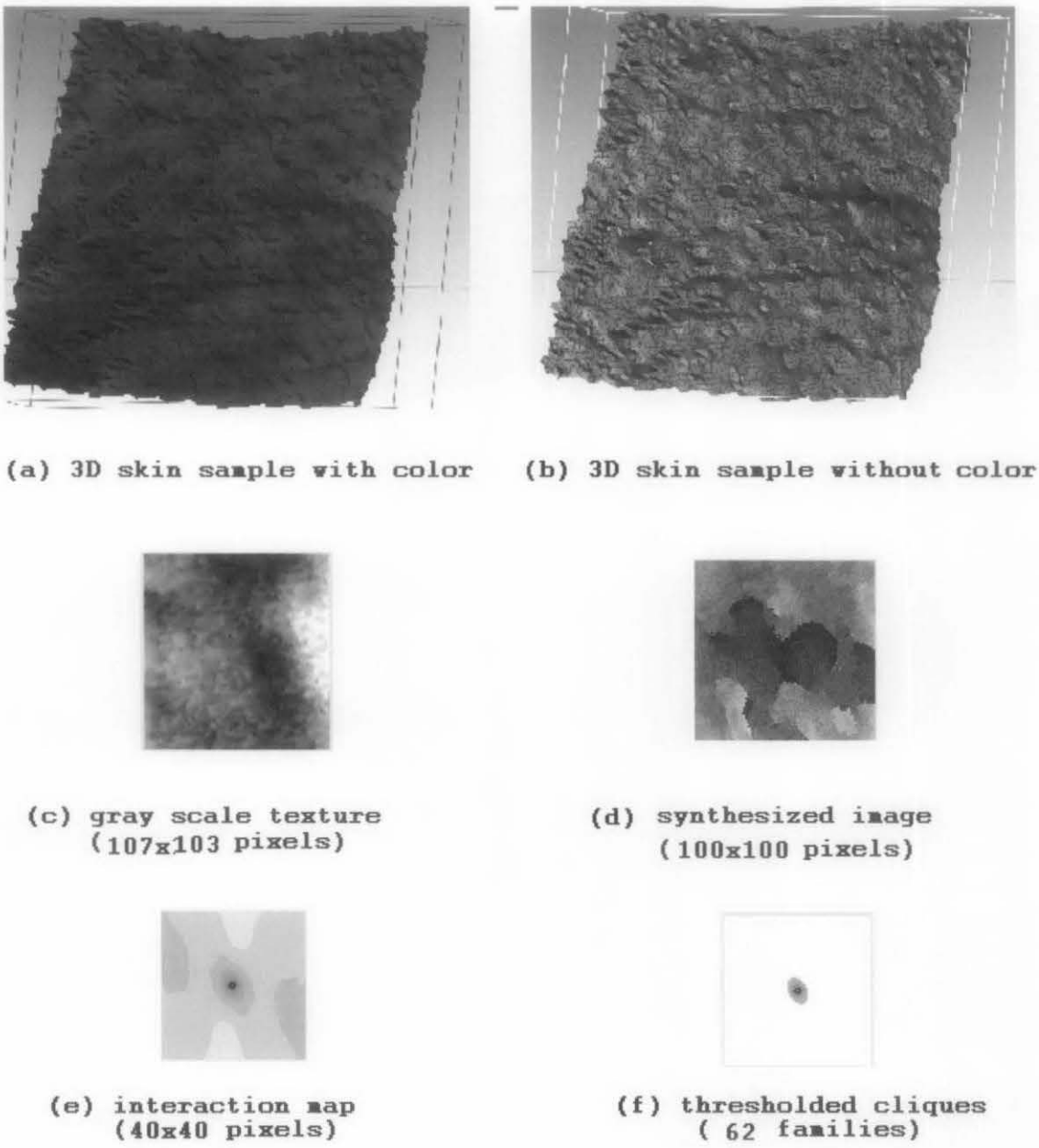

Figure 5-20: Set 1 - Patient 1 – Arm diseased sample # 3 (22.30mm x 17.72mm x 1.08mm)

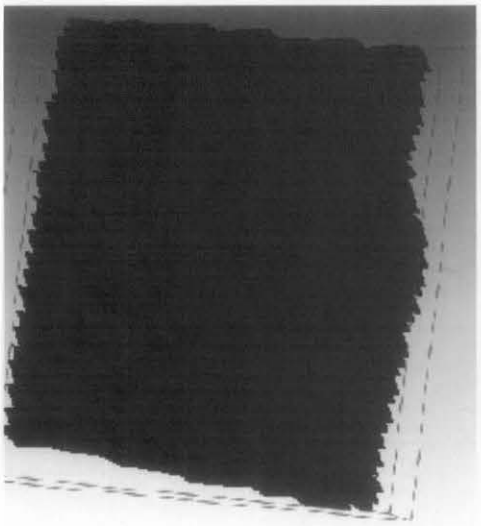

(a) 3D skin sample with color

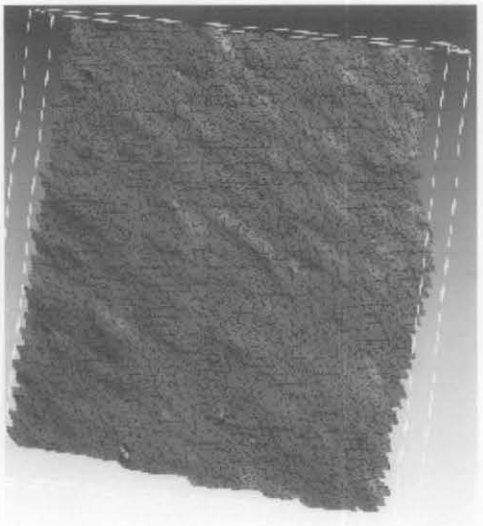

(b) 3D skin sample without color

(c) gray scale texture
(86x91 pixels)

(d) synthesized image
(100x100 pixels)

(e) interaction map
(40x40 pixels)

(f) thresholded cliques
(279 families)

Figure 5-21: Set 1 - Patient 2 - Trunk healthy sample # 2 (18.23mm x 16.39mm x 1.64mm)

5.6.2 Skin Textures – Set 2

For skin textures in set 2 the body curvature has been eliminated. These samples contain wrinkles/lines and fine textures where wrinkles are prominent among the underlying fine texture. The interaction maps for these samples do not show identifiable pattern, as for those of set 1. Secondly, for almost all of them, the high interaction energy is concentrated in short range cliques, as can be seen from darker shades around the center for these maps. For this reason, these centered cliques are included in thresholded families for these samples. When synthesized textures are observed, they show mixed level of visual similarity with the input textures. The wrinkle/line-like features are totally lost (or filtered) in synthesized textures for these samples. The reasons behind this varying response of modeling will be discussed in detail under analysis in section 5.7. Figures 5-23 to 5-30 show modeling results for 1 healthy and 7 diseased skin samples for set 2 (See Appendix G for more results of set 2). The types of wrinkle/line like features present in skin sample (partially present/completely present) and the level of visual similarity (Low/Medium) have also been mentioned in figures.

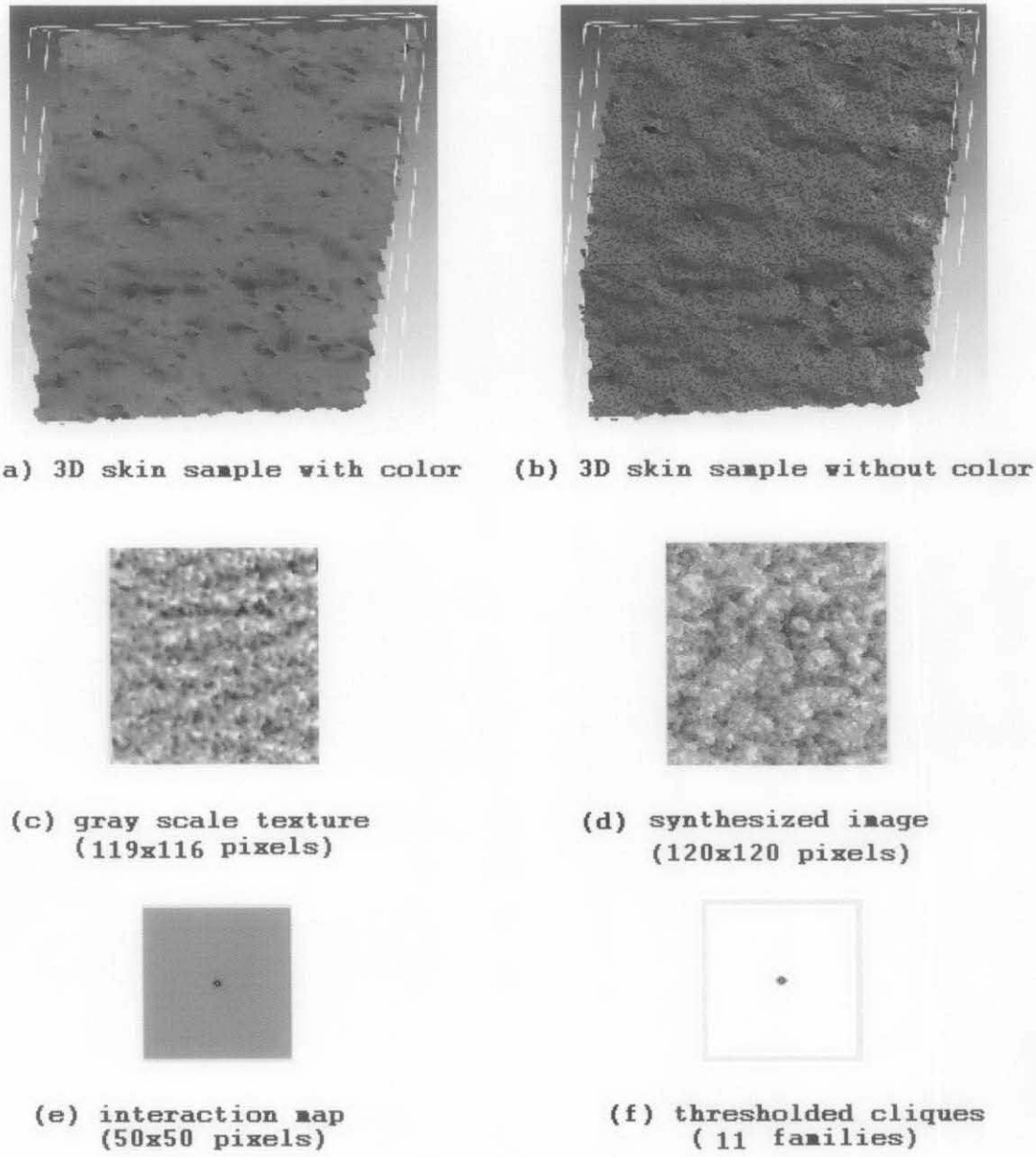

Figure 5-22: Set 2 – Patient 1 – Arm healthy sample # 3 (24.61mm x 22.56mm x 1.76 mm)
Wrinkles are present throughout image but spatially variant – Low visual similarity

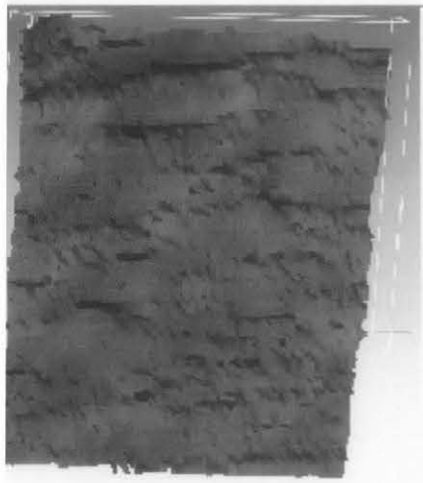

a) 3D skin sample with color

(b) 3D skin sample without color

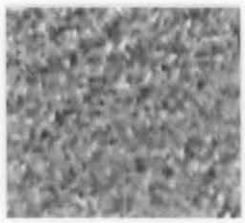

(c) gray scale texture
(107x120 pixels)

(d) synthesized image
(120x120 pixels)

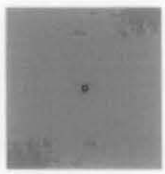

(e) interaction map
(50x50 pixels)

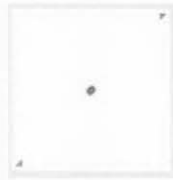

(f) thresholded cliques
(14 families)

Figure 5-23: Set 2 – Patient 1 – Arm diseased sample # 2 (22.01mm x 16.862mm x 2.11mm)
Wrinkles are present partially in image – Low visual similarity

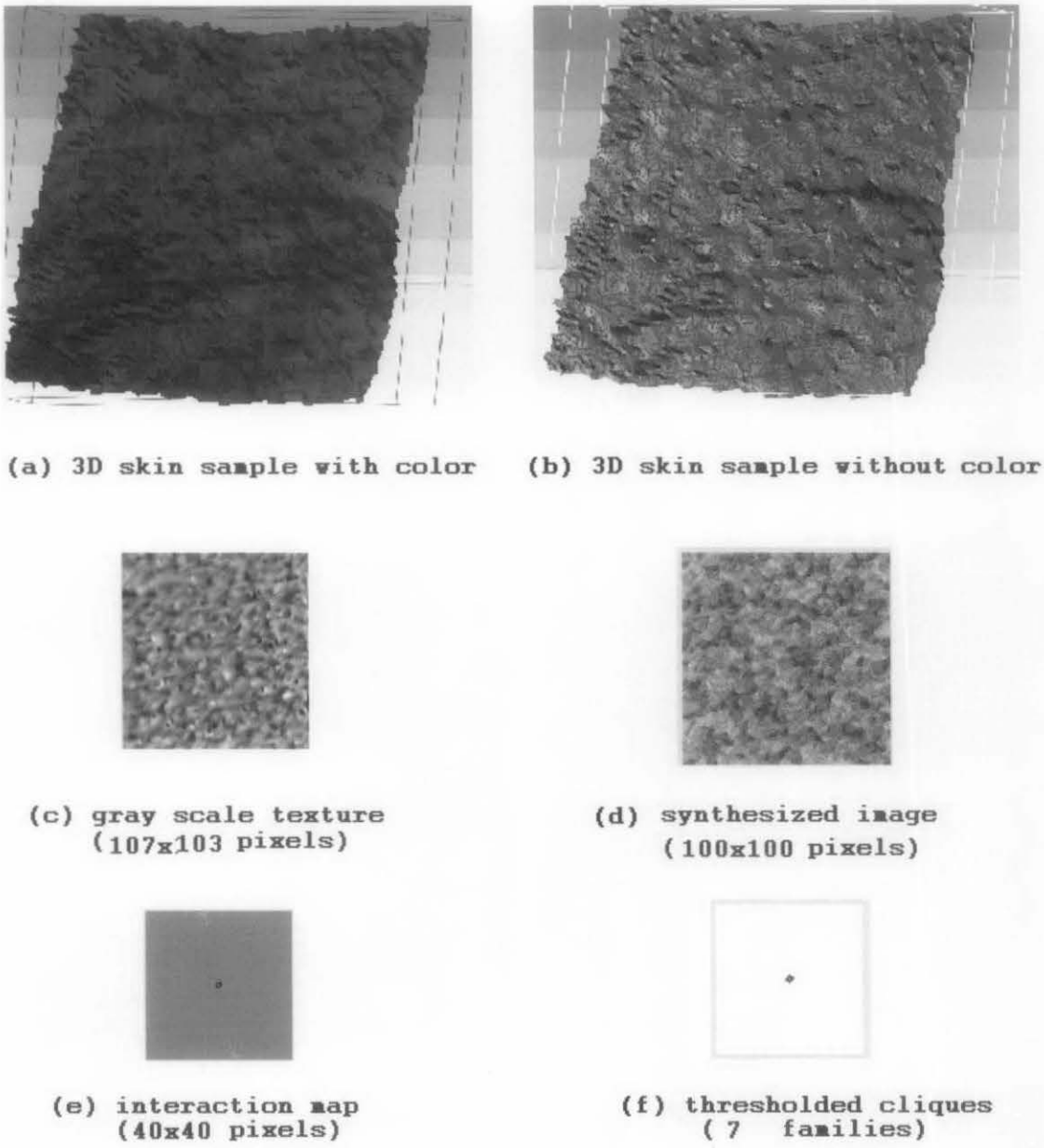

Figure 5-24: Set 2 – Patient 1 – Arm diseased sample # 1 (22.30mm x 17.72mm x 1.08mm)
Wrinkles are present throughout image but spatially variant – Low visual similarity

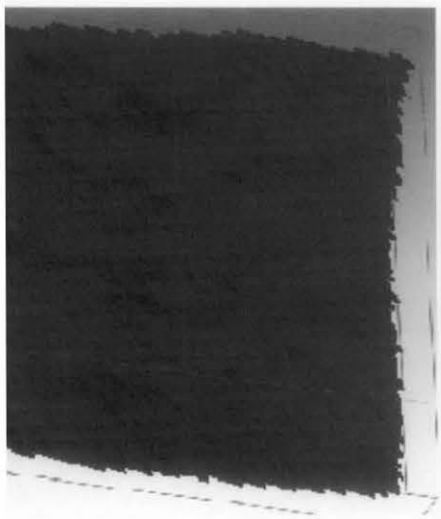

a) 3D skin sample with color

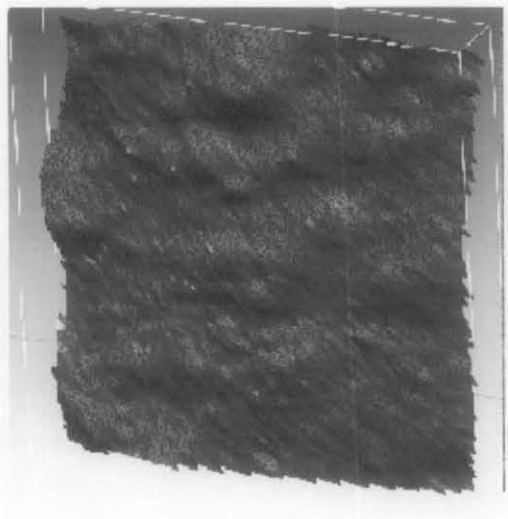

(b) 3D skin sample without color

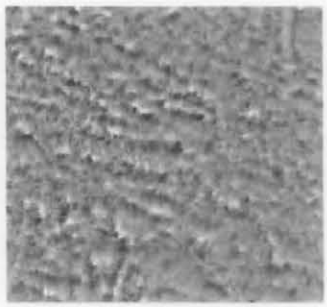

(c) gray scale texture
(195x196 pixels)

(d) synthesized image
(120x120 pixels)

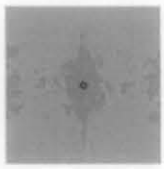

(e) interaction map
(40x40 pixels)

(f) thresholded cliques
(14 families)

Figure 5-25: Set 2 – Patient 2 – Arm diseased sample # 2 (22.89mm x 20.75mm x 3.49mm)
Wrinkles are present partially in image – Low visual similarity

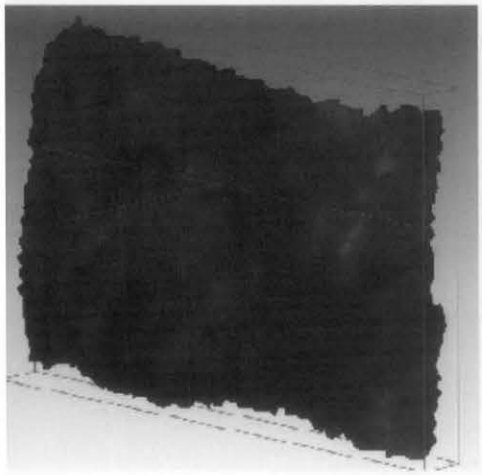

a) 3D skin sample with color

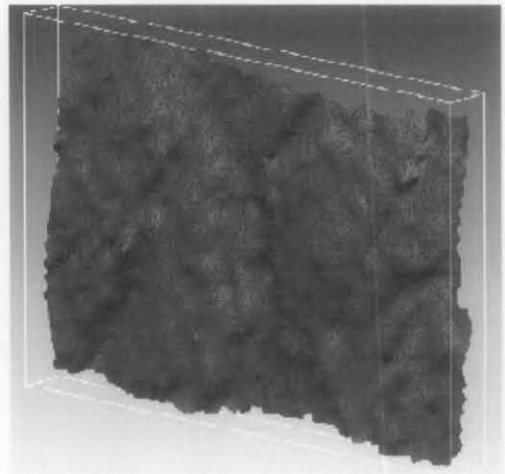

(b) 3D skin sample without color

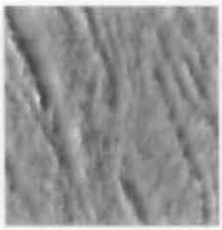

(c) gray scale texture
(120x120 pixels)

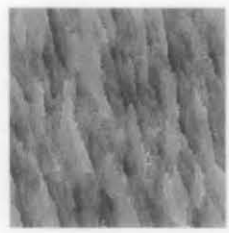

(d) synthesized image
(120x120 pixels)

(e) interaction map
(40x40 pixels)

(f) thresholded cliques
(28 families)

Figure 5-26: Set 2 – Patient 4 - Leg diseased sample # 2 (20.53mm x 15.07mm x 1.77mm)
Wrinkles are present throughout image and spatially invariant – Medium visual similarity

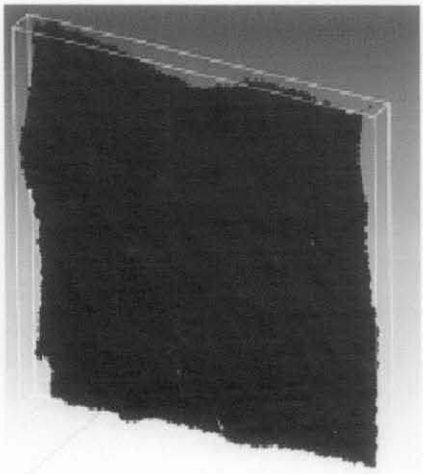

(a) 3D skin sample with color

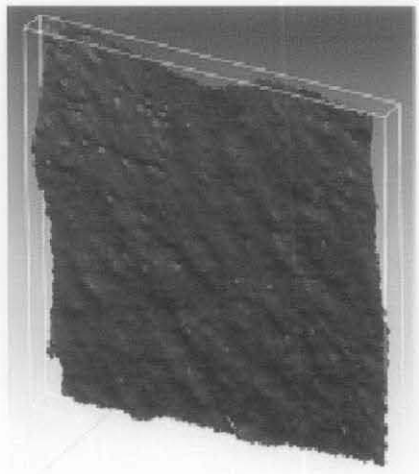

(b) 3D skin sample without color

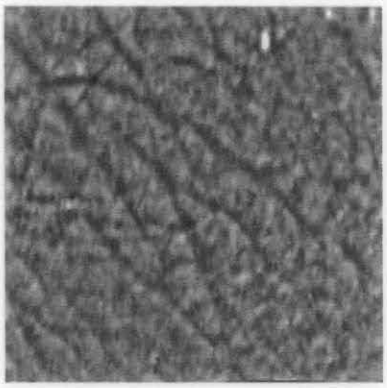

(c) gray scale texture
(201x206 pixels)

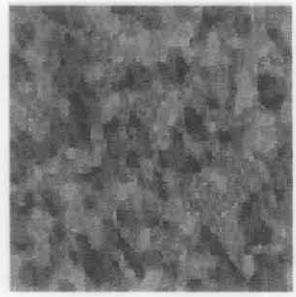

(d) synthesized image
(120x120 pixels)

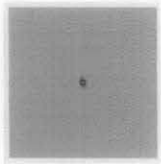

(e) interaction map
(40x40 pixels)

(f) thresholded cliques
(26 families)

Figure 5-27: Set 2 – Patient 3 - Arm diseased sample # 1 (23.95mm x 16.56mm x 3.15mm)
Lines are present throughout image but spatially variant – Low visual similarity

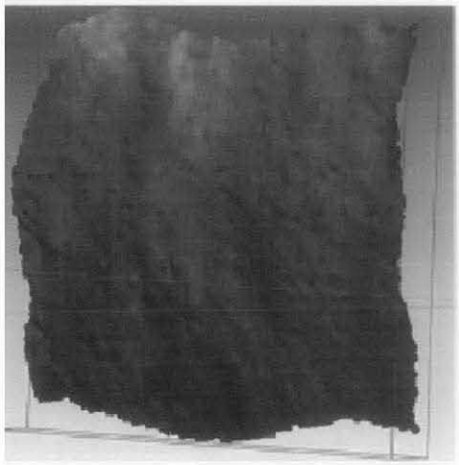

a) 3D skin sample with color

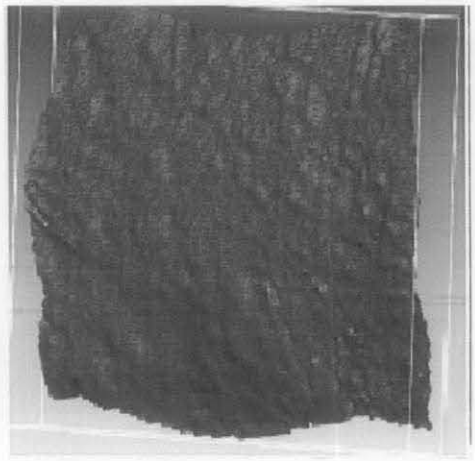

(b) 3D skin sample without color

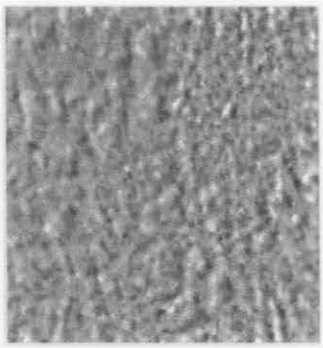

(c) gray scale texture
(190x180 pixels)

(d) synthesized image
(120x120 pixels)

(e) interaction map
(40x40 pixels)

(f) thresholded cliques
(9 families)

Figure 5-28: Set 2 – Patient 4 - Arm diseased sample # 1 (23.76mm x 20.45mm x 2.83mm)
Lines are present throughout image but spatially variant – Low visual similarity

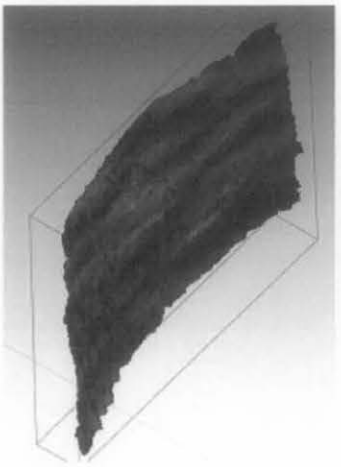

(a) 3D skin sample with color

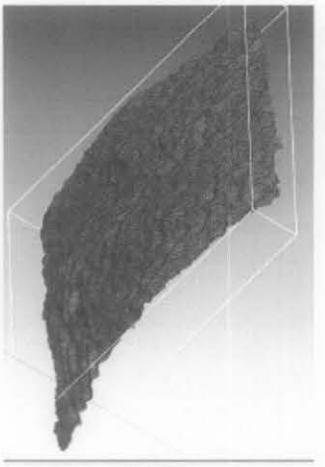

(b) 3D skin sample without color

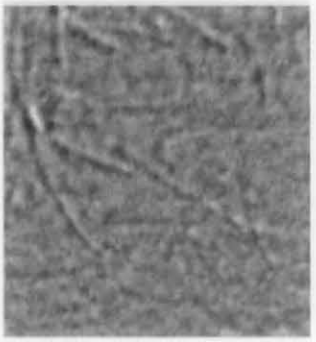

(c) gray scale texture
(183x173 pixels)

(d) synthesized image
(120x120 pixels)

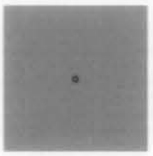

(e) interaction map
(40x40 pixels)

(f) thresholded cliques
(26 families)

Figure 5-29: Set 2 – Patient 4 - Arm diseased sample # 2 (20.09mm x 17.32mm x 2.91mm)
Lines are present partially in image – Low visual similarity

.6.3 Skin Textures – Set 3

ɔr skin textures in set 2 the body curvature has been eliminated and in contrast with set 2, ese samples contain only fine texture. However, it can be observed from the following sults that these textures, though very minute in scale (~0.1 mm) present significant ıriation in their patterns. As it has been indicated before, this is owing to the fact that the ıe textures, though homogeneous locally, vary a lot from one portion of body to another. gain the interaction energy for these samples is concentrated around centered cliques which ıve been thresholded. As the results illustrate, the synthesized textures for these samples ostly show high visual similarity with the original ones. Figures 5-31 to 5-35 show odeling results for 2 healthy and 3 diseased skin samples for set 3 (See Appendix H for ore results of set 3). The level of visual similarity (Medium/High) has also been mentioned figures.

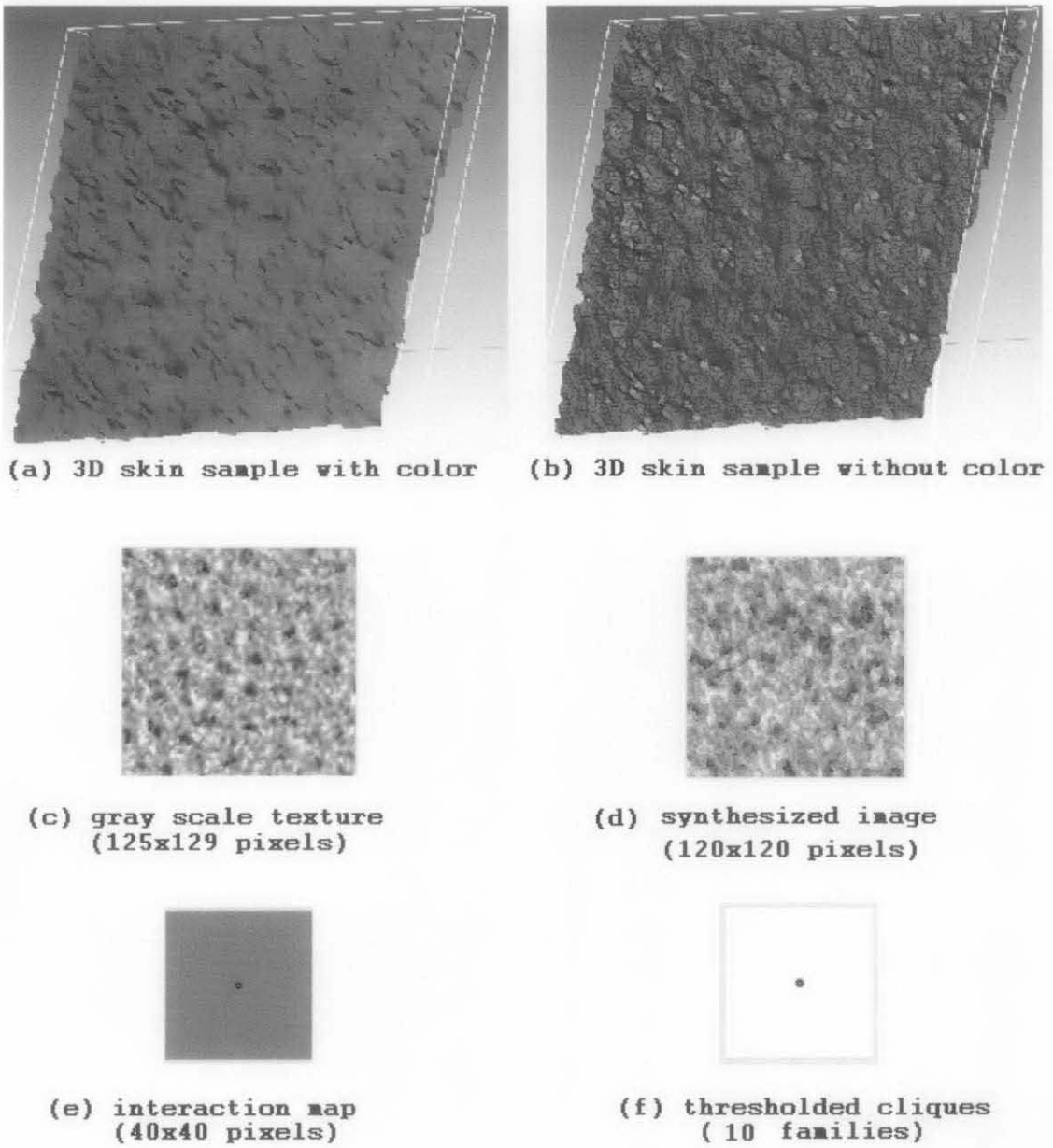

Figure 5-30: Set 3 – Patient 1 – Trunk healthy sample # 3 (24.61mm x 22.56mm x 1.76mm)
Medium visual similarity

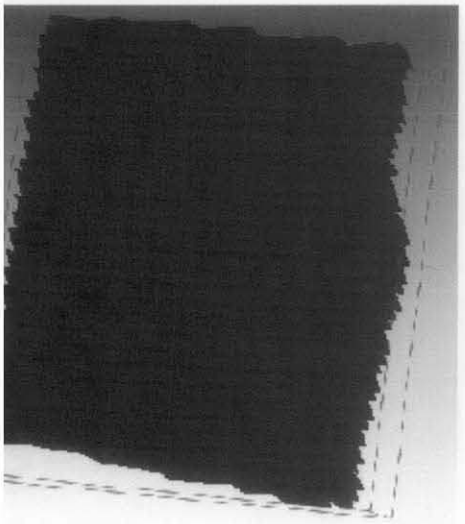

a) 3D skin sample with color

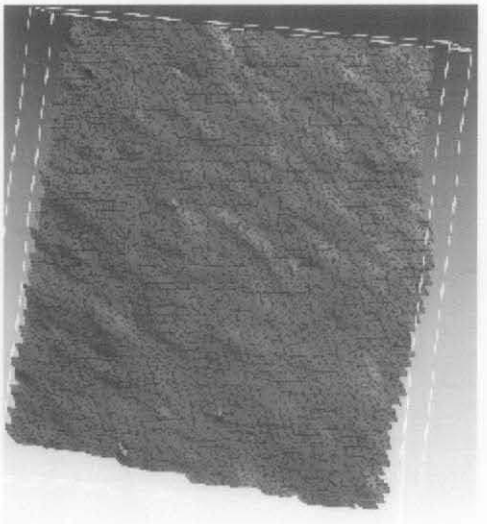

(b) 3D skin sample without color

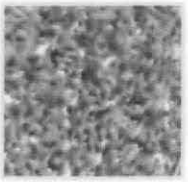

(c) gray scale texture
(86x91 pixels)

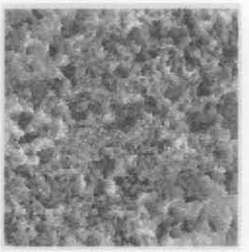

(d) synthesized image
(120x120 pixels)

(e) interaction map
(40x40 pixels)

(f) thresholded cliques
(77 families)

Figure 5-31: Set 3 – Patient 2 – Trunk healthy sample # 2 (18.23mm x 16.39mm x 1.64mm)
High visual similarity

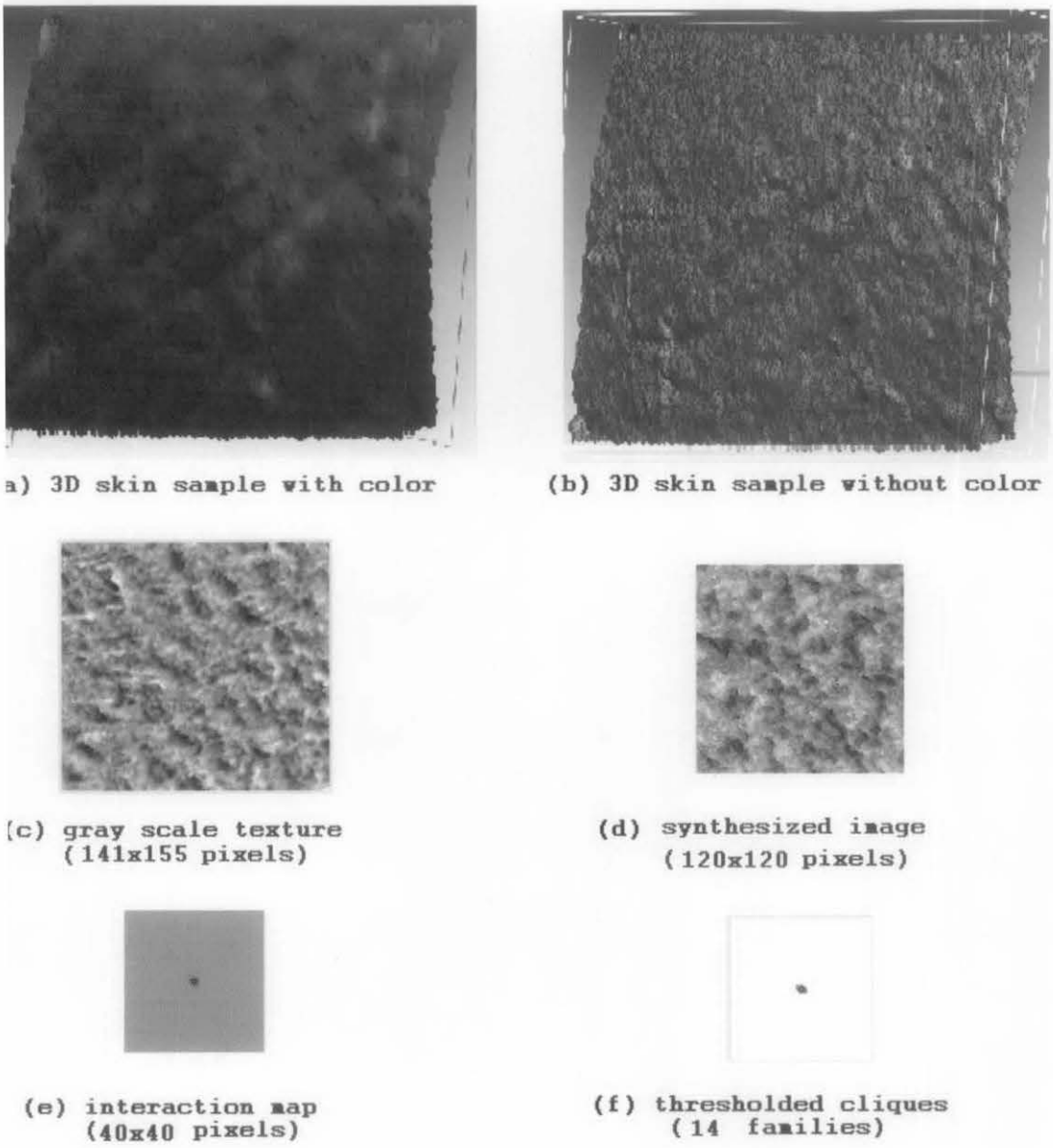

Figure 5-32: Set 3 – Patient 3 - Leg diseased sample # 1 (22.01mm x 22.78mm x 1.3mm)
High visual similarity

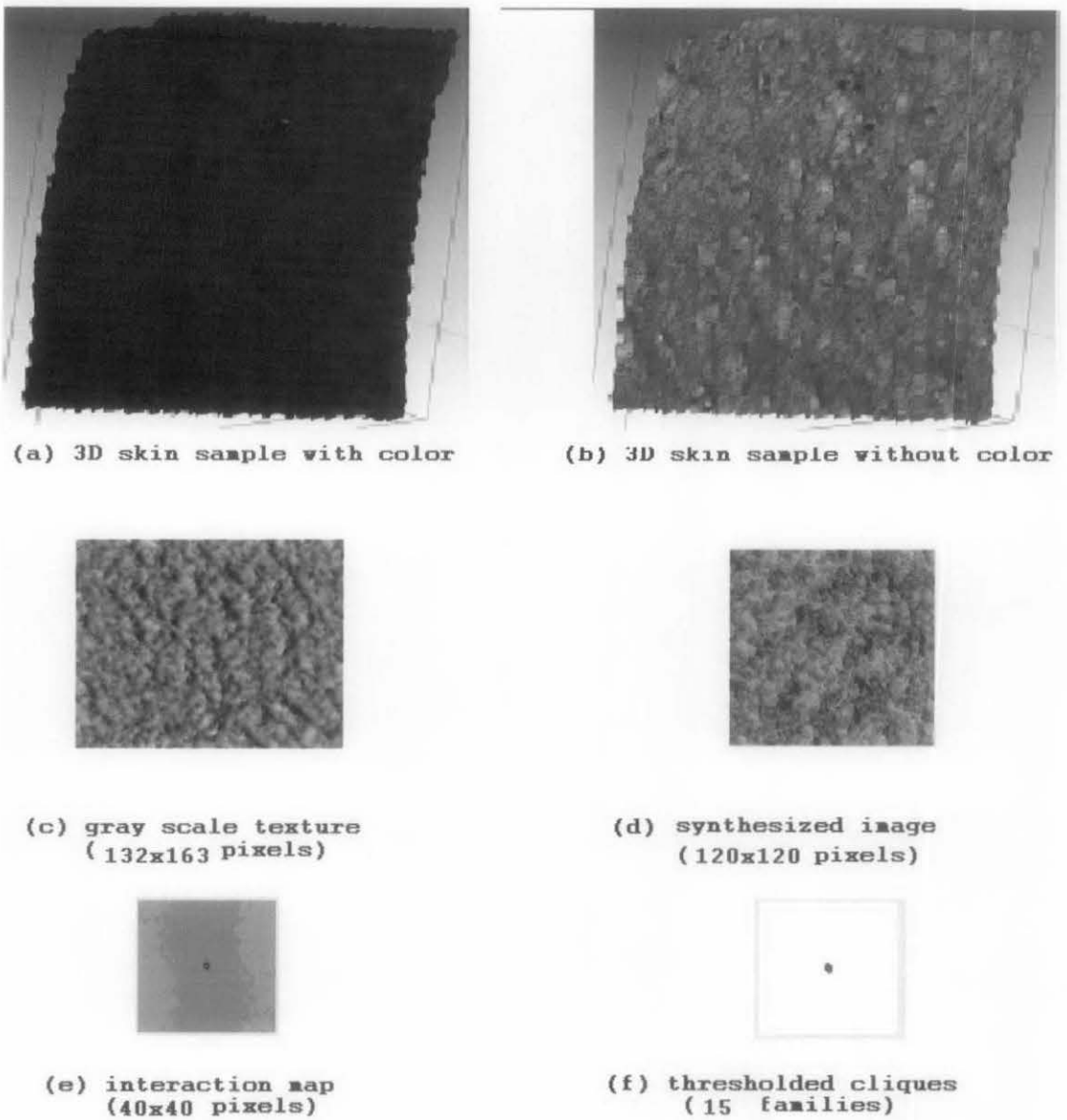

Figure 5-33: Set 3 – Patient 4 – Leg diseased sample # 2 (31.57mm x 30.8mm x 3.03mm) Medium visual similarity

a) 3D skin sample with color

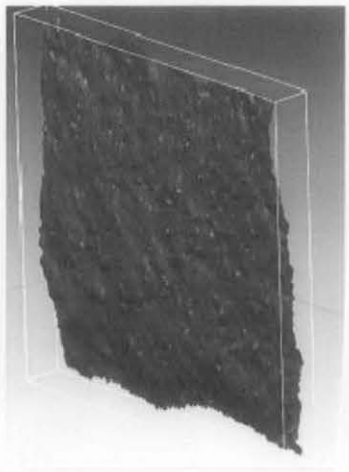

(b) 3D skin sample without color

(c) gray scale texture
(158x98 pixels)

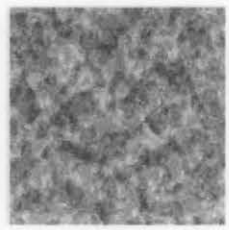

(d) synthesized image
(120x120 pixels)

(e) interaction map
(40x40 pixels)

(f) thresholded cliques
(10 families)

Figure 5-34: Set 3 – Patient 5 – Leg diseased sample # 1 (26.85mm x 25.83mm x 2.89mm)
High visual similarity

.7 Analysis of Results

previous section, the modeling results for a wide range of skin texture samples were esented. The results show high to low visual similarities for the three input sets. In this ction a detailed analysis of these results will be presented.

s discussed in Chapter 4 (section 4.4.1), the MGRF model works for the homogenous xtures where pairwise pixel interactions remain constant throughout the image. The finitions of homogeneous and inhomogeneous textures are given by Gimel *et al* [Gimel 99]. Both texture types represent repetitive grayscale patterns. However, for homogeneous textures, the overall gray level for patterns changes throughout image. These tterns can be regular (made from texels) or natural (without regular texels). Figure 5-36 ows examples of both types of textures. The model has been tested on these regular and tural textures and results in high visual similarity for homogeneous regular and natural xtures [Gimel 1999]. Skin also poses natural textures and has been modeled by MGRF odeling.

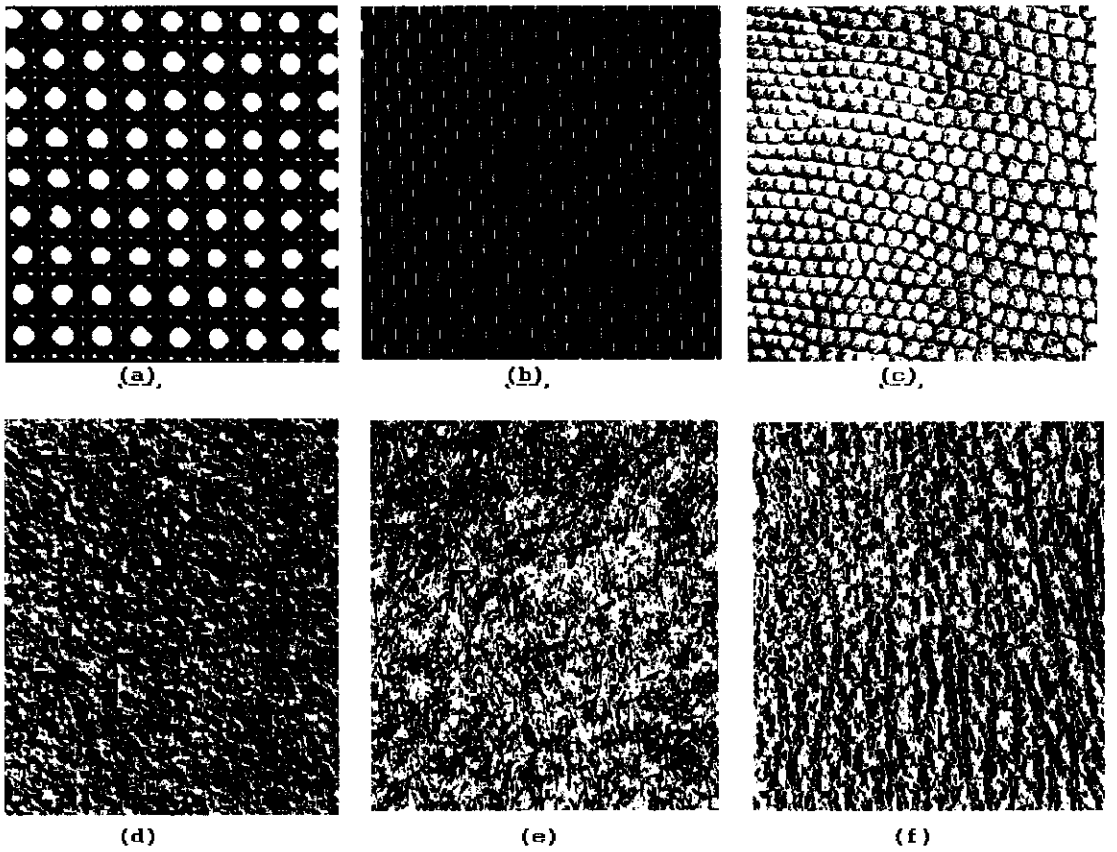

Figure 5-35: Homogeneous Textures – (a)-(c) Regular Textures (made from texels) (d)-(f) Natural Textures

ased on the analysis of modeling results, skin features (and resulting textures) are ıaracterized as homogenous/inhomogeneous following the example by Gimel *et al* [Gimel)99]. The successfully modeled homogeneous textures are identified from set of natural xtures and named as 'stochastic' textures. For example Figure 5-37 shows two classes of ıtural textures, the textures which are homogeneous and modeled with high visual similarity e classified as 'stochastic textures', and the textures which result in limited visual similarity ıly.

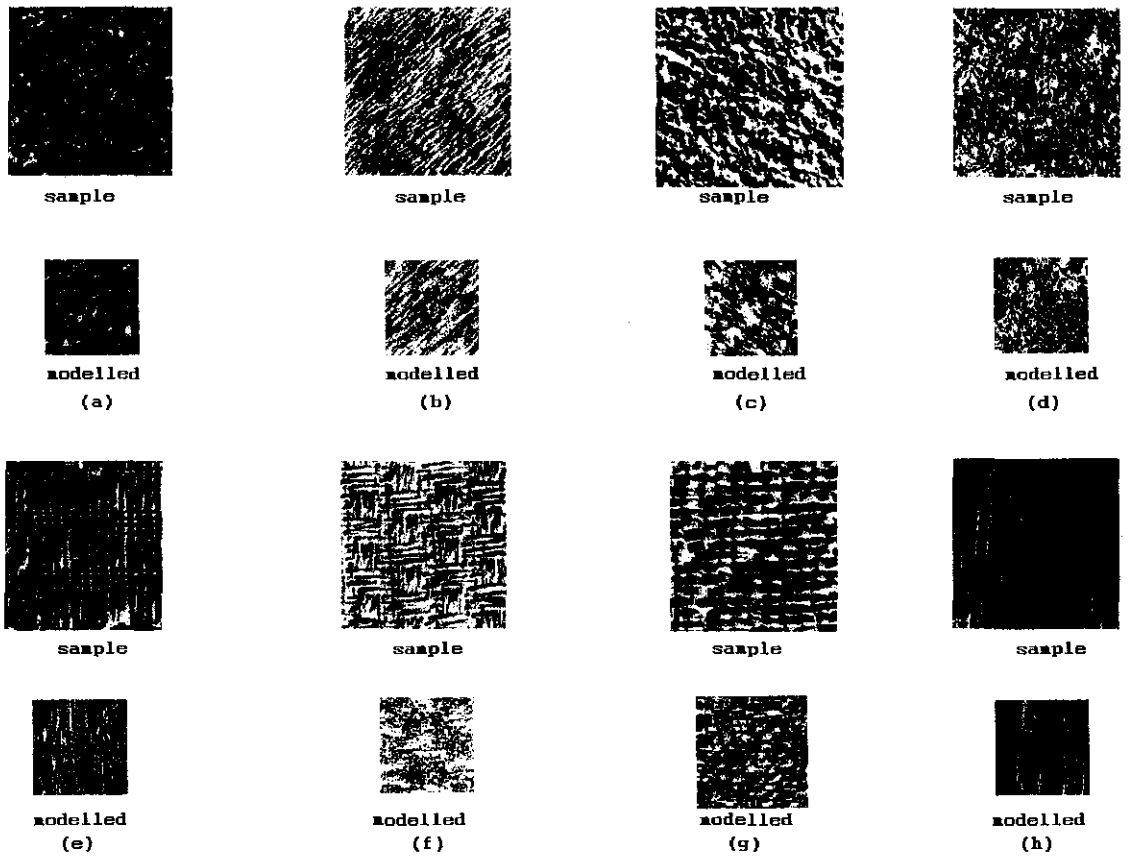

Figure 5-36: Natural textures – (a)–(d) Stochastic textures modeled successfully (e)-(h) non-stochastic textures modeled with limited visual similarity

he model's response to skin textures can be explained on the basis of gray level co-
currences for clique families in sample images. The collection of GLCHs is critical from
hich the conditional probabilities of gray level co-occurrences, first approximations of
ibbs potentials, and interaction energies for clique families in the search window are
rived. The model is successful for homogenous textures because of the spatially invariance
f characteristic pixel interactions. The gray level co-occurrences for these interactions
main similar throughout sample image and hence appear as clique families with high
nergies in interaction map. As a result, when these clique families are thresholded, most of
ıe pattern present in sample image is maintained and textures with high visual similarity are
produced. Following this reasoning it can be concluded that the two factors are essential for
ıccessful modeling a) the gray level co-occurrences remain almost constant for a clique
mily to represent a characteristic interaction in texture b) the family possesses high

teraction energy so that it is thresholded and contribute in the synthesis process. The alysis of results is based on these important observations about the MGRF model.

:t 1: The analysis of results for set 1 is the most complicated. It is a failure scenario with most non-existent visual similarity between training and synthesized textures. However, it ves comprehensive insight of the working of model and the structure of 3D skin features. ıe textures in set 1 present the most realistic picture of 3D skin height profiles for the ason that all 3D skin features (curvature, wrinkles/lines and fine texture) are present. For me samples the curvature dominates other features completely whereas for the rest other atures are visible but overshadowed by curvature. For example Figure 5-38 below shows e grayscale textures for the sample skin sample with and without curvature. It can be seen Figure 5-38(a) that the curvature dominates completely the underlying wrinkle/fine texture hich are observed only after curvature elimination in texture Figure 5-38(b). However in gure 5-38(c) the underlying features are not dominated by the curvature and can be)served easily.

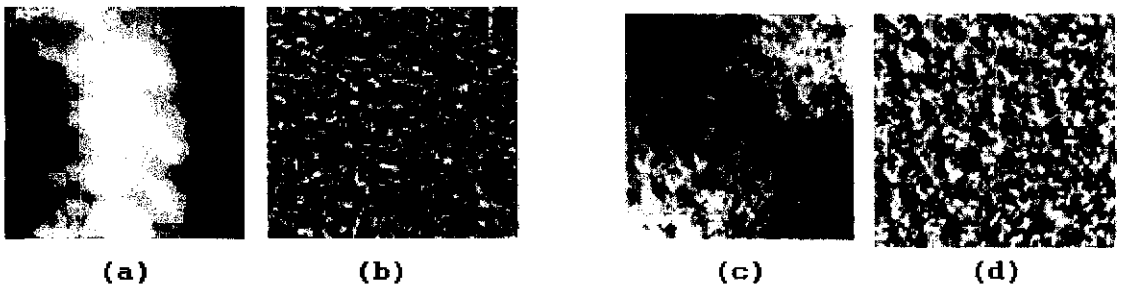

Figure 5-37: (a)-(b) Curvature dominates wrinkles/fine texture (c)-(d) Curvature is only partially overshadowing wrinkles/fine texture

)r MGRF, only the pixel interactions with consistent gray level co-occurrences among petitions throughout image appear as characteristic clique family in interaction map. The :in samples in set 1 present two types of repetitive 3D skin features i.e. wrinkles with less ımber of repetitions and more frequent fine texture. But the pattern in fine texture cannot be entified in grayscale texture because it is overshadowed by wrinkles and curvature. The ıttern in wrinkles is identifiable but its grayscale level varies across the image because of .e curvature. The human eye can easily perceive the curvature and the gradual changes in

rinkle pattern because of the curvature. However, for MGRF model, the curvature appears spatially variant gray level co-occurrences creating an inhomogeneity in the image.

ıe corresponding interaction maps can be observed to have somewhat visual resemblance to e skin texture samples demonstrating that the MGRF model indeed captures the pixel teractions for 3D features during analysis but these interactions do not end in high visual milarity during synthesis. The reason lies in the gathered GLCH for every clique family hich record the gray level co-occurrences. Although the gray level co-occurrences for these ique families deviate from those of Independent Random Field (equation 4.32) and result in gh interaction energy in map, these vary drastically within same clique family. The result is at their GLCHs are averaged out during synthesis and do not present any characteristic ıttern. Figures 5-39 and 5-40 explain this with two examples. The interactions for edium/long range wrinkle/lines and for short range fine textures are marked in ırresponding interaction maps. It can be seen that these repetitive patterns appear in map as ique families of high interaction energy but the gray levels vary for same clique family and ɔnce fail to pose any significant gray level interaction for that family.

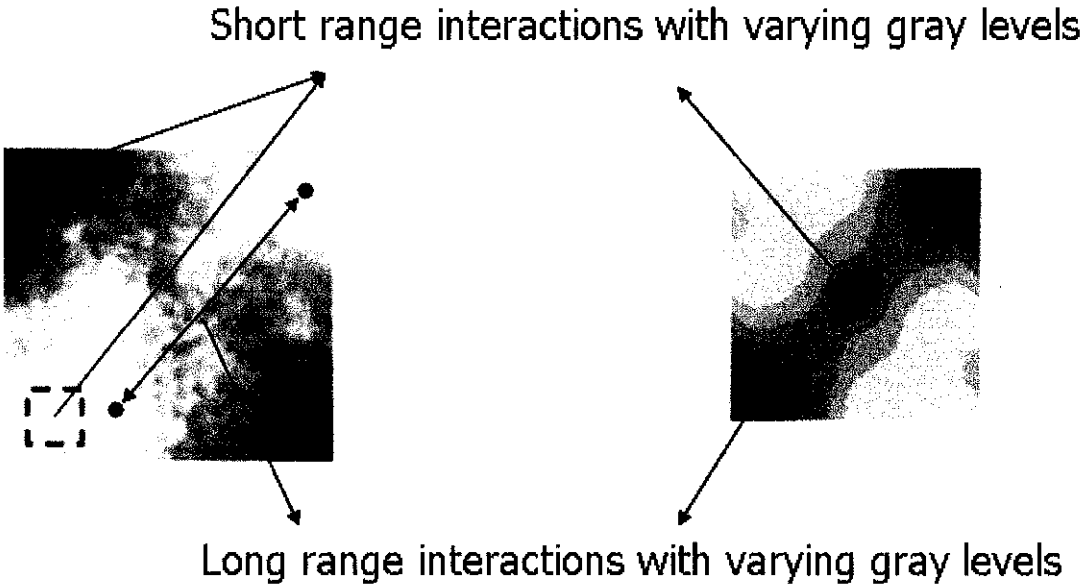

Figure 5-38: The multi range pixel interactions for a sample texture from set 1

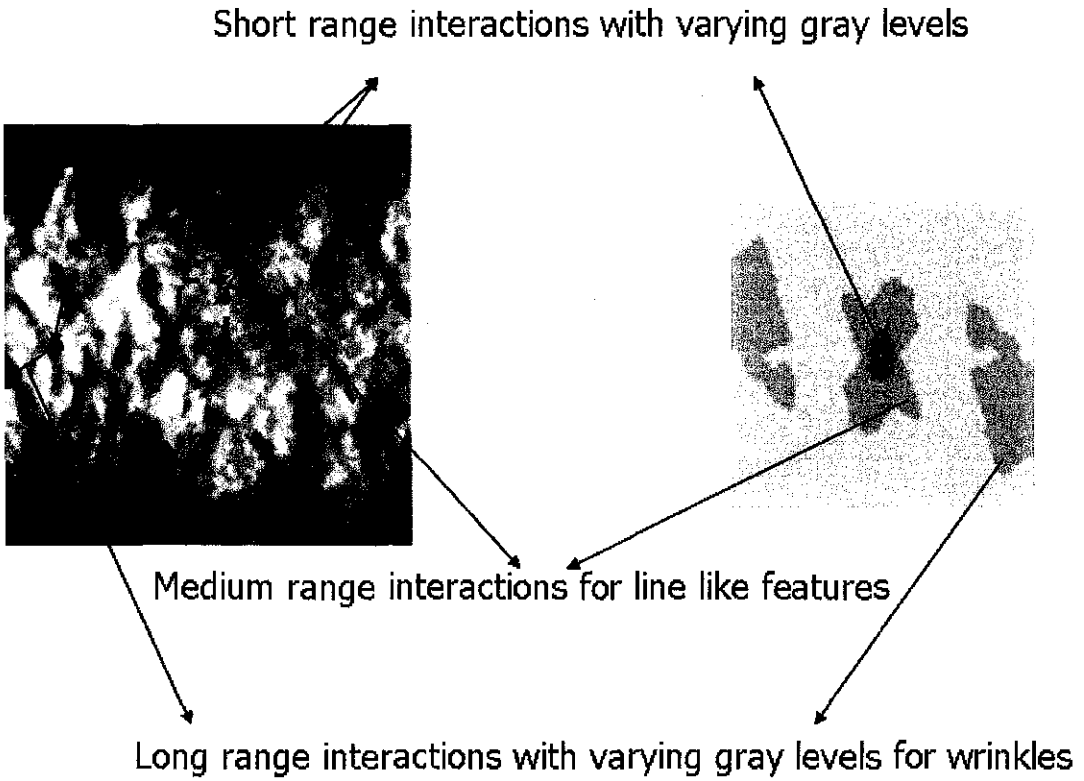

Figure 5-39: The multi range pixel interactions for a sample texture from set 1

ıe further validation of this reasoning is provided by including more clique families for nthesizing textures. The inclusion of more clique families is supposed to improve the nthesized pattern by providing more information about pixel interactions in sample image. ır set 1, even the inclusion of more clique families does not improve the visual similarity. ıis observation proves the inconsistency of gray level co-occurrences for these clique milies which fails to capture any significant pattern. Figure 5-41 shows the results for the me texture sample with 253 and 577 clique families. It can be observed that the visual nilarity does not improve by including more clique families.

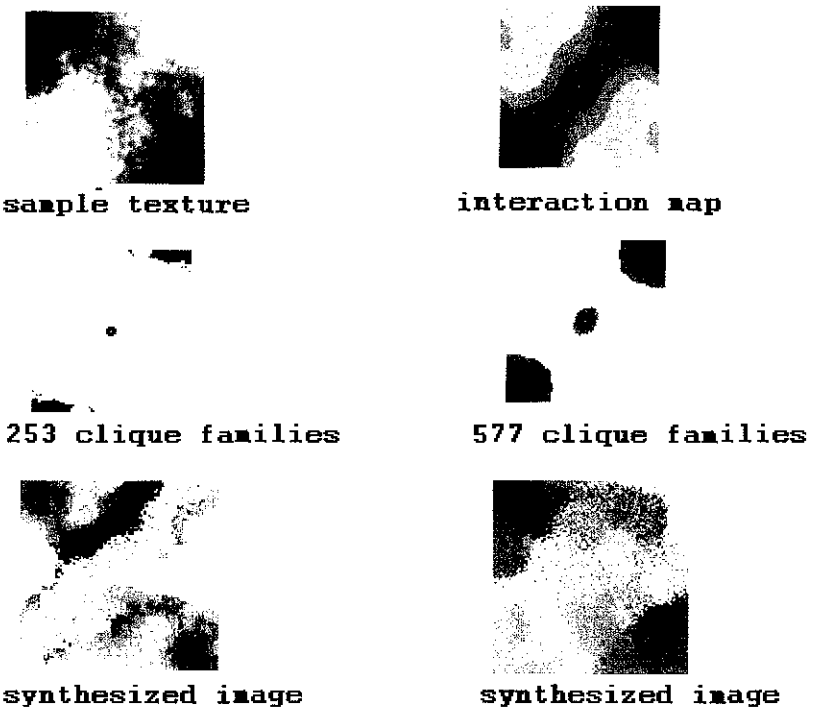

Figure 5-40: Synthesis with different number of clique families (visual similarity is not improved)

om this analysis it is concluded that the curvature creates a noticeable visual homogeneity in skin samples and cannot be modeled successfully. So it would be teresting to eliminate curvature and observe the model's response to other features. :cordingly, the samples in set 2 and set 3 are modeled without any curvature present. The alysis of MGRF modeling for set 2 follows.

t 2: The second set is obtained by eliminating curvature through pre-processing of set 1 d the underlying line-like or wrinkle-like features (along with fine texture) become parent. The modeling results for set 2 presented in section 5.6 show mixed results with gh and low visual similarity. Again, the results can be explained on the basis of spatial riance of pixel interactions in sample images.

ıe interaction maps for set 2 show the short range interactions only and the long-range :eractions appearing due to curvature are mostly eliminated. As it was shown in figure 5- , the line-like features cause short to medium range interactions only. These short-range que families are thresholded and contribute to the synthesis. However, most of the results

set 2 show poor visual similarity (Section 5.6). The reason lies in the pattern of rinkles/lines affecting the overall synthesis. The pattern of wrinkles/lines can be roughly tegorized into three types i.e. partially present in the image (Figure 5-42a,b), covering the hole image but spatially variant (Figure 5-42c,d), covering the whole image and spatially variant (Figure 5-42e). Figure 5-42 shows the examples for three types and their synthesis sults. For first two types, the gray level co-occurrences for wrinkles and lines do not remain nstant throughout the image and the averaging out in GLCHs results in the loss of pattern. ence, in synthesized samples somewhat spatially invariant short-range texture patterns tochastic) appear but wrinkles/lines are completely filtered. For the third type (5-42e) the ttern is present in complete image and is almost spatially invariant. The corresponding ort-range clique families are well able to maintain the pattern which appears visibly in nthesized texture (Figure 5-42e).

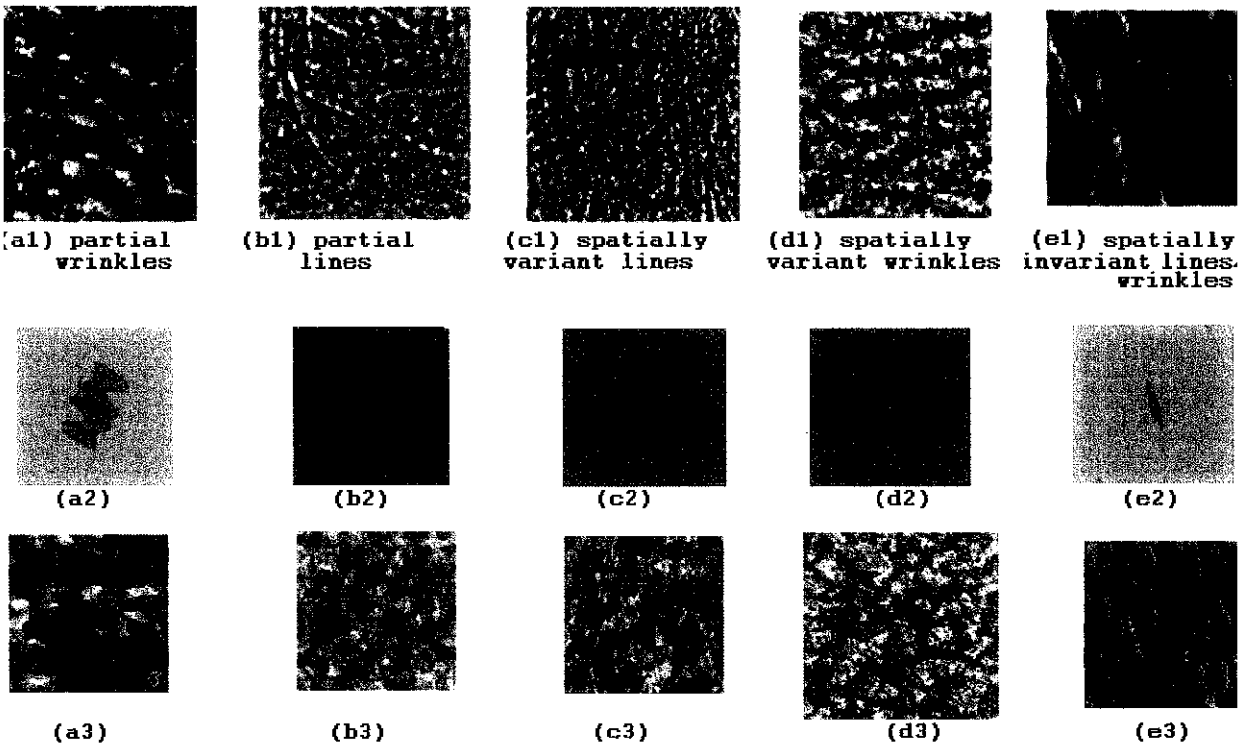

Figure 5-41: Three types of patterns in set 3 for wrinkle/line like features & their modeling results – (a) Texture with wrinkles present partially (b) Texture with lines present partially (c) Texture with spatially variant lines (d) Texture with spatially variant wrinkles (e) Texture with spatially invariant wrinkles/lines

can be concluded from above analysis that MGRF model is able to reproduce the inkles/line like features of skin (both healthy and diseased) provided that their pattern mains spatially invariant. However, as the results show, these features of skin are more ten inhomogeneous and are filtered during the synthesis.

t 3: The set 3 is obtained after elimination of curvature and consists of patterns due to fine cture of skin only. The wrinkles and lines are excluded completely to see the MGRF odel's response to fine texture. These are small scale patterns homogeneous locally but rying for different parts of the body. As these samples range around the size of 1.8x1.8 cm, ese patterns remain almost the same throughout the corresponding sample images with ongly invariant gray level co-occurrences. The exceptions occur when the fine texture is dly distorted due to wrinkle/lines/diseased surface irregularities. It can be anticipated that e model should be able to reproduce these fine textures with high visual similarity.

ie interaction maps for set 3 show the short-range blob-like pixel interactions near center. ie long range interactions of curvature or the medium range interactions due to inkles/lines are absent. Since fine texture remains almost the same throughout sample iage, the gray level co-occurrences of pixel interactions remain spatially invariant. ierefore, the pattern in sample image is well preserved in GLCHs for clique families and e thresholded clique families result in synthesis of textures with high visual similarity.

ie consistency in GLCHs and the consequent visual similarity can be further verified by obing into the modeling results for set 3. The synthesized images for set 3 in section 5.6 ow that the sample images strongly invariant pattern result in high visual similarity iereas the others with some overall local variance of pattern result in medium visual nilarity only. Figure 5-43 shows examples of texture samples resulting in medium and high sual similarity. However, the modeling results in overall high visual similarity for set 3 and can be concluded that fine textures of skin make a spatially invariant, homogeneous 3D ature.

ıe interaction maps for set 3 (Figure 5-43b) show high interaction energies around centre d hence centered clique families are thresholded only to contribute to synthesis. The ımber of these clique families ranges around 20. These interaction structures demonstrate rious configurations of short-range neighbourhoods which deviate from the fixed ıditional neighbourhood systems. Thus the MGRF model improves the recovery of accurate ighbourhood system even for typical short-range interactions present in natural textures of in.

) visual appearance: Another important aspect to be noted is overall 3D appearance of ıture features. The 3D features of skin can be perceived by human eye to have 3D rve/groove/ridge like appearances. The MGRF modeling only addresses the capturing of ıy scale co-occurrences where 3D appearances may not appear visually as accurately as in ıple images. Hence it can be observed that successfully modeled images of set 2 and set 3 not mimic the 3D appearances of curves, grooves or ridges noticeably (Figure 5-43).

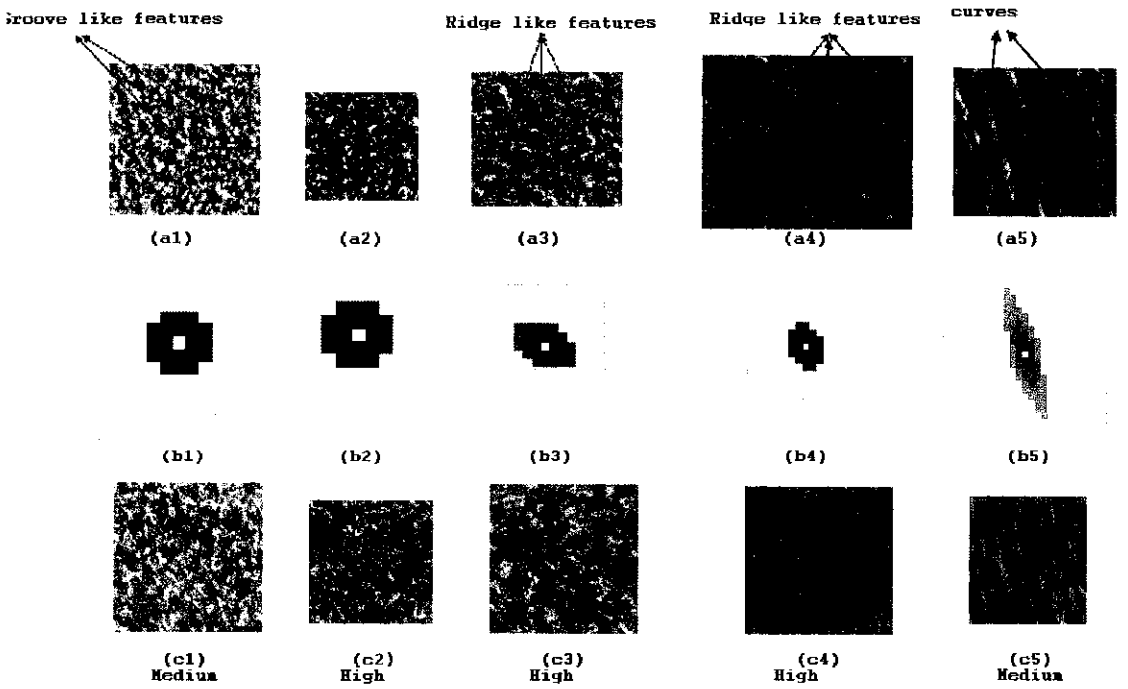

Figure 5-42: Modeling results for set 3 with medium and high visual similarity – (a) skin sample (b) zoomed interaction structures (c) synthesized samples

ıis work is targeted towards modeling of 3D skin features for haptic applications where ɜse features are on the scale of 0.1-1mm. On this small scale the surface irregularities on in give rise to the tactile perception of roughness only and their curve/groove like pearance cannot be perceived by human finger. For this reason the poor visual perception 3D appearances does not pose a significant drawback.

.8 Summary

this chapter, the overall set up for 3D data acquisition was presented. The laser scanning uipment used for data acquisition is discussed. The algorithm for pre-processing of 3D data extract the 2D grayscale textures has been presented. The variety of surface textures thered from case studies provide information about 3D surface features found on skin at gh resolution of 0.1-1 mm. These features are arranged in different input sets to observe ɜ MGRF model's response to each of them individually. The pseudo code for analysis and nthesis under MGRF model and results of modeling for these input set are presented. nally, the detailed analysis of modeling results enables us to conclude about the patterns ɜated by skin features on skin surface and the extent to which these can be reproduced ccessfully by MGRF model.

ıe investigation on MGRF modeling of skin images shows that the 3D features of skin can ɜ categorized as naturally stochastic/homogeneous or inhomogeneous patterns. The ımogeneous features are modeled successfully by MGRF model. Where the curvature of ıderlying limb always creates non-homogeneity, the fine texture on skin is almost always ınsistent locally and results in homogeneity in grayscale textures. Hence, the fine textures ı skin can be reproduced with high visual similarity and the curvature always fails to be produced in synthesis. The wrinkles and line-like features of skin usually do not occur as ımogeneous patterns and therefore are not modeled successfully.

hapter 6

onclusion

.1 Summary & Contribution

edical imaging for dermatology or skin imaging mainly covers the 2D or 3D image quisition of skin and analysis of images to draw conclusions about skin condition for fferent applications e.g. detection, classification and monitoring of skin diseases. The nventional 2D imaging captures color information of skin which is incorporated in mputer-based image analysis systems. However, in addition to color, other skin atures like surface textures and roughness are also altered by skin diseases, ageing, etc. ese surface features can be obtained by 3D imaging and incorporated in image analysis stems to make more precise conclusions about skin condition.

in imaging (both 2D and 3D) mainly targets to assist dermatologists in visual spection of skin. However, there are two modes of clinical inspection in dermatology . visual inspection and tactile inspection. In several diseases, the tactile inspection of in gives important clues to the state of diseases. The computer-based tactile inspection dermatology remains unaddressed. In this thesis, it was proposed that haptic hnology from virtual environments can provide the computer-based tactile inspection. e real skin can be modeled and represented in a virtual environment as virtual skin. A er can then touch the virtual skin through a haptic device. Where a dermatologist nnot touch the skin directly (tele-dermatology or severe skin conditions) or an objective

cision about skin condition has to be made, the virtual skin along with a haptic device n provide the necessary tactile inspection.

ıe virtual skin requires several skin parameters to be modeled. The friction and stiffness ake mechanical parameters whereas the surface profile can be obtained from 3D ıaging. The research objective of this work was the modeling of 3D surface textures of in for haptic applications. For this objective, the 3D images of skin were acquired using gh resolution (~0.1 mm) accurate laser scanning equipment. The images were captured ɔm nine patients of psoriasis and included both healthy and diseased skin samples from ms, trunk and legs. Since fast haptic texture rendering algorithms require input textures be in 2D grayscale images (height maps), the 3D data were transformed to 2D data and ɔdeled with Markov-Gibbs Random Field (MGRF) modeling. Following is a summary results for modeling presented in detail in last chapter.

rst of all, skin samples show us typical skin surface profiles found on healthy and seased skin. These 3D surface profiles are created by curvature of underlying limb, inkles/line like features of skin and fine local textures of skin which make key 3D ıtures of skin. These 3D features appear in both healthy and diseased skin samples. ıe next step is to observe MGRF model's response to each of these features separately observe that which features can be modeled successfully. For this reason, skin samples ere distributed in three sets. In first set, the texture samples consisted of all three ıtures where curvature dominated the other two. Second set of textures was obtained er elimination of curvature and contained both wrinkle/line like features and fine ctures. The textures in third set were also obtained after elimination of curvature but nsisted of fine textures only.

ıe MGRF model's response is determined by visual similarity of synthesized images th the sample images. The MGRF model works best for strongly homogeneous natural ctures with spatially invariant pixel interactions [Gimel 1999]. Therefore, the nthesized images for homogeneous textures present high visual similarity to the sample ıages. Based on this, the visual similarity in synthesized images can be used to conclude

the homogeneity/inhomogeneity of the features present in sample texture image. nilarly, the MGRF model's response for three input sets determines the homogeneity 3D skin surface features in skin texture images. In set 1 curvature of underlying limb minated. The results of MGRF modeling for set 1 showed no visual similarity between nthesized and sample textures (Figure 6-1). Hence, it can be concluded that curvature ıkes an inhomogeneous 3D skin feature with no spatial invariance of texture pattern d cannot be modeled successfully.

ıe set 2 consisted of skin samples where both wrinkle/line like features and fine textures ɜre present. The modeling results of set 2 (Figure 6-2) showed low/medium visual nilarity. Thus wrinkle/line like features can vary between inhomogeneous to mogeneous features. This implies that, since the fine texture is almost homogeneous ɜ shown by results of set 3), the wrinkle/line like features are the main inhomogeneous ‹ture features. This shows us that the pattern of wrinkle/line like features do not cessarily always appear as spatially invariant on skin.

ıe set 3 consisted of fine textures only and its modeling results almost always presented ɛdium/high visual similarity (Figure 6-3). Thus, the fine texture of skin can be ncluded as homogeneous 3D feature implying that local fine textures on skin are ɔstly spatially invariant.

able 6-2 presents an overview of modeling results.

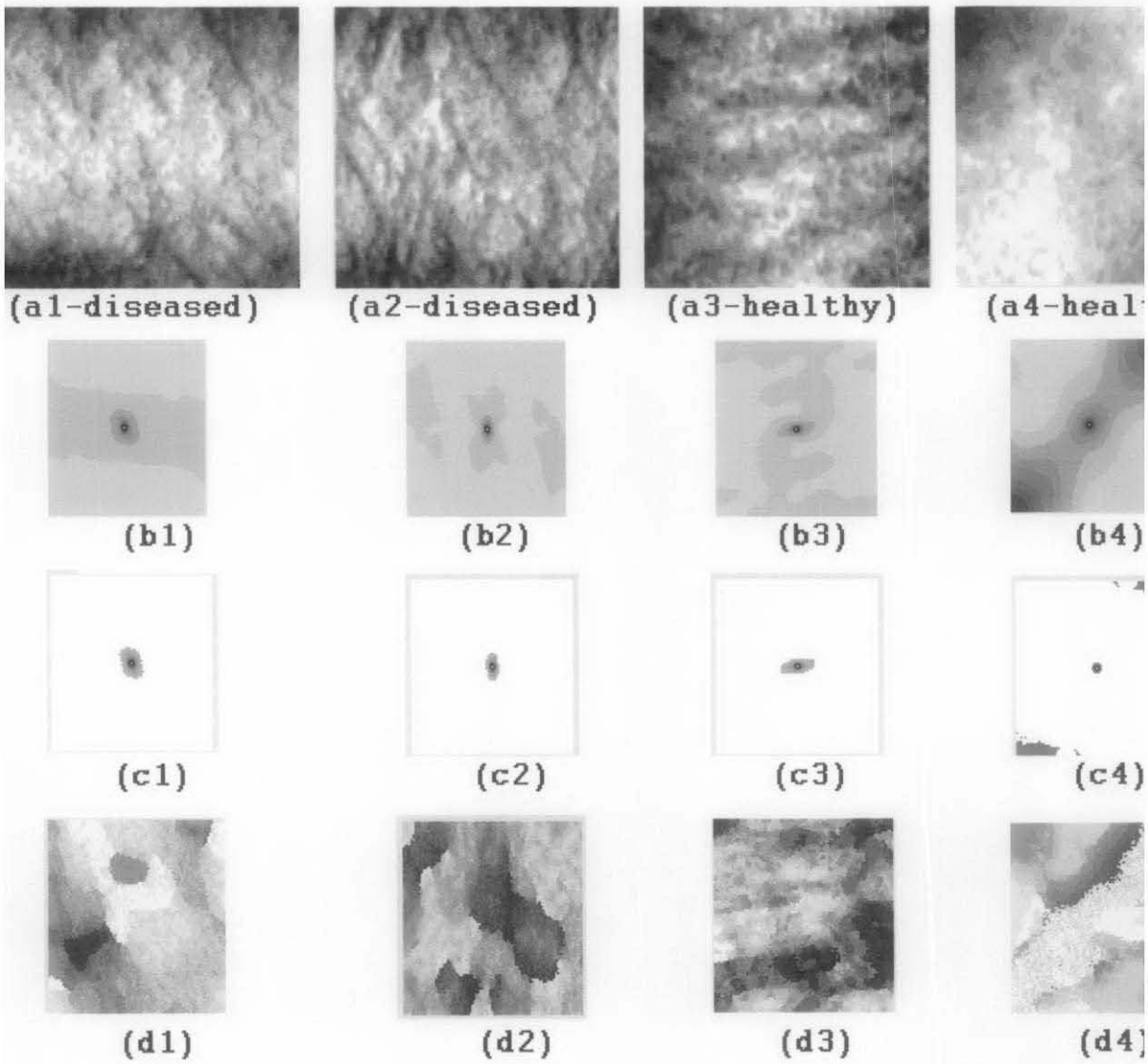

Figure 6-1: Modeling results for set 1 (skin textures including curvature) – (a) Training images of skin textures (b) Interaction maps (c) selected cliques (d) Synthesized images

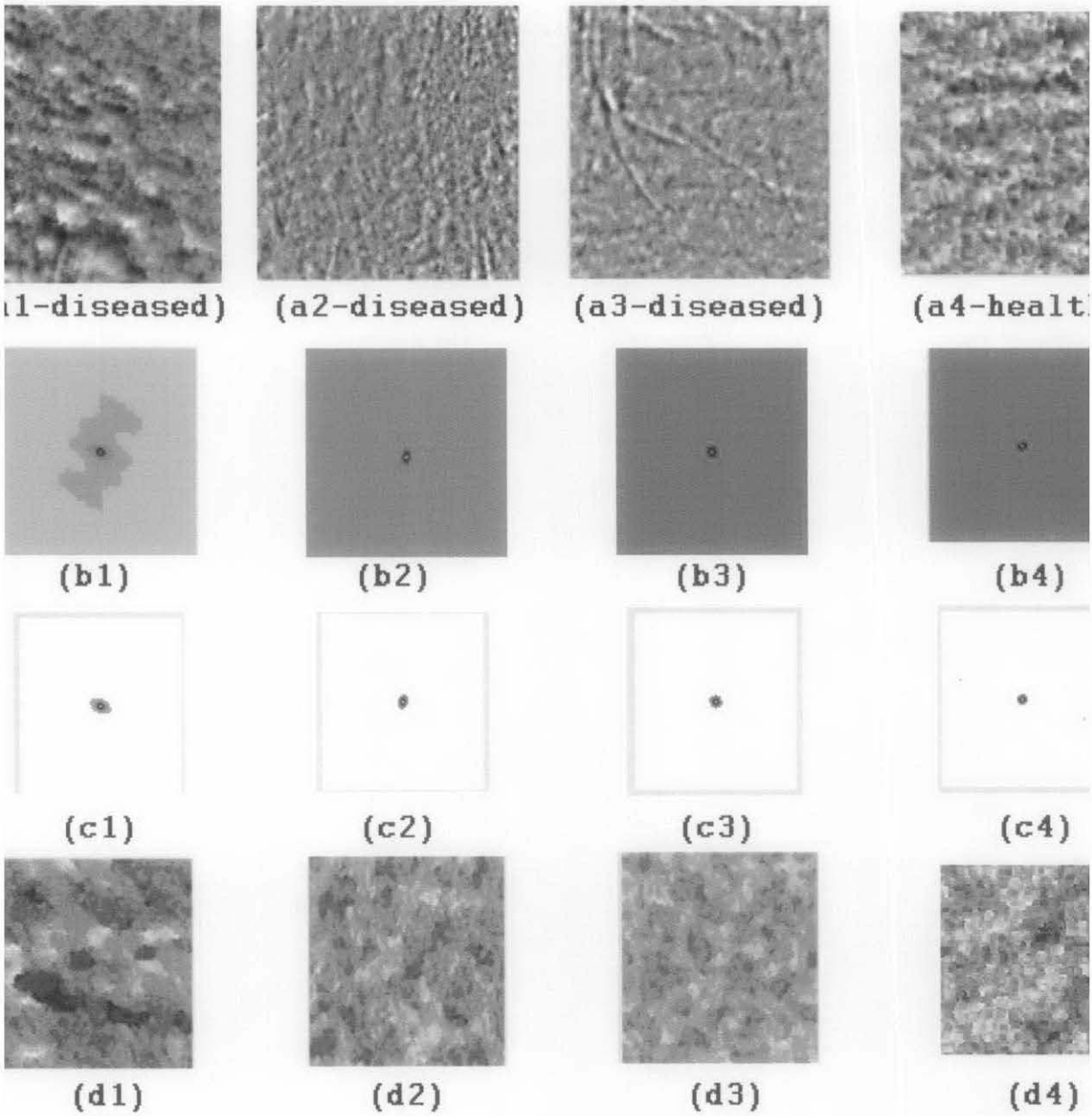

igure 6-2: Modeling results for set 2 – (a) Training images of skin textures (b) Interaction maps (c) selected cliques (d) Synthesized images

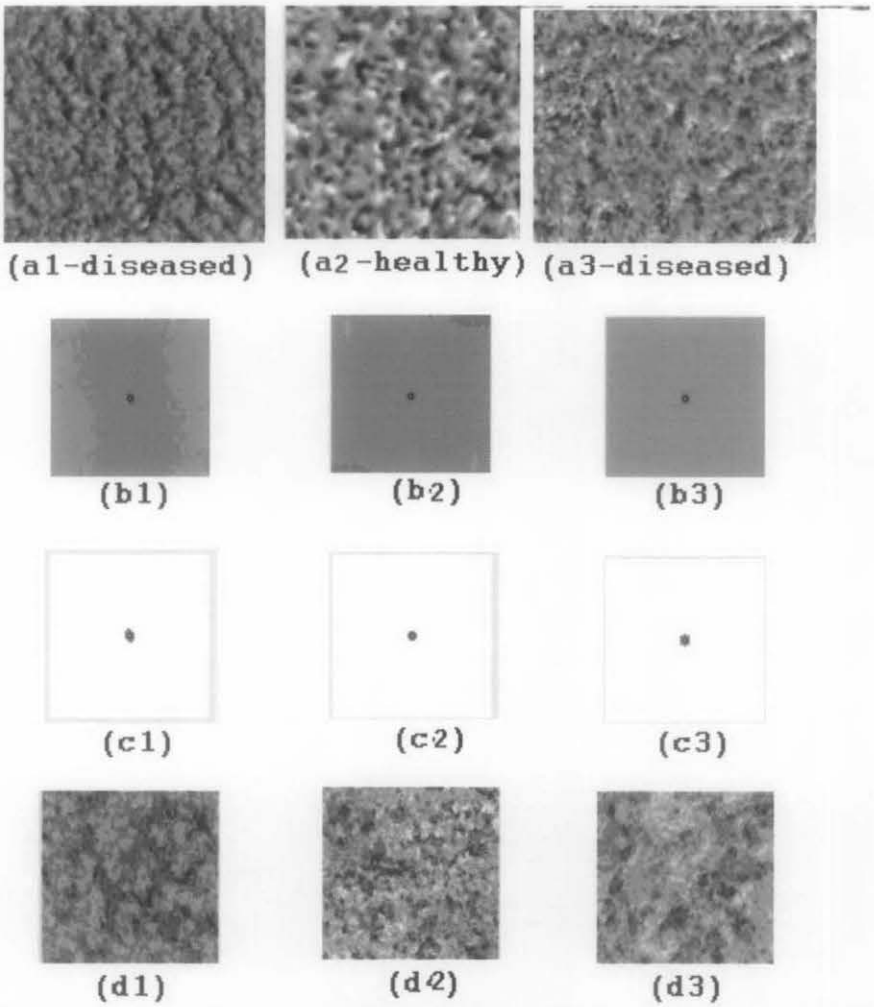

ure 6-3: Modeling results for set 3 – (a) Training images of skin textures (b) Interaction maps (c) selected cliques (d) Synthesized images

) Skin Feature	Interaction Range	Visual Similarity	Comments
Curvature	Short range – Long range	None	*Inhomogeneous*
/rinkles/Lines	Short range – Medium range	Low	*Inhomogeneous*
		Medium	*Homogeneous*
Fine Texture	Short range	Medium	*Homogeneous*
		High	*Homogeneous*

Table 6-1: Summary of modeling results for 3D skin features using MGRF modeling

was observed that the curvature of underlying limbs is a large scale feature whereas inkles/lines/fine textures are small scale features on the scale of 1-0.1 mm. The 3D rface profiles at this small scale give the tactile feeling of roughness. The object of odeling is the integration of 3D skin profiles for haptic applications where a user can ich and feel the surface of skin through haptic device. The tactile feeling of skin is ostly dependent on high resolution, small scale features. Hence the successfully odeled fine textures of skin can be integrated in a virtual environment for haptic feeling roughness. The curvature of underlying limb is not a skin feature contributing to the tile inspection of disease for the reason that skin diseases do not alter curvatures of ibs. Therefore, the poor modeling of curvature through MGRF does not pose a nificant draw back. The successfully modeled fine textures can be superimposed on y arbitrary curvature to present the virtual skin of a body part.

e mixed results of modeling with low/medium visual similarity for wrinkle/line like tures of skin were also observed. These features, present in both healthy and diseased n, do play an important role in tactile inspection. Most of wrinkle/line like features sent inhomogeneous patterns and MGRF model cannot reproduce them successfully. nce, if incorporated in virtual skin, the reproduced wrinkle/line like features will be s accurate than reproduced fine textures of skin.

erall, the research work presented in this thesis provides the following.

1. **3D Skin Surface Features:** A variety of skin surface textures have been acquired from healthy and diseased skin of patients. It has been proposed after observation of these textures that the diversity of textures is composition of three basic 3D skin surface features namely curvature, wrinkle/line like features and fine textures.

2. **MGRF Modeling for Natural Textures of Skin:** The capability of recently proposed MGRF, pairwise-pixel model of Markov/Gibbs random fields, modeling has been tested in modeling the natural textures as skin. The model has

been shown to work successfully for natural textures such as wood, stones, fabric, etc. However, the inclusion of skin textures to the set of these natural textures varies the results and it can be concluded that not all natural textures can be modeled successfully by MGRF and some improvements may be inevitable.

3. **Simulated Annealing for Optimization:** The optimization algorithm Simulated Annealing has been applied to refine initial analytic approximations and to synthesize texture images. The simulated annealing algorithm reaches global maxima in this case where Gibbs Probability Distribution is maximized.

.2 Future Work

ıis work proposed haptic applications for dermatology to assist tactile inspection. The mprehensive virtual representation of materials, including human tissues and skin, for ptic applications is an extensive field of research as was reviewed in Chapter 3. This ›rk presents a starting point for this virtual presentation where the necessary 3D skin rface profile information has been modeled. From the diversity of skin textures tained, the important information of key 3D skin features and their texture aracteristics (long-range/short range, homogeneous/inhomogeneous) were determined. ıis information can aid in developing more advanced modeling techniques for computer ıphics or haptic rendering of skin. Later, 3D surface profiles can be integrated with ıer mechanical properties for a complete virtual skin model. This work can be tended in following possible dimensions to improve the modeling technique and to :grate this model with applications in haptic technology, 3D animation or image alysis.

- **Improved Modeling for Skin Surface Textures:** The modeling technique can be improved to include the inhomogeneous features of wrinkle/lines and other surface irregularities as well. In addition the sample space for 3D skin surface textures can be increased from healthy and psoriatic skin to other diseases.

- **Haptic Applications:** The 3D surface textures can be integrated in a haptic application for haptic rendering. The MGRF model can be applied to synthesize grayscale height maps corresponding to real skin surface textures. The height maps can then be incorporated with mesh models of limbs for haptic feeling of roughness. In addition the mechanical properties of friction and stiffness can be added for more comprehensive virtual skin model.

- **3D Animation:** Until now, modeling of human skin has been limited to 3D animation purposes in computer graphics. And that also the capturing of patterns from *real* skin samples is not covered mainly and only approximations to skin textures are made basis of modeling. This work includes modeling of real skin covering both healthy and diseased skin. In this attempt of looking into real skin patterns of wide range, the 3D data is obtained from patients in collaboration with dermatologists. Thus the successfully modeled surface textures for healthy skin can be used for more accurate skin rendering in computer animations.

- **3D Image Analysis**: The 3D skin surface profiles obtained can also be used for image analysis apart from haptic applications for dermatology. The high resolution and accurate 3D surface profile features can be quantized in terms of parameters (for example see Moon *et al* [Moon 2002]) which can be used along with 2D features to offer improved skin analysis results.

ppendix A

minous Flux (lumens): visible power, or light energy per unit of time from source

uminance (lux): luminous flux incident on a surface per unit area, measured in lux, nen per square meter, foot-candle (fc), or lumen per square foot

lor Temperature (Kelvin): the temperature to which one would have to heat a oretical "black body" source to produce light of the same visual color as that of the irce

w color temperature implies warmer (more yellow/red) light while high color nperature implies a colder (more blue) light. *Daylight* has a rather low color nperature near dawn, and a higher one during the day.

lor Rendering Index CRI: How well colors are rendered by different illumination nditions in comparison to a standard (i.e. a thermal radiator or daylight). CRI is culated on a scale from 1-100

ecular Reflection: Reflection off from smooth surfaces such as mirrors or a calm body water or typical oily skin

ffused Reflection: Reflection off from rough surfaces such as clothing, paper, es/wrinkles of a non-oily skin

ıppendix B

ndom Variable: In probability theory a random variable (r.v) is a quantity whose lues are random and therefore the random variable can be assigned with a probability ıtribution function. Random variables are used to describe the random events e.g. ling of a dice, raining at a particular day, outcome of a test experiment, etc.

ınt Probability Distribution: Given two random variables X and Y representing two ferent events, the joint probability distribution of X and Y is the distribution of X and Y gether i.e. how probable the two events are to occur *together* and can be denoted by $(X = x \textbf{ and } Y = y)$ or $P(X \cap Y)$.

ınditional Probability Distribution: Given two events X and Y, the conditional ɔbability is the probability of event X given the occurrence of event Y and is denoted by $(X \mid Y)$. In terms of joint probability distribution, it is defined as

$$P(X \mid Y) = \frac{P(X \cap Y)}{P(Y)}$$

ırdinality: The cardinality of a set A is a measure of the number of elements of set A d is denoted by $|A|$.

arkov Chain: A Markov process or Markov chains is a sequence (chain) of events fined in temporal domain. Markov chain can be represented as a sequence of random riables x_n defined for states in time $n = 0,1,2,...$ and has the property

$$P(x_i \mid x_{i-1}, x_{i-2}, ...) = P(x_i \mid x_{i-1})$$

ıich implies that the current state is dependent on past state only or in other words, ven the present state, past and future states are independent.

ırginal Probability: It is the probability of one event $P(X)$, regardless of the other ənt Y. Marginal probability is obtained by summing (or integrating, more generally) ; joint probability $P(X \cap Y)$ over the unrequired event Y.

ior Probability: A prior probability $P(X)$ is a marginal probability, interpreted as a scription of what is known about a random event in the absence of some evidence. It presses *uncertainty* about the event X before the data are taken into account thus ributing uncertainty rather than randomness to the uncertain event.

sterior Probability: The posterior probability of a random event X is the conditional obability $P(X \mid Y = y)$ that is assigned when the relevant evidence or data $Y = y$ is ɛen into account.

kelihood Function: If *probability* allows us to predict unknown outcomes based on own parameters, then *likelihood* allows us to determine unknown parameters based on own outcomes. In this sense, likelihood works backwards from probability: given Y, ; use the conditional probability $P(X \mid Y)$ to reason about X, and, given X, we use the elihood function $L(Y \mid X)$ to reason about Y. Thus, it is a conditional probability nction $P(X \mid Y)$ considered as a function of its *second* argument with its first argument ld fixed at $X = x$.

$$L(Y \mid X = x) = \alpha P(X = x \mid Y)$$

ıfficient Statistics: In statistics, a statistic is *sufficient* for the parameter θ, which dexes the distribution family of the data, precisely when the data's conditional obability distribution, given the statistic's value, no longer depends on θ. Intuitively, a fficient statistic for θ captures all the possible information about θ that is in the data. A

tistic $T(X)$ is sufficient for θ precisely if the conditional probability distribution of the ta X, given the statistic $T(X)$, is independent of the parameter θ, i.e.

$$P(X = x \mid T(x) = t, \theta) = P(X = x \mid T(x) = t)$$

ylor Series: The Taylor series is a representation of a function as an infinite sum of ms calculated from the values of its derivatives at a single point. The Taylor series of a ıl or complex function f that is infinitely differentiable in a neighbourhood of a real or mplex number a, is the power series

$$f(a) + \frac{f'(a)}{1!}(x-a) + \frac{f''(a)}{2!}(x-a)^2 + \frac{f^{(3)}(a)}{3!}(x-a)^3 + \cdots$$

ıich in a more compact form can be written

$$\sum_{n=0}^{\infty} \frac{f^{(n)}(a)}{n!}(x-a)^n,$$

ıere $n!$ is the factorial of n and $f^{(n)}(a)$ denotes the nth derivative of f at the point a; the roth derivative of f is defined to be f itself and $(x-a)^0$ is defined to be 1.

ppendix C

IATLAB code for 2D texture extraction and surface tting

```
**********************************************************************
his function extracts the 2D grayscale textures from 3D vertices
ven for the surface texture information of skin
nput: An array of vertices having x,y,z co-ordinates of the vertices
utput: The Q level grayscale images for skin with curvature (skin) %
nd without curvature (texture) along with the dimensions of image
dimensions) in millimeters and in pixels
NOTE: The portion of this code having implementation of function
gridfit' has been obtained from MATLAB CENTRAL
http://www.mathworks.com/matlabcentral/fileexchange/loadFile.do?objec
Id=8998)
**********************************************************************

nction [texture skin dimensions] = getTexure (vertices);

xtract the co-ordinate information
 x = vertices(:,1);
 y = vertices(:,2);
 z = vertices(:,3);
 lengthx = max(x)-min(x);
 lengthy = max(y)-min(y);
 lengthz = max(z) - min(z);

ubic interpolation to interpolate vertices to a 3D surface at regular
rid

 sz=size(vertices);
 samples = uint8(sqrt(sz(1,1)))+5;
 xlin = linspace(min(x),max(x),samples);
 ylin = linspace(min(y),max(y),samples);
 [X,Y] = meshgrid(xlin,ylin);
 surface2=griddata(x,y,z,X,Y,'cubic');

urface fitting to eliminate curvature
 surface1=gridfit(x,y,z,xlin,ylin,'smooth',15);


 surf(X,Y,surface1);
 colormap('hot');
 hold on;
 grid on;
 mesh(X,Y,surface2);
```

```
ubtract the fitted surface from interpolated surface to eliminate
rvature
 diff = surface2-surface1;
 figure;
 surf(X,Y,diff);

he texture is cropped manually to get a rectangular representative
mple
 mn = min(min(diff));
 mx = max(max(diff));
 Z = ((diff-mn)/(mx-mn)) * 256;
 Z = uint8(Z);
 figure;
 [cropped rect] = imcrop(Z);
 rect=uint8(rect);
 figure;
 imshow(cropped);

he cropped sample is output for skin and texture information
 texture =
ff(rect(1,2):rect(1,2)+rect(1,4),rect(1,1):rect(1,1)+rect(1,3));
 skin =
rface2(rect(1,2):rect(1,2)+rect(1,4),rect(1,1):rect(1,1)+rect(1,3));
 figure;
 mn = min(min(skin));
 mx = max(max(skin));
 Z = ((skin-mn)/(mx-mn)) * 256;
 Z = uint8(Z);
 imshow(Z);
 dimensions = [lengthx lengthy lengthz size(texture)]
```

,ppendix D

[ATLAB code for analysis of 2D grayscale textures for [GRF parameter estimation

```
*********************************************************************
*
he function retrieves the interaction structure and corresponding
bbs
otentials for a Q-level input grayscale image under MGRF modeling

nput: a gray-level image image=(g[i,j]: i = 1,...,M; y=1,...,N])
Q=15 or 31 for 16 or 32 gray levels
earch window dimensions [Di, Dj] should be [40, 40] to represent a
uadrant of [80, 80]search window
igma = 3 … 4 for interaction structure thresholding

Output: a set of K most characteristic Gibbs potentials represented
ch by a 2D table Vk = (Vk[q,s]: q=0,...,Q-1;s=0,...,Q-1]); k=1,...,K
and their corresponding gathered co-occurrence probabilities from
put image freq_image_k[q,s] : q=0,...,Q-1;s=0,...,Q-1]); k=1,...,K
alculated value of 'lambda_0'
*********************************************************************
*

nction [RelEnergy POT freq lambda_0] = GibbsPots(image, grayLevels,
ndowWidth, sigma)


= grayLevels;
= windowWidth;
 = w(1,1);
 = w(1,2);
age=double(image);

. Quantise a given image into Q gray levels if it has higher signal
solution
 = min(min(image));
 = max(max(image));

= round(((image-mn)/(mx-mn))*Q);
show(g,[0 Q]);
gure;

 = size(g);
= sz(1,1);
= sz(1,2);

ray level co-occurrence histograms (GLCH) gathering:
```

```
. Collect co-occurrence histograms COOC(di,dj) = (COOC(di,dj)[q,s]:
),...,Q-1;
=0,...,Q-1) for all inter-pixel shifts (di,dj) in a search window
ach pair ((i,j),(i+di,j+dj)) is a clique
f the clique family with this shift) W=((di,dj): if dj=0 di=1,...,Di;
se di = -Di,...,0,...,Di; dj=1,...,Dj):


 2a) Initialise each COOC: for all di,dj,q,s: COOC(di,dj)[q,s]=1

OC = zeros(Q+1,Q+1,2*Di+1,Dj+1);
H = zeros(1,Q+1);
eq = COOC;
T = freq;
mm = ones(2*Di+1,Dj+1);
an_freq = zeros(2*Di+1,Dj+1);
riance_freq=mean_freq;
lEnergy=variance_freq;
teractMap = zeros(2*Di+1,2*Dj+1);
lectedCliques = interactMap;
an_Energy=0;
D = 0;

 2b) Collect histograms
r j=1:N
  for i=1:M
      q = g(i,j);

      for dj = 0:Dj
          sdi=0;

          if(dj == 0)
              sdi=1; % sdi=1 (and not sdi=0 because di=sdi=0 and dj=0
uld be the pixel itself and not the clique)
          else
              sdi=-Di;
          end

          for (di=sdi:Di)
              if((0<i+di && i+di<M+1) && (0<j+dj && j+dj<N+1))
                  s=g(i+di,j+dj);
                  COOC(q+1,s+1,di+Di+1,dj+1) =
OC(q+1,s+1,di+Di+1,dj+1) + 1;

              end
          end

      end



  end
```

```
i

) Gray level co-occurrence probabilities calculation:
  Normalise histograms to get relative frequencies:
    for each (di,dj) in W:
       freq(di,dj)[q,s] = COOC(di,dj)[q,s]/sum_(q'=0,...,Q-
s'=0,...,Q-1)COOC(di,dj)[q',s']

  % i.e. TO GET frequencies from histograms we have to divide
stogram
  % vector for every clique family by the total number of cliques
ınd
  % in an image under that clique which is = |Ca| and |Ca|= sum of
l
  % possible combinations of q,s computed under that family, thus
  % |Ca| = sum_(q'=0,...,Q-1,s'=0,...,Q-1)COOC(di,dj)[q',s']



)Interaction energies calculation:
ind relative energies for all clique families: RelEne(di,dj) =
riance(freq(di,dj)):
ariance(freq(di,dj) = sum_(q=0,...,Q-1;s=0,...,Q-1){freq(di,dj)[q,s]-
an_freq(di,dj)}^2
here mean_freq(di,dj) = sum_(q=0,...,Q-1;s=0,...,Q-
{freq(di,dj)[q,s]}/(Q^2)


r i=1:2*Di+1
  for j=1:Dj+1
        %THE VALUES OF summ ARE ZERO FOR +VE Y AXIS IN THIS CASE SO
 AVOID 'divide by zero' WARNING
        summ(i,j)= sum(sum(COOC(:,:,i,j)));
        if(summ(i,j)==0)
            summ(i,j)=1;
        end
        freq(:,:,i,j) = COOC(:,:,i,j)/summ(i,j);
        mean_freq(i,j)=  mean(mean(freq(:,:,i,j)));
        variance_freq(i,j) = sum(sum((freq(:,:,i,j)-
an_freq(i,j)).^2));
  end
d

elEnergy=variance_freq;

complete the whole interaction map

teractMap(1:2*Di+1,Dj+1:2*Dj+1) = RelEnergy(1:2*Di+1,1:Dj+1);

Mirroring along y-axis

r j=1:Dj
  interactMap(:,j)=interactMap(:,(2*Dj+2)-j);
```

```
i

Mirroring along x_ axis

r i=1:Di
  temp=interactMap(i,1:Dj);
  interactMap(i,1:Dj+1)=interactMap((2*Dj+2)-i,1:Dj+1);
  interactMap((2*Dj+2)-i,1:Dj)=temp;

i

Show the interaction map

 = min(min(interactMap));
 = max(max(interactMap));
teractMapIM = round(((mx-interactMap )/(mx-mn)) * Q); %shows the
teraction map in reverse color
show(interactMapIM,[0 Q]);

5) Thresholding and Interaction Structure Extraction:
calculate statistics for independent random field IRF
qs_irf = 1/((Q+1)^2);
r_irf = M_qs_irf * (1-M_qs_irf);

= M*N;
nom = sum(sum( (variance_freq).*((summ/r).^2) ))
um = sum(sum(  (variance_freq).*((summ/r).^3) ))

calculation of lambda_0 (equation 4.33)
mbda_0 = (denom)/(var_irf*neum); % rhos are splitted here |Ca| and
|

) Select K top-energy clique families by thresholding the energy
stribution
e.g. all the clique with energies above mean_energy +
3..4)*standard_deviation

an_Energy = mean (mean(interactMap));
D = std(std(interactMap));
eta = Mean_Energy+sigma*S_D;

) Gibbs Potentials Learning
r i=1:2*Di+1
  for j=1:2*Dj+1
      if(interactMap(i,j) > theta)
          selectedCliques(i,j) = interactMap(i,j);
      end

      if(j<Dj+2)
          if (RelEnergy(i,j)<=theta)
              RelEnergy(i,j)=0;

          else
```

```
        POT(:,:,i,j) = lambda_0 *(freq(:,:,i,j)-mean_freq(i,j));

          end
      end


  end
d

show selected clique families (retrieved interaction structure) in a
figure
 = min(min(selectedCliques));
 = max(max(selectedCliques));
gure;
lectedCliquesIM = round(((mx-selectedCliques )/(mx-mn)) * Q);
show(selectedCliquesIM,[0 Q]);
```

.ppendix E

:ATLAB code for synthesis of 2D grayscale texture using mulated annealing

```
**********************************************************************
The function synthesizes the texture images by sampling Gibbs
obability
distribution under MGRF model. The Metropolis sampler with simulated
annealing is used.
Input:
1)     K most characteristic Gibbs potentials Vk gathered from
alysis algorithm
2)     lambda_0
3)     Gray level co-occurrence probabilities for selected K families
 sample image freq_image_k

Output: synthesized gray-level image g=(g[i,j]: i = 1,...,M; j
,...,N]) with Q
**********************************************************************

nction image = CSA(cliques, GibbsPots, freq, lambda_0, im_range,
put_image )

m_range is Q = 15/31
ibbsPots is a 2w x w array as is calculated in GibbsPots file

 = size(cliques)
ze1 = [120 120];
= sz(2)-1;
eq_new = freq;

Start with a random image
= round(im_range*rand(size1(1),size1(2)));

Start with an initial uniform energy field
erg = -1000 * ones (size1(1),size1(2));

Initialize temperature T and lambda_t
mbda_t = lambda_0
.9;
  c1 = 1;
  c2=.001;
  COOC = zeros(size(freq));
  summ = zeros(sz);



FIRST PUT THE NEIGHBOURHOOD IN REDUCED DATA STRUCTURE
```

```
lex=1;
: (w1 = 1:sz(1))
  for (w2 = 1:sz(2))
      if (cliques(w1,w2) ~= 0)
          x = (w1-1-w);
          y = (w2-1);
          cliques_red (index,1) = x;
          cliques_red (index,2) = y;
          cliques_red (index,3) = w1;
          cliques_red (index,4) = w2;
          index=index+1;
      end
  end
i

ze(cliques_red)

epeat for sufficient number of macro steps t

r  macro_step = 1 : 200

   lambda_t = lambda_0/((c1+c2*macro_step));
   random = 1;
   visit = zeros(size1(1),size1(2));

   %   select a random trace over the image lattice

  while(random < (2*size1(1))*(2*size1(2)))
     i = floor(size1(1)*rand(1,1))+1;
     j = floor(size1(2)*rand(1,1))+1;
     random = random+1;

      if(visit(i,j) == 0)
          visit(i,j)=1;

          new = fix((im_range+1)*rand(1,1));
          new_energ = 0;

Calculates the pixel energy associated to the new configuration as:
% Checks every pixel in the image in turn and calculated its
associated energy for a new gray level value based on its
neighboors. If the new energy is smaller accept the change. If it
is higher, accept the change with a probability based on system
mperature


          for (index = 1:size(cliques_red,1))
                    x = cliques_red(index,1);
                    y = cliques_red(index,2);
                    w1 = cliques_red(index,3);
                    w2 = cliques_red(index,4);
```

```
                    if ((0<x+i && x+i<=size1(1)) && (0<j+y &&
r<=size1(2)))
                        new_energ = new_energ +
ɔbsPots(new+1,a(x+i,y+j)+1,w1,w2);

                    end

                    if ((0<i-x && i-x<=size1(1)) && (0<j-y && j-
=size1(2)))
                        new_energ = new_energ + GibbsPots(a(i-x,j-
+1,new+1,w1,w2);

                    end
        end   %for


        diff = new_energ - energ (i,j);
        r = exp(diff);

        % Accept the change if the new enegy is lower
        if  (diff >= 0) %CHANGES > TO >=
            a(i,j) = new;
            energ(i,j) = new_energ;

        elseif (rand(1,1) < r*T)

            a(i,j) = new;
            energ(i,j) = new_energ;
        end %if
        % else reject the change
    end %if (visiting)
  end %while(visiting)



  % Collect Gray level co-occurrence histograms COOC(di,dj) from
rrent sample g[i,j]

    COOC = zeros(size(freq));
  for i=1:size1(1)
      for j=1:size1(2)

      q = a(i,j);

      for (index = 1:size(cliques_red,1))
          x = cliques_red(index,1);
          y = cliques_red(index,2);
          di = cliques_red(index,3);
          dj = cliques_red(index,4);

          if((0<i+x && i+x<size1(1)) && (0<j+y && j+y<size1(2)))
                 s = a(i+x,j+y);
                 COOC(q+1,s+1,di,dj) = COOC(q+1,s+1,di,dj) + 1;
```

```
            end
        end


        end
    end


    %Calculate Gray level co-occurrence probabilities freq(di,dj) from
    %COOC(di,dj) above
    r=(size1(1)*size1(2));
    for (index = 1:size(cliques_red,1))
       di = cliques_red(index,3);
       dj = cliques_red(index,4);

       summ(di,dj) = sum(sum(COOC(:,:,di,dj)));
       freq_new(:,:,di,dj) = COOC(:,:,di,dj)/summ(di,dj);

       %update Gibbs Potentials
        GibbsPots(:,:,di,dj) = GibbsPots(:,:,di,dj) + lambda_t *
ɹmm(di,dj)/r)*(freq(:,:,di,dj)-freq_new(:,:,di,dj));

ɐnd


  disp('iteration='); disp(macro_step);

  % Reduce the temperature for convergence

  T = T /log((100+macro_step))*log(100);
  if (mod(macro_step,25) == 0)
      figure;
      imshow(a,[0 im_range]); axis image;
      drawnow;
  end
d %macrostep
```

Appendix F

MGRF Modeling results for Set 1

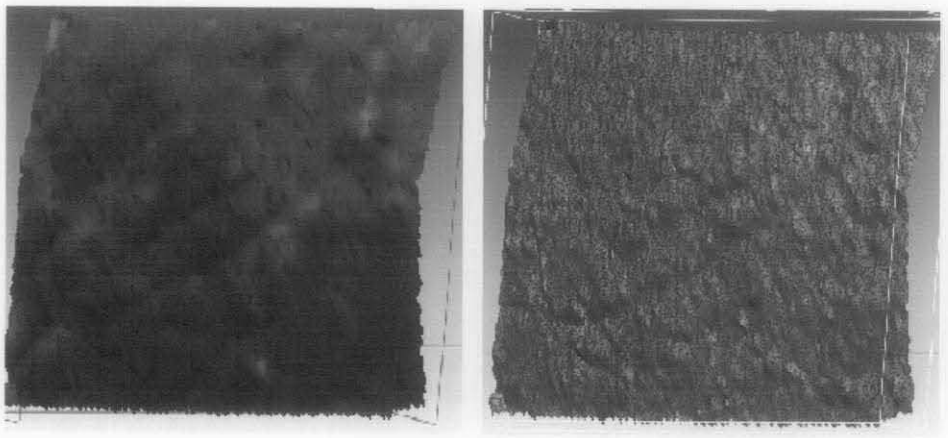

(a) 3D skin sample with color (b) 3D skin sample without color

(c) gray scale texture
(201x206 pixels)

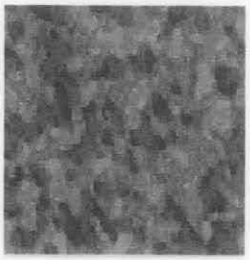

(d) synthesized image
(120x120 pixels)

(e) interaction map
(40x40 pixels)

(f) thresholded cliques
(154 families)

Set 1 - Patient 3 – Arm diseased sample # 1 (23.95mm x 16.56mm x 3.15mm)

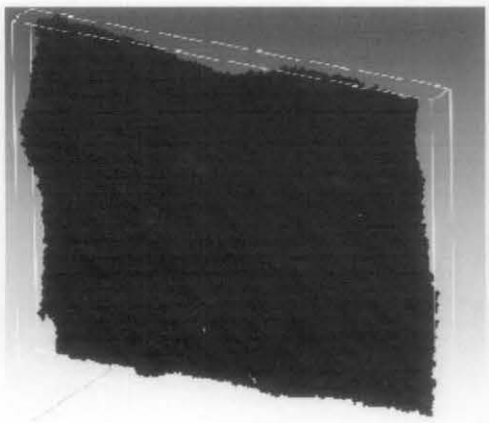

(a) 3D skin sample with color

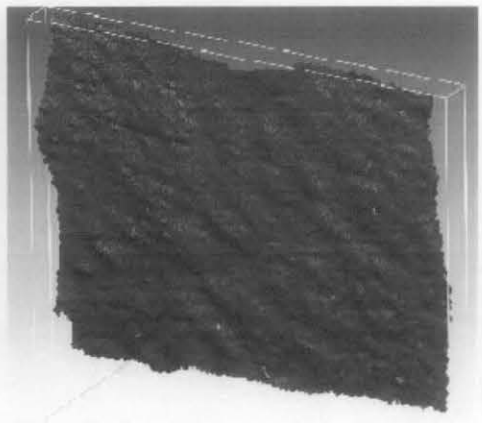

(b) 3D skin sample without color

(c) gray scale texture
(186x196 pixels)

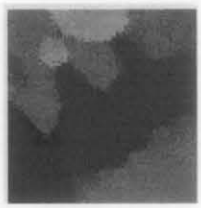

(d) synthesized image
(120x120 pixels)

(e) interaction map
(40x40 pixels)

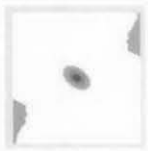

(f) thresholded cliques
(167 families)

Set 1 - Patient 3 – Leg diseased sample # 1 (20.95mm x 15.5mm x 2.5mm)

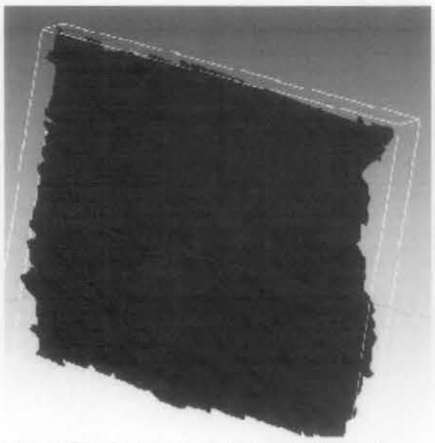

(a) 3D skin sample with color

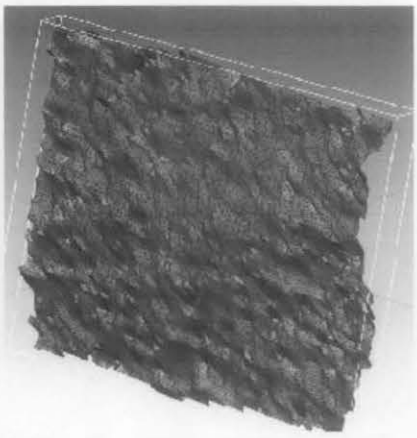

(b) 3D skin sample without color

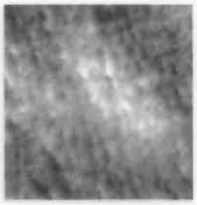

(c) gray scale texture
(121x121 pixels)

(d) synthesized image
(120x120 pixels)

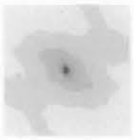

(e) interaction map
(40x40 pixels)

(f) thresholded cliques
(95 families)

Set 1 - Patient 4 – Trunk diseased sample # 1 (12.10mm x 10.50mm x 1.30mm)

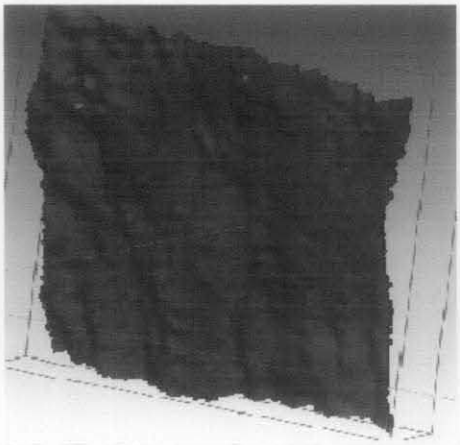

(a) 3D skin sample with color

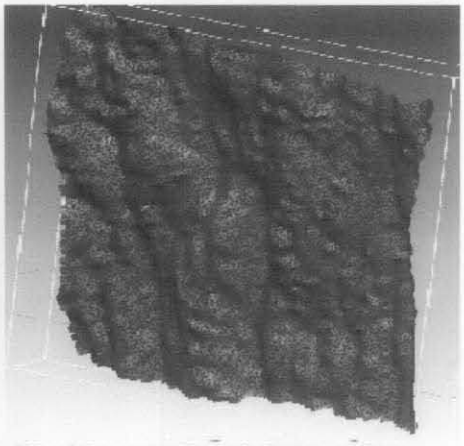

(b) 3D skin sample without color

(c) gray scale texture
(180x156 pixels)

(d) synthesized image
(120x120 pixels)

(e) interaction map
(40x40 pixels)

(f) thresholded cliques
(27 families)

Set 1 - Patient 5 – Trunk Sample # 2 (28.66mm x 30.58mm x 3.61mm)

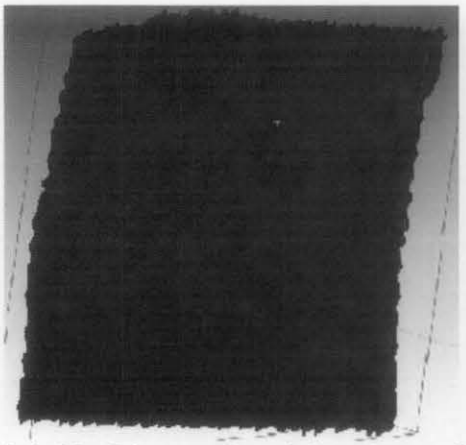

(a) 3D skin sample with color

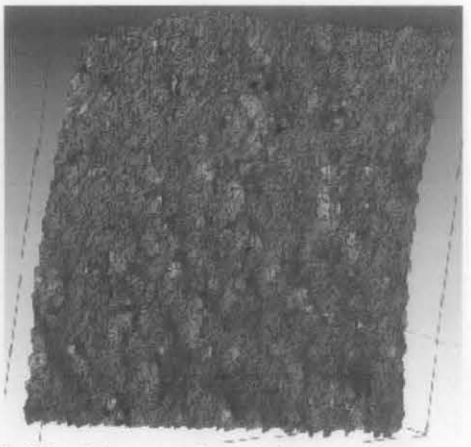

(b) 3D skin sample without color

(c) gray scale texture
(132x163 pixels)

(d) synthesized image
(120x120 pixels)

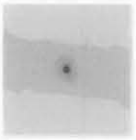

(e) interaction map
(40x40 pixels)

(f) thresholded cliques
(76 families)

Set 1 - Patient 4 – Leg diseased sample # 2 (31.57mm x 30.81mm x 3.03mm)

Appendix G

MGRF Modeling results for Set 2

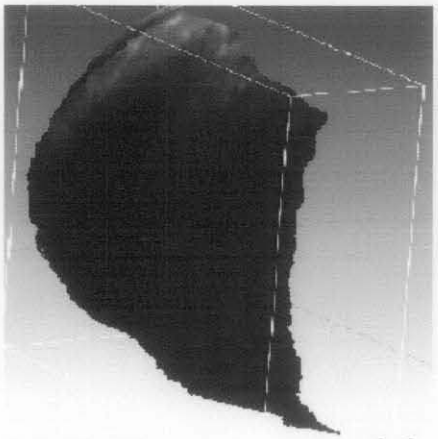

(a) 3D skin sample with color

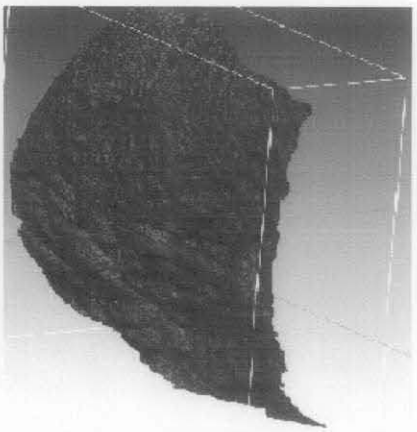

(b) 3D skin sample without color

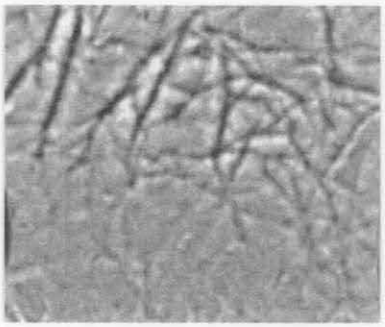

(c) gray scale texture
(200x239 pixels)

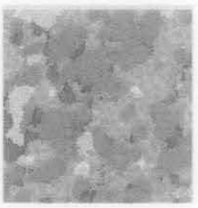

(d) synthesized image
(120x120 pixels)

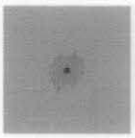

(e) interaction map
(40x40 pixels)

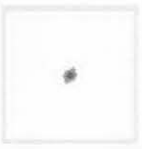

(f) thresholded cliques
(30 families)

Set 2 - Patient 5 – Arm diseased sample # 1 (40.33mm x 39.44 x 11.29mm)
Line like features partially present in image – Low visual similarity

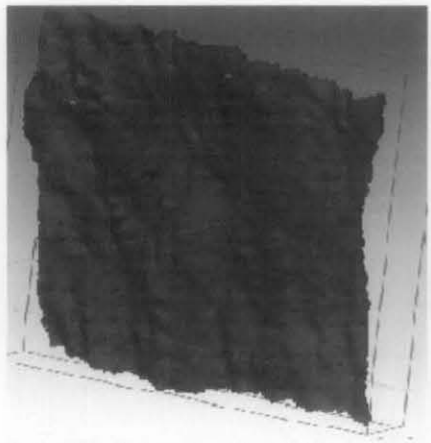

(a) 3D skin sample with color

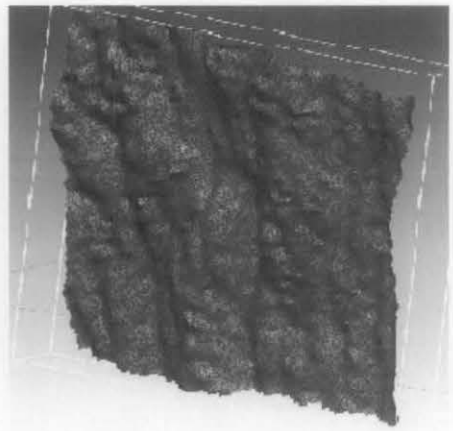

(b) 3D skin sample without color

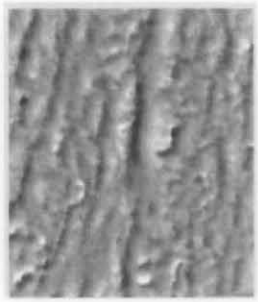

(c) gray scale texture
(180x156 pixels)

(d) synthesized image
(120x120 pixels)

(e) interaction map
(40x40 pixels)

(f) thresholded cliques
(85 families)

Set 2 - Patient 5 – Trunk diseased sample # 2 (28.66mm x 30.58mm x 3.61mm)
Wrinkles present throughout image but spatially variant – Medium visual similarity

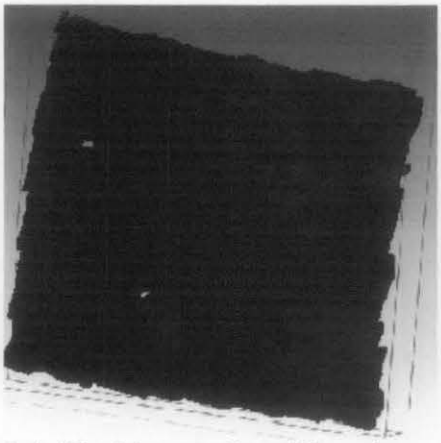

(a) 3D skin sample with color

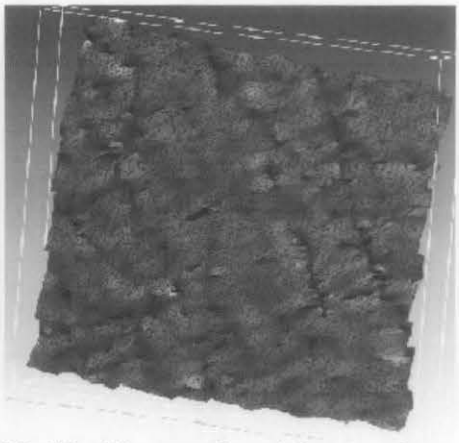

(b) 3D skin sample without color

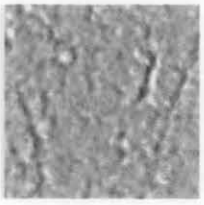

(c) gray scale texture
(123x126 pixels)

(d) synthesized image
(120x120 pixels)

(e) interaction map
(40x40 pixels)

(f) thresholded cliques
(30 families)

Set 2 - Patient 6 – Arm diseased sample # 3 (20.61mm x 19.94mm x 2.21mm)
Wrinkles present partially in image – Low visual similarity

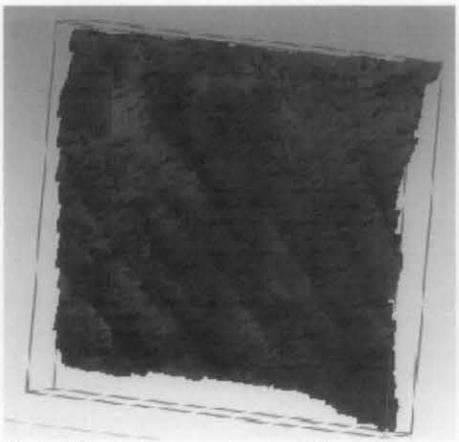

(a) 3D skin sample with color

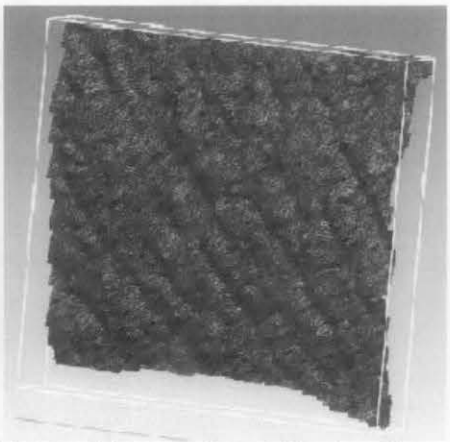

(b) 3D skin sample without color

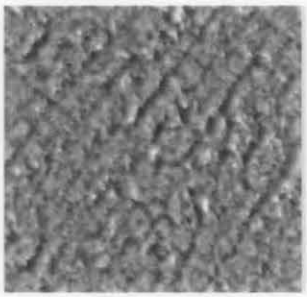

(c) gray scale texture
(181x189 pixels)

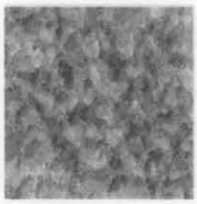

(d) synthesized image
(120x120 pixels)

(e) interaction map
(40x40 pixels)

(f) thresholded cliques
(13 families)

Set 2 - Patient 6 – Leg diseased # 1 (34.14mm x 34.80mm x 4.41mm)
Line like features present throughout image but spatially variant – Medium visual similarity

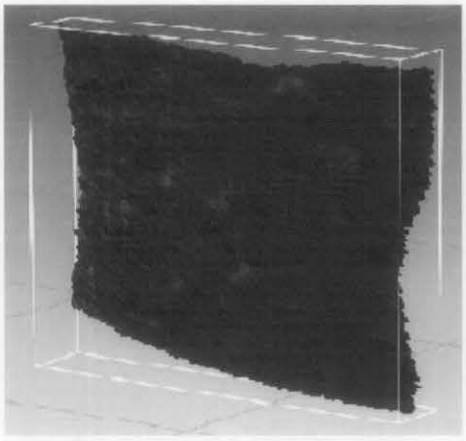

(a) 3D skin sample with color

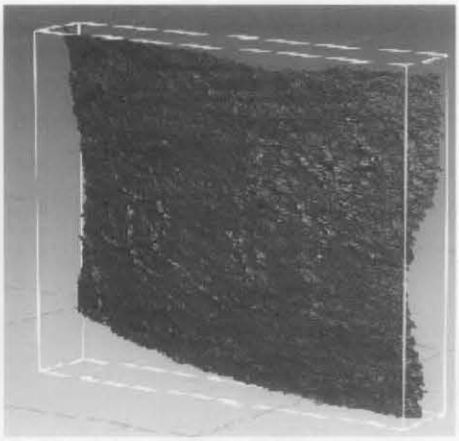

(b) 3D skin sample without color

(c) gray scale texture
(212x217 pixels)

(d) synthesized image
(120x120 pixels)

(e) interaction map
(40x40 pixels)

(f) thresholded cliques
(16 families)

Set 2 - Patient 7 – Leg diseased sample # 3 (43.57mm x 35.28mm x 7.18mm)
Line like features partially present in image – Medium visual similarity

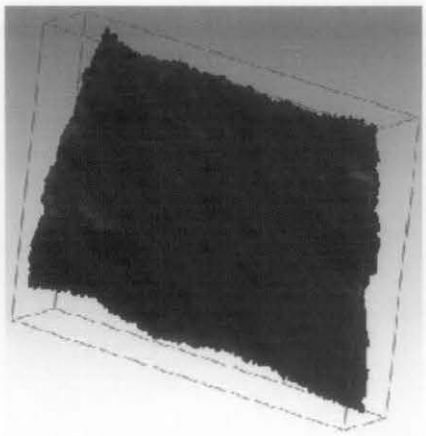

(a) 3D skin sample with color

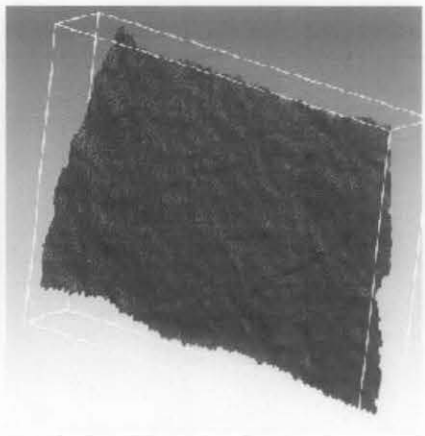

(b) 3D skin sample without color

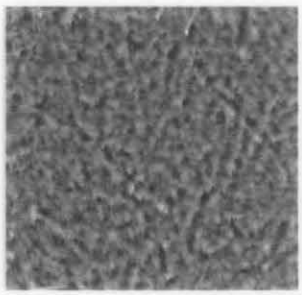

(c) gray scale texture
(178x188 pixels)

(d) synthesized image
(120x120 pixels)

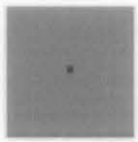

(e) interaction map
(40x40 pixels)

(f) thresholded cliques
(10 families)

Set 2 - Patient 8 – Leg diseased sample # 1 (27.12mm x 23.86mm x 4.00mm)
Line like features present throughout image but spatially variant – Low visual similarity

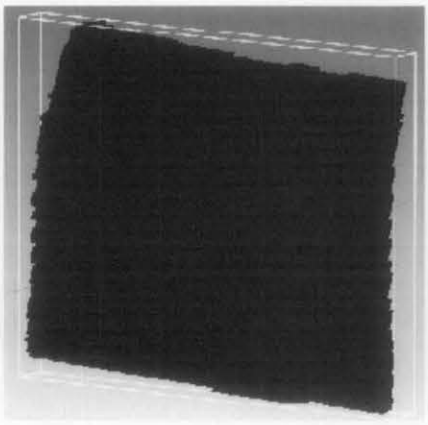

(a) 3D skin sample with color

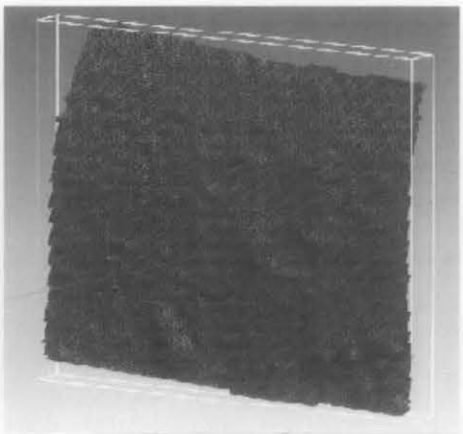

(b) 3D skin sample without color

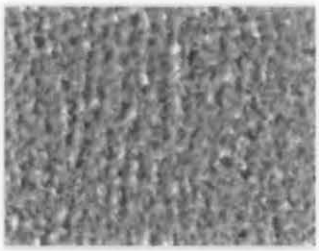

(c) gray scale texture
(149x198 pixels)

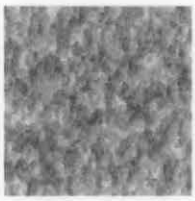

(d) synthesized image
(120x120 pixels)

(e) interaction map
(40x40 pixels)

(f) thresholded cliques
(10 families)

Set 2 - Patient 9 – Trunk diseased sample # 1 (25.68mm x 22.71mm x 2.07mm)
Wrinkles present throughout image but spatially variant – Low visual similarity

Appendix H

MGRF Modeling results for Set 3

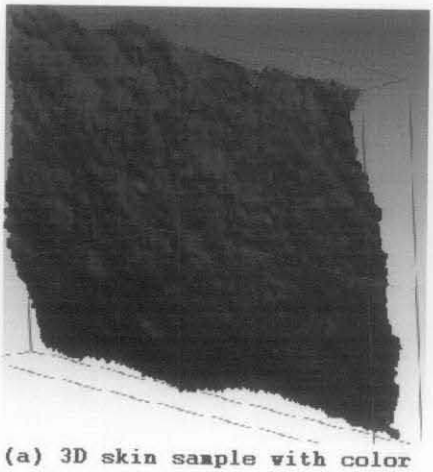

(a) 3D skin sample with color

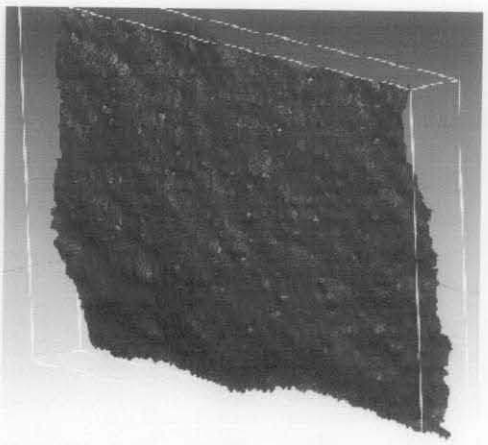

(b) 3D skin sample without color

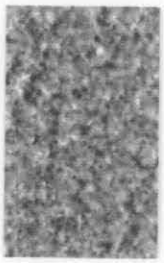

(c) gray scale texture
(158x98 pixels)

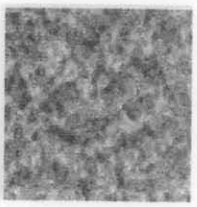

(d) synthesized image
(120x120 pixels)

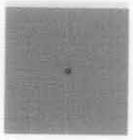

(e) interaction map
(40x40 pixels)

(f) thresholded cliques
(10 families)

Set 3 - Patient 5 – Leg diseased sample # 1 (26.85mm x 25.83mm x 2.89mm)
Medium visual similarity

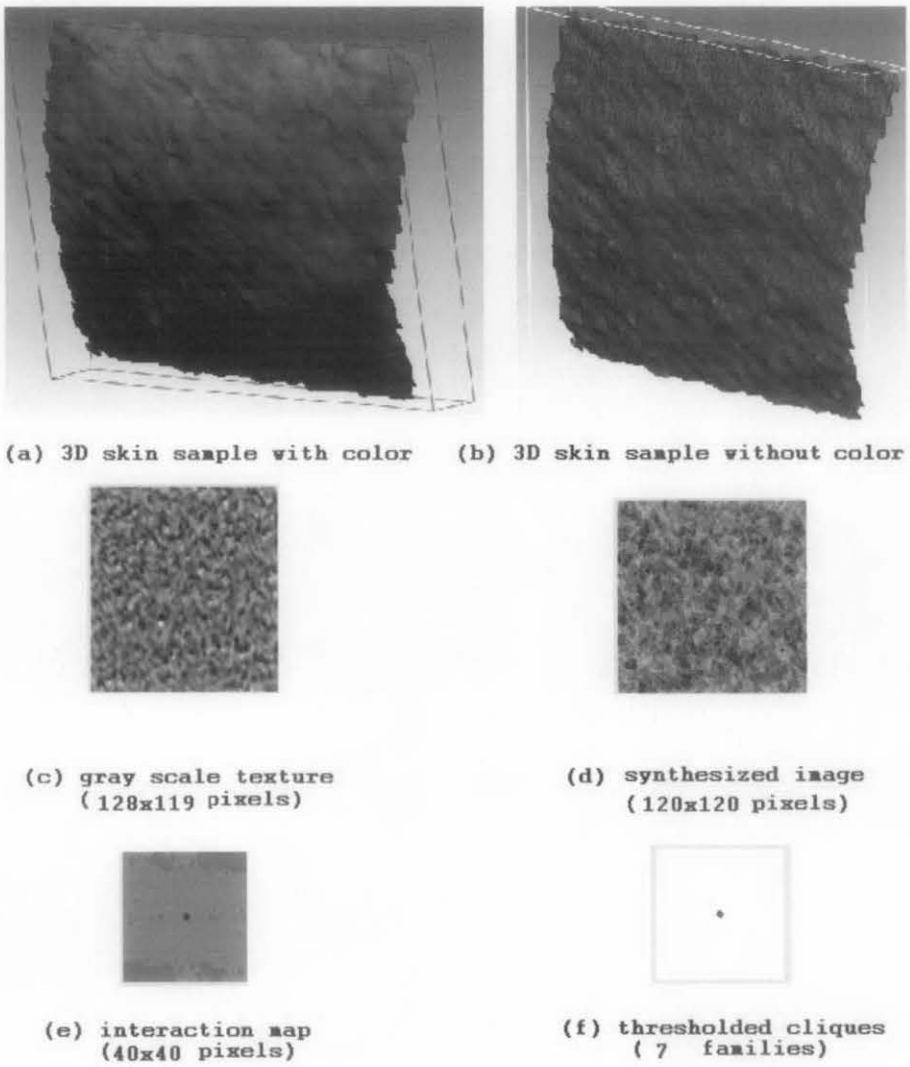

Set 3 - Patient 6 – Arm diseased sample # 1 (20.48mm x 18.04mm x 2.15mm)
Medium visual similarity

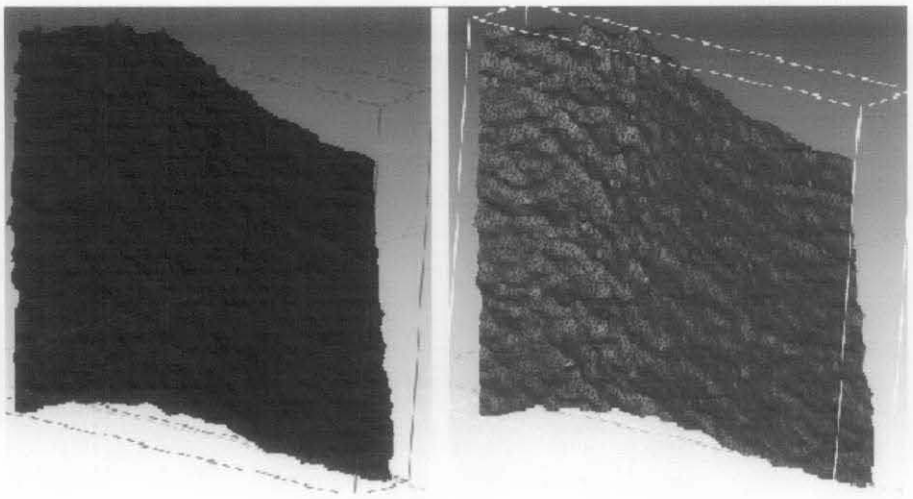

(a) 3D skin sample with color (b) 3D skin sample without color

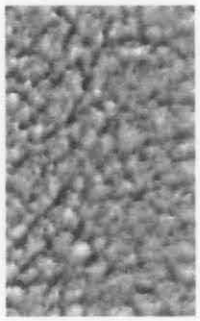

(c) gray scale texture
(186x126 pixels)

(d) synthesized image
(120x120 pixels)

(e) interaction map
(40x40 pixels)

(f) thresholded cliques
(13 families)

Set 3 - Patient 6 – Trunk diseased sample # 5 (47.15mm x 50.91mm x 8.69mm)
High visual similarity

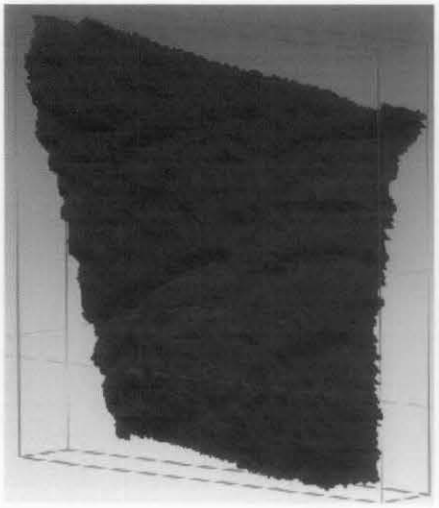

(a) 3D skin sample with color

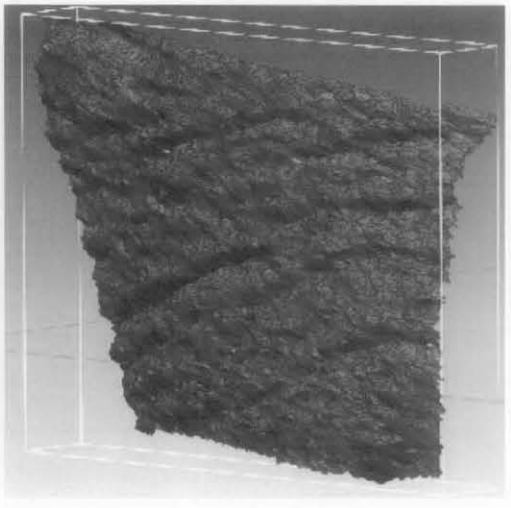

(b) 3D skin sample without color

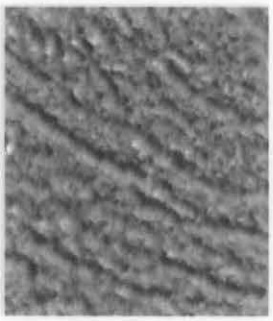

(c) gray scale texture
(1195x171 pixels)

(d) synthesized image
(120x120 pixels)

(e) interaction map
(40x40 pixels)

(f) thresholded cliques
(20 families)

Set 3 - Patient 6 – Trunk diseased sample # 6 (53.83mm x 33.59mm x 7.90mm)
High visual similarity

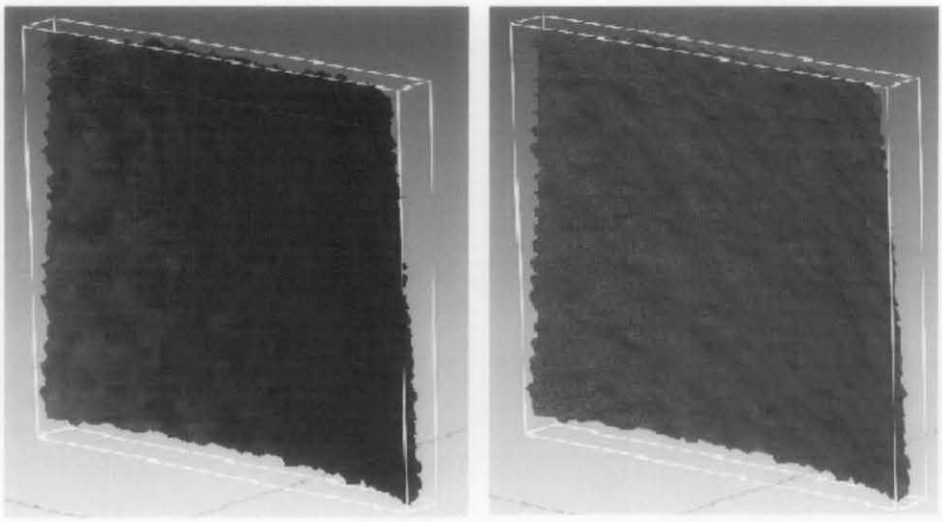

(a) 3D skin sample with color (b) 3D skin sample without color

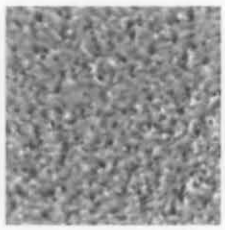

(c) gray scale texture
(139x139 pixels)

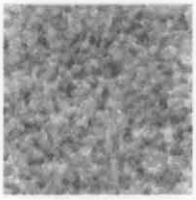

(d) synthesized image
(120x120 pixels)

(e) interaction map
(40x40 pixels)

(f) thresholded cliques
(6 families)

Set 3 - Patient 7 – Arm healthy sample # 2 (17.58mm x 17.96mm x 1.66mm)
Medium visual similarity

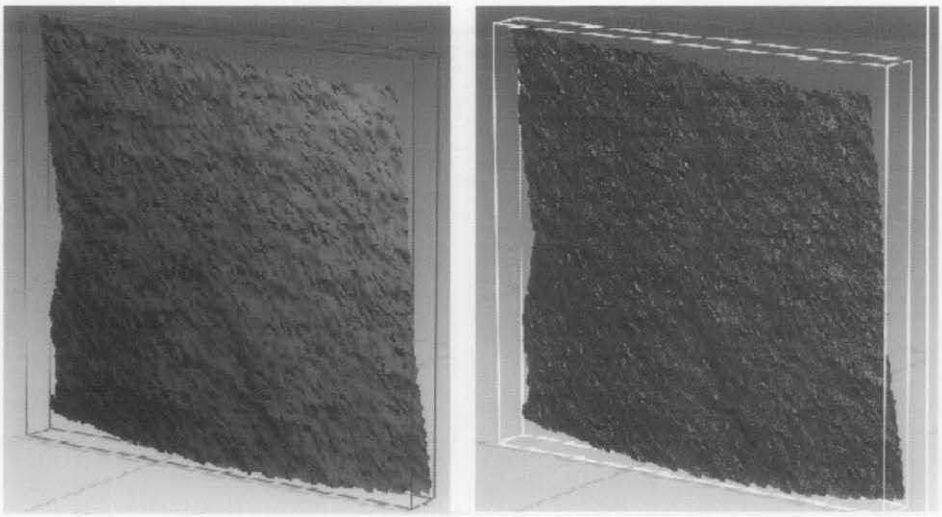

(a) 3D skin sample with color (b) 3D skin sample without color

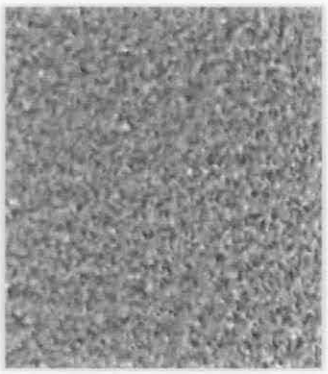

(c) gray scale texture
(226x202 pixels)

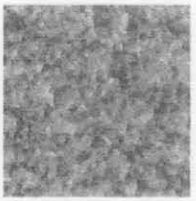

(d) synthesized image
(120x120 pixels)

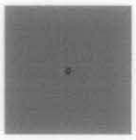

(e) interaction map
(40x40 pixels)

(f) thresholded cliques
(5 families)

Patient 7 – Leg healthy sample # 1 (44.66mm x 34.75mm x 3.76mm)
Medium visual similarity

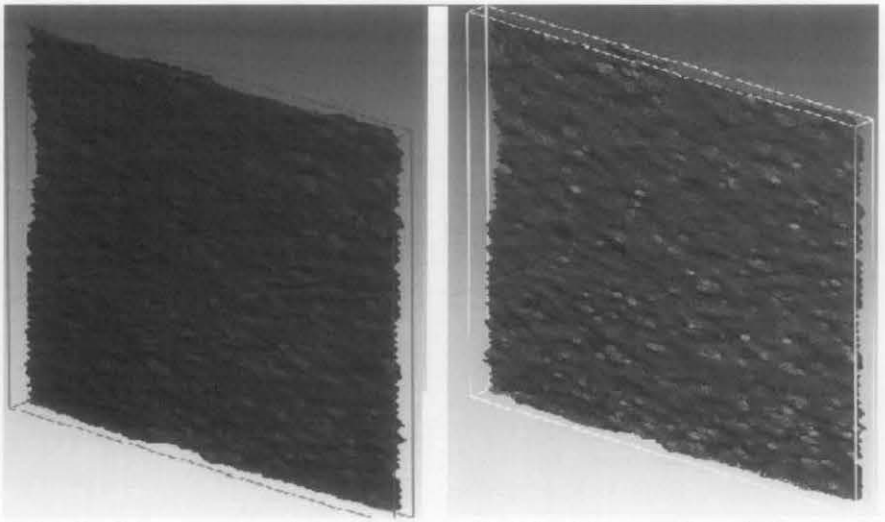

(a) 3D skin sample with color (b) 3D skin sample without color

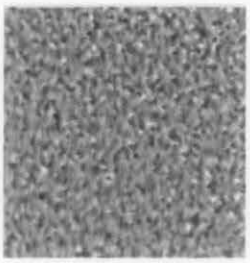

(c) gray scale texture
(156x156 pixels)

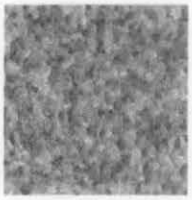

(d) synthesized image
(120x120 pixels)

(e) interaction map
(40x40 pixels)

(f) thresholded cliques
(6 families)

Patient 8 – Trunk healthy sample # 1 (19.54mm x 17.67mm x 0.99mm)
Medium visual similarity

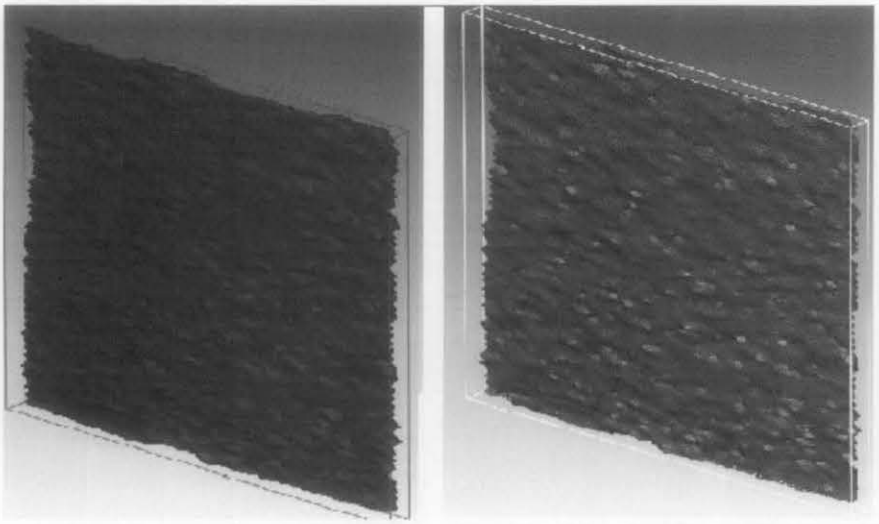

(a) 3D skin sample with color (b) 3D skin sample without color

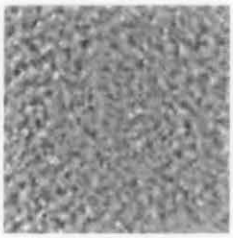

(c) gray scale texture
(143x146 pixels)

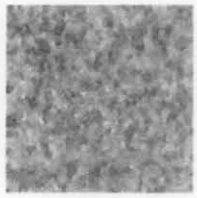

(d) synthesized image
(120x120 pixels)

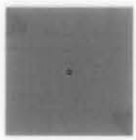

(e) interaction map
(40x40 pixels)

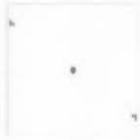

(f) thresholded cliques
(12 families)

Patient 9 – Arm healthy sample # 1 (16.24mm x 16.31mm x 1.55mm)
Medium visual similarity

References

Acosta, E., Temkin, B., Griswold, J. A., Deeb, S. A., and Haluck, R. S., (2001). *Haptic Texture Generation - A Heuristic Method for Virtual Body Structures,* Proceedings of the Fourteenth IEEE Symposium on Computer-Based Medical Systems, CBMS. IEEE Computer Society, Washington, DC, 395

Aysal, T. C., Barner, K. E., (2006). *Stochastic and Deterministic Models for Haptic Pseudo-Textures,* Proceedings of the Symposium on Haptic interfaces For Virtual Environment and Teleoperator Systems Volume 00, HAPTICS. IEEE Computer Society, Washington, DC, 71

Bando, Y., Takaaki Kuratate, Tomoyuki Nishita (2002). *A Simple Method for Modeling Wrinkles on Human Skin*, 10th Pacific Conference on Computer Graphics and Applications, pp. 166-175

Boissieux, L., Kiss, G., Magnenat-Thalmann, N., Kalra, P., (2000). *Simulation of Skin Aging and Wrinkles with Cosmetics Insight,* Computer Animation and Simulation, pp. 15-27

Bowcock, A. M., Cookson, William O.C.M., (2004). *The genetics of psoriasis, psoriatic arthritis and atopic dermatitis,* Human Molecular Genetics, Vol. 13, Review Issue 1 R43-R55

Callieri, M., Paolo Cignoni, Paolo Pingi, Roberto Scopigno, M. Coluccia, G. Gaggio, Maria Novella Romanelli (2003). *Derma: Monitoring the evolution of skin lesions with a 3D system,* Proc. Vision, Modeling, and Visualization Conf., Munich, 167-174

Campion, G., Hayward, V. (2005). *Fundamental Limits in the Rendering of Virtual Haptic Textures,* Proceedings of the First Joint Eurohaptics Conference and Symposium on Haptic interfaces For Virtual Environment and Teleoperator Systems - Volume 00, WHC, IEEE Computer Society, Washington, DC, 263-270

Chee Sun Won and Derin, H. (1988). *Maximum likelihood estimation of Gaussian Markov random field parameters,* International Conference on Acoustics, Speech, and Signal Processing, pp. 1040-1043, vol.2, New York, NY, USA

Choi, S., Tan, H. Z., (2003). *Aliveness: Perceived Instability from a Passive Haptic Texture Rendering System,* Proc. IEEE/RSJ Int'l Conf. Intelligent Robots and Systems, IEEE CS Press, pp. 2678-2683

Choi, S., Tan, H. Z., (2004). *Toward Realistic Haptic Rendering of Surface Texture,* IEEE Comput. Graph. Appl. 24, 2, 40-47

Cotton, S. D., E. Claridge (1996). *Developing a predictive model of human skin colouring,* Proceedings of the SPIE Medical Imaging, R. L. Vanmetter, Beutel, J. Eds, vol. 2708, 814-825

Cotton, S. D., E. Claridge, P. N. Hall (1997). *Noninvasive skin imaging*, Information Processing in Medical Imaging, J. S. Duncan and G. Gindi, Eds. Lecture Notes In Computer Science, vol. 1230. Springer-Verlag, London, 501-506

Cotton, S. D., E. Claridge, P. N. Hall (1999). *A skin imaging method based on a colour formation model and its application to the diagnosis of pigmented skin lesions,* Proceedings of Medical Image Understanding and Analysis (Hawkes D et al Eds), 49-52

Cotton, S. D.,, E. Claridge, P. N. Hall, M. Moncrieff (2002). *From colour to tissue histology: Physics based interpretation of images of pigmented skin lesions,* Medical Image Computing and Computer-Assisted Intervention, Dohi T and Kikinis R (Eds). LNCS 2488, vol I, 730-738: Springer-Verlag

Cula, O. G., K. J. Dana, F. Murphy, B. K. Rao (2005). *Skin texture modeling,* International Journal of Computer Vision, vol. 62, no. 1-2, pp. 97-119

Cula, O. G., Kristin J. Dana, Frank P. Murphy, Babar K. Rao (2004). *Bidirectional Imaging and Modeling of Skin Texture*, IEEE Transactions on Biomedical Engineering, vol. 51, No. 12, pp. 2148 - 2159

Cybernet Corp.: http://www.cybernet.com/

Delgado, D., B. Ersbøll, J. M. Carstensen (2003). *Building an Image-Based System to automatically Score psoriasis*, Proceedings Scandinavian Conference, pp. 557-564

Delgado, D., B. Ersbøll, J. M. Carstensen (2004). *Automatic Scoring of the Severity of Psoriasis Scaling,* Proceedings of the machine Irish conference in machine vision and image processing, Dublin, Ireland, pp. 204-209

Delgado, D., J. M. Carstensen, B. Ersbøll (2004). *Precise multi-spectral dermatological imaging*, Proceedings of the IEEE 2004 medical imaging conference, Rome, Italy, Volume 5, Page(s): 3262 - 3266

Derin, H. and H. Elliot (1987). *Modeling and segmentation of noisy and textured images using Gibbs randm fields,* IEEE Transactions on Pattern Analysis and Machine Intelligence 9(1), 39-55

Dhawan, A. P., Patwardhan, S. V., and Relue, P. A., (2003). *Multi-Spectral Light Interaction Modeling for Imaging of Skin Lesions,* Proceedings of the 25th Annual International Conference of the IEEE EMBS, Cancun, Mexico, 2: 1019 - 1022

FCS robotics: http://www.fcs-cs.com/robotics

FD Tech.: http://www.forcedimension.com/

Fritz, J. P., Barner, K. E., (1996). *Stochastic Models for Haptic Textures,* Proceedings of Photonics East '96 - the SPIE's International Symposium on Intelligent Systems and Advanced Manufacturing, Boston, USA, volume 3901, pages 34–44

Gimel'Farb, G. L., (1999). *Image Textures and Gibbs Random Fields*, Dordrecht, The Netherlands: Kluwer

Gimel'Farb, G. L., Farag, A. A., (2005). *Texture analysis by accurate identification of simple Markovian models*, Cybernetics and Systems Analysis, vol. 41 no. 1, pp. 27-38

Gomez, D. D., Allan Nielsen, Bjarne Ersbøll, Gabriela Maletti (2004). *Multi-Set Multi- Temporal Canonical Analysis of Psoriasis Images,* Proceedings of the IEEE International Symposium on Biomedical Imaging Washington, United States, pp. 1151-1154

Govindaraj, M., A. Garg, A. Raheja, G. Huang, D. Metaxas (2003). *Haptic Simulation of Fabric Hand,* Eurohaptics. Dublin, Ireland, pp. 253-260

Haro, A., Essa, I. A., Guenter, B. K., (2001). Real-time, P*hoto-realistic, Physically Based Rendering of Fine Scale Human Skin Structure,* Proceedings of the 12th Eurographics Workshop on Rendering Techniques, pp. 53 - 62

Healthy Skin. *Healthy Skin Structure and Function, Transdermal and Topical Drug Delivery,* Pharmaceutical Press, 2003

Ho, C.-H., C. Basdogan, M. A. Srinivasan (1999). *Efficient point based rendering techniques for haptic display of virtual objects.* Presence, 8(5):477-491

Ilias Maglogiannis (2003). *Automated segmentation and Registration of Dermatological Images,* Journal of Mathematical Modelling and Algorithms, 2: 277-294

Ilias Maglogiannis, D. Kosmopoulos (2003). *A digital image acquisition system for skin lesions,* SPIE Int. Conf. Medical Imaging, San Diego, United States, 5034: 337-346

Ilias Maglogiannis, S. Pavlopoulos, D. Koutsouris (2005). *An Integrated Computer Supported Acquisition, Handling, and Characterization System for Pigmented Skin Lesions in Dermatological Images,* IEEE Transactions on Information Technology in Biomedicine, vol. 9, No. 1, pp. 86 - 98

Immersion Corp.: http://www.immersion.com

J. H. Nobbs (1985). *Kubelka-Munk theory and the prediction of reflectance,* Rev. Prog. Color. Relat. Top. 15, 66-75

J. Johansson, J. Linde (1999). *Using simple force feedback mechanisms as haptic visualization tools,* Proceedings of the 16th IEEE Conference on Instrumentation and Measurement Technology, Volume: 2, page(s): 820-824

Jiahui Wang, Hideo Saito, Shinji Ozawa, Tomohiro Kuwahara, Toyonobu Yamashita, Motoji Takahashi (2003). *Extraction of Dermo-Epidermal Surface from 3D Volumetric Images of Human Skin,* Int. J. Image Graphics 3(4): 589-608 (2003)

Juha, R., Robrect Jacques, Jukka Kontinen (1999). *Area Assessment of Psoriatic Lesions Based on Variable Thresholding and Subimage Classification,* Proc. of Vision Interface, Canada, pp. 303-311

Khoudja, M. B., Hafez M., Alexandre J.M., Kheddar A., (2004). *Tactile Interfaces. A State of the Art Survey,* International Symposium on Robotics, March 23-26, Paris 2004, pp. 721-726

Kim, L., Kyrikou, A., Sukhatme, G. S., Desbrun, M. (2002). *An implicit-based haptic rendering technique*, IEEE/RSJ International Conference on Intelligent Robots and System, Volume 3, Page(s): 2943 - 2948

Kim, L., Sukhatme, G. S., Desbrun, M. (2004). *A Haptic-Rendering Technique Based on Hybrid Surface Representation,* IEEE Comput. Graph. Appl. 24, 2 (Mar. 2004), 66-75

Klatzky, R. L., Lederman, S. J., C. L. Hamilton, M. Grindley , R. H. Swendsen (2003). *Feeling textures through a probe: Effects of probe and surface geometry and exploratory factors,* Perception and Psychophysics, 65, 613--631.

Kumar, A. Dhawan, P. Relue, P. K. Chaudhuri (2004). *Multi-Spectral Optical Imaging of Skin to Diagnose Malignant Melanoma,* Proceedings of the First Joint BMES/EMBS Conference Serving Humanity, Advancing Technology, Atlanta, USA, Vol.2: 1098-1103

L. Wang, S. Jacques (1992). *Monte Carlo Modeling of Light Transport in Multi Layered Tissues in Standard C* [Online]. Available:http://omlc.ogi.edu/pubs/pdf/man_mcml.pdf

Lakshmanan, S. and Derin, H. (1989). *Simultaneous Parameter Estimation and Segmentation of Gibbs Random Fields Using Simulated Annealing.* IEEE Trans. Pattern Anal. Mach. Intell. 11, 8 (Aug. 1989), 799-813

Lederman, S. J., R. L. Klatzky, C. L. Hamilton, G. I. Ramsay (1999). *Perceiving roughness via a rigid probe: Psychophysical effects of exploration speed and mode of touch*, Haptics-e, The Electronic Journal of Haptics Research, 1, 1.

Li, S. Z., (1995). *Markov Random Field Modeling in Computer Vision,* London: Springer-Verlag

Louden, B. A., Pearce, D. J., Lang, W., Feldman, S. R., (2004). *A simplified psoriasis area severity index (SPASI) for rating psoriasis severity in clinic patients*, Dermatology Online Journal 10 (2): 7, online: http://dermatology.cdlib.org

M. C. Lin, M. A. Otaduy (2005). *Sensation-Preserving Haptic Rendering*, IEEE Comput. Graph. Appl. 25, 4 (Jul. 2005), 8-11

M. Lin, K. Salisbury (2004). *Haptic Rendering--Beyond Visual Computing,* IEEE Comput. Graph. Appl. 24, 2 (Mar. 2004), 22-23

Maletti, G., B. Ersbøll (2003). *Illumination correction from psoriasis image data,* 13th Scandinavian Conference on Image Analysis, Lecture Notes in Computer Science, 2749: 549-556

Maletti, G., B. Ersbøll (2005). *A combined alignment and registration scheme of psoriasis lesions images,* International Journal in Information Sciences, 175: 141-159

Maletti, G., Bjarne Ersbøll, Allan Nielsen, David Delgado Gómez (2004). *Analysis of Time-Varying Psoriasis Lesion Image Patterns,* Proceedings of the IEEE International Symposium on Biomedical Imaging, Washington, United States, pp. 448-451

McGee, M. R., Gray, P., Brewster, S. (2001). *Haptic perception of virtual roughness,* Extended Abstracts on Human Factors in Computing Systems, Seattle, Washington, ACM Press, New York, NY, 155-156

McLaughlin, M. L., Joao P. Hespanha, Gaurav S. Sukhatme (2001). *Touch in Virtual Environments: Haptics and the Design of Interactive Systems,* Pearson Education

Mercier, B. L., A. Kheddar, (2005). *A simple way of integrating texture in virtual environments for haptic rendering,*12th International Conference on Advanced Robotics, Page(s): 755 - 760

Moon, J., Yi, G., Oh, C., Lee, M., Lee, Y., Kim, M., (2002). A *new technique for three-dimensional measurements of skin surface contours: evaluation of skin surface contours according to the ageing process using a stereo image optical topometer,Physiol. Meas.* 23: 247-259 3B3

NPF (2006). *Benchmark survey on psoriasis and psoriatic arthritis - summary of top-line results, National Psoriasis Foundation,* retrieved June 2006, online: http://www.psoriasis.org/

Pai, D. K., Doel, K. v., James, D. L., Lang, J., Lloyd, J. E., Richmond, J. L., Yau, S. H. (2001). *Scanning physical interaction behavior of 3D objects,* Proceedings

of the 28th Annual Conference on Computer Graphics and interactive Techniques SIGGRAPH '01, ACM Press, New York, NY, 87-96

Pai, D. K., L.-M. Reissell (1997). *Haptic Interaction with Multiresolution Image Curves,* Computers and Graphics, Vol. 21, No. 4, pp. 405-411

Park SY, Ha SH, Yu DS, Son SW, Kim DJ, Kim IH, Moon JS, Kim MK, Oh CH (2004). *Quantitative evaluation of severity in psoriatic lesions using three-dimensional morphometry,* Exp. Dermatology 13: 223–228

Patwardhan, S. V., Atam P. Dhawan, Patricia A. Relue (2005). Monte Carlo Simulation of Light-Tissue Interaction: *Three-Dimensional Simulation for Trans-Illumination-Based Imaging of Skin Lesions,* IEEE Trans. On Biomedical Engineering, Vol. 52, No. 7, pp. 1227 – 1236

Patwardhan, S. V., Atam. P. Dhawan (2004). *Multi-Spectral Imaging and Analysis for Classification of Melanoma*, Proceedings of the 26th Annual International Conference of the IEEE EMBS, San Francisco, USA, 1: 503 - 506

Penn, P., H. Petrie, C Colwell, D Kornbrot, S Furner, A Hardwick (2000). *The perception of texture, object size and angularity by touch in virtual environments with two haptic devices*, Proc. First Int. Workshop on Haptic Human Computer Interaction, pp. 92-97

Penn, P., Petrie, H., Colwell, C., Kornbrot, D., Furner, S., Hardwick, A. (2001). *The Haptic Perception of Texture in Virtual Environments: An Investigation with Two Devices,* Proceedings of the First international Workshop on Haptic Human-Computer interaction, S. A. Brewster and R. Murray-Smith, Eds. Lecture Notes In Computer Science, vol. 2058. Springer-Verlag, London, 25-30

Preece, S. J., E. Claridge (2004). *Spectral filter optimisation for the recovery of parameters which describe human skin,* IEEE Trans. PAMI 26(7), 913-922

Preece, S. J., S. Cotton, E. Claridge (2003). *Imaging the pigments of human skin with a technique which is invariant to changes in surface geometry and intensity of illuminating light,* Medical Image Understanding and Analysis 2003, Barber D Ed., 145-148

Psoriasis Treatments (2006). *Psoriasis Newsgroup FAQ,* retrieved May 2006, online: http://www.psoriasisfaq.com/

Quanser Inc.: http://www.quanser.com/

Rapidform http://www.rapidform.com/

S. T. Flock, M. S. Patterson, B. C. Wilson, D. R. Wyman (1989). *Monte Carlo modeling of light propagation in highly scattering tissue-I: Model predictions and comparison with diffusion theory,* IEEE Trans. Biomed. Eng., vol. 36, no. 1, pp. 1162–1168

S. V. Patwardhan (2004). *Multi-Spectral Light Interaction Modeling and Imaging of Skin Lesions,* Ph.D. dissertation, New Jersey Inst. Technol., Newark

Salisbury, J. K., Mandayam A. Srinivasan (1997). *Phantom-Based Haptic Interaction with Virtual Objects,* IEEE Computer Graphics and Applications, vol. 17, no. 5, pp. 6-10

Savolainen, L., Kontinen, J., Roening, J., Oikarinen, A., (1997). *Application of Machine Vision to access involved surface in patients with psoriasis*, British Journal of Dermatology, 137: 395-400

Sensable Tech.: http://www.sensable.com/

Sharman, K.C. (1988). *Maximum likelihood parameter estimation by simulated annealing,* International Conference on Acoustics, Speech, and Signal Processing, page(s): 741-2744, New York, NY, USA

Shi, Y., Pai, D. K., (1997). *Haptic display of visual images,* Proceedings of the 1997 Virtual Reality Annual international Symposium, IEEE Computer Society, Washington, DC, 188-191

Shirado, H., Nonomura, Y., Maeno, T., (2006). *Realization of Human Skin-like Texture by Emulating Surface Shape Pattern and Elastic Structure,* 14th Symposium on Haptic Interfaces for Virtual Environment and Teleoperator Systems, Page(s):295 – 296

Shopf, J., Olano, M., (2006). *Procedural haptic texture,* Proceedings of the 19th Annual ACM Symposium on User interface Software and Technology, Montreux, Switzerland, ACM Press, New York, NY, 179-186

Siira, J., Pai, D. K., (1996). *Haptic texturing—A stochastic approach*, Proc. IEEE International Conference on Robotics and Automation, Minneapolis (1996), 557–562

Tsai, J. S., (2003). *Neuro-Fuzzy Approach to the Segmentation of Psoriasis Images,* Journal of VLSI Signal Processing, Taichung, Taiwan, 35: 19-27

Tsai, J. S., Tao, C. W., Chen, C. C., Yang, C. W., (2002). *Segmentation of Psoriasis Vulgaris Images Using Orthogonal Subspace Techniques,* The Seventh Conference on Artificial Intelligence and Applications, pp. 667-671

Taylor, R. M., (2005). *Haptics for scientific visualization*, ACM SIGGRAPH 2005 Courses, Los Angeles, California, J. Fujii, Ed. SIGGRAPH '05, ACM Press, New York, NY

Theoktisto, V., Fairen, M., Navazo, I., Monclus, E., (2005). *Rendering detailed Haptic Textures,* Workshop on Virtual Reality Interaction and Physical Simulation

Tzovaras D., Nikolakis G., Fergadis, G., Malasiotis, S., Stavrakis, M., (2004). *Design and implementation of haptic virtual environments for the training of the visually impaired,* IEEE Transactions on Neural Systems and Rehabilitation Engineering, Volume 12, Issue 2, Page(s): 266 – 278

Uchida, T. Komeda, T. Miyagi, M. Koyama, H. Funakubo, H. (1996). *Quantification of skin aging by three-dimensional measurement of skin surface contour,* IEEE International Conference on Systems, Man and Cybernetics, Volume: 1, page(s): 450-455

Virtual Tech.: http://www.virtualtechnologiesltd.com/

VIVID 910 http://www.konicaminolta-3d.com/

Wall, S.A., Brewster, S. A., (2003). *Assessing haptic properties for data representation,* SIGCHI conference on Human Factors in Computing Systems, Ft. Lauderdale, Florida, USA, pp. 858-859,

Wall, S.A., Brewster, S. A., (2003). *Scratching the Surface: Preliminary Investigations of Haptic Properties for Data Representation,* Proceedings of Eurohaptics, Dublin, Ireland, pp. 330-342

Wu Y., Nadia Magnenat Thalmann, Daniel Thalmann (1995). *A dynamic wrinkle model in facial animation and skin ageing,* The Journal of Visualization and Computer Animation, vol. 6(4), pp. 195-205

Wu Y., Prem Kalra, Nadia Magnenat Thalmann (1996). *Simulation of Static and Dynamic Wrinkles of Skin,* Proceedings of the Computer Animation , CA. IEEE Computer Society, Washington, DC, 90

Yamada, T., Saito, H., and Ozawa, S., (1998). *3D reconstruction of skin surface from image sequence,* IAPR Workshop on Machine Vision Applications (MVA98)

Yu, W., Brewster, S., (2002). *Comparing Two Haptic Interfaces for Multimodal Graph Rendering,* Proceedings of the 10th Symposium on Haptic interfaces For Virtual Environment and Teleoperator Systems (March 24 - 25, 2002). HAPTICS. IEEE Computer Society, Washington, DC, 3

Yune, Y.-M., Sang Yong Park, Hyun Sook Oh, Dong-Jun Kim, Dong-Su Yoo, Il-Hwan Kim, Jong-Sub Moon, Min-Ki Kim, Chil-Hwan Oh (2003). *Objective assessment of involved surface area in patients with psoriasis,* Skin Research and Technology , 9: 339-342

ist of Publications

1. Nazr-e-Batool, Ahmad Fadzil M Hani. Vooi Voon Yap, "Markov-Gibbs random field modeling of 3D skin surface textures for haptic applications", Proc. ICCSA '07, Kualalumpur, Malaysia, *Lecture Notes in Computer Science, LNCS,* Springer Berlin/Heidelberg, vol. 4706, pages 694-705.

2. Hermawan Nugroho, Nazr-e-Batool, Ahmad Fadzil M.H, P. A. Venkatachalam, "Surface Analysis of Psoriasis for PASI Scaliness Assessment", The International Conference on Intelligent and Advanced System (ICIAS 2007), Kualalumpur, Malaysia.